Detecting solar-like oscillations in the giant star ξ Hydrae

New prospects for asteroseismology throughout the HR-diagram

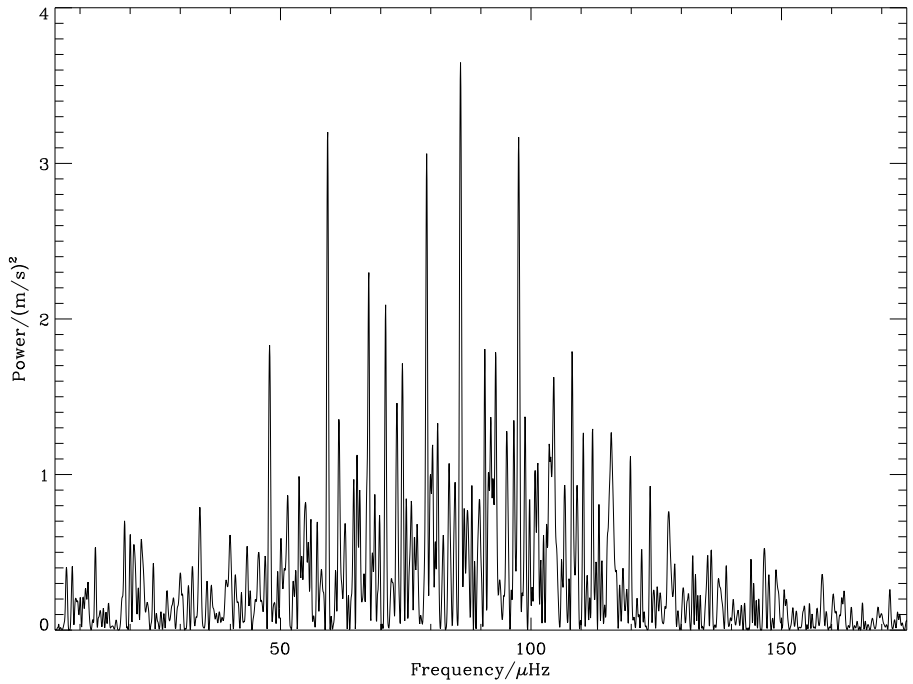

Master's Thesis

Dennis Stello

Department of Physics and Astronomy
University of Aarhus
DK-8000 Aarhus C

August 2002

Preface

Through the years I always nurtured my childlike interest in exploration. I knew that I wanted to explore the unexplored. In the spring of year 2000 it became clear as the Chilean night sky that my exploration of the unknown should be exploring the heavens above. At that time, I stood in front of the large astronomical observing facility of the European Southern Observatory (ESO), La Silla, in Chile. For the first time as an astronomy student I had the opportunity to do real astrophysical science ... I was excited!!!

The project which I then faced, was to perform the observations which form the basis of this thesis. It was part of an overall strategy to find out if information about the structure and evolution of stars in different positions in the Hertzsprung-Russell diagram (i.e stars of different mass, evolutionary stage, and composition) could be obtained using the sophisticated tools of asteroseismology (seismology of the stars). Helioseismology (seismology of the Sun) has provided an incredible amount of detailed information about the Sun's physical state (Christensen-Dalsgaard, 1998b, 2002). This thesis describes my part of the project, which is focused on evolved stars of roughly solar temperature, the so-called red giant stars. This investigation has special interest in relation to the science preparation of near-future asteroseismic space missions like RØMER/MONS, MOST, COROT, and Eddington.

Hans Kjeldsen and my supervisor Søren Frandsen both from Aarhus University, were granted observing time in the spring of year 2000 on the Danish 1.54m telescope at La Silla. The observing time was dedicated to the observation of the giant star ξ Hydrae, which was the target of my project, and to an additional asteroseismic investigation of the sdB star PG1605+072, the latter in collaboration with Simon O'Toole and Timothy Bedding from University of Sydney (O'Toole et al., 2002) (**Paper II**). Only the project on ξ Hydrae will be discussed in this thesis. The total amount of observation time used for the ξ Hydrae observations was 175 hours, distributed over a period of 29 successive nights in March and April and a shorter period of 11 nights in May of the same year. The total time coverage of the observations was 71 days (cf. Table 2.2, Chapter 2). In order to investigate the asteroseismic properties, we wanted to measure the small stellar oscillations of ξ Hydrae through their effect on the equivalent width of selected spectral lines due to temperature variations. In the spring of year 2002 additional observations were made based on radial velocity measurements.

In the following I will use the opportunity to thank the persons who made it an instructive, exciting, and pleasant time working at the institute during the past year.

First of all I would like to thank both Hans Kjeldsen and my supervisor Søren Frandsen for their guidance during my work on the ξ Hydrae project and in the first place for letting me do real astrophysical observations, which I enjoyed very much. A special thanks to Hans Kjeldsen for assisting and introducing me to the telescope the first few days at La Silla. I also appreciate Hans' unfailing enthusiastic attitude towards the project even at the moments when the thought crossed my mind to throw it all away, forget about astronomy, and just be a lawyer instead.

During the time working on the data reductions of ξ Hydrae, I also investigated the distance problem of the Pleiades cluster (Stello, 2000b). Even though the subject did not directly relate to my project on ξ Hydrae, I at least owe these few lines of the preface of this thesis to thank Poul Erik Nissen and Frank Grundahl for encouraging me to make my first publication based on my investigation of the Pleiades cluster (Stello & Nissen, 2001) (**Paper III**). This process taught me a great deal about the more practical aspects of astrophysical science. The experience I gained from doing that work has been a tremendous help in my current investigation of ξ Hydrae and in the writing of this thesis.

I would like to thank Hans Bruntt, Teresa Teixeira, Frank Pijpers and Jørgen Christensen-Dalsgaard for helping me obtaining the stellar parameters and model calculations of ξ Hydrae. I thank Martin Knudsen for letting me analyse his data on HR1217 to compare with my own data. Frank Grundahl, Kim Lang, and Martin Knudsen should be thanked for helping me in the start-up phase as I was a novice IDL user. My officemates Svend Runge, Steffen Hokland, and Mathias Egholm deserve credit for the good atmosphere, including the smell of *Yum-yums*, fruitful discussions on IDL, Latex, and Unix commands, and the leftovers of cake from the General Physics Colloquiums - which was greatly appreciated during late working hours.

Hans Kjeldsen should be thanked for fruitful discussions and for reading the first draft of this thesis, which has greatly improved the presentation of my results. I also thank Teresa Teixeira for her comments on the scientific presentation of this thesis. I am indebted to Brandon Tingley for reading through the entire thesis, to correct my non-perfect English grammar, which I appreciate very much.

Last but not least a cordial thanks to my wonderful girlfriend Kristine. Thanks for all the things you did for me (non mentioned non forgotten) especially during the time of writing this thesis ... grazie mia principessa ;o)

Dennis Stello
Århus, August 15, 2002

Structure and notations

This short introductory chapter explains the overall structure of the thesis and the applied general notations.

This thesis outlines the data reduction and analysis of two independent data sets. The first data set was partly collected by myself in the spring of 2000 and will be designated *the equivalent width data set*. Using another instrument, a new data set on the same target star was collected in the spring of 2002. This second data set will be designated *the radial velocity data set*.

Instead of dividing the thesis in two parts, one for each data set, following the chronological order of the observing process, I decided to make a subject structure. Within each subject or chapter the two data sets are then described in separate sections (see further the table of contents).

For the entire data reduction and analysis a total of 36 IDL[1] programs were created. These programs are described through detailed headers and comments for each part of the code of the programs. Due to their specific nature, the source codes of these programs are not included in the thesis, but can be supplied by request to the author. The programs are marked with **bold face** in the thesis.

At the end of the thesis, my publications are included:

- Paper I: *Detection of solar-like oscillations in the G7 giant star ξ Hya.*
  Contribution: Got the idea for observing ξ Hya using the CORALIE spectrograph. Shared primary author together with Søren Frandsen. Have been involved in all parts except the modeling.

- Parer II: *Time-series spectroscopy of pulsating sdB stars - II. Velocity analysis of PG1605+072.*
  Contribution: Performed part of the observations.

- Parer III: *The problem of the Pleiades distance. Constraints from Strömgren photometry of nearby field stars.*
  Contribution: All the data analysis and the writing of the paper.

[1] Interactive Data Language (IDL).

In order to use simple notation the following denotes

- the average of x: $\langle x \rangle$;
- c equals the average of a and b: $c = \langle a, b \rangle$;
- short notation for *seconds*: 's', e.g. 12s;
- quantity 'Q' and its error 'E': Q(E), e.g. $12.2(3)$ means 12.2 ± 0.3, or $12.2(3.1)$ means 12.2 ± 3.1.

Contents

List of Tables

List of Figures

Chapter 1

Introduction

An understanding of the structure and evolution of stars is central to much of astrophysics, which, besides the astronomical interest, also has large impact on a range of physical areas like gas and plasma theory. To be able to understand stellar structure and evolution, we must study stars at different evolutionary stages.

As briefly described in the preface of this thesis, the goal of the current investigation is to test to what extent the concepts of asteroseismology (i.e. the investigation of convectively powered oscillations, also called solar-like oscillations; cf. Sect. 1.2) can be applied to the red giant stars. In order to examine this, the properties of the oscillations of giant stars, and in particular the target star ξ Hydrae (for short, ξ Hya), are investigated. If it turns out that the observations support the theoretical asteroseismic predictions, the concepts of asteroseismology will provide a powerful tool to study the stellar structure of stars in this late evolutionary state, the red giant phase.

I will in this chapter give the background information needed to understand how this goal can be achieved. First, I introduce the type of stars which this current investigation focuses on, namely the red giant stars. I explain the state of evolution and give the characteristic ranges of the basic stellar parameters mass, luminosity, and radius for these kind of stars (cf. Sect. 1.1). Second, in Sect. 1.2, an introduction is given to the basic concepts of asteroseismology, especially related to solar-like oscillations. Based on the presented theoretical predictions and known observational results, the oscillation properties of red giant stars are discussed with the aim of determining the prospects for studying giant stars with asteroseismic tools. This will include a specific list of goals which are expected to be attained (cf. Sect. 1.3). This will be followed by a presentation of observational tools and a description of the techniques used in this investigation to detect stellar oscillations in the target star ξ Hya (cf. Sect. 1.4). Finally at the end of this chapter, I introduce the target star, ξ Hya, and present its basic stellar parameters and expected asteroseismic properties (cf. Sect. 1.5).

I will in the following not present a complete overview of the theory of stellar evolution but merely stress a few parts relevant for the introduction of the red giant stars. An excellent introductory text on the theory of stellar evolution is written by Christensen-Dalsgaard (1995). As a background, the general stellar evolution of a $5\,M_\odot$ star is nevertheless shown in Fig. 1.1. It shows an illustrative, though not state-of-the-art, stellar evolutionary track, including specified evolutionary characteristics of the different phases, of a $5\,M_\odot$ star in a luminosity vs. effective temperature diagram, the so-called Hertzsprung-Russell (HR) diagram. The evolutionary track ranges from the beginning of central hydrogen burning (at the zero age main sequence, or ZAMS, marked at point 1 in Fig. 1.1) to the asymptotic giant branch (after point 14) where the star finally shows massive mass loss and develops into a white dwarf.

1.1 The red giant stars

1.1.1 Evolutionary state

Theoretical stellar models predict that a star close to the end of its evolution after roughly 90% of its life time when core hydrogen is exhausted, will expand and become a red giant star. The onset of the first[1] giant phase is indicated at point 6 in Fig. 1.1.

The red giant stars occupy a very muddled region of the HR diagram positioned on the right-hand side of the instability strip[2]. The evolutionary tracks of stars with main sequence spectral classes ranging from late B to K all converge in this region as they enter the red giant phase, with spectral class late G to M. The evolutionary tracks corresponding to the phase from point 6 to point 8 in Fig. 1.1 are therefore quite close to each other. The effect is clearly seen in Fig. 1.2. This makes it difficult to determine the stellar progenitor of a giant star, especially if the typical errors of the observed stellar parameters of these stars and thus the stellar position in the HR diagram are taken into account (typical errors are: $\sigma_{T_{\rm eff}} \sim$ 50-100 K, $\sigma_{L/{\rm L}_\odot} \sim$ 3-9). The exact evolutionary stage of a red giant star is also subtle due to the difficult determination whether the star is ascending (from point 6 to 7; Fig. 1.1) or descending (from point 7 to 8) the red giant phase.

1.1.2 Basic parameters and interior characteristics

Models of red giants have masses ranging from 0.2-10 $M_\odot$ and radii ranging from 2-100 $R_\odot$ (Hatzes & Cochran, 1998). Luminosities of red giants range from a few tenths to one thousand times the luminosity of the Sun. Thus, in general, red giant stars are large compared to their progenitor and have consequently low surface density ($\log g \sim$ 1.5-3.0 cm/s^2), temperature ($\sim$ 3500-5000 K), and rotation rate ($v \sin i \sim$ 1-10 km/s) (Allen, 1973; Pasquini et al., 2000). Additionally, they may suffer mass loss

[1] The second giant phase following point 14 on Fig. 1.1 will not be discussed in this thesis.

[2] The instability strip and three red giant stars are indicated in Fig. 1.3, on page 6.

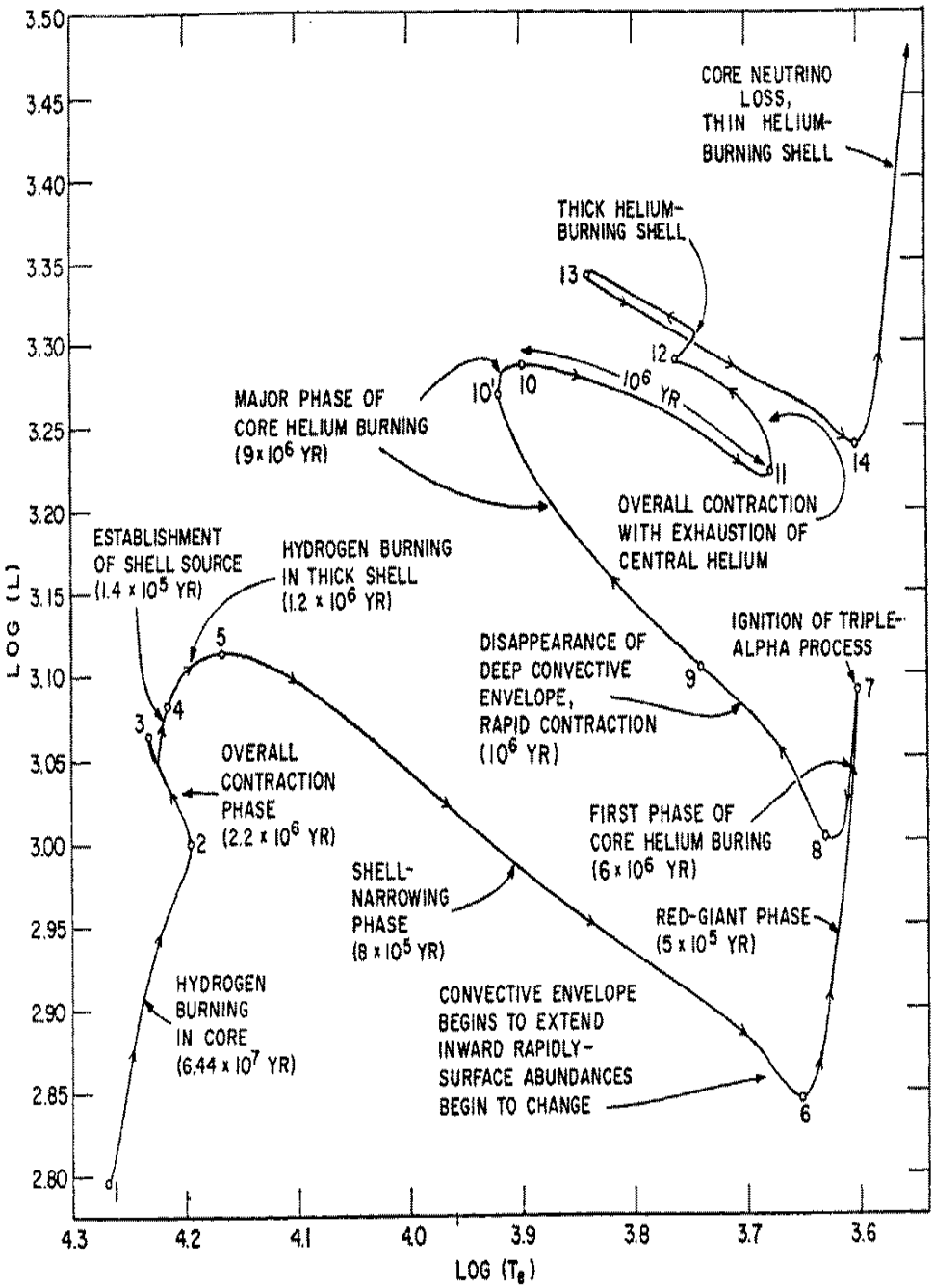

Figure 1.1: The stellar evolutionary track of a metal rich $5\,M_\odot$ star in the Hertzsprung-Russell diagram. The abscissa indicates the luminosity L in solar units, and the ordinate indicates the effective temperature in Kelvin. Labeled evolutionary times between successive indicated points are given in years. (From Iben, 1967).

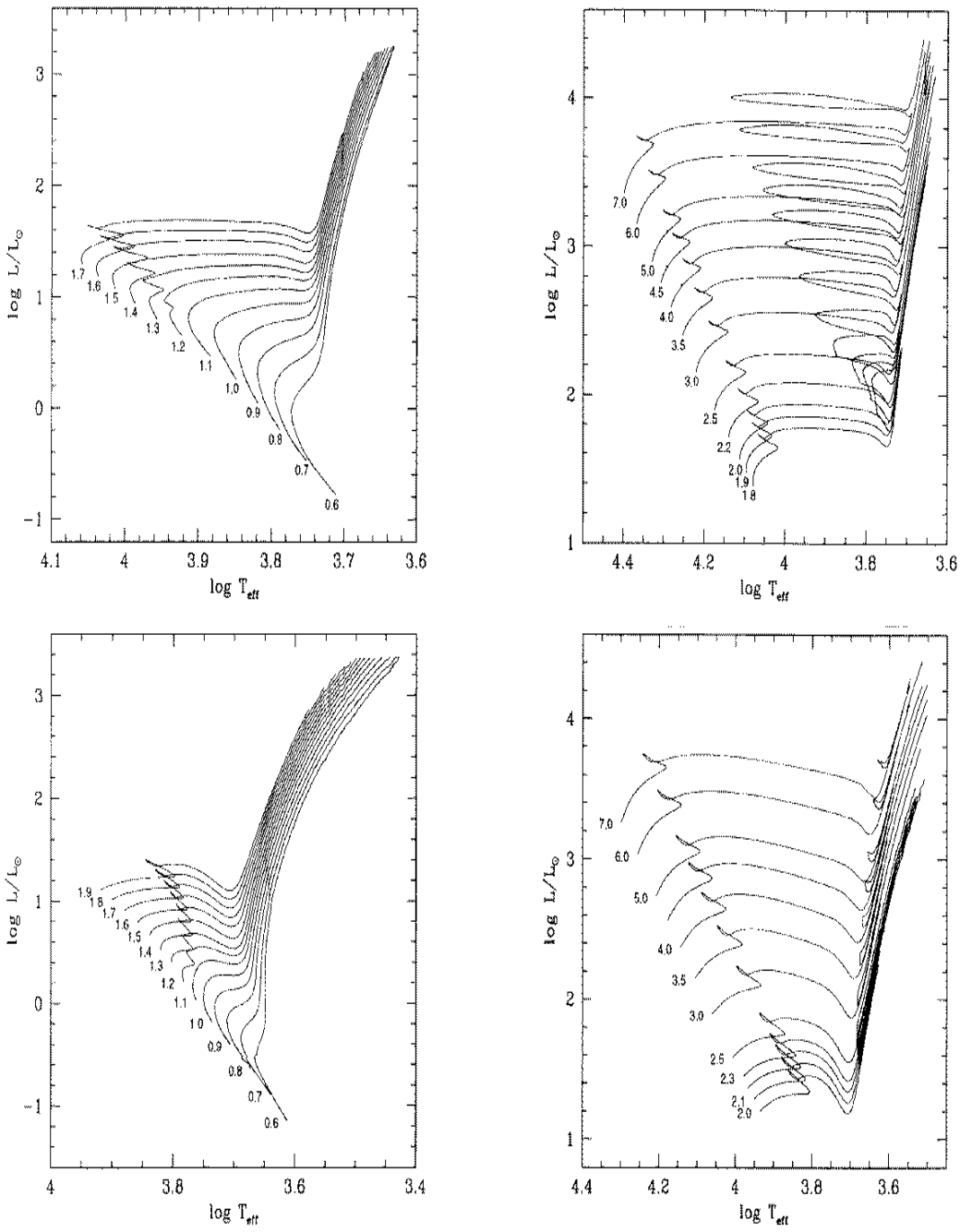

Figure 1.2: The stellar evolutionary tracks in the Hertzsprung-Russell diagram (*top panels*) of metal pour (Z=0.0004) stars and (*bottom panels*) of metal rich (Z=0.03) stars. The different masses are indicated in solar units at the ZAMS. The abscissa and ordinate are the same as in Fig. 1.1. (From Girardi et al., 2000).

in this late evolutionary phase. Spectroscopically they show very narrow absorption lines. The stellar parameters of the target star ξ Hya are given in Sect. 1.5.

Due to the low surface temperature, the opacity in the outer envelope of giant stars is high and therefore the radiative temperature gradient (i.e. the gradient required to transport the entire luminosity by radiation) becomes correspondingly higher than the adiabatic gradient. Hence energy transport will take place via gas motion where relatively hot gas cells rise and cooled gas falls. This process is known as convection. The convection zone of giant stars starts at the surface and penetrates deeply into the interior as the star expands on its way up the Hayashi track (from point 6 to 7 in Fig. 1.1) (Christensen-Dalsgaard, 1995; Gray & Nagel, 1989).

1.2 Asteroseismology

In this section I describe the concepts of asteroseismology necessary to understand the observational and theoretical methods used in the current investigation.

Many stars, positioned differently in the HR diagram, are known to be variable. Fig. 1.3 shows an HR diagram where the approximate regions of known variable stars are indicated (see figure caption). Inside the instability strip, between the two parallel nearly vertical dashed lines, are the classical large amplitude ($\sim$ 1 magnitude; Cox (1980)) variable stars, the Cepheids. The variability of these stars has been known for many years and has provided information on e.g. the intergalactic distance scale (Sandage & Tammann, 1968). The general excitation mechanism for the stars inside the instability strip is the so called κ-mechanism, which is opacity driven (Cox, 1980). For further details about the κ-mechanism consult Baker & Kippenhahn (1962).

The group of variable stars including the Sun (labeled "Solar-like" in Fig. 1.3) show much lower variability than the classical Cepheids (amplitudes are in the order of 10^{-6} mag; Kjeldsen & Bedding (1995)), requiring sophisticated observational techniques to detect (cf. Sect. 1.4). The oscillations that cause this low amplitude variability were identified for the first time in the Sun (Leighton et al., 1962), hence the designation solar-like oscillations. The period of these oscillations is roughly 5 minutes for the Sun.

The now well-known five-minute oscillations of the Sun are believed to be stochasticly excited by turbulence in the outer convection envelope of the Sun (Goldreich & Keeley, 1977). These oscillations are characterized as acoustic waves, with the pressure gradient being the dominant restoring force, hence their name - p-modes. In e.g. white dwarf stars another type of oscillations has been observed (e.g. Winget et al., 1991), called g-modes. The dominant restoring force for these modes is buoyancy. Even though there have been a few claims of detections of g-modes (e.g. Gabriel & the GOLF Team, 1998), only p-modes have clearly been detected in the Sun (Appourchaux et al., 2000).

The solar p-modes contain information about the sound speed in the gas which

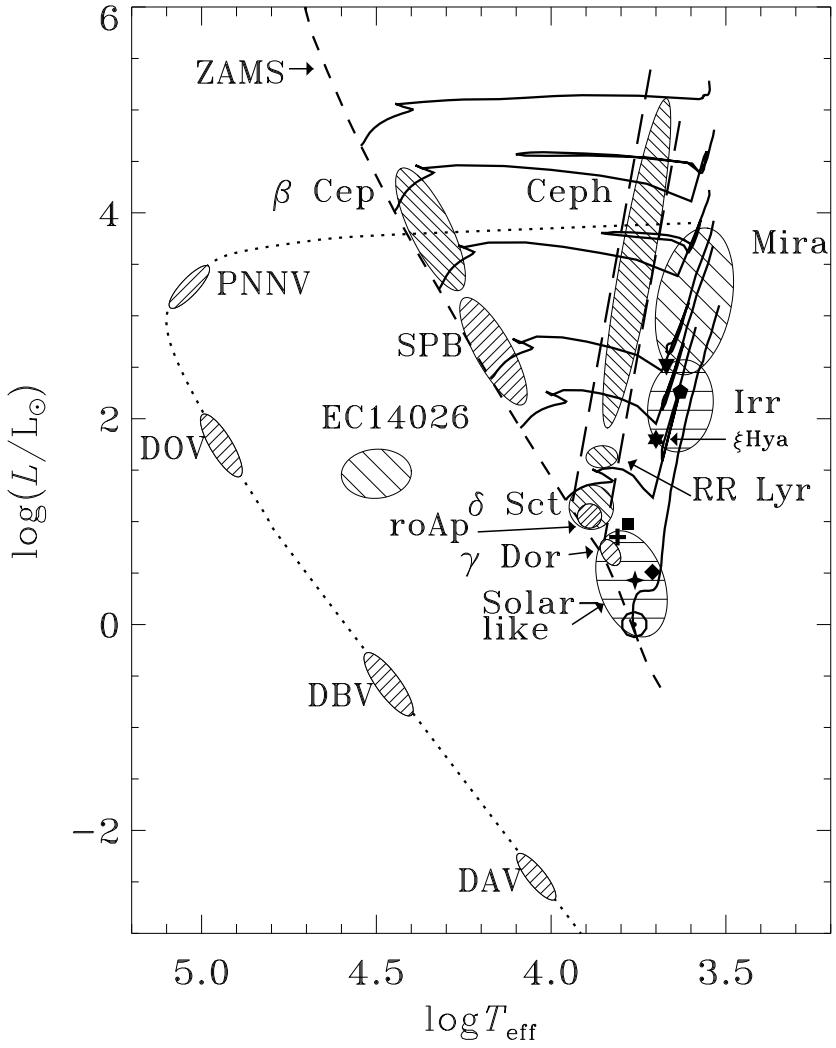

Figure 1.3: The Hertzsprung-Russell diagram with indicated names and approximate locations of known groups of variable stars. The diagonal and the two parallel vertical dashed lines indicate the ZAMS and the instability strip, respectively. Stellar evolutionary tracks of different masses are shown as thick solid lines. The single symbols to the right of the instability strip indicate the position of ξ Hya and other stars which are of particular importance in the context of this and other asteroseismology investigations made so far. The stellar designations of these stars are (most luminous first): α Ursae Majoris (triangle); Arcturus (pentagon); ξ Hydrae (six hooked star); η Bootis (square); Procyon (plus); δ Eridani (diamond); β Hydri (four hooked star); α Centauri and the Sun (both $\odot$). (The figure is slightly modified compared to the original, which has kindly been supplied by J. Christensen-Dalsgaard.).

is related to physical parameters in the interior of the Sun (e.g. the density and the mean molecular weight). It is from seismic investigations of these oscillations (Helioseismology) that we can study the solar structure. That has provided valuable information about the depth of the solar convection zone, the large-scale rotation, and is beginning to yield information about the complex subsurface structure and dynamics of sunspot regions. (Christensen-Dalsgaard, 1998b, 2002)

Extending the sophisticated tools of Helioseismology to other stars (Asteroseismology) can reveal important information about different stellar parameters. The theoretical stellar models can be tested and stellar parameters thereby constrained. Additionally, a better knowledge of the excitation and damping mechanism of the oscillations can be gained, which would lead to a more correct treatment of convection in stellar modeling.

Asteroseismology suffers, though, from the fact that the oscillations are of extremely small amplitudes[3], or more correctly expressed, that the stars are so far away from us[4] compared to the Sun. A star of 3.5 magnitudes like ξ Hya (cf. Table 1.1), would provide only $\sim 10^{-12}$ the number of photons relative to whole disk integrated light observation of the Sun. Furthermore, it is not possible to resolve the stellar surface like in the solar case. Thus many oscillation modes which require high spatial resolution (those of many sign changes across the stellar hemisphere) will not be detected in the whole disk integrated light observation of other stars. It is therefore not expected, that asteroseismology on other stars will reveal information of such detail as in the solar case.

The observational results actually obtained in recent years are beginning to reveal very interesting information in a handful of dwarf stars and sub giants in the solar-like region (indicated in Fig. 1.3). In particular, the last year has been exciting, which suggests that the coming decade will be a breakthrough for asteroseismology observations. A short summary of what has been achieved will be given in Sect. 1.2.2 after the basic properties of the oscillations have been given in Sect. 1.2.1.

Before emphasizing the oscillation properties which will be used to understand and interpret the observational data in later sections (cf. Chapter. 5) I give a few relevant references to the subject. For a thorough introduction to the physical basis for understanding stellar pulsations consult the text of Cox (1980), or Christensen-Dalsgaard (1998a). In addition, a brilliant review of asteroseismology has been written by Brown & Gilliland (1994).

[3]The solar oscillation amplitudes are roughly 23 cm/s in radial velocity, which in luminosity is a variation of 4 ppm (parts per million) (Kjeldsen & Bedding, 1995).

[4]That the solar-like oscillations display such small amplitudes assures in fact that the modes only have a small influence on the stellar structure, and that linear theory is adequate to describe the mode characteristics (Brown & Gilliland, 1994).

1.2.1 Oscillation properties

If a star is assumed to be spherical, which is a reasonable assumption[5], each oscillation mode is characterized by a function ξ, which is a product of a radial component, $\xi(r)$, and a spherical harmonic, $Y(\theta, \phi)$, (with notation of Brown & Gilliland, 1994)

$$\xi_{nlm}(r, \theta, \phi, t) = \xi_{nl}(r) Y_l^m(\theta, \phi) e^{-i2\pi\nu_{nlm}t} \ . \tag{1.1}$$

ξ could be any scalar perturbation (e.g. luminosity, radial velocity, equivalent width; cf. Sect. 1.4) which is associated with the small radial displacements of the oscillation mode. Here r, θ, ϕ are the usual spherical coordinates, t is the time, and ν_{nlm} is the mode frequency, which depends on the set of mode quantum numbers (n, l, m) defining each mode. The radial order n specifies the number of nodes of the mode between the center and the surface of the star. Since n is related to the depth structure of the mode it is not directly observable. The angular degree l, or rather $\sqrt{l(l+1)}$, is roughly speaking the number of wavelengths along the stellar circumference (Christensen-Dalsgaard, 1998a). Thus high degree modes show many variations (sign changes) across the stellar hemisphere. The azimuthal order m is the projection of l onto the stellar equator, thus taking values between $-l$ and $+l$.

When a wave associated with a given oscillation mode penetrates into the interior of a star it bends due to the increasing sound speed, and therefore reaches a certain depth, called the turning point, and moves outward again, to be reflected at the surface, etc. Modes of lower degree reach larger depths; a special case is the $l = 0$ mode which is purely radial.

Observational response

When observing a distant star the stellar surface cannot be resolved, and therefore the high degree modes tend to cancel out. The cancellation-effect as a function of degree l can be described by the so-called response function, which is the ratio of the observed amplitude to the actual amplitude. The response depends on both center-to-limb variations of the intensity (classical limb darkening; cf. Gray (1992)) and on the particular perturbation under consideration (i.e. the observed oscillation signal).

The radial velocity oscillation signal (cf. Sect. 1.4) has a projection factor into the line-of-sight, which makes it less sensitive to $l = 0$ and $l = 1$ modes compared to the luminosity signal. However, due to higher weight of the central parts of the stellar disk relative to the edge, radial velocity measurements allow one to detect modes of higher degree ($l \lesssim 3$) than by taking only luminosity measurements. (cf. Christensen-Dalsgaard, 1998a, Fig. 2.2).

The equivalent width of the Balmer lines (cf. Sect. 1.4) also contains spatial information, through an effect analogous to limb darkening. Manifested by a possible

[5]This assumption is especially good for slowly rotating stars, like red giants.

detection of a $l = 3$ mode in the star η Bootis, the investigation of Kjeldsen et al. (1995) indicated for the first time that a "limb darkening" effect of the equivalent width of the Balmer lines existed. This effect was confirmed by Bedding et al. (1996) who analysed stellar atmosphere models with temperatures around solar to produce intensity spectra at different points on the stellar disk. Due to changes in the formation depth of the spectral lines, the equivalent width of the H_α and H_β line decreased from center to limb. The approximate decrease at 70° degrees from the center of the stellar disk was $\sim 70\%$ relative to the center. This can be compared to the decrease in intensity by classical limb darkening which at 70° degrees yields roughly 40-50% using the Eddington approximation for the temperature structure in the stellar atmosphere (the grey case) (Gray, 1992). The "limb darkening" effect of the equivalent width of the Balmer lines is significantly larger than the classical limb darkening. The conclusion drawn by Bedding et al. (1996) was that this Balmer line "limb darkening" effect enables detection of modes with $l \leq 4$ for whole disk integrated light observations.

Interpretation of frequencies and amplitudes

Observations of the stellar oscillations yield their frequencies and amplitudes. The frequency can provide information on the density of the star, while the amplitude can reveal information about the driving and damping mechanism of the modes and the surface gravity. Furthermore through comparison between theoretical predicted frequencies and the observed frequencies it is possible to place constraints on the parameter space for the observed stars.

Frequencies: In general there is no simple relation between frequency, ν_{nlm}, and the quantum numbers n, l, and m. But as long as the star does not rotate, which in general is a fair approximation in the case of red giant stars, the orientation of the polar axis is arbitrary, hence the frequencies are independent of m.[6] In the limit where $l \ll n$, asymptotic theory can be applied (e.g. Christensen-Dalsgaard, 1998a; Tassoul, 1980) and the frequency can be approximated by (with notation of Brown & Gilliland, 1994)

$$\nu_{nl} = \Delta\nu_0\big(n + \frac{l}{2} + \epsilon\big) - \frac{Al(l+1) - \eta}{n + l/2 + \epsilon} \tag{1.2}$$

where $\Delta\nu_0$, A, ϵ, and η are constants involving integrals over the structure of the stellar interior. If the second term on the right-hand side (which is small) is ignored, the power spectrum of the time series is expected to show an equally spaced frequency pattern with a primary separation of $\Delta\nu_0$, called the *large separation*, between successive values of n. Modes with odd values of l fall halfway between even l modes, which are degenerate with those of successive n (thus: $\nu_{n,l} = \nu_{n+1,l-2}$).

[6] This m independency is due to the cancellation of the equal regions of positive and negative sign of the modes with $m \neq 0$, when the polar axis is chosen as the line of sight. A visualization of selected modes (or rather the spherical harmonic part) with different quantum numbers (l, m) can be seen in Christensen-Dalsgaard (1998a, Fig. 2.1).

$\Delta\nu_0$ is roughly equal to the inverse of two times the sound travel time from the surface to the center, which is related to the mean density, $\bar{\rho} = M/R^3$, of the star (Kjeldsen & Bedding, 1995):

$$\begin{aligned} \Delta\nu_0 &= \left(2\int_0^R \frac{\mathrm{d}r}{c_s}\right)^{-1} \\ &= \left(\frac{M/\mathrm{M}_\odot}{R^3/\mathrm{R}_\odot^3}\right)^{1/2} \times (134.92 \pm 0.02)\,\mu\mathrm{Hz}\ . \end{aligned} \tag{1.3}$$

Here, c_s is the local sound speed, and R and M are the stellar radius and mass. The $\odot$ indicates the solar values, and $\Delta\nu_{0,\odot} = 134.92(2)\,\mu$Hz is adopted from Toutain & Froehlich (1992).

The deviation from the perfect equally spaced frequency pattern comes from the last term on the right-hand side of Eq. 1.2 and is defined as: $\delta_{nl} \equiv \nu_{n,l} - \nu_{n+1,l-2}$, which is not constant. This is called the *small separation* and contains information about the molecular weight in the stellar core and hence the age, due to the changing molecular weight during nuclear burning (Ulrich, 1986).

The frequencies of solar-like oscillations are distributed in a broad frequency range reflecting the stochastic nature of the excitation mechanism (cf. Christensen-Dalsgaard & Frandsen, 1983). The frequency distribution is modulated by an envelope, which has a maximum "peak" and two tails reflecting the balance between acoustical energy generation by turbulent convection and linear damping. Houdek et al. (1999) stress that it is the modulation of the turbulent fluxes (heat and momentum) by the pulsations that seems to be the predominant mechanism for the excitation and damping of solar-like oscillations. The comparison of the amplitude distribution of the Sun with that predicted by theory shows a non-perfect match, especially at the high frequency range (Houdek et al., 1999, Fig. 8). The imprecise theoretical description of the amplitude distribution is primarily due to the lack of a proper theory of convection in a pulsating environment.

The frequency $\nu_{\max}$, which has maximum amplitude, indicates the position of the oscillation envelope. Brown et al. (1991) presented a scaling relation to estimate $\nu_{\max}$ for an arbitrary star, given its mass, radius, and effective temperature. They assume that $\nu_{\max}$ scales with the acoustic cut-off frequency, which sets the intrinsic upper limit to the observed frequencies (cf. Christensen-Dalsgaard & Frandsen, 1983), and hence can be written as:

$$\nu_{\max} = \frac{M/\mathrm{M}_\odot}{(R/\mathrm{R}_\odot)^2\sqrt{T_{\mathrm{eff}}/\mathrm{T}_{\mathrm{eff},\odot}}} \times 3.05\,\mathrm{mHz}\,, \tag{1.4}$$

when using the solar values, designated with $\odot$, $\nu_{\max,\odot} = 3.05\,$mHz, and $\mathrm{T}_{\mathrm{eff},\odot} = 5777\,$K. Ignoring A and η in Eq. 1.2, using $\epsilon_\odot \simeq 1.6$, and inserting Eqs. 1.3, 1.4 yields the prediction of the order n with maximum power:

$$n_{\max} = \left(\frac{M/\mathrm{M}_\odot}{(R/\mathrm{R}_\odot)\,(T_{\mathrm{eff}}/\mathrm{T}_{\mathrm{eff},\odot})}\right)^{1/2} \times 22.6 - 1.6\,. \tag{1.5}$$

Amplitudes: Christensen-Dalsgaard & Frandsen (1983) calculated the expected oscillation amplitudes of a variety of stars in the near solar-like region (cf. Fig. 1.3). These calculations were based on the equipartition between the oscillation energy integrated over the star and the kinetic energy in one convective eddy having the same turnover time as the period of the oscillation[7]. This simplified description for the excitation mechanism was suggested by Goldreich & Keeley (1977).

To be able to estimate the oscillation amplitude for any given star, Kjeldsen & Bedding (1995) introduced a scaling relation of the radial velocity amplitude, $v_{\rm osc}$, based on the model calculations of Christensen-Dalsgaard & Frandsen (1983) and the measured solar velocity amplitude ($v_{\rm osc,\odot} = 23.4 \pm 1.4\,{\rm cm/s}$). The scaling relation given by Kjeldsen & Bedding (1995, Eq. 7)[8] is

$$v_{\rm osc} = \frac{L/{\rm L}_\odot}{M/{\rm M}_\odot} \times (23.4 \pm 1.4)\,{\rm cm/s}\ , \tag{1.6}$$

where L and M is the luminosity and mass respectively, and $\odot$ indicates the solar values.

Subsequent detections of solar-like oscillations in a handful of stars (cf. Sect. 1.2.2) have recently given rise to a revision of this relation by the same authors (Kjeldsen & Bedding, 2001), who proposed a $1/g$ scaling relation, where g is the stellar surface gravity. Noting that $L/M \propto T_{\rm eff}^4/g$, the $1/g$ relation is

$$v_{\rm osc} = \frac{L/{\rm L}_\odot}{(M/{\rm M}_\odot)(T_{\rm eff}/{\rm T}_{\rm eff,\odot})^4} \times (23.4 \pm 1.4)\,{\rm cm/s}\ , \tag{1.7}$$

which can be expressed in terms of luminosity variations if combined with the relation between $v_{\rm osc}$ and $(\delta L/L)_{\rm bol}$ (Kjeldsen & Bedding, 1995, Eq. 5)[9],

$$\begin{aligned}(\delta L/L)_{\rm bol} &= \frac{v_{\rm osc}/ms^{-1}}{T_{\rm eff}/{\rm T}_{\rm eff,\odot}} \times (17.7 \pm 0.4)\,{\rm ppm} \\ &= \frac{L/{\rm L}_\odot}{(M/{\rm M}_\odot)(T_{\rm eff}/{\rm T}_{\rm eff,\odot})^5} \times (4.1 \pm 0.3)\,{\rm ppm}\ ,\end{aligned} \tag{1.8}$$

where ${\rm T}_{\rm eff,\odot} = 5777\,{\rm K}$ (note that 1 ppm equals $1.086\,\mu$mag).

Using $L \propto R^2 T_{\rm eff}^4$ and neglecting any variation in the radius due to the extremely small amplitudes of the solar-like oscillations, the relative change in the bolometric luminosity is related to the relative change in temperature by $(\delta L/L)_{\rm bol} = 4\,\delta T_{\rm eff}/T_{\rm eff}$. Combining this with Eq. 1.8 and the temperature dependence of the

[7] They neglected any damping.

[8] This scaling relation was confirmed by Houdek et al. (1999, Fig. 15), who found it to be in good agreement with their more thorough theoretical predictions, at least for stars situated close to the Sun in the HR diagram.

[9] The velocity-luminosity relation of Kjeldsen & Bedding (1995) is based on a fit to observed luminosity and velocity amplitudes for 90 stars, which display p-mode oscillations of relatively large variability (amplitudes) driven by the κ-mechanism (Baker & Kippenhahn, 1962), and has an accuracy of 2.2%.

equivalent width, W, $\frac{\delta W}{W} = \frac{\partial \ln W}{\partial \ln T} \cdot \frac{\delta T}{T}$, (cf. Eq. 1.12, Sect. 1.4) finally gives an estimate of the equivalent width variation:

$$\frac{\delta W}{W} = \frac{\partial \ln W}{\partial \ln T_{\rm eff}} \cdot \frac{L/{\rm L}_\odot}{(M/{\rm M}_\odot)(T_{\rm eff}/{\rm T}_{{\rm eff},\odot})^5} \times (1.0 \pm 0.1)\,{\rm ppm}\ . \tag{1.9}$$

where $\partial \ln W / \partial \ln T$, the temperature sensitivity, can be found for different spectral lines through the analysis of synthetic stellar spectra (Bedding et al., 1996) (cf. Sect. 1.4).

Testing these predicted amplitudes for the red giant stars could provide valuable information about the the excitation mechanism and the damping effects.

1.2.2 Achieved results

This section shortly summarizes the observational results obtained until now from a handful of dwarf stars and sub giants in the solar-like region (cf. Fig. 1.3).

Using the equivalent width method (cf. Sect. 1.4), Kjeldsen et al. (1995) showed indications for p-mode oscillations in the sub giant star η Boo (cf. Fig. 1.3, *square*), with an observed excess of power centered approximately 40% above the expected frequency range (using Eq. 1.4). The estimated amplitude was ~ 45 ppm, approximately 30% above what is expected from the scaling relation of Bedding et al. (1996, Eq. 3), which corresponds to Eq. 1.9 based on L/M scaling (Eq. 1.6) instead of $1/g$ scaling (Eq. 1.7). They identify individual frequencies and estimate the large frequency separation to be fairly close to the expected value based on scaling from the solar case (Eq. 1.3).

Later research using radial velocity measurements (cf. Sect. 1.4) by Brown et al. (1997) did not confirm p-mode oscillations with the observed amplitude for the frequency interval reported by Kjeldsen et al. (1995), setting a limit on the amplitude which was three times smaller than the earlier estimate.

Radial velocity measurements provided clear detection of power excess at the expected frequency range by Martić et al. (1999) on the sub giant star α CMi (Procyon) (cf. Fig. 1.3, *plus*). Their estimate, which is an upper limit for the oscillation amplitude is approximately 50% smaller compared to the L/M relation (Eq. 1.6). Nevertheless, the derived large separation ($\sim 55\,\mu$Hz) is in very good agreement with the predicted value (Eq. 1.3).

Also using velocity measurements, Bedding et al. (2001) made a clear detection of excess power, providing strong evidence of solar-like oscillations, in the sub giant star β Hyi (cf. Fig. 1.3, *four hooked star*). A fit to the asymptotic relation (Eq. 1.2) gave a large separation in excellent agreement with that predicted by scaling from the solar case (Eq. 1.3). Their analysis showed significant departures from the asymptotic relation (Eq. 1.2). The estimated oscillation amplitude was roughly 30% below what is implied by the L/M scaling relation (Eq. 1.6).

The detection by Bedding et al. (2001) was confirmed by Carrier et al. (2001), who found significant excess power at the same frequency interval with approximately the same large frequency separation, but at a slightly lower amplitude.

With observations in velocity, Bouchy & Carrier (2001) made a clear detection of p-mode oscillations in the dwarf star α Cen A (cf. Fig. 1.3, within the $\odot$-mark). The excess power, the frequency splitting, and the amplitude all show excellent agreement with whose predicted by theory[10]. Finally, clear detection of p-mode oscillations has been found in the sub giant δ Eri (cf. Fig. 1.3, *diamond*) by Carrier, F., et al. (2002).

1.3 Asteroseismic prospects of giant stars

After an outline of the asteroseismic results obtained for giant stars, the goals of the current investigation will be emphasized more specifically, based on the introduced asteroseismic concepts (cf. Sect. 1.2).

Based on theoretical calculations, it is expected that the turbulent outer convection in the near-surface layers of giant stars (cf. Sect. 1.1.2) causes the same type of stochasticly excited oscillations as seen in the Sun (Goldreich & Keeley, 1977; Christensen-Dalsgaard & Frandsen, 1983) (cf. Sect. 1.2).

Due to the high luminosities of giant stars (cf. Sect. 1.1.2), it is in general possible to detect many photons from these stars, and from the scaling relations (Eqs. 1.6, 1.7) they are expected to display significantly larger oscillation amplitudes compared to stars positioned closer to the ZAMS (cf. Fig. 1.3). This makes the giant stars interesting candidates for asteroseismic studies, because it should be possible to achieve a fair signal-to-noise, enabling detection of the relatively small solar-like oscillations. It is, however, not known if the characteristics of the solar-like oscillation frequencies, such as the distribution of frequencies and their amplitudes, known from the extended investigations of the Sun and the more "solar-like" stars (e.g. Kjeldsen & Bedding, 2001), apply to the giant stars, and hence if it would be possible to identify modes and measure e.g. the large frequency separation (cf. Sect. 1.2).

Until now very little has been done observationally and theoretically concerning variability caused by solar-like oscillations of red giant stars. This investigation is expected to be a breakthrough in that field, especially regarding the quality of the observational data. Previous detections had periods ranging from a few days to several hundred days, which are most likely of different origin[11]. The long period

[10] The very good agreement in the α Cen case is expected since it is nearly a solar twin with mass $1.09\,M/\mathrm{M}_\odot$, luminosity $1.45\,L/\mathrm{L}_\odot$, and radius $1.20\,R/\mathrm{R}_\odot$.

[11] The very luminous *Mira*-variables (cf. Fig. 1.3) which have very long pulsation periods are not discussed here.

variations ($\gtrsim$ 100 days) are probably due to rotational modulation of surface features and are not discussed in this thesis (consult e.g. Hatzes & Cochran, 1993).

The red giant star which has received the most attention in the context of short-term variability is α Bootis (Arcturus) (cf. Fig. 1.3, *pentagon*). The variability of α Bootis has been studied by several authors (e.g. Smith et al., 1987; Cochran, 1988; Belmonte et al., 1990; Hatzes & Cochran, 1994a) all based on velocity measurements. In general these investigations rely on data sets spanning over a relatively short time compared to the expected variability periods. This insufficient sampling of the variability leads to inferred frequencies that should not be trusted too much. However, there are general indications of excess power for periods of 2-3 days (corresponding to 3-6 μHz), which is in agreement with the predicted oscillation period based on Eq. 1.4 (cf. Sect. 1.2.1) using the following stellar parameters for α Bootis: $L/\mathrm{L}_\odot = 184$, $M/\mathrm{M}_\odot = 0.7$, $R/\mathrm{R}_\odot = 24.5$, $T_{\mathrm{eff}} = 4300\,\mathrm{K}$ (adopted from Kjeldsen & Bedding, 1995, see references herein).

A few other red giants have been investigated and variability periods been estimated (Hatzes & Cochran, 1994b; Walker et al., 1989; Horner, 1996). The results of these investigations do not give a clear picture, since variability is detected in some of the common target stars in one investigation but not in the other and vice versa.

To classify and extract general properties of the variability of red giants based on these studies is very difficult due to the very sparse and often non-consistent results. One paper, though (Hatzes & Cochran, 1998), presents frequencies of α Bootis based on velocity data from different studies. It suggests that the combined data show a solar-like pattern of nearly equally spaced frequencies, even though most frequencies are given without a corresponding amplitude. However, errors have been found in this paper including faulty references to the adopted frequencies, and therefore the paper will not be taken into consideration in the following discussion.

Henry et al. (2000) made a thorough survey for photometric variability in 187 G0-M0 giants[12] with an absolute visual magnitude range of $-3 < M_V < 3$, extending over a period of five years, where most of the stars were observed for 1-3 seasons. They were able to detect variability above 0.002 magnitude in 43% of the stars in their sample, most with periods ranging from approximately 1-3 weeks[13]. Included in their sample were the stars from the Hatzes & Cochran (1998) paper, and even though variability was observed in most of these stars, they could not confirm any of the radial velocity periods reported by Hatzes & Cochran (1998). This could of course be because the stars show different periods at different epochs. The sample rate of the observations presented in Henry et al. (2000) is not mentioned, but seen from their plotted time series it is possible that they are simply not able to sample periods of only a few days or below.

[12] Their sample covered the region of ξ Hya in the HR-diagram (cf. Table 1.1, page 20).

[13] Although many of these stars exhibited coherent variability at least during a portion of the observation interval, periodogram analysis failed, in general, to reveal convincing periodicities. The periods given are therefore representing the time-scales of the typical interval between successive maxima or minima.

From the survey of Henry et al. (2000), it can be concluded that the variability mechanism is different for red giants on the left/hot side of the coronal dividing line[14] (earlier than K2) compared to those on the right/cool side[15]. In most cases, rotation modulation of surface features is a highly unlikely explanation for the observed variability. On the cool side of the coronal dividing line the variability periods are comparable to those of radial pulsations computed by the formulae of Cox et al. (1972), whether stars on the hot side have predicted periods much shorter than observed. Without further discussion the final conclusion given by Henry et al. (2000) is that the variability of the red giants on the hot side of the coronal dividing line are most likely due to g-modes.[16]

Apart from the investigations on single field stars, Edmonds & Gilliland (1996) investigated K giants in the globular cluster 47 Tucanae using photometry exposures with the Hubble Space Telescope. They also find periods of $\sim$ 2-4 days, though it should be noted that the observation time span was only 39 hours. The stars which Edmonds & Gilliland focus on have amplitudes of 5-15 mmag and they have a similar position in the HR diagram as α Bootis (cf. Fig. 1.3) while being somewhat more luminous[17]. Both radial and non-radial modes excited by convection are suggested as the origin of the observed variations, but due to the short time series no clear conclusion can be made.

Buzasi et al. (2000) claimed detection of solar-like oscillations in the giant star α UMa A (cf. Fig. 1.3, *triangle*). It is however questionable whether their detected signal is due to solar-like oscillations or not since the observed amplitudes do not match those predicted by theory. In order to make the frequencies predicted by theory (Guenther et al., 2000) fit with those observed requires a totally arbitrary mode selection (cf. Stello, 2000a; Dziembowski et al., 2001).

Theoretical calculations by Guenther et al. (2000) and Guenther (2001) predict that, for intermediate mass stars ($\sim$ 2-5 $M_\odot$), the Brunt-Väisälä and Lamb frequencies which define the regions of the star where g- and p-modes are allowed will cross when the stars reach the red giant phase (point 6 in Fig. 1.1). This will allow both g- and p-modes in the same frequency interval to mix in a certain region, called mode bumping. Due to mode bumping the p-mode frequencies are perturbed, and eventually the g-modes will completely dominate the non-radial p-modes. Hence only radial p-modes and g-modes (which are only non-radial) are expected to be ob-

[14]The coronal dividing line separates giants with hot coronae on the left from giants with cool, massive winds on the right.

[15]ξ Hya is on the left/hot side of the coronal dividing line.

[16]In connection to ξ Hya, it should be noted that the investigation of Henry et al. (2000) is limited to stars which show variability with amplitudes larger than 0.002 magnitude. This is much larger than the expected amplitude for solar-like oscillations in ξ Hya (actually a factor of $\sim$ 10 times larger) (cf. Table 1.2, page 22).

[17]The sample of stars investigated by Edmonds & Gilliland (1996) also contained stars of similar luminosity to ξ Hya. For these stars a few were designated possible variables (cf. Edmonds & Gilliland, 1996, Fig. 1a). Related to Edmonds & Gilliland's Fig. 1a, ξ Hya would be positioned at ($B - V \simeq 0.95$, $V \simeq 14$) if it was in 47 Tucanae.

served in red giant stars. This also implies that only the large frequency separation (Eq. 1.3) will be identifiable.

There are still some uncertainties about the physical processes which take place in the interior of giant stars, e.g. how deeply the convection zone penetrates the stellar interior. Very little is known about calculated oscillation frequencies for particular giant stars (Guenther et al., 2000; Dziembowski et al., 2001)[18]. In sum, a thorough investigation of the possibilities for applying the concepts of asteroseismology to test the structure and evolution of these stars combined with good quality observational data has not yet been made.

The specific goals which I want to achieve in this investigation are:

- To determine if the target star, ξ Hya, displays typical solar-like p-mode oscillations (cf. Sect. 1.2) with multiple excited, equally spaced frequencies distributed in a broad frequency envelope.

- To verify whether the position and amplitude of the frequency envelope follow the predicted values based on the scaling relations of Sect. 1.2.1 (Eqs. 1.4, 1.7, 1.6).

- In the case of a clear detection of oscillations and subsequent verification of the typical solar-like p-mode nature of these oscillations, the frequencies will be estimated with the aim to provide a value for the large frequency separation which yields the stellar mean density of ξ Hya (Eq. 1.3).

- Finally, the observed frequency spectrum will be compared to a theoretical spectrum of ξ Hya, in order to determine if the theoretical model can reproduce what is observed.

The achievement of these goals is expected to impact future investigations using asteroseismology tools which would lead to a better insight on the physical processes which take place in the interior of these "old" stars, such as mixing processes, energy transport, and possible mass loss. This will lead to a better understanding of the stellar structure and evolution at this late evolutionary phase.

This investigation will undoubtedly provide extremely useful information for the future planning of asteroseismic observation programs, in particular the upcoming space missions RØMER/MONS (Kjeldsen et al., 2000), MOST (Matthews et al., 2000), COROT (Baglin & The COROT Team, 1998), and Eddington (an accepted ESA mission).

[18]The results presented in Chapter 5 subsequently lead to yet another theoretical paper about solar-like oscillations, especially focused on ξ Hya (Houdek & Gough, 2002).

1.4 Observational tools

This section presents the observational tools used to detect the tiny solar-like oscillations. In this current investigation only the equivalent width method and the radial velocity method are applied. Each method is only applied on one of the two independent data sets obtained for this investigation (cf. Chapter 2).

Photometry

The stellar oscillations cause small temperature fluctuations on the surface and hence variability in the stellar luminosity. If photometry is used to measure these luminosity variations, one uses the entire amount of detected stellar light in a broad spectral range to reach a high signal-to-noise (S/N) level; a big advantage of this method. But, due to turbulence in the Earth's atmosphere, the stellar light is constantly perturbed, which makes the stars twinkle. This effect is called scintillation. A few attempts to detect solar-like oscillations from ground-based photometric observations have been made, but no clear detections have been obtained. The ambitious multi-site campaign on the M67 cluster by Gilliland et al. (1993) reached a noise level of 250 μmag/min, yielding a detection threshold of 20 μmag from one week of observation, which is more than five times solar. To detect oscillations with solar amplitude ($\sim 5\,\mu$mag) at the fairly low, 4σ detection level, would require 10 months of full night observation, using a 4 meter class telescope (single site), adopting the noise of 250 μmag/min reached by Gilliland et al. (1993).[19] Due to the scintillation it seems therefore not feasible to use photometry to detect solar-like oscillations in other stars than the Sun from the ground. However, it is in principle relatively easy to detect the oscillations even with a small ($\sim 30\,$cm) telescope if one observes from space (cf. Kjeldsen et al., 1999b).

Equivalent width

The temperature fluctuations due to the stellar oscillations which influence the luminosity also give rise to changes in the absorption lines in the stellar spectrum, and therefore they can be measured through spectroscopy. The appearance of an atomic absorption line at a particular wavelength in the stellar spectrum depends on the state of the atom creating the line. To be specific, the line strength depends on the number of electrons in the right excitation level, which depends on the temperature.

If F_c and F_λ denotes the continuum flux and the flux in a spectral line, the line profile can be described by the relative line depth (see Fig. 1.4)

$$R_\lambda = \frac{F_c - F_\lambda}{F_c} \ , \tag{1.10}$$

[19] The dependence of the telescope aperture, D, on the scintillation is only: scint$\propto D^{-2/3}$.

if any instrumental distortion is neglected. The equivalent width, W, is a measure of the total strength of an absorption line and is defined as

$$W = \int_{line} R_\lambda \, \mathrm{d}\lambda \; . \tag{1.11}$$

W can be regarded as the width of a perfectly black rectangular absorption line having the same total absorption as the real line (dotted box in Fig. 1.4) (Gray, 1992). W is independent of scintillation because it measures the spectral line strength relative to the continuum, so the effect of scintillation cancels out. Hence the precision of an equivalent width measurement is, in theory, only limited by photon noise.

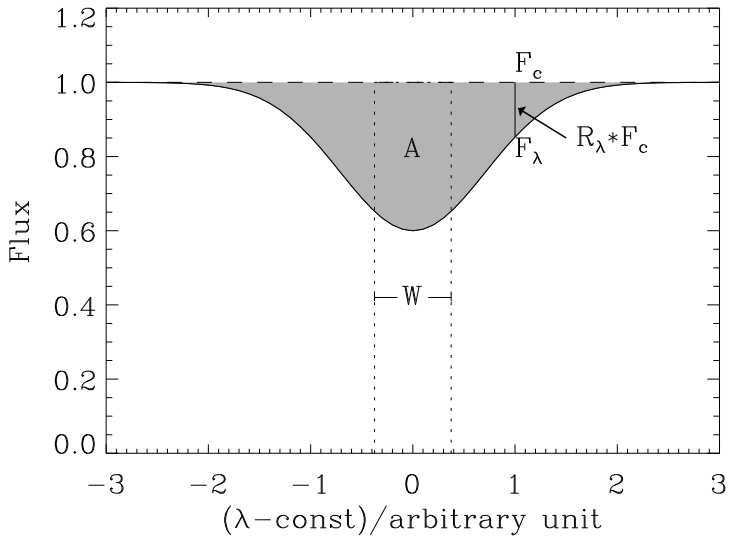

Figure 1.4: Illustration of a spectral absorption line, simulated as a totally isolated line with a Gaussian profile (solid line), not affected by other lines or any noise source; the continuum (dashed line) has been normalized. The parameters introduced in Eq. 1.10 are indicated: the continuum flux F_c, the line flux F_λ, and the relative line depth R_λ. The concept of the equivalent width (Eq. 1.11) is shown as $W = A/F_c$, the width of the rectangular dotted box, which have an area equal to the area A of the shaded region, indicating the total absorption of the real line.

Temperature is the variable that most strongly affects the strength and hence the equivalent width of e.g. the hydrogen Balmer absorption lines for stars in the temperature regime around solar. Kjeldsen et al. (1995) proposed for the first time a method to detect stellar oscillations which makes use of the fact that the temperature fluctuations induced by the oscillations affect the equivalent width of the hydrogen Balmer lines. Due to the limited spectral range used to detect the oscillations, the fundamental problem of this method is to collect enough photons. Hence this method can only by applied to relatively bright stars.

Using $\partial \ln x = \delta x/x$, the temperature dependence of the equivalent width can be written

$$\frac{\delta W}{W} = \frac{\partial \ln W}{\partial \ln T} \cdot \frac{\delta T}{T} \ , \tag{1.12}$$

where $\partial \ln W/\partial \ln T$ is the temperature sensitivity.

Bedding et al. (1996) made a thorough investigation of the temperature sensitivity of the Balmer lines and other spectral features using synthetic stellar spectra. This investigation only concerned stars in the temperature regime of 5600-6600K and with solar metallicity and surface gravity. As stated by the authors, calculations of the H_α line by Fuhrmann et al. (1993) indicate that changing these parameters has little effect on the equivalent width, which is true for the temperature regime around solar. The change in temperature sensitivity of the equivalent width due to changes of the surface gravity sets in for temperatures above $\sim 7500\,\mathrm{K}$ (Gray, 1992, Fig. 13.8), and is thus of no concern in the investigation of red giant stars (cf. Sect. 1.1.2).

If the results of Bedding et al. (1996) are roughly linearly extrapolated into the regime of $T_{\rm eff} \simeq 5000\,\mathrm{K}$, which is the approximate effective temperature of the target star ξ Hya, the temperature sensitivity of the primary target line, H_α, would read, $\partial \ln W/\partial \ln T \simeq 7$. The reason for choosing the H_α line as primary target line is discussed in Sect. 2.1.2.

Radial velocity

Since part of the data used in the data analysis is based on radial velocity measurements, a introduction of the concept of radial velocities is necessary.

Like the equivalent width method, measurements of the radial velocity rely on the absorption lines in the stellar spectrum. But instead of measuring the line strength, the radial velocity method measures the position of the spectral lines. The position of an absorption line in the spectrum depends on the difference between the energy levels of the atomic transition causing the absorption

$$\lambda_{(1,2)}^{-1} = \frac{E_2 - E_1}{hc} \ , \tag{1.13}$$

where E_2 and E_1 are the upper and lower atomic energy levels of the transition, and $\lambda_{(1,2)}$ is the wavelength of the photon which is absorbed by the atom.

The stellar oscillations cause physical displacement of the gas which can be measured as a wavelength shift of the light emitted by the gas; the Doppler shift. Hence the stellar spectrum will move relative to a reference spectrum, e.g. a calibration lamp. The radial velocity, V_r, of the gas projected onto the line-of-sight gives rise to a shift $\delta\lambda$

$$\frac{\delta\lambda}{\lambda} \simeq \frac{V_r}{c} \ . \tag{1.14}$$

The relative shift $\delta\lambda/\lambda$ is very small for solar-like oscillations (in the solar case: $\delta\lambda/\lambda \simeq 8 \times 10^{-10}$), and so the radial velocity technique requires an extremely stable high-resolution spectrograph.

1.5 Stellar parameters of ξ Hydrae

In this section, the observed stellar parameters of ξ Hya, partly taken from the literature, are presented. The theoretical stellar parameters are estimated and expected asteroseismic properties are calculated based on the scaling relations described in Sect. 1.2.1. This includes stellar evolutionary tracks for ξ Hya, which, in addition to the mass determination, are used to select a theoretical stellar model for pulsation analysis in Sect. 5.3.4.

Table 1.1: Parameters for ξ Hya

Parameter	Designation/Unit	Value & (error)
Basic parameters:		
Star ID	HR/HD/HIP	4450/100407/56343
Coordinate[a]	RA(J1991.25)	$11^h\,33^m\,00^s.26$
Coordinate[a]	Dec(J1991.25)	$-31^\circ\,51'\,27''.1$
Distance[a,b]	d/pc	39.6(1.3)
Visual magnitude[c]	V/mag	3.541(7)
Atmospheric parameters:		
Spectral type[d]	MK-type	G7 III
Effective temperature	$T_{\rm eff}$/K	5022(100)
Rotation[e]	$V \sin i$/km/s	1.8(1.0)
Gravity[f]	$\log g$/cm/s^2	2.9(2)
Metallicity	[M/H]	0.06(7)
Absolute visual magnitude	M_V/mag	0.55(10)
Absolute bolometric magnitude	$M_{\rm bol}$/mag	0.28(12)

[a] *The Hipparcos Catalogue* (Perryman et al., 1997).
[b] Based on the parallax: $\pi = 25.23(83)$ mas.
[c] Mean value from *Lausanne photometric database GCPD* (Mermilliod et al., 1997).
[d] *The [Fe/H] Catalogue* (Cayrel de Strobel et al., 1997).
[e] Using $\langle i \rangle = 60^\circ \pm 30^\circ$ the expected rotation is $\langle V \rangle = 2.1(1.3)$ km/s.
[f] McWilliam (1990).

Table 1.1 presents both known basic parameters and those parameters characterized by the properties of the stellar atmosphere. Some of the parameters are specially determined for this investigation, while others are adopted from the literature. The errors are assigned within parenthesis.

According to the literature the quoted effective temperature of ξ Hya ranges from 4963 K to 5058 K all with quoted errors of approximately 50-100 K. McWilliam

(1990) corrected[20] and combined published Johnson broad-band photometry and calculated effective temperatures based on different methods in order to recalibrate the $T_{\rm eff}$-color relations for different color indices. The temperature derived for ξ Hya (5010 K) was an average based on 10 different color indices. Each $T_{\rm eff}$-color relation had an error of 50-200 K, so a reasonable error for the estimated temperature would be $\sim$ 100 K. Blackwell & Lynas-Gray (1998) used the infrared flux method and *Hipparcos* parallaxes to calculate $T_{\rm eff}$, and obtained a value of $T_{\rm eff} = 5058 \pm 46$ K for ξ Hya. Using high-precision broad-band $(V-K)$ photometry, *Hipparcos* parallaxes, and new interferometric measurements of stellar radii of standard stars, di Benedetto (1998) derived accurate effective temperatures with an error of only 1%. The derived value for ξ Hya is $T_{\rm eff} = 4985 \pm 50$ K. The value quoted by Mallik (1999), $T_{\rm eff} = 4963 \pm \sim 50$ K, is based on the color index $B-V$ from *The Bright Star Catalogue* (Hoffleit & Jaschek, 1982) and the $T_{\rm eff}$-$(B-V)$ calibration of Flower (1996).

It is expected that the results of Blackwell & Lynas-Gray (1998) and di Benedetto (1998) are the most reliable, due to the fact that these results rely on new direct measurements (i.e. parallaxes and interferometry) and are based on long wavelength bands which are not affected by metal absorption lines[21]. Hence it is believed that these temperature estimates are less likely to be affected by large systematic errors. The final effective temperature used in the current investigation is the mean of the estimates from Blackwell & Lynas-Gray (1998) and di Benedetto (1998). The error assigned to this mean value is more conservative than quoted by the source papers in order to cover the full range of quoted values (cf. Table 1.1).

The rotation was estimated through line profile comparison of several lines of synthetic spectra with a subset of observed stellar spectra of ξ Hya obtained with the CORALIE spectrograph (cf. Sect. 2.2). It is however quite difficult to distinguish the effects from rotation and from the macro turbulence with the spectra available. Hence the macro turbulence was fixed to 5.0 km/s, which is a typical value for a red giant star (cf. Gray, 1992, Fig. 18.9). In that case the estimated rotation is $v \sin i = 1.8(1.0)$ km/s in agreement with Glebocki et al. (2000) who report $v \sin i = 2.4$ km/s.

The $\log g$ value is adopted from McWilliam (1990) but with an error slightly more conservative than the one quoted in the source paper[22].

Due to its low rotation rate (cf. Table 1.1), the spectral lines of ξ Hya are extremely narrow, hence many spectral lines are unblended and a reliable estimate of the metallicity can be made. Based on the $\log g$ estimate of McWilliam (1990), Bruntt (2002) calculated the metallicity of ξ Hya to be [M/H]$= 0.06 \pm 0.07$ (corres-

[20] Corrections were performed due to improved measurements of stellar angular diameters, and reddening effects.

[21] Thus the continuum can better be described by theoretical models.

[22] A change in $\log g$ of plus/minus the error quoted in the current investigation was quite uncritical for the spectral analysis e.g. the metallicity determination.

ponding to $Z = 0.019 \pm 0.006$)[23] using a semi-automatic method which is described by Bruntt et al. (2002). This value is based on the abundance of six elements from the iron group (Ti, V, Cr, Fe, Co, Ni) with a total of 110 spectral lines.

Estimates of the asteroseismic properties of ξ Hya (i.e. $\Delta\nu_0$, $\nu_{\rm max}$, $n_{\rm max}$, and $v_{\rm osc}$) can be calculated from the stellar parameters L, M, R, and $T_{\rm eff}$, using the scaling relations described in Sect. 1.2.1.

The luminosity, L, is derived from the measured visual magnitude, distance, effective temperature, log g, and the metallicity (cf. Table 1.1), using the following formulae:

$$M_{\rm bol} - {\rm M}_{\rm bol,\odot} = -2.5\log(L/{\rm L}_\odot) \quad (1.15)$$

$$M_{\rm bol} = m_{\rm bol} - 5\log(d) + 5 \quad (1.16)$$

$$m_{\rm bol} = V + BC\ . \quad (1.17)$$

Combining these formulae yields:

$$\log\left(\frac{{\rm L}_{\xi{\rm Hya}}}{{\rm L}_\odot}\right) = -\frac{1}{2.5}[{\rm V}_{\xi{\rm Hya}} + {\rm BC}_{\xi{\rm Hya}} - 5\log({\rm d}_{\xi{\rm Hya}}) + 5 - {\rm M}_{\rm bol,\odot}] \quad (1.18)$$

$$= 1.788(46)$$

where $M_{\rm bol}$, $m_{\rm bol}$ are the absolute and apparent bolometric magnitudes, respectively, and BC is the bolometric correction. The BaSeL grid (Lejeune et al., 1998), which is calibrated to the absolute bolometric magnitude of the Sun (${\rm M}_{\rm bol,\odot} = 4.746$), has been used to obtain ${\rm BC}_{\xi{\rm Hya}}$ based on ${\rm T}_{{\rm eff},\xi{\rm Hya}}$, $\log {\rm g}_{\xi{\rm Hya}}$ and $[{\rm M/H}]_{\xi{\rm Hya}}$. The interstellar absorption, A_V, of ξ Hya is found from photometry $(B-V)$ to be $A_V = 0.00(8)$ magnitude (Pijpers, 2002)[24] and is therefore omitted in the above equations. However, the error of A_V is including in the error calculations and it is in fact the dominant error source.

In order to obtain an estimate of the mass, M, for ξ Hya, stellar evolutionary tracks were calculated using the evolutionary code of Christensen-Dalsgaard (1982) and the metallicity quoted in Table 1.1 (Teixeira, 2002)[25]. Fig. 1.5 shows the computed evolutionary tracks (see figure caption). The error in the mass due to the uncertainty in the metallicity and the stellar position in the HR-diagram is roughly $0.3\,{\rm M}_\odot$, which is the value quoted in the current investigation (cf. Table 1.2).

The stellar radius, R, is calculated from the formula: $L = 4\pi\sigma R^2 T_{\rm eff}^4$.

The model- and asteroseismic parameters are presented in Table 1.2. The asteroseismic parameters are derived from the scaling relations presented in Sect. 1.2.1. The best-fit evolutionary track assigns ξ Hya to a stage where the stellar evolution

[23] The quoted metallicity errors are formal.

[24] A_V is derived using $A_V = 3.1[(B-V) - (B-V)_0]$, where $(B-V)_0$ is found from the BaSeL grid.

[25] The models are computed using the EFF equation of state (Eggleton et al., 1973), OPAL opacities (Iglesias et al., 1992), Bahcall & Pinsonneault (1992) nuclear cross sections, and the mixing-length formalism (MLT) for convection.

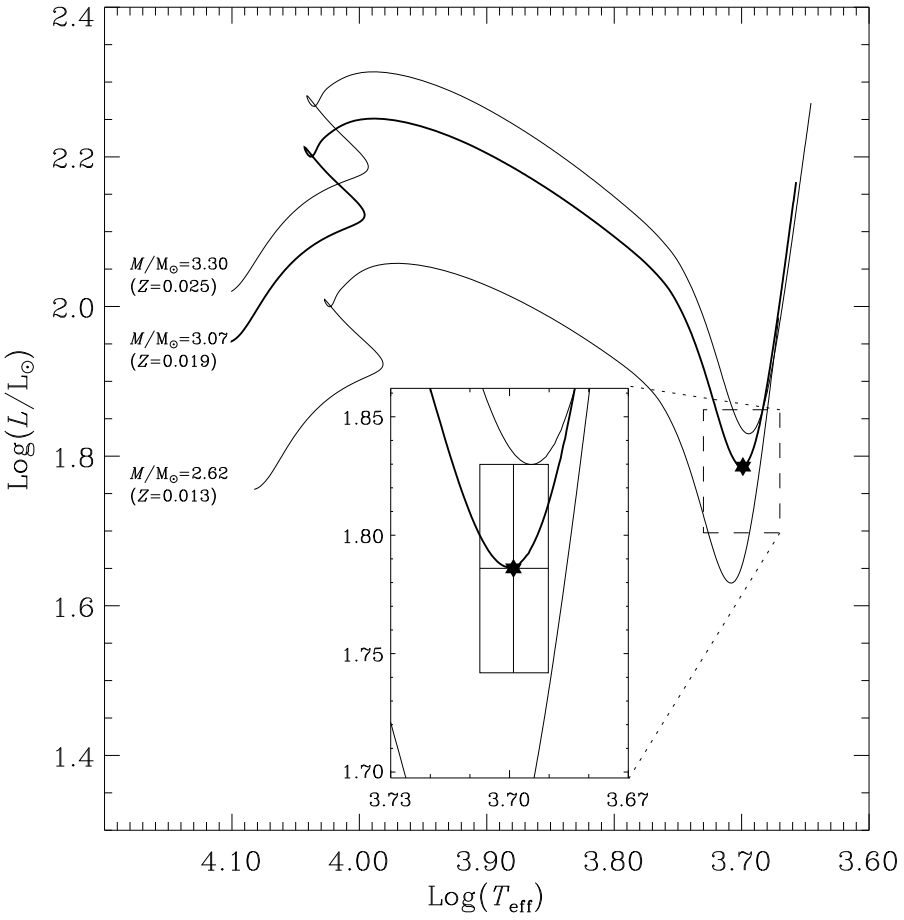

Figure 1.5: The Hertzsprung-Russell diagram showing evolutionary tracks from the ZAMS to a point half way up the red giant branch for stellar models with different mass and metallicity. The mass and metallicity is shown at the ZAMS point for each track. The star and the box (in the inset) indicates the position of ξ Hya and the quoted errors, respectively (cf. Tables 1.1, 1.2). The thick solid line is the evolutionary track which gives the best fit to ξ Hya, with the adopted metallicity of [M/H]= 0.06. The thin solid lines are the tracks which graze the error box if the adopted metallicity is changed by plus or minus 1σ (0.07 dex).

Table 1.2: Calculated parameters for ξ Hya

Parameter	Unit	Value & (error)
Model parameters:		
Luminosity	$L/\mathrm{L}_\odot$	61.4(6.6)
Mass[a]	$M/\mathrm{M}_\odot$	3.07(30)
Radius	$R/\mathrm{R}_\odot$	10.4(7)
Expected asteroseismic parameters:		
Large separation	$\Delta\nu_0/\mu$Hz	7.0(7)
Dominant frequency	$\nu_{\max}/\mu$Hz	93(14)
Dominant order	$n_{\max}$	21(1)
Oscillation amplitude (L/M-scaling)	v_{osc}/m/s	4.7(6)
Oscillation amplitude ($1/g$-scaling)	v_{osc}/m/s	8.2(1.2)
Oscillation amplitude ($1/g$-scaling)	$\delta W/W$/ppm	282(57)
Oscillation amplitude ($1/g$-scaling)	$\delta L/L$/ppm[b]	165(29)

[a] The mass determination may be more uncertain than quoted in this table due to systematic effects observed between different evolutionary codes and whether overshoot is included in the model calculations or not. This mass is based on an evolutionary code (Christensen-Dalsgaard, 1982) which does not reach the He core burning phase. If ξ Hya is a He core burning star this code is thus insufficient.

[b] Note that 1 ppm equals 1.086 μmag.

is very fast, and where one is thus more unlikely to find a star. One should therefore be cautious about the determination of the exact evolutionary state of ξ Hya. It should be noted that, after reaching the most luminous point of the Hayashi track, the evolutionary track moves down the Hayashi track again to a point which has higher likelihood (slower evolutionary speed in the HR diagram) only 1-2 sigma[26] away from where ξ Hya is situated in the HR diagram.

Fig. 1.6 (*top panel*) shows an evolutionary track (solid thick line) comparable to those plotted in Fig. 1.5 ($M/\mathrm{M}_\odot = 3.0$, $Z = 0.019$, no overshoot) calculated by Girardi et al. (2000). This track proceeds after the triple-alpha ignition and hence further shows the evolutionary track at the He burning phase. Compared to the stellar error box (small rectangular box) it is clear that the exact evolutionary state of the star is difficult to determine from such a plot. Furthermore, introducing overshoot in the stellar evolutionary model would change the estimated mass significantly ($\sim 0.3\,\mathrm{M}_\odot$ for a relatively fixed evolutionary stage)[27] (Fig. 1.6, *top panel*, solid thin line). The degree of overshoot in the model may possibly be tested through the frequency analysis (cf. Chapter 6).

Fig. 1.6 (*bottom panel*) shows the luminosity versus stellar age of the evolutionary track denoted by the solid thick line in the *top panel*. Considering only the

[26] Depending on the exact evolutionary track.

[27] The change can be even larger if the evolutionary state is changed as well, due to the nearly vertical evolutionary tracks at the red giant phase.

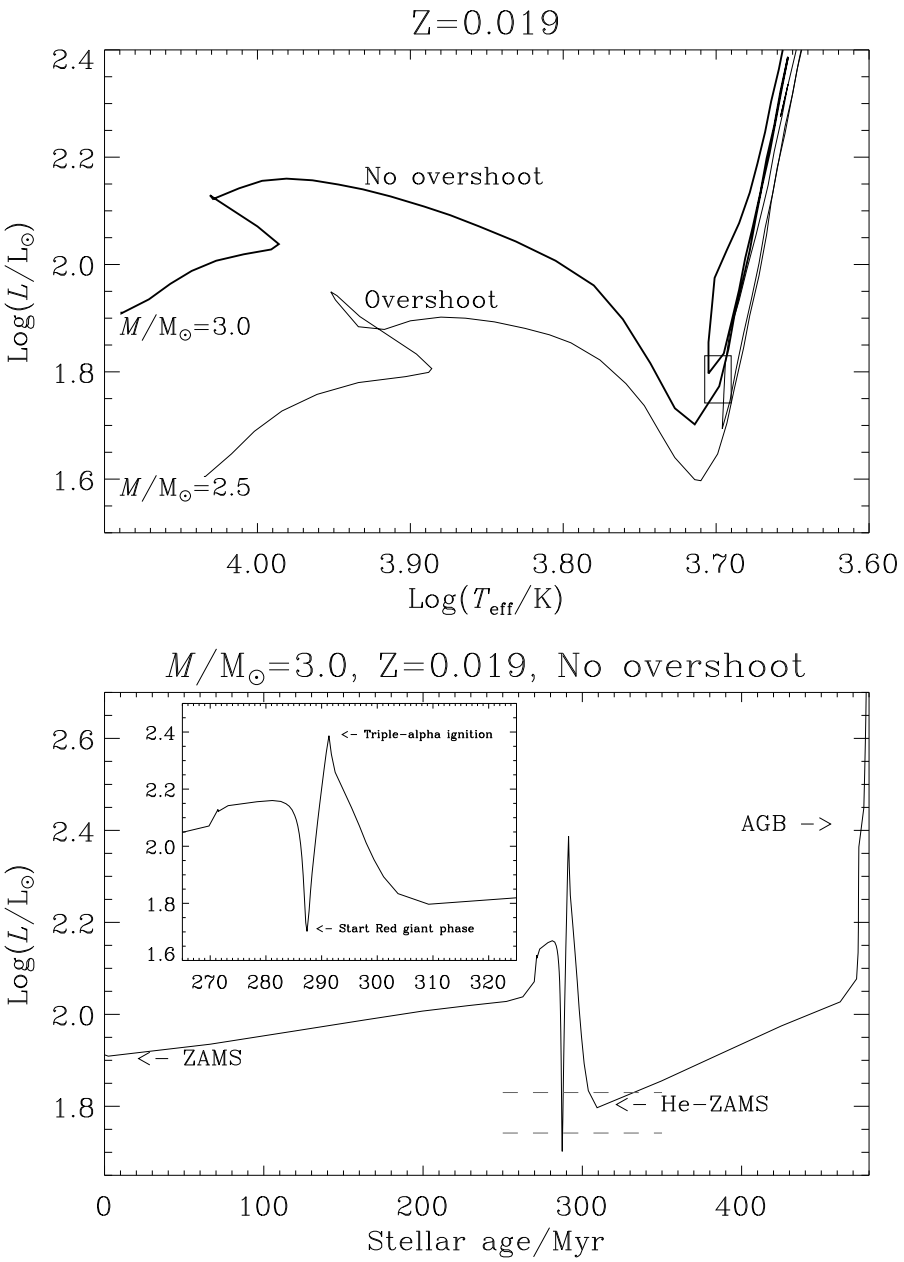

Figure 1.6: **Top panel:** The Hertzsprung-Russell diagram showing evolutionary tracks from the ZAMS to the asymptotic giant branch for stellar models with different masses and degree of overshoot. The mass is shown at the ZAMS point for each track. The *small box* indicates the position of ξ Hya and the quoted errors similar to the box in Fig. 1.5 (cf. Tables 1.1, 1.2). The *thick solid line* is the evolutionary track which has similar input parameters to those shown in Fig. 1.5. The *thin solid line* is a track with overshoot which has a significantly lower mass and still goes through the error box. The evolutionary tracks are taken from Girardi et al. (2000). **Bottom panel:** The evolutionary track corresponding to the *thick solid line* in the top panel, where the abscissa has been replaced by the stellar age. The inset shows in detail what happens during the red giant phase. *Dashed lines* are the luminosity range of ξ Hya (cf. Table 1.2), indicating the possible ages (or evolutionary stages) of ξ Hya based on this evolutionary track.

luminosity range of ξ Hya (dashed lines), this plot clearly shows the extremely short time the star is at the dip just before moving up the Hayashi track compared to the time at the core He burning phase. The evolutionary stage of ξ Hya will be discussed furthermore in connection to the pulsation analysis in Chapter 5 (Sect. 5.3.4).

The asteroseismic parameters of ξ Hya given in Table 1.2 have never been tested because no search for acoustic oscillations has previously been made for this or any similar star. ξ Hya is intermediate between the very luminous giant stars, which have been studied by several science groups (cf. Sect. 1.3), like α Boo and α UMa A (cf. Fig. 1.3, page 6), and the more solar-like stars like e.g. α Cen A and β Hyi. The expected oscillation amplitude of ξ Hya is significantly below the thresholds of both Edmonds & Gilliland (1996) and Henry et al. (2000) by more than a factor of 10, but compared to the amplitudes of the more solar-like stars for which positive detection has been achieved, it is roughly ten times larger. Applying the newest techniques used to detect oscillations in the solar-like stars to ξ Hya is thus likely to give promising results.

Chapter 2

Observations and data

Two independent data sets are collected for this current investigation. The data set partly collected by myself concerning the equivalent width method is described in most detail (cf. Sect. 2.1). However, the additional data set, comprised of radial velocity measurements collected by collaborating scientists, is shortly introduced in Sect. 2.2.

This chapter will describe how the observations were made in order to detect the tiny solar-like oscillations in the target star ξ Hya. First, I present the observational strategy discussing the requirements for different parameters (i.e. count rates, sampling rates, observation duration, and number of required data points) which are necessary to achieve a clear detection in such challenging observational program. Subsequently, I give a presentation of the observations and the obtained images, which are later reduced to 1D spectra (cf. Chapter. 3) and finally converted to time series which should reveal the oscillating signal of ξ Hya (cf. Chap. 4).

2.1 Equivalent width observations

2.1.1 Observational strategy

The expected stellar oscillation signal of ~ 280 ppm (cf. Table 1.2) is much smaller than the ultimate noise limit of the equivalent width method (pure photon noise; cf. Sect. 1.4), which is ~ 1000 ppm per data point[1]. Hence it is critical that the number of detected photons is maximized in order to reduce the final noise to a level where it is possible to get a clear detection, which requires a high duty cycle. To obtain that, only a small window of the entire CCD[2] camera was read out. A further reduction of the read out time was gained using two amplifiers (A and B; cf.

[1] Based on a reference spectrum, simulated spectra were created adding only photon noise. Calculating the equivalent width of these spectra, using the same software as in the later described spectral analysis (cf. Chapter 4), provided a noise level of roughly 1000 ppm (only considering the H_α-line).

[2] A CCD (Charge Coupled Device) is a two-dimensional array of light sensitive pixels that detect incoming photons.

Fig. 2.1) simultaneously to read out the windowed CCD. In order to increase the detected flux further, the stellar image was defocused (cf. Sect. 2.1.2; Fig. 2.2). The chosen exposure time of 35 seconds provided peak intensities of $\sim$ 30000-45000 ADU in the most illuminated pixels of the CCD, which was safely below the saturation point of the CCD (cf. Table 2.1). The obtained sampling rate was 48 images per hour ($\sim$ 160 data points per cycle of the expected dominant mode (cf. Table 1.2), with a duty cycle of 47%.

With the observation time dedicated to this project it was possible to get approximately 9000 data points[3] which yields a final $(S/N)_{expect} \simeq 14$, assuming only photon noise. The frequency resolution was $1/T = 0.16\,\mu$Hz, where T is the time span of the observations[4].

2.1.2 Data and configuration

The observations were performed during the periods March 15th - April 12th and May 10th - May 24th 2000, with DFOSC[5] mounted on the Danish 1.54 m telescope at La Silla (ESO[6], Chile), which covered 39 nights, or 175 hours, of observations over a period of 71 days (cf. Table 2.2, page 33).[7]

The relevant characteristics of the CCD and the optical setup of DFOSC are given in Table 2.1. For further details about the instrument specifications I refer the reader to the telescope and instrument user manual by Brewer & Storm (1999).

Table 2.1: Characteristics for the Lorel/Lesser CCD (high gain mode)

CCD dimension	2052×2052 pixel	
Pixel size	15 μm	
Pixel scale	0.39 $''$/pixel	
Dark current	12.3 ± 7.7 e^-/pixel/hour	(amplifier A)
Readout Noise	7.7/20 e^-/pixel	(amplifier A/B)
Mean bias level	$\sim$ 1145/1165 ADU (measured)	(amplifier A/B)
Saturation point	$\sim$ 44200/52750 ADU (measured)	(amplifier A/B)

The images are echelle spectra of ξ Hya, with a wavelength coverage from $\sim$ 400 to 730 nm. Only a 700×1900 pixel central region of the entire CCD, just including the spectral orders containing the first three Balmer lines, was read out (cf. Fig. 2.1). The stellar spectra were obtained using a $1\farcs5$ echelle slit and an echelle grism

[3]The actual number of obtained images can be seen in the observation log, Table 2.2, page 33.

[4]This frequency resolution does not enable a detection of the stellar rotation period which corresponds to a frequency separation of $0.04 \pm 0.08\,\mu$Hz (cf. Table 1.1, page 20).

[5]Danish Faint Object Spectrograph and Camera.

[6]European Southern Observatory.

[7]The observations were performed by Simon O'Toole (School of Physics, Sydney University, Australia), Hans Kjeldsen, and Dennis Stello (Institute of Physics and Astronomy, Aarhus University, Denmark).

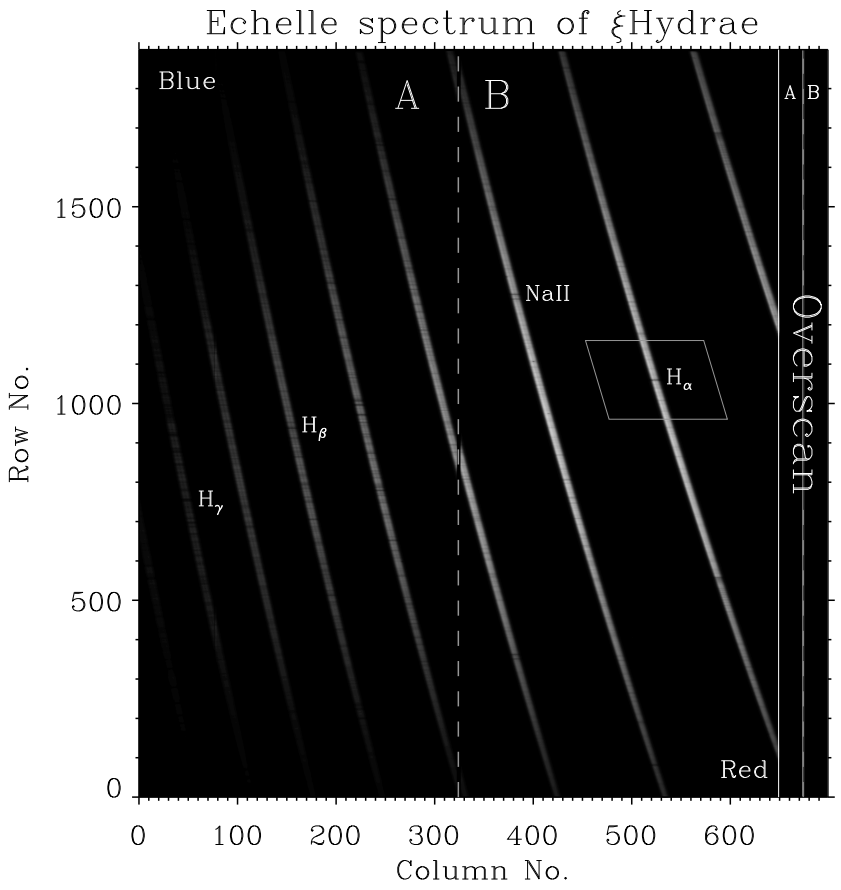

Figure 2.1: Echelle spectrum of ξ Hya including 9 spectral orders. In addition to the first three Balmer lines (H_α, H_β, and H_γ) the NaII doublet is indicated. The *solid white line* indicates the boundary between the physical CCD and the overscan region. The *dashed lines* indicate the boundaries between amplifier A and B regimes in both spectrum and overscan regions. *Small solid lined box* around the H_α spectral line indicates the sub-image which is cut out and aligned for the investigation of the H_α spectral line. A similar sub-image around NaII is also cut out and aligned. Following the spectral orders from the bottom right to the top left, corresponds to moving from "long" ($\sim$ 730 nm) to shorter wavelengths ($\sim$ 400 nm).

with a resolving power of 4300 ($\lambda/\Delta\lambda$).[8] The highest count rates were in the spectral orders around the primary target line H_α in the B amplifier regime of the CCD. The main reason why the H_α line was chosen as primary target line is its relatively high temperature sensitivity and large equivalent width. Furthermore, the continuum around the H_α line is not significantly affected by other strong lines as the bluer part of the spectrum (cf. Fig. 2.1). In addition to the H_α line, the NaII doublet was investigated but it turned out to provide much poorer results relative to those from the H_α line and will not be discussed in such detail as the H_α line (cf. Chapter 4).

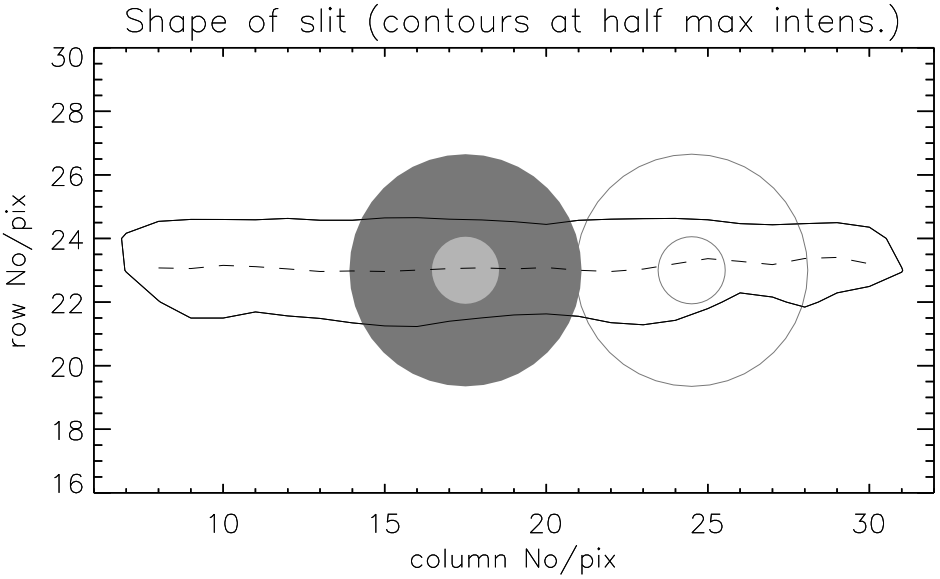

Figure 2.2: The 50% maximum intensity contour of a spectral emission line from a thorium lamp indicating the slit shape (*solid black line*) and a simulated stellar image of a representative size (*large shaded circle*). The *small, less shaded circle* indicates the lower central intensity of the defocused stellar image seen at good seeing conditions. The stellar image then had an annulus shape. *Solid grey circles* (unshaded) indicate the maximum observed drift of the stellar image along the slit. The drift in the row direction (direction of dispersion) was not measured. The *dashed line* indicates the midway between upper and lower slit edge, found by Gaussian fits to a spectral emission line along the dispersion (using **slit_align_test.pro**).

Fig. 2.2 shows a plot of the slit illuminated by a simulated defocused stellar image[9]. The stellar image drifts both parallel and perpendicular to the slit. The maximum drift along the slit is indicated as the stellar image on the right. It was necessary to reposition the stellar image on the slit after approximately every 100 exposures ($\sim$ 2 hours). The irregular slit shape and the repositioning of the stellar image on the slit introduced a significant error in the data set (cf. Chapters 4, 5).

[8]The setup was: 1″.5 echelle slit (aperture wheel), Grism#11 as cross disperser (filter wheel), and echelle Grism#9 (grism wheel). Both amplifier A and B in high readout mode.

[9]The maximum slit width indicated by Fig. 2.2 is $\sim$ 3.5 pix which is comparable to (but slightly below) its specifications: (1″.5 slit width)/(0″.39/pix) = 3.85 pix.

Additionally to the stellar spectra, calibration images (spectral flat fields, bias and linearity test frames) were recorded during daytime, in order to remove noise from instrumental effects (cf. Chapter. 3). Further descriptions of the calibration images and their setups are provided in Chapter 3.

The data reduction is simplified by extracting sub-images around the spectral lines which are investigated (cf. Fig. 2.1, box around H_α). The sub-images are

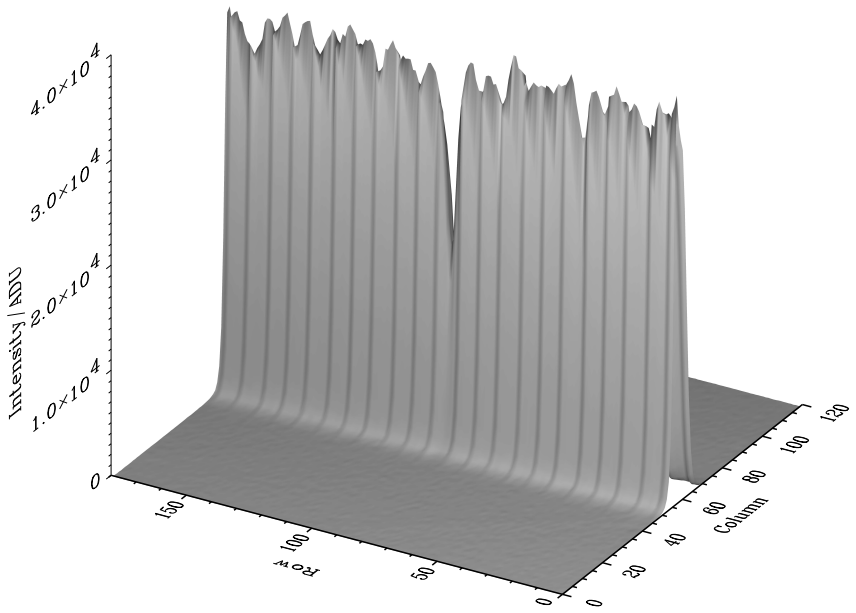

Figure 2.3: 3D plot of the aligned sub-image of the H_α spectral line. The wavelength coverage of this sub spectral order is: 6511 Å-6615 Å.

aligned relative to the row direction by subtracting the mean slope between the row direction and the spectral order[10]. Both extraction and alignment were performed

[10]This crude way of aligning echelle orders which in fact bend slightly, is reasonable because the length of the sub orders are small, and thus the bending can be neglected. The correction by the mean slope lead to lower resolution though, since the order is projected in the row direction by a factor $\cos\theta$, θ being the angle between the column- and slit-directions, which is small however (cf. Fig 2.2).

using **align_sub_order_region.pro**[11], which produces spectra similar to long-slit spectra. The following spectral analysis is based only on these aligned sub-images (cf. Fig. 2.3).

In Table 2.2 I present the number of images obtained during the observing periods dedicated to the equivalent width investigation. The He-Ne/Th spectra were not used for a detailed wavelength calibration but to obtain an image of the shape of the echelle slit (cf. Fig. 2.2). The last column shows the number of linearity sequences, which are of 3×8 exposures each (cf. Sect. 3.1.2).

[11] In the extraction process all the saturated sub-images were ignored. There were 80 H_α sub-images and 16 NaII sub-images ignored in that process. The final number of sub-images for each spectral line can be found by subtracting the number of saturated images from the total number of obtained images given in Table 2.2.

Table 2.2: Observation log of the equivalent width measurements (number of images).

Date -2000	ξ Hya Spectra	Bias Images	Flat Field Spectra	He-Ne/Th Spectra	Linearity Sequences
1503	440	30	20	-	1
1603	300	-	-	-	4
1703	443	-	20	-	-
1803	270	20	20	-	-
1903	250	20	40	-	-
2003	421	20	20	-	-
2103	460	10	-	-	6
2203	380	20	20	-	-
2303	240	-	-	-	4
2403	469	50	-	-	-
2503	460	-	50	-	3
2603	450	50	-	-	-
2703	125	-	-	-	-
2803	175	-	-	-	-
2903	136	50	-	-	4
3003	177	-	-	-	-
3103	132	-	20	-	-
0104	123	50	-	-	-
0204	-	-	-	100	-
0304	120	-	-	-	-
0404	115	50	-	-	4
0504	112	-	-	-	-
0604	106	-	-	100	-
0704	107	50	-	-	-
0804	226	50	-	-	-
0904	149	50	-	-	-
1004	320	-	-	-	-
1104	330	50	-	-	5
1204	40	50	20	-	-
1005	98	-	-	-	-
1105	50	23	40	-	-
1205	340	-	-	-	-
1305	13	40	40	-	-
1405	-	160	-	-	-
1505	-	-	-	-	-
1605	-	-	-	-	-
1705	130	-	-	-	-
1805	50	-	-	-	-
1905	140	40	-	-	-
2005	180	-	-	-	-
2105	124	40	-	-	-
2205	117	40	-	-	-
2305	-	40	-	-	-
2405	50	40	-	-	-
Total	8368	1043	310	200	31

2.2 Radial velocity observations

2.2.1 Observational strategy

The CORALIE spectrograph, used to obtain the stellar spectra for the radial velocity investigation, is an extremely stable instrument (Queloz et al., 1999). The expected noise in this particular data set is much lower than in the equivalent width measurements (cf. Fig. 5.3, *bottom panel*, page 86) and hence the collected flux was not as critical as it was for the observations for the equivalent width investigation (cf. Sect. 2.1).

In order to estimate the exposure time, number of required data points (exposures), sampling rate, and total time span of the observations, known results from the star δ Eri ($V = 3.54$ mag), based on spectra obtained with the same spectrograph (Carrier, F., et al., 2002), was used for comparison.

The V-magnitude of δ Eri and ξ Hya is the same (cf. Table 1.1), hence the exposure time should be equal to that of δ Eri: $t_{exp} = 3$ min. The noise level in the amplitude spectrum of δ Eri around the expected dominant mode of ξ Hya ($\nu_{\max} \simeq 90\,\mu$Hz; cf. Table 1.2) is ~ 4 m/s. Due to their equal magnitude and nearly equal effective temperature, the noise level of the ξ Hya measurements is expected to be the same[12]. To have a clear detection (S/N $\gtrsim 10$), the minimum number of data points required is:

$$\left(\frac{S}{N}\right)^2_{\text{total}} = \frac{S^2_{\text{expect}} \cdot n_{\text{data points}}}{\pi \cdot N^2_{\text{point-to-point}}} > 100$$

$$\Rightarrow \quad n_{\text{data points}} > \pi \cdot 100 \cdot \left(\frac{4\,\text{m/s}}{8.2\,\text{m/s}}\right)^2 = 75 \qquad (2.1)$$

where the expected velocity amplitude of ξ Hya is $v_{\text{expect}} = 8.2$ m/s (cf. Table 1.2).[13]

Based on the estimated oscillation period of ξ Hya ($\sim$ 3 hours), the requested sampling rate is ~ 30 min^{-1} in order to obtain a good sampling, which gives a Nyquist frequency of $\sim 280\,\mu$Hz. Due to the expected large separation (cf. Table 1.2) the separation between a mode and the daily aliases from the neighbouring modes is: $2 \times (7.0\,\mu\text{Hz}) - 11.57\,\mu\text{Hz} = 2.43\,\mu$Hz, corresponding to 5 days of observation. In order to separate such modes, data from at least 14 nights are needed.[14]

[12] It should be noticed, that the $1/f$ noise (instrumental instability and drifts) at these low frequencies rises fast. If the peak of the dominant mode falls 1-2 sigma below the estimated $\nu_{\max}$, the noise from the δ Eri amplitude spectrum gives 7 m/s, hence the minimum number of data points required is rather sensitive to the actual frequency of the dominant mode.

[13] Using an expected noise of 7 m/s instead of 4 m/s, more than 185 data points would be required to be able to reach S/N > 10.

[14] 30 nights would allow separation of the modes in the case where the observed large separation is 1 sigma below the estimated large separation.

2.2.2 Data and configuration

The observations for the radial velocity investigation were performed between February 18th - March 18th 2002 with the CORALIE spectrograph mounted on the 1.2 m Swiss telescope at La Silla (ESO, Chile).[15]

The CORALIE spectrograph has a resolving power ($\lambda/\Delta\lambda$) of 48000 and provided science images (echelle spectra) of ξ Hya with a wavelength coverage ranging from 3875-6820 Å recorded on 68 orders. During the exposure of a stellar spectrum, a thorium spectrum is exposed simultaneously on the CCD to provide a reference which enables one to obtain high precision velocity measurements. Further details about the obtained images and the data reduction, including calculation of radial velocities, will not be described in this thesis, but are described in Bouchy & Carrier (2001, and references herein).[16]

A total of 27 clear nights provided 433 data points yielding $(S/N)_{expect} \simeq 27$, with a frequency resolution of 0.41 μHz. The sampling rate varied through the time series: the first 5 nights (or 64 points) were separated on average by 44 min, while the following 18 nights (or 338 points) were separated by 31 min, and the last 4 nights (or 31 points) were separated by 79 min. The mean separation between all exposures is 34 min, which corresponds to a Nyquist frequency of 245 μHz.

In Table 2.3 I present the number of images obtained during the entire observing period.

[15] The observations were performed by Michel Burnet (Observatoire de Genève, Switzerland), and Thomas Maas (Instituut voor Sterrenkunde, Katholieke Universiteit Leuven, Belgium).

[16] The data reduction, including calculation of radial velocities, has been performed by Fabien Carrier (Observatoire de Genève, Switzerland).

Table 2.3: Observation log of the radial velocity measurements (number of images).

Date -2002	ξ Hya Spectra	Mean sampling interval/min.
1802	13	43
1902	12	48
2002	14	42
2102	12	48
2202	13	44
2302	17	33
2402	16	36
2502	17	34
2602	14	43
2702	15	38
2802	17	35
0103	22	27
0203	17	36
0303	22	27
0403	21	29
0503	22	27
0603	20	30
0703	24	25
0803	0	-
0903	19	32
1003	18	30
1103	19	33
1203	19	32
1303	19	32
1403	0	-
1503	9	72
1603	8	78
1703	8	86
1803	6	79
Total	433	34

Chapter 3

Data reduction

This chapter contains a description of the data reduction, which is the transformation of the raw images into the final 1D spectra to be used for the oscillation analysis. In addition to the fundamental calibrations of the CCD (Sect. 3.1), including an extensive outline of a new high accuracy CCD linearity test (Sect. 3.1.2), the reduction especially related to spectra is also presented (Sect. 3.2), all based on IDL[1] programs made for this particular purpose.

Only the equivalent width data set is described in this chapter, since I have not been involved in the reduction of the raw images of the radial velocity data set (cf. Sect. 4.2).

3.1 CCD calibrations

To calibrate the CCD, the digital output signal[2] from every pixel in the CCD images should be converted to the number of photons hitting the pixel during the exposure (the flux). For the differential spectral analysis applied in this investigation (cf. Chapter 4), the flux does not have to be known on an absolute scale. The main goal of these CCD calibrations is therefore to reduce different noise components of the signal, with the aim of reaching a S/N level high enough to allow the detection of stellar oscillations in ξ Hya.

The number of photons (N_p) hitting within a pixel is related to the number of "released" electrons (N_e) in the pixel through the quantum efficiency $\eta(\lambda)$ ($N_e = N_p \cdot \eta(\lambda)$), where λ is the wavelength of the light. To a good approximation, $\eta(\lambda)$ is a slowly varying function within the very narrow ranges of wavelengths considered in the applied spectral analysis.

N_e is by amplification and Analogue-to-Digital (A/D) conversion related to the output signal through an amplifier gain $\tilde{g}$ of unit "e^-/ADU" or the equivalent "de-

[1] Interactive Data Language (IDL).

[2] The output of the CCD is measured in ADU (Analogue to Digital Unit).

tected photons/ADU".[3] During the amplification process a readout noise is introduced. To avoid negative input at the A/D converter due to readout noise fluctuations, an electronic offset significantly larger than the readout noise, called *bias*, is applied before the signal is converted to ADU.

For long exposures, additional thermally "released" electrons, called *dark current* (N_d), will be detected as a sort of "false light". The accumulated charge coming from the dark current is proportional to the exposure time if the CCD is held at constant temperature.

Concisely stated, the digital output signal, S, from every single pixel can be expressed as (McLean, 1996):

$$S = \frac{N_e + N_d}{\tilde{g}} + bias. \tag{3.1}$$

In the DFOSC manual (Brewer & Storm, 1999, Table 2.2) the dark current is quoted to be $\sim 12e^-$/pixel/hour ($\sim 0.1e^-$/pixel/image, for the exposure time used in this investigation). Compared with the readout noise ($\sim 8 - 20e^-$/pixel/images, for amplifiers A and B; Table 2.1, page 28) the contribution from dark current is negligible, and will be ignored in the following calibrations.

Every pixel in the CCD has slightly different characteristics. In order to correct for the small intrinsic and flux-dependent pixel-to-pixel variations, the CCD calibration is performed on single pixels. The calibration includes the following steps (the resulting signal, S, is indicated in parenthesis):

- Bias subtraction ($S = \frac{N_e}{\tilde{g}}$); (Sect. 3.1.1)
- Linearity correction ($S \propto N_e = N_p \cdot \eta(\lambda)$)[4]; (Sect. 3.1.2)
- Flat fielding ($S \propto N_p$); (Sect. 3.2.1)

In addition to these standard calibration steps, spectral data reduction also includes scattered light subtraction; (Sect. 3.2.2).

3.1.1 Bias and overscan subtraction

Bias can be regarded as the signal coming from a pixel with no accumulated charge (an empty pixel). However the bias level is not exactly the same from one pixel to the other, i.e. a zero-second exposure (bias image) would show small pixel-to-pixel variations on top of a mean bias level.

The mean bias level can suffer from a sort of hysteresis effect, i.e. it depends on the past of the CCD, and can vary during the night. This effect is partly due to

[3] The gain $\tilde{g}$ is constant if the CCD is linear (see further Sect. 3.1.2).

[4] The linearity correction performed in this investigation used a normalized gain so that, after linearity correction, we have: $S \propto N_e$.

"old" trapped charge[5] from the physical image slowly leaking out, and partly due to variations in the applied electronic offset (McLean, 1996, page 279).

In order to measure the variation of the mean bias level, most CCDs, including the DFOSC CCD, have an *overscan* region. The overscan region is comprised of extra virtual columns created by reading more pixels out than actually exist in the real CCD, and lies therefore outside the physical area of the CCD. The signal from the overscan region will therefore measure the mean bias level of the image plus any charge that might have leaked from the real pixels.

When correcting for bias, one must first subtract the overscan level from every image, to remove the instant mean bias level. Second, the small pixel-to-pixel variations in the bias level must be found by combining a large sample of bias images to a master bias, which finally must be subtracted, to finish the bias correction.

The CCD was read out in two halves by two amplifiers simultaneously to minimize readout time (maximize the duty cycle). The two halves of the CCD therefore have two amplifier characteristics, and hence two different overscan regions (25 columns wide for each amplifier) (cf. Fig. 2.1).

The overscan columns are collapsed in the column direction into a 1D array with the mean overscan level of row 'i' in the i'th entry. Plotting these collapsed overscan regions shows that the level along the row direction can vary up to 1.3% within the same image (using **overscan_test.pro**; see Fig. 3.1, *upper left panel.*). Fig. 3.1 (*left panels*) shows clearly the accumulated charge at low row number in the images taken after the CCD had not been used in a while. This effect nearly disappears in the following exposures (see similar plots in Fig. 3.1 (*right panels*)). The mean overscan levels and the standard deviations are also plotted in Fig. 3.1.

Based on the investigation of the overscan behaviour, the complete bias calibration procedure can be written down. If x='column number' and y='row number', the calibration corresponds to the following expression:

$$Data_0(x,y) = Data(x,y) - \langle Data_{\rm scan}(y_{\rm boxcar})\rangle - [Bias_0(x,y)]_{\rm master} \qquad (3.2)$$

where $[Bias_0(x,y)]_{\rm master}$ is the median of a large series of $Bias_0(x,y)$ images:

$$Bias_0(x,y) = Bias(x,y) - \langle Bias_{\rm scan}(y_{\rm boxcar})\rangle. \qquad (3.3)$$

$Data(x,y)$ is the value of pixel (x,y) in the raw data, $\langle Data_{\rm scan}(y_{\rm boxcar})\rangle$ means the average overscan level in the rows $y \pm 10$ pixels[6] of the $Data$ image, and the subscript '0' indicates the corrected image. The same is true where $Data$ is replaced by $Bias$.

The calibration procedure was performed using the following programs:

[5] Charge is trapped if the *charge transfer efficiency* is below 100%.

[6] Calculated by collapsing the scan region in the column direction followed by smoothing along the row direction with a 21 pixel wide boxcar (cf. Fig. 3.1 thick black line).

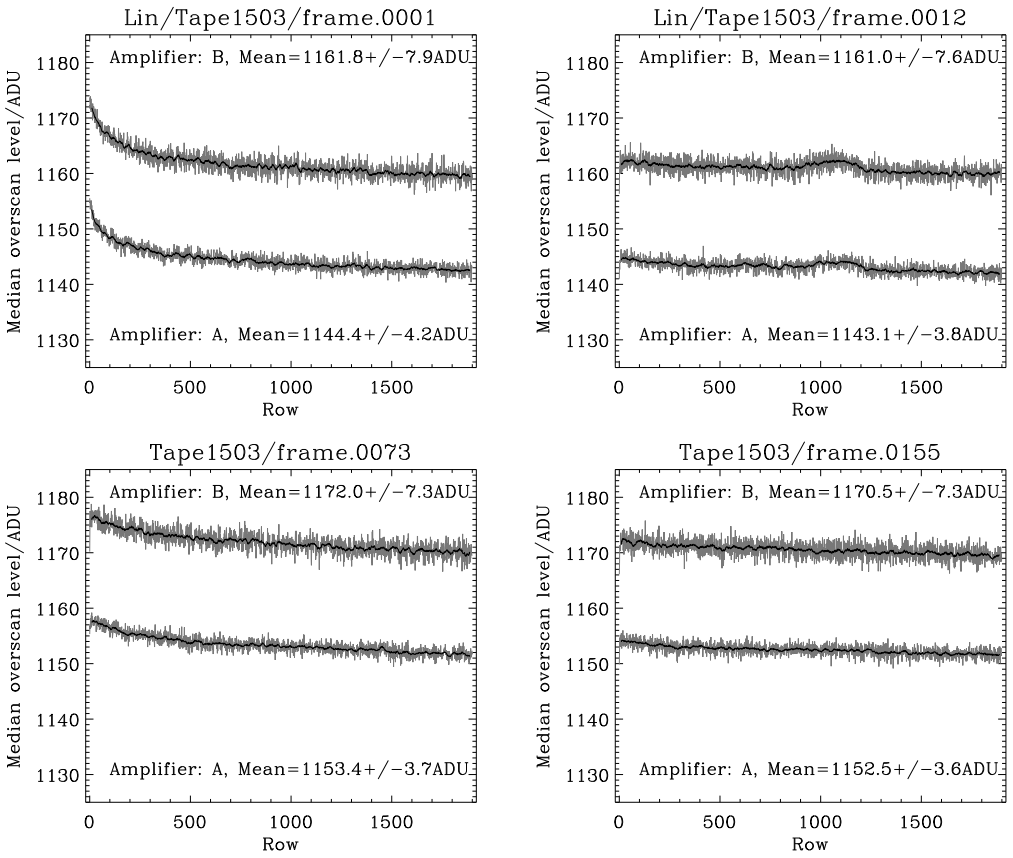

Figure 3.1: Mean overscan levels of four selected images, with smoothed mean over plotted (thick black line). *Left panels*: First images taken after the camera had not been used in a while. *Right panels*: Images which are in the middle of a sequence. *Top panels*: Linearity images; leakage is clearly seen around row $\sim$ 1100 for the right-hand side plot which is the overscan from an image similar to Fig. 3.3 on page 44. *Bottom panels*: Science images; significantly higher overscan level.

- **overscan_lin.pro** and **test_res_overscanstrip.pro**, which perform the subtraction of the overscan level from every image related to the linearity test. **overscan_sub_region.pro** for the same operation on the science images.

- **median_bias_lin.pro**, which constructs temporary master bias images by using bias images related to the linearity test. **median_sub_region.pro**, which performs the same operation using bias images related to the science images. **mean_sub_region.pro**, which constructs one final master bias using the temporary master bias images related to the science images.

- **bias_lin.pro**, which subtracts the $[Bias_0(x,y)]^{\rm lin}_{\rm master}$ images from every linearity image. **bias_sub_region.pro**, which subtracts the $[Bias_0(x,y)]^{\rm science}_{\rm master}$ from every science image.

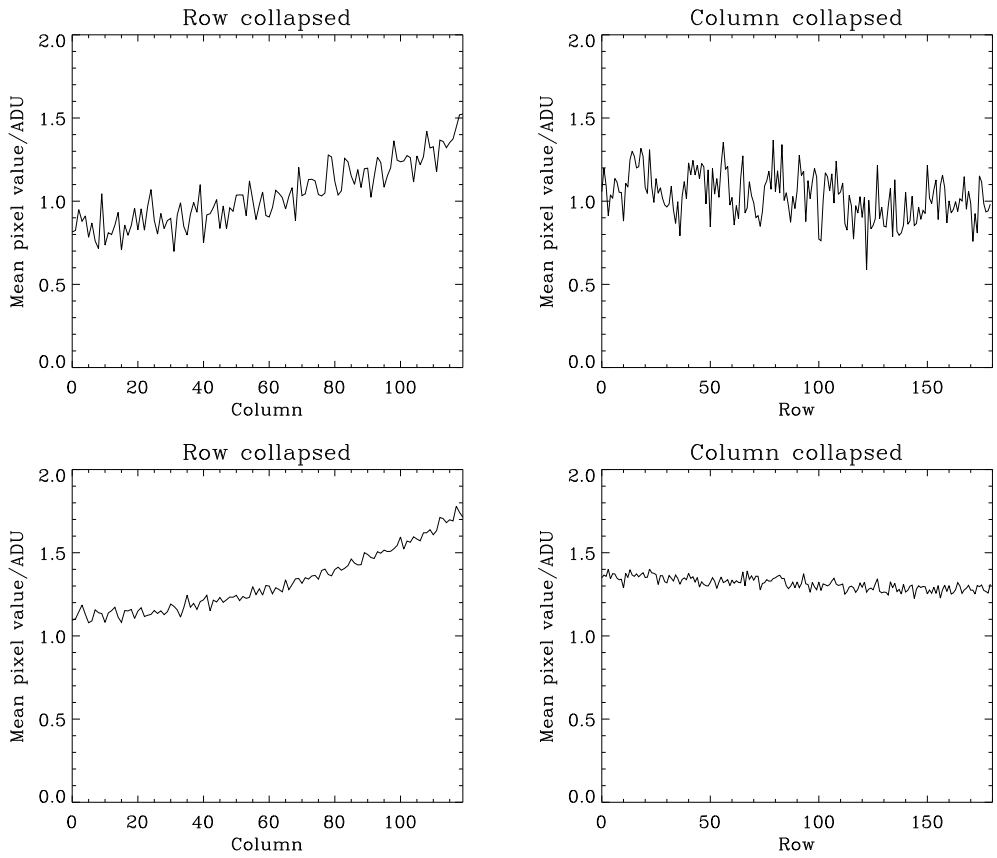

Figure 3.2: Mean bias levels in the column (*left panels*) and the row (*right panels*) direction of the CCD sub-image around the H_α line. *Top panels*: Master bias from a single night (11/04-00). *Bottom panels*: Mean of all master bias images.

A few detailed tests were done before the bias images were collapsed into single master images using the *median* operator.

- First one temporary master bias image per night was made - more precisely one full frame for the linearity test and one sub frame for the science images.

- A group of 100 simulated bias images of the same scatter as the real bias images and their master image were made for comparison using **bias_sim.pro**.

- The statistical properties (max, min, mean, median, standard-deviation) for every master bias and its underlying bias images were inspected using **im_stat.pro**.

- The simulated master bias showed a lower scatter than the real master bias images, indicating that there were large scale trends in the real bias images which propagated through to the master bias images.

- All real bias and master bias images were visually inspected by **mean_row_plot.pro**. Clear gradients were seen in the column direction of all images but not in the row direction (removed in the overscan subtraction) (see Fig. 3.2 *top panels*).

- To test if the observed gradients in the temporary master bias images were similar, different master bias images were subtracted from each other (using **im_subtract.pro**). The residual master bias images showed no significant trends (compared to the scatter).

Based on these tests, it was decided that one mean master bias image should be made from all the temporary master bias images (using **mean_sub_region.pro**). The trends in the mean master bias image for the H_α region are plotted in Fig. 3.2 (*bottom panels*)[7].

3.1.2 CCD linearity test

If a perfectly linear CCD is considered, the output signal will be proportional to the exposure time if it is exposed to a light source which is absolutely stable in time ($\tilde{g}$ in Eq. 3.1 will be constant). Simply put, a short and a long exposure give the same amount of "measured" photons per second, if one neglects dark current and bias.

At some level, every CCD deviates from a perfect linear detector because the amplifier gain $\tilde{g}$ will depend on the intensity of the incoming light. If the required accuracy is higher than can be achieved due to a relatively high level of non-linear effects displayed by the CCD, it is essential to get accurate knowledge of the non-linear behaviour. With this knowledge in hand, it is possible to correct the data for these non-linear effects. In order to detect stellar oscillations in a star like ξ Hya, the data must be of very high precision, which puts a high demand on the precision to which the non-linear effects must be known.

In the following, a new method is introduced to perform extremely precise CCD linearity tests. The basic idea of this method is to read the CCD gain (normalized) through the variations of the *gain ratios* between images of different exposure times (cf. Eq. 3.9), as a function of measured intensity. The present method is a variation of a method based on the same idea, which was previously outlined and applied by Knudsen (2000). Compared to the linearity test of Knudsen (2000), the test presented here gives a more precise determination of the gain ratios for all measured intensities[8]. The final result of the presented linearity test is the CCD gain (normalized) which is not the case in Knudsen (2000).

[7]The statistical properties of this final master image are: Max = 2.75, Min = −0.11, Mean = 1.32, Median = 1.31, Standard deviation = 0.38.

[8]By not using iterations to find the gain ratios, this method avoids the accumulation of errors seen in Knudsen (2000, Fig. 4.17).

To give a general view of this method, a short description of it will be presented, followed by an outline of every step, showing the details of the method and how the complications which appeared during the analysis were dealt with.

The cookbook way of performing this linearity test can be summarized as:

- **Observations:** Take a series of images with different exposure times which have a large, smoothly-varying intensity in one direction, with longest exposure close to the CCD saturation point.
- **CCD reductions:** Collapse the images in the non-varying direction into 1D *intensity curves*.
- **Gain ratio maps:** Map the 1D intensity curves of different exposures relative to the intensity curve of the longest exposure as a function of the intensity of the curve of the longest exposure (normalized) (called *gain ratio maps*).
- **Master gain ratio map:** If the above maps are similar, make a master gain ratio map R_1 and use it as the first estimation for the *gain* ($G_1 \equiv R_1$).
- **Inversion:** Construct the gain ratio map R_2 based on G_1 ($G_1 \curvearrowright R_2$), and let R_i converge to R_1 via an iterative loop: $G_i = \frac{R_1}{R_i} G_{i-1}$;
  $\Rightarrow G_i$ will then be the gain.

Observations

Contrary to "classical" flat field images, every image in this linearity test contains a large intensity variation, ranging from approximately the bias level to some maximum which is determined by the exposure time (cf. Figure 3.3)[9].

Linearity images ("flat fields") of four different exposure times were made (1s, 3s, 12s, and 40s) where the maximum intensity of the 40s exposure is close to the saturation limit of the CCD. The sequence with which the linearity images were made is: 3×1s, 3×3s, 3×12s, 3×40s, 3×12s, 3×3s, 3×1s, 3×0s (i.e. 3×8 images per sequence); the 0s exposures being the *bias* images for this sequence. These tests were performed throughout the entire observing period and mostly as multiple sequences (see Table 2.2, page 33).

CCD reductions

The groups of three images per non-zero exposure time per sequence were median filtered with **median_frames.pro**, resulting in 7 images per sequence. All the 0s exposures of a given night with multiple linearity sequences were median filtered to one master bias with **median_bias_lin.pro**. The median filtered images were

[9]The DFOSC setup for these images were: long slit (1.5″), V filter (ESO #451), grism #7, high-AB read out, and the light source was the DFOSC flat field lamp. Both amplifiers are used in order to map their linearity behaviour since both are used to obtain the stellar spectra.

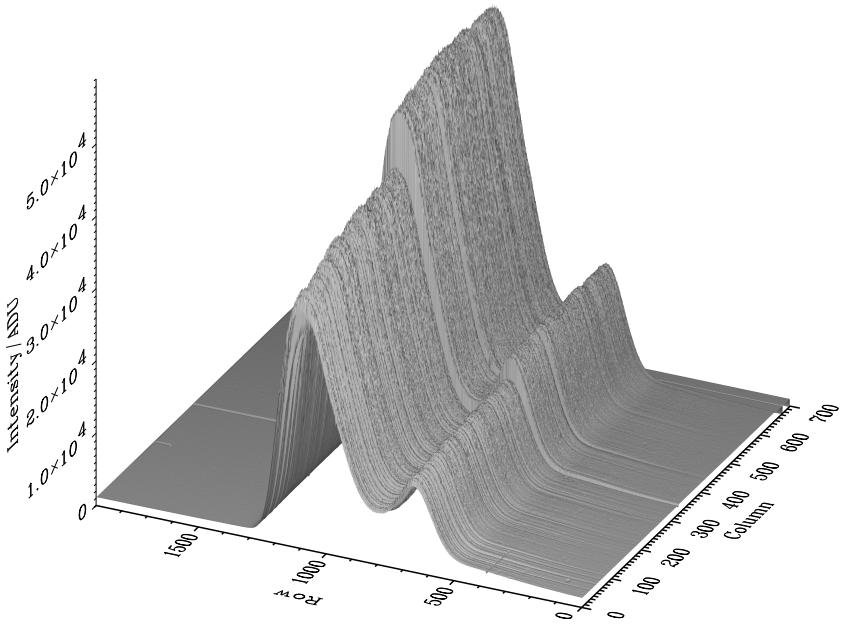

Figure 3.3: 3D plot of a typical raw linearity test image. Read-out was performed by two different amplifiers operating simultaneously; column 0:324 was read out through amplifier 'A' and column 325:649 by amplifier 'B'. A small gradient is seen in the column direction, which is probably due to slit width variations. The CCD is therefore more illuminated at higher column numbers.

overscan subtracted (with **overscan_sub_lin.pro**), and the non-bias images were furthermore bias subtracted using **bias_sub_lin.pro** (cf. Sect. 3.1.1).

After the basic CCD reductions, each image was collapsed into two 1D intensity curves (using **column_collaps.pro**), one for amplifier 'A' and one for amplifier 'B' (cf. Fig. 3.4), which were treated *separately* and *similarly*, and hence will not be specified in the following outline.

Gain ratio maps

To make it possible to understand what a gain ratio map is, I first describe in detail what a measured *1D intensity curve* is, and how *relative intensity curves* can be interpreted as *gain ratio maps*. This will be followed by a description of the steps taken to create gain ratio maps based on the intensity curves.

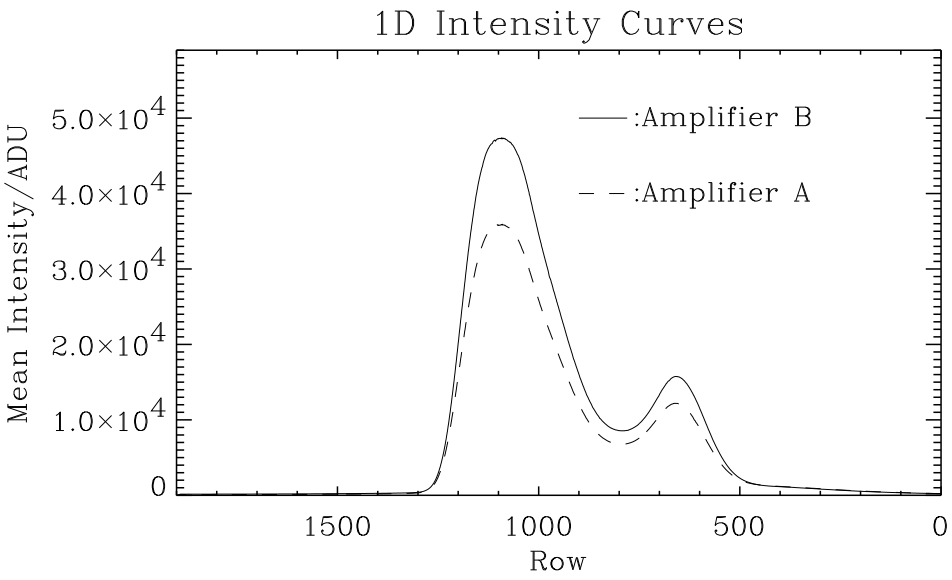

Figure 3.4: 1D column collapse of a typical linearity test image (40s exposure). Solid line indicates the collapse of the amplifier 'B' part. Dashed line indicates the amplifier 'A' part.

If the CCD were completely linear, the shape of the *1D intensity* curves would all be similar if scaled inversely with their exposure time. In that case the "measured" mean intensity in the n'th row, for a given amplifier, would be (cf. Fig. 3.4):

$$I_{\text{measure}}(n,t) = I_{\text{receive}}(n,t) = T_{\text{expose}} \times S(n,t), \tag{3.4}$$

where

$$S(n,t) = \int_n^{n+1} S(x,t)\,\mathrm{d}x, \qquad x \in \mathbb{R} \tag{3.5}$$

where I_{receive} is received intensity, T_{expose} is the effective exposure time[10] and $S(x,t)$ is the normalized shape of the intensity curves, with t indicating that the shape can change in time (from one curve to the other) due to instrumental instabilities.

Because of non-linear effects in the CCD, the "measured" mean intensity in the n'th row is instead:

$$\begin{aligned} I_{\text{measure}}(n,t) &= I_{\text{receive}}(n,t) \cdot \tilde{g}(I_{\text{receive}}(n,t)) \\ &= T_{\text{expose}} \cdot S(n,t) \cdot \tilde{g}(I_{\text{receive}}(n,t)) \\ &= T_{\text{expose}} \cdot S(n,t) \cdot g(I_{\text{measure}}(n,t)), \end{aligned} \tag{3.6}$$

where $\tilde{g}$ is the amplifier gain of the CCD (Eq. 3.1), which is a function of the "received" amount of photons, and g is the gain as a function of the "measured" amount of photons. The function g exists if there is a one-to-one relation between

[10]Including possible dead time of the shutter and non-constant effects from the light source.

the "received" and "measured" amount of photons. Since a well functioning CCD amplifier does have a well-defined output signal for every input signal, it is equivalent to regard the gain either as a function of the "received" or the "measured" light. The known quantity is $I_{\text{measure}}(n,t)$, so in the following linearity analysis it is the variation of the gain function g that will be measured. Below $I_{\text{measure}}(n,t)$ will be written as $I(n,t)$ or I for simplicity.

Consider the intensity curves of two different images , say a 12s and 40s exposure taken at time $t^{12\text{s}}$ and $t^{40\text{s}}$, with the following measured mean intensities for the n'th row (using Eq. 3.6)

$$I(n,t^{12\text{s}}) = T^{12\text{s}}_{\text{expose}} \cdot S(n,t^{12\text{s}}) \cdot g(I(n,t^{12\text{s}})) \tag{3.7}$$

and

$$I(n,t^{40\text{s}}) = T^{40\text{s}}_{\text{expose}} \cdot S(n,t^{40\text{s}}) \cdot g(I(n,t^{40\text{s}})). \tag{3.8}$$

The *relative intensity curve* then is:

$$\frac{I(n,t^{40\text{s}})}{I(n,t^{12\text{s}})} = \frac{T^{40\text{s}}_{\text{expose}}}{T^{12\text{s}}_{\text{expose}}} \cdot \frac{S(n,t^{40\text{s}})}{S(n,t^{12\text{s}})} \cdot \frac{g(I(n,t^{40\text{s}}))}{g(I(n,t^{12\text{s}}))}. \tag{3.9}$$

Possible dead time for the shutter and intensity variations of the light source, which in principle changes the effective exposure times, can be neglected because this linearity analysis is differential[11]. This allows their relative effective exposure time to be a free parameter used for normalization.

Assuming that there are no instrumental drifts in the time interval from $t^{12\text{s}}$ to $t^{40\text{s}}$ (or $S(x,t^{12\text{s}}) = S(x,t^{40\text{s}})$), the relative intensity curve (Eq. 3.9) is a *map of the gain ratio*[12], but in this case it is a function of the two different measured intensities! This in fact means that every point on a map $I^{40\text{s}}/I^{12\text{s}}$ (or equivalent $g(I^{40\text{s}})/g(I^{12\text{s}})$) versus $I^{40\text{s}}$, is linked to another point corresponding to the lower intensity $I^{12\text{s}}$. To find $g(I)$ from such gain ratio maps can therefore be a complex inversion problem. The solution to this inversion problem will be outlined later in this thesis (cf. page 52), after a description of the construction of the gain ratio maps.

Due to the fact that the light source used is almost inevitable slightly varying, the intensity curves could not simply be combined to obtain master curves. Instead, several careful steps, itemized below and later described in full detail, had to be performed.

- First, the intensity curves must be tested to determine if they have a similar shape ($S(x,t_1) = S(x,t_2)$); (**Stability test**).

[11] This is only correct when considering the relative intensity curves (Eq. 3.9) but not in the later inversion process which calculates the gain from the measured relative intensity curves (cf. page 52).

[12] When I in the following use the words 'gain ratio map' instead of 'relative intensity curve', I practically mean the same thing, because the relative exposure time can be ignored.

- Next, the small shape deviations must be corrected so that similar shapes can be obtained; (**Corrections**).

- Finally, the intensity curves of the same exposure time must be combined and gain ratio maps for each exposure time constructed; (**Combination**).

Stability test: Relative intensity curves (cf. Eq. 3.9) are plotted to test if the intensity curves have a similar shape, (see examples in Fig. 3.5 *top-* and *middle panels*). From these plots it is seen that a trace of the relative intensity curves from $I^{40s} = 0$ ADU to $I^{40s} = I^{max}$ and back again does not follow the same path because there are instrumental drifts, which alter the shapes of the intensity curves from one curve to the next. The change in shape is more obvious when there is a larger time span between the exposures and at the beginning of a multiple linearity sequence, which one can see by comparing Fig. 3.5 *left panels* (beginning of multiple sequence) with *right panels* (end of multiple sequence). These changes in the shape of the intensity curves between early and later images always show the same trend. This could indicate that the linearity sequences were started before the flat field lamp and instrument had reached maximum temperature (cf. App. A).

Corrections: In the following the observed shape difference between the intensity curves is investigated, to identify its cause and to determine how to correct for it properly. For this purpose, intensity curves are smoothed by a 30 pixel wide boxcar and approximately 17 spline interpolations are made per pixel. These operations enable the curves to be "pictured" at the sub-pixel level.

To test if the non-similar shape of the curves can be explained by a simple shift, the intensity curves were shifted relative to each other until the best match is obtained. Fig. 3.6 (dashed line) shows the result of such a shift. The conclusion is that the deviation from the similar shape assumption is partly due to a relative shift in the shape. For $I^{40s} \lesssim 12000$ ADU (Fig. 3.6, dashed line) effects from additional higher order shape deformations are still seen which probably originate from color changes of the flat field lamp.

Generally, the shifts of the curves $I(n, t_1)$ and $I(n, t_2)$ relative to $I(n, t_3)$ are of equal size and opposite sign when $t_3 = \langle t_1, t_2 \rangle$, if the shift is linear ($|t_1 - t_2| \ll T_{\text{instability}}$; $T_{\text{instability}}$ being the instability time scale). Plots like Fig. 3.5 (*top-* and *middle panels*) support the assumption that a linear shift occurs between the two 12s exposures taken before and after ("symmetric" in time) the 40s exposure in a linearity sequence[13]. If the two "symmetric" 12s intensity curves are combined by taking the mean, the output should be "nearly" of the same shape as the in-between 40s exposure[14].

Finally, an estimation of how large the maximum shift may be must be made, to prevent the slightly changed mean shape from dominating the higher order shape

[13]This assumption is more critical for the 3s and 1s exposures which have a larger time span in between them.

[14]This "nearly" is because $\langle S(x - \delta x, t), S(x + \delta x, t) \rangle \neq S(x, t), \forall\ \delta x > 0$.

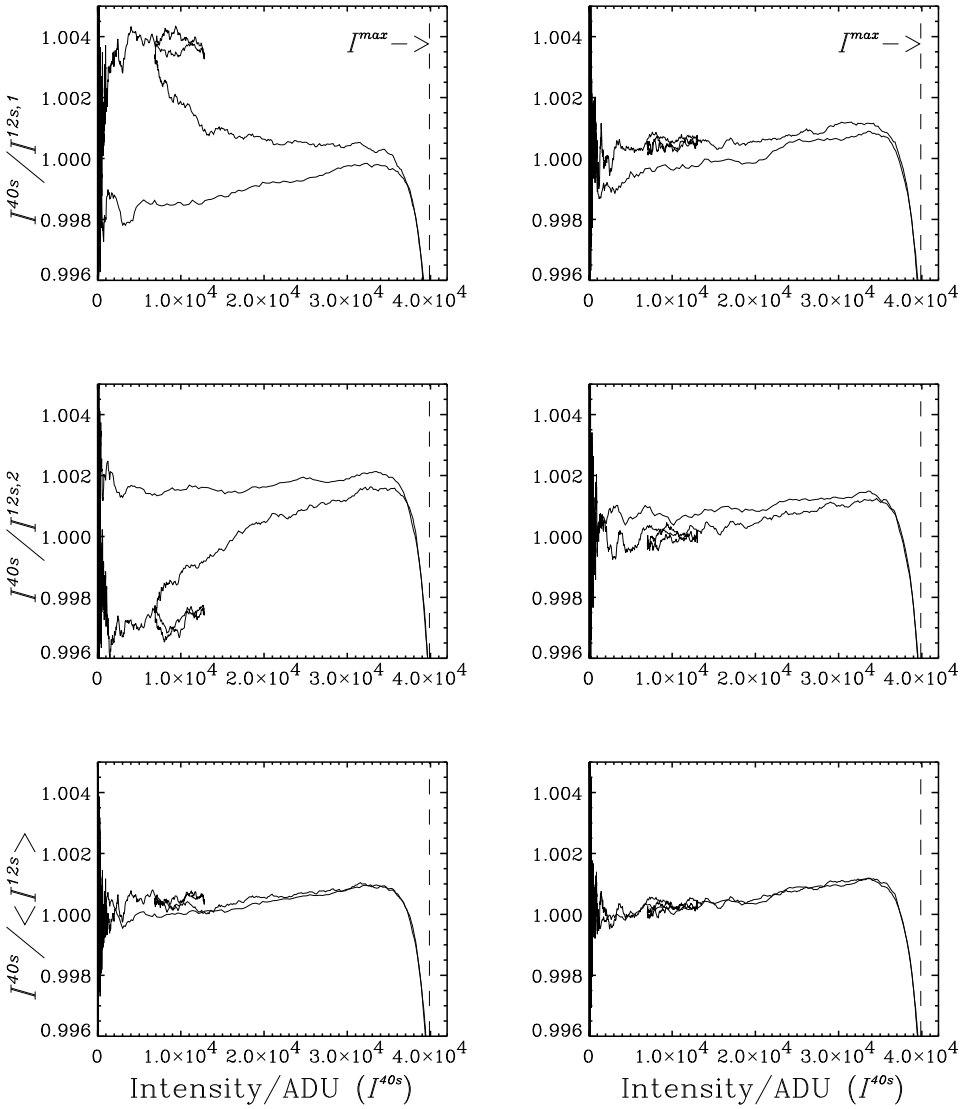

Figure 3.5: Relative intensity curves (cf. Eq. 3.9) (smoothed and normalized) between 40s and 12s exposure curves versus intensity of the 40s curves from the first (*left panels*) and the last (*right panels*) linearity sequence of 29/03/2000. *Top panels:* The 40s exposure relative to the 12s exposure which was made before the 40s exposure in the linearity sequence. *Middle panels:* The 40s exposure relative to the 12s exposure which was made after the 40s exposure in the linearity sequence. *Bottom panels:* The 40s exposure relative to the mean of the two 12s exposures. The increasing noise at the low intensity part ($I^{40s} \lesssim 2000\,\mathrm{ADU}$) is due to the relatively low number of photons in this domain, which means that photon noise and variations in zero point begin to dominate. The small loops at roughly 10000 ADU are due to the lowest peak in the intensity curves (cf. Fig. 3.4).

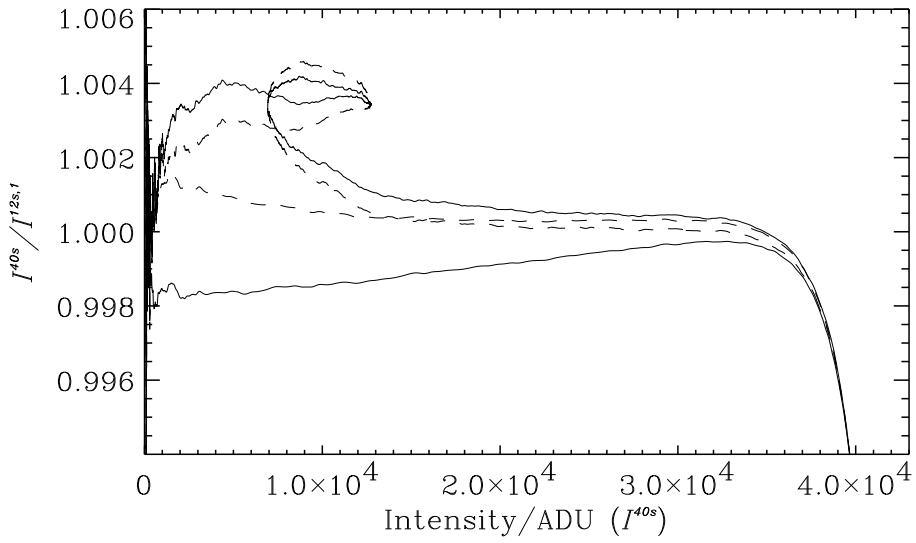

Figure 3.6: *Solid line*: Relative intensity curves (smoothed and normalized) between the same 40s and 12s exposures as in Fig. 3.5 *top left plot*. *Dashed line*: A relative shift of 0.06 pixel (corresponding to 0.9 μm) between the two intensity curves resulted in the best match.

deformations seen in Fig. 3.6 for $I^{40s} \lesssim 12000$ ADU. A requested maximum relative deviation of the shapes below the 0.0005 level (1/2 of a thousandth) is a safe limit. A 12s exposure is used as reference shape to create $I(x, t^{12s})/\langle I(x - \delta x, t^{12s}), I(x + \delta x, t^{12s})\rangle$ for different values of δx, and the result is seen in Fig. 3.7. Based on this test, the maximum allowed deviation expressed as a maximum shift is $\delta x < 0.6$ pixel, which is fulfilled in all the linearity sequences[15].

Thus, the creation of mean curves (one for each exposure time: 1s, 3s, 12s) of the two related curves which are taken before and after the 40s exposure ("symmetric" in time) within the same sequence safely eliminates the shape-shifting deformation without introducing uncontrolled systematic errors.

Combination: To make sure that the above shape correction gives good results, plots similar to Fig. 3.5 (*bottom panels*) of the three different exposure times 1s, 3s, and 12s, were all inspected using **lin_test_plot.pro**. The following step combines the curves within the same multiple sequence into one master for each exposure time using **lin_test_comb.pro**[16]. The output from this is 8 master curves per exposure time, distributed over the entire observation run. The curves of the same exposure

[15]The shift of 0.06 pixel (corresponding to 0.9 μm) shown in Fig. 3.6 is one of the largest observed shifts between a 12s and 40s exposure.

[16]During the combination of intensity curves, single lined curves are obtained. This is done by calculating the mean of the relative intensity curve along the abscissa (I^{40s}) within 250 ADU wide intervals ranging from 0 ADU to I^{max}.

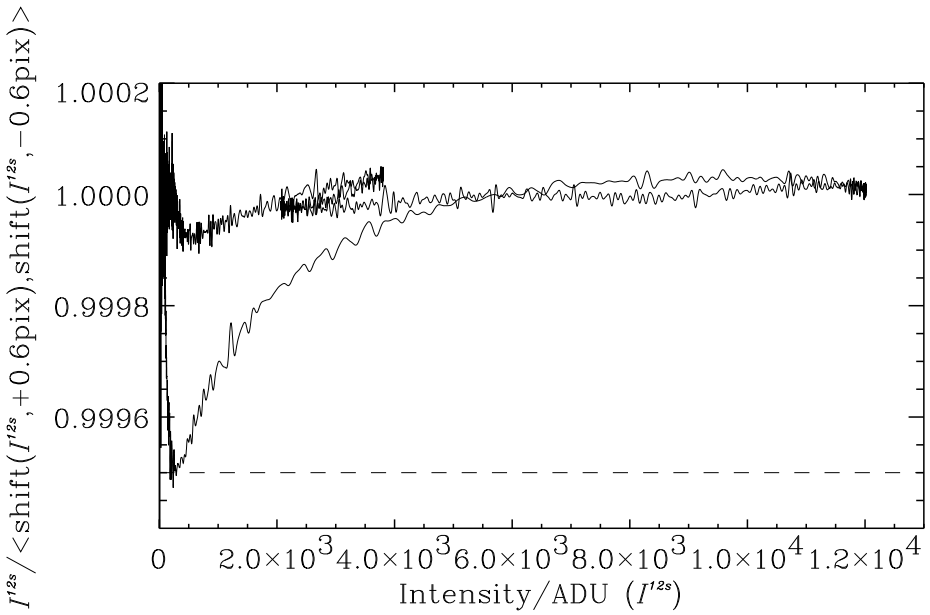

Figure 3.7: Smoothed relative intensity curves (normalized) between the 12s exposure and the mean of its two shifted editions. The shift is 0.6 pixel. Dashed line indicates the maximum allowed deviation.

time are very similar and no significant changes are detected during the approximately one month of observations. On this basis, all curves of the same exposure time are combined to one master curve for each amplifier using **lin_test_total_comb.pro**.

Master gain ratio map

The constructed master curves have in common a particular feature (cf. Fig. 3.8). A very small bump at approximately 12000 ADU for amplifier A (15000 ADU for amplifier B), which is the result of the extra number of data points combined just below 12000 ADU compared to above. This is due to an imperfect match between the two parts of the intensity curve coming from the low and the high peaks (see Fig. 3.4), which arises partly because no corrections were made for high order shape deformations. The bump would of course not be seen if $S(n,t_1) = S(n,t_2)$. For the $\langle I^{40\mathrm{s}}\rangle/\langle I^{3\mathrm{s}}\rangle$ vs. $\langle I^{40\mathrm{s}}\rangle$ curve this bump is larger than seen in Fig. 3.8, and even larger in the $\langle I^{40\mathrm{s}}\rangle/\langle I^{1\mathrm{s}}\rangle$ vs. $\langle I^{40\mathrm{s}}\rangle$ curve. This growing bump trend is due to non-linear instabilities, in this case seen as a larger shift between the 40s exposure and the earlier exposures than between the later. The assumption $|t_1 - t_2| \ll T_{\mathrm{instability}}$ therefore does not hold and $\langle S(n, t^{1\mathrm{s},3\mathrm{s}}_{\mathrm{former}}), S(n, t^{1\mathrm{s},3\mathrm{s}}_{\mathrm{later}})\rangle \neq S(n, t^{40\mathrm{s}})$.[17] (cf. App. A).

[17] The bump would be somewhat suppressed if the setup of Knudsen (2000, Fig. 4.9) were used (Grism#4 instead of Grism#7, and the quartz-halogen dome lamp instead of the DFOSC flat field lamp), which gives intensity curves with only one "hill top". However, the quartz-halogen dome lamp showed variability of $\sim 4\%$ (Knudsen, 2000, Fig. 4.11) significantly larger than the variability of the DFOSC flat field lamp (cf. App. A).

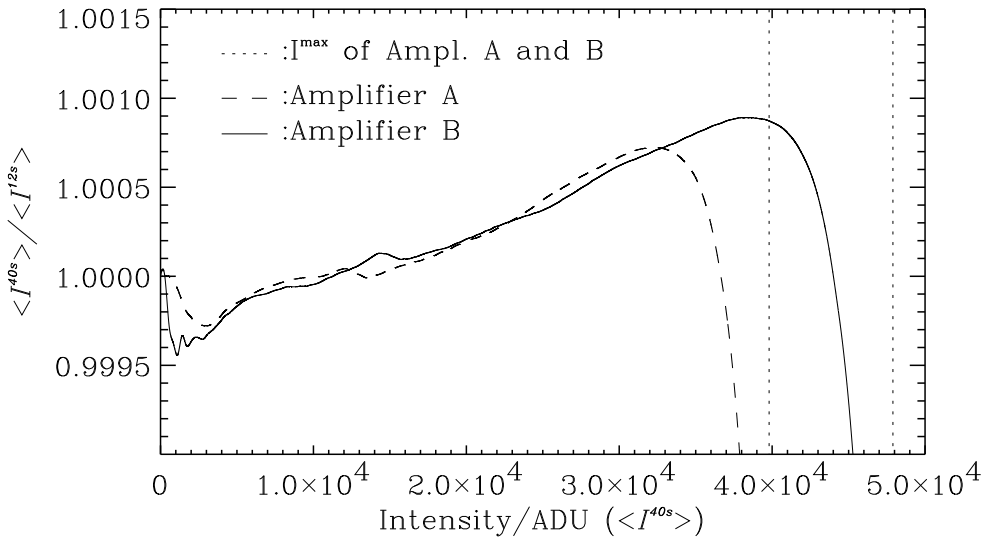

Figure 3.8: Master gain ratio maps (smoothed) based on all 40s and 12s exposures as a function of I^{40s}.

Only the 40s and 12s exposures are used in the following development of the final linearity curve, because it turned out to be more accurate.

It is possible, though extremely unlikely, that some non-linear effects of the gain will not be detected by this gain ratio-based linearity test. If these non-linear effects repeat themselves every time the intensity goes up by T_1/T_2 (the relative exposure time), they can still vary significantly, as seen in Fig. 3.9. To determine if the CCD accidently display such odd non-linear effects, the final gain ratio map $\langle I^{40s}\rangle/\langle I^{12s}\rangle$ was visually compared with the two others which are based on different relative exposure times (T_1/T_2 = 40s/3s and T_1/T_2 = 40s/1s). Apart from the growing bump, the three curves looked quite similar, so it could be concluded that *no such hidden non-linear behaviour is present.*

The measured master gain ratio map $\langle I^{40s}\rangle/\langle I^{12s}\rangle$, hereafter called R_1, will in the following be used as a first estimation for the normalized gain curve G_1.

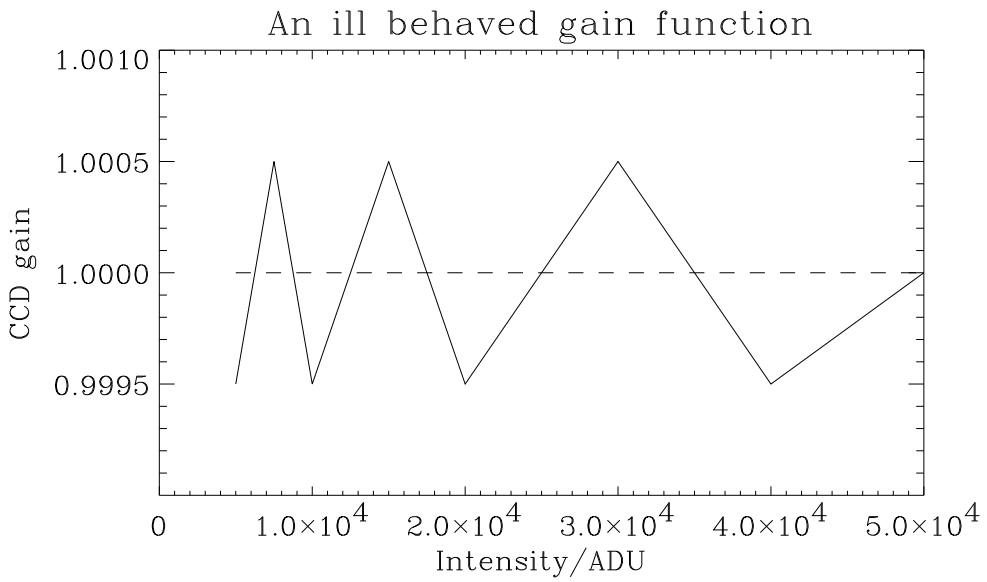

Figure 3.9: Example of a normalized gain function (*solid line*) which would produce a linear looking gain ratio map (*dashed line*) if the relative exposure times between the intensity curves were: $T_1/T_2 = 2$.

Inversion

In this section the inversion technique used to find the underlying normalized gain curve which causes the measured gain ratio map will be explained.

To see how well G_1 reproduces the measured gain ratio map R_1, the gain ratio map R_2 is computed, based on G_1.[18] The new estimation for the gain can then be corrected by the relative deviation between R_1 and R_2 ($G_2 = \frac{R_1}{R_2} G_1$), etc. This iterative process stops when G_i reaches the gain curve whose gain ratio map R_{i+1} matches the measured R_1.

The above solution of the inversion problem is performed with the **lin_curve_converge.pro** program, and a plot of the inversion process is seen in Fig. 3.10, for both amplifier 'A' and 'B'. Selected gain curves G_i and all gain ratio maps R_{i+1} are indicated on the amplifier 'A' plot. For amplifier 'A', the iteration stops after only four iterations (G_4), while the amplifier 'B' curve is not determined until

[18]The computation is done by calculating $R_2(I) = G_1(I)/G_1(I \times 12/40)$ for all $I \in [1, I_{\max}]$. The error introduced by assuming that the effective relative exposure time is 40/12, is at out-most 0.5% (cf. App. A) which includes both dead time error ($\sim$ 30 msec corresponding to a $\sim$ 0.25% error) and intensity variability of the flat field lamp. This error propagates to the estimated $G_i(I \times 12/40)$, but is negligible when the change of gain (the derivative) is small. The maximum error in estimated gain due to this error is $\lesssim$ 500 ppm (parts per million) (maximum is at the saturation point where the change of gain is very large). In the range $I \in [3000, 40000]$ (for amplifier B) the error is only $\lesssim$ 10 ppm.

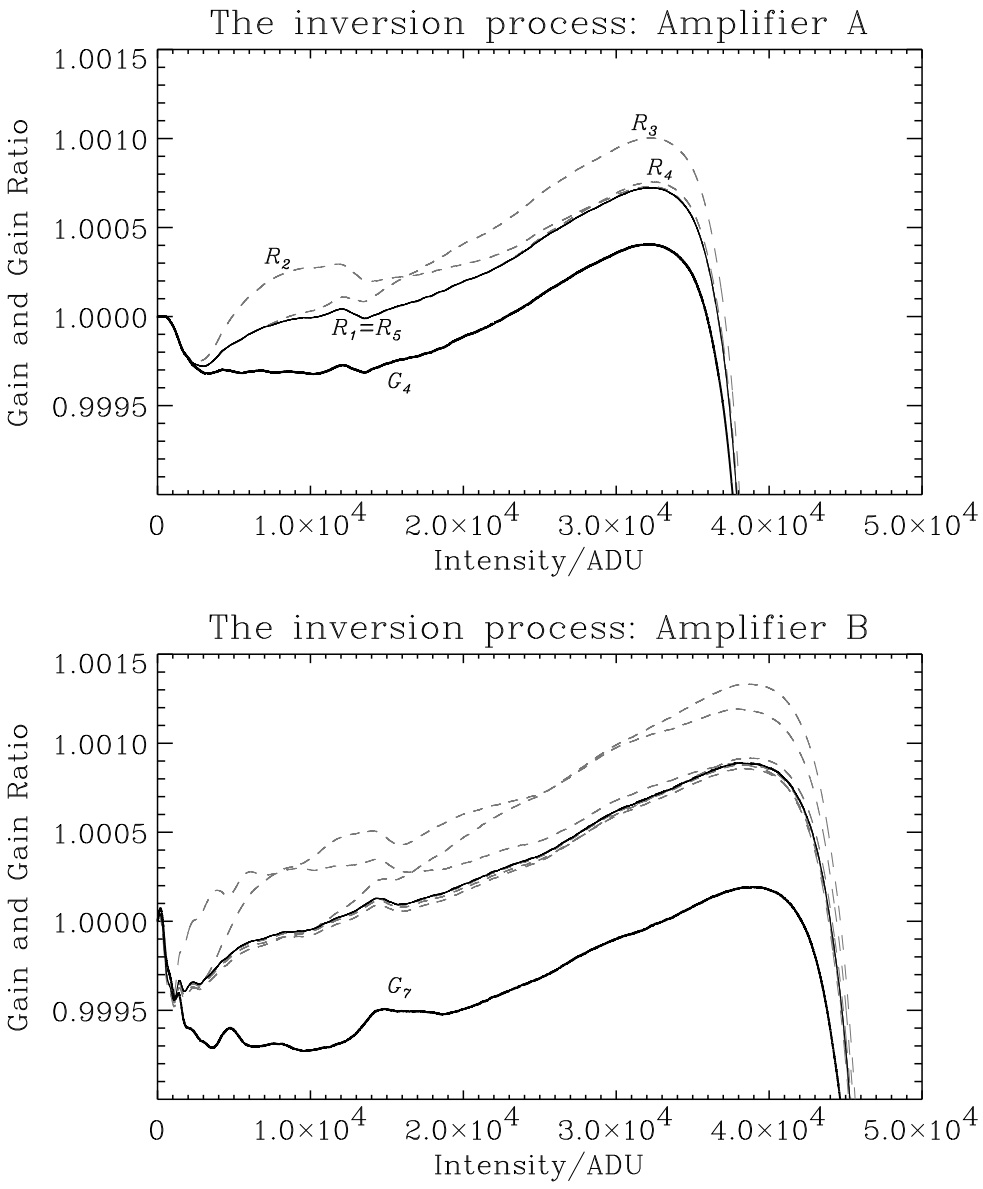

Figure 3.10: Iteration from measured gain ratio map to gain. Selected gain curves G_i and all gain ratio maps R_{i+1} are indicated in the top plot (about G_i and R_{i+1}, see text). The measured gain ratio map R_1 (*thin black dashed line*) is hardly seen because it is perfectly matched by the final iterated gain ratio map (*thin black solid line*). All iterations R_i in the inversion process are marked by *grey dashed lines*, and the final achieved gain curve is the *thick black solid line*.

G_7. The measured gain ratio map which is used as the first estimation ($G_1 \equiv R_1$) is plotted with a thin black dashed line, but it cannot be seen since it is perfectly matched by the final gain ratio map from the iteration R_5 and R_8, for amplifier 'A' and 'B', respectively (*thin black solid line*).

The final gain curves or linearity curves (G_4, G_7 for amplifier 'A' and 'B', respectively) are saved as a linearity look-up table, which in its i'th entry has the value of the gain curves corresponding to 'i' ADU (using **make_lookup_tab.pro**). The look-up table ranges from 0 ADU to 39800 ADU and 47900 ADU for amplifier A and B, respectively, and it is used by **linearity_correct.pro** to correct for the fairly small non-linear effects of the CCD.

Linearity summary

- The linearity behaviour of the CCD has been measured to a very high precision of 100 ppm (parts per million).
- The CCD showed no non-linear effects above the $1^0/_{00}$ level.
- It is shown that the CCD does not have additional hidden non-linear effects not seen in the final linearity curve (cf. Fig. 3.10, *thick black line*).
- The linearity curve is stable over a period of approximately one month.
- The analysis showed clear indications that the DFOSC flat field lamp was an unstable light source (color change and temperature fluctuations), and therefore not suited for absolute calibrations.

3.2 Spectral reductions

The part of the data reduction described in this section is unique for observations of spectra compared to photometry. It includes spectral flat fielding (Sect. 3.2.1), correction for scattered light (Sect. 3.2.2), and finally the extraction of the 1D spectra (Sect. 3.2.3) used for the spectral analysis (cf. Chapter 4).

3.2.1 Spectral flat fielding

In this section the process called flat fielding, which corrects for the pixel-to-pixel variation of the quantum efficiency is outlined.

Every pixel of the CCD has a different quantum efficiency, $\eta(\lambda)$ (see page 37), due to imperfections in the CCD semiconductor material. This pixel-to-pixel sensitivity variation will cause a non-flat structure in images of an uniform illuminated field (flat field images), which ideally should be flat. The relative sensitivity of each pixel seen in the normalized flat field images also influences the science images. The correction can in short notation be expressed as:

$$Data_{\rm flat\_corr}(x,y) = \frac{Data_0(x,y)}{[Flat_0(x,y)/\langle Flat_0\rangle]_{\rm master}}\,, \tag{3.10}$$

where

$$Flat_0(x,y) = Flat(x,y) - \langle Flat_{\rm scan}(y_{\rm boxcar})\rangle - [Bias_0(x,y)]_{\rm master}. \tag{3.11}$$

$Data_0(x,y)$ is the bias corrected image (Eq. 3.2, page 39), $Data_{\rm flat\_corr}(x,y)$ the image corrected for flat field structure, and further the notation of Eq. 3.2 is adopted. Dividing $Data_0(x,y)$ with the normalized master flat field provides the data image (stellar spectrum) corrected for flat field structures[19].

The flat field images, which are recorded with the same setup as the data images, are spectra of the inside of the dome illuminated by scattered light coming from a quartz-halogen lamp (Fig. 3.11). The flat fields were recorded on several nights during the entire observing period (see Table 2.2, page 33).

Position and width of the spectral flat field orders are inspected using **calc_starpos_parm.pro**; no images turned out be deviant. Before the groups of flat field images from a single night could be combined, they were collapsed in the row direction to get the mean shape. Then it was tested if these mean shapes could be matched by simple shift and scaling. These tests showed excellent correlation, and therefore the normalized images made on the same night were combined, through

[19]The variations in the flat field structure caused by dust on the entrance window of the CCD vacuum chamber are by this division treated as if it was quantum efficiency variations in the CCD.

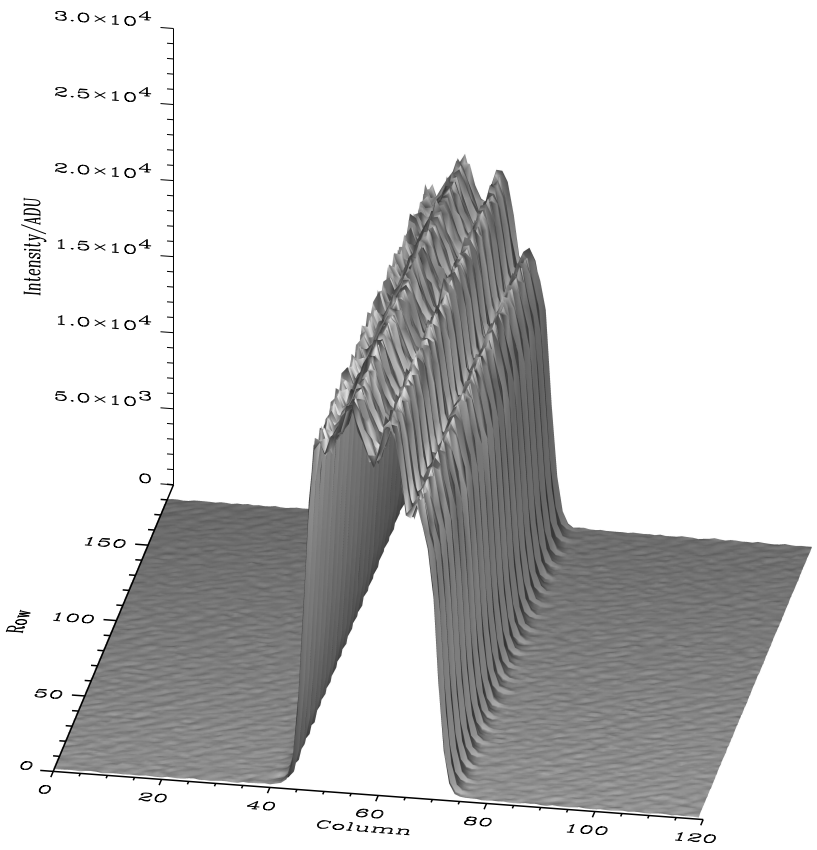

Figure 3.11: 3D plot of a flat field image for the region around the H_α spectral line. Relatively large irregularities are seen on top of the flat field order in the column direction (along the slit) due to varying slit width (see text, page 57).

the use of a median filter (using **normalize_flat.pro**[20] and **median_sub_region.pro**). The combined flat field images were plotted on top of each other (using **scat_cor_test.pro**), and the maximum shift between two combined images turned out to be approximately 1.5 pixel (corresponding to $\sim 22\,\mu$m) (cf. Fig. 3.12).

The combined flat field images are furthermore combined to one master flat field image using **mean_sub_region.pro**. The irregularity in the column direction is slightly smoothed by the creation of the master flat, nevertheless the relative pixel-to-pixel sensitivity is preserved. The master flat is overscan- and bias-subtracted (Sect. 3.1.1), and finally corrected for scattered light (Sect. 3.2.2).

A spectral flat field image is only illuminated within the spectral orders, hence

[20]The normalization is more simple compared to "standard" flat fielding of echelle spectra (cf. Rasmussen & Dall, 2001), because the normalization is done with respect to the counts in the entire image.

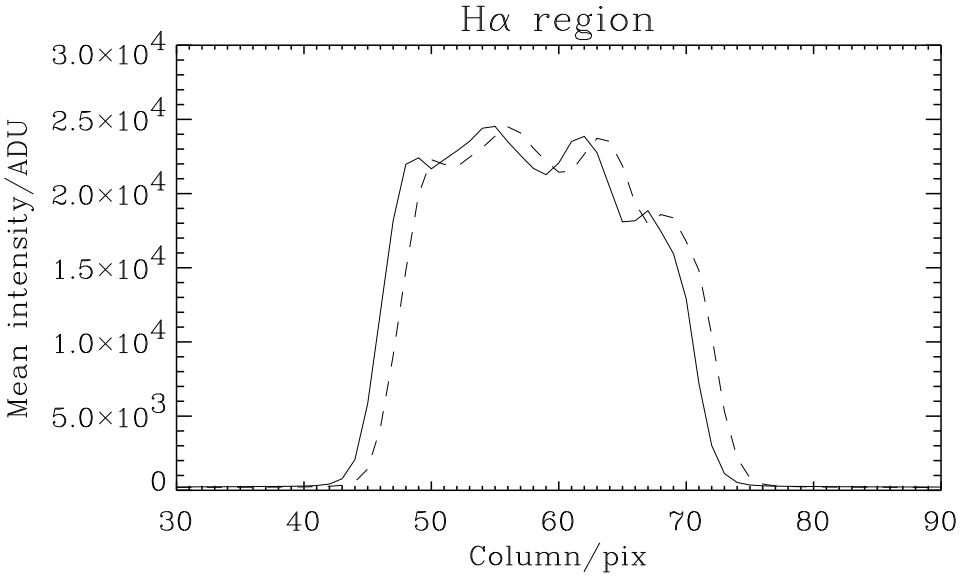

Figure 3.12: Median filtered flat field images collapsed in the row direction. The images are from night 17/03- (*solid line*) and 12/04-00, (*dashed line*) and show the maximum shift between flat fields from two different nights.

the flat fielding process could only be performed well within the spectral orders to avoid the low ADU values at and outside the spectral order edges. Including the outside regions would assign relatively higher weights, thus overestimate, the data points, $Data_0(x, y)$, in the outer regions which contain less signal compared to the central region of the order containing the highest S/N (cf. Eq. 3.10).

The actual flat fielding was performed during the extraction process, and details about the optimum spectral order boundaries are described in the corresponding section (Sect. 3.2.3).

The relatively large irregularities along the slit direction (perpendicular to the dispersion) seen in the flat field orders (Fig. 3.11) are not due to odd quantum efficiency behaviour, but are the result of large slit width variations. This is clearly seen in Fig. 3.12, where the irregularities follow the general shift (also seen in Rasmussen & Dall, 2001, Fig. 14). The slit width variations are seen in Fig. 3.13, which shows the 50% maximum intensity contour of a spectral emission line in a spectrum of the He-Ne calibration lamp.

The varying slit width also causes real intensity variations in the stellar spectra, and due to this effect, the flat field procedure outlined in Eq. 3.10 overestimates pixels with lower signals relative to higher signals, reducing the S/N. In order to perform the flat fielding of these irregular spectra correctly, weights should be assigned to each column within the spectral order boundary, to correct for this irregular slit width.

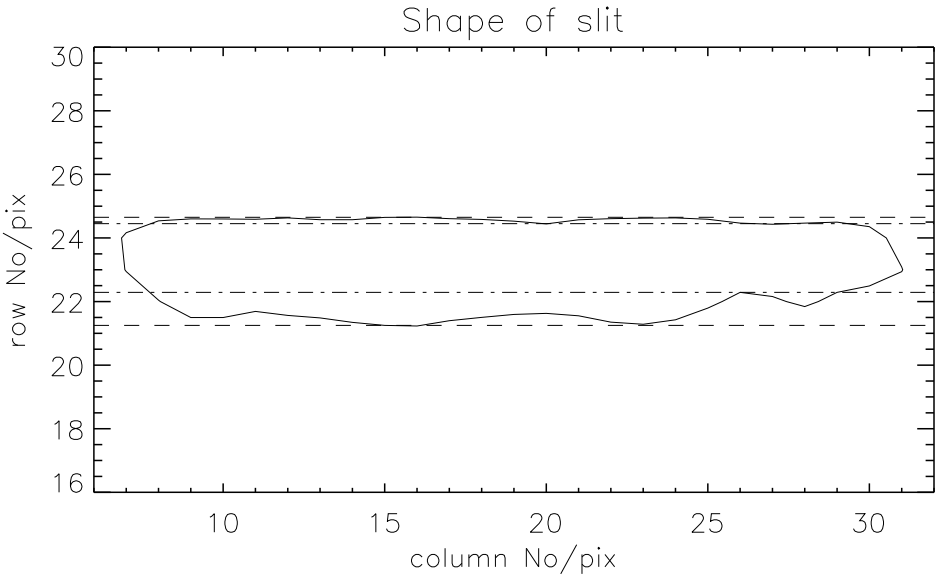

Figure 3.13: The 50% maximum intensity contour of a spectral emission line (*solid line*). Clear indications of slit width variations at the 30-40% level are seen along this contour. The narrowest point ($\sim$ 2.2 pixels wide) is indicated by *dashed dotted lines* whether the widest point ($\sim$ 3.4 pixels wide) is indicated by *dashed lines*.

The weights which were tested were the normalized mean shape of the master flat field itself, thus:

$$Data_{\mathrm{flat\_corr}}(x,y) = \frac{Data_0(x,y)}{[Flat_0(x,y)/\langle Flat_0\rangle]_{\mathrm{master}}} \cdot \left[\frac{\langle Flat_0\rangle}{\langle Flat_0(x)\rangle}\right]_{\mathrm{master}} \tag{3.12}$$

where the factor, $[\langle Flat_0(x)\rangle/\langle Flat_0\rangle]_{\mathrm{master}}$, is the normalized mean flat field shape at column x, adopting the notation of Eq. 3.10.

Based on a few test nights, it turned out that the flat field procedure outlined in Eq. 3.10 provided a slightly higher S/N in the final analysis of the 1D spectra. In principle, Eq. 3.12 is the better solution to the irregular slit problem. The reason why it in practise is not, could be related to the fact that the fixed mean shape of the master flat field does not describe the irregularities perfectly. Weighting by the normalized mean master flat field is in this case just as "good" as the raw flat fielding procedure (Eq. 3.10), and the latter is implemented in the extraction procedure (Sect. 3.2.3).

3.2.2 Scattered light correction

Due to imperfections in the optical path of the telescope and the spectrograph, scattered light will be seen on the CCD images outside the spectral orders, where an ideal instrument would not receive any photons. The scattered light also hits the

CCD where the spectrum is located, reducing the S/N.[21] Both the images of stellar spectra and flat field images are corrected for scattered light.

In order to estimate the scattered light level within the order, the structure of the scattered light in the neighbourhood of the order must be investigated. A few images like Fig. 3.11 are divided into three sub-images (*lower*, row 0:59; *middle*, row 60:119; *upper*, row 120:179) which are separately collapsed in the row direction, providing three mean shapes, each with a scattered light level representative for that particular sub-image (using **scatlight_test.pro**). Fig. 3.14 (thin lines) shows the plot of such collapsed sub-image triplet, which show the same scattered light level indicating no significant gradient of the scattered light level in the row direction.

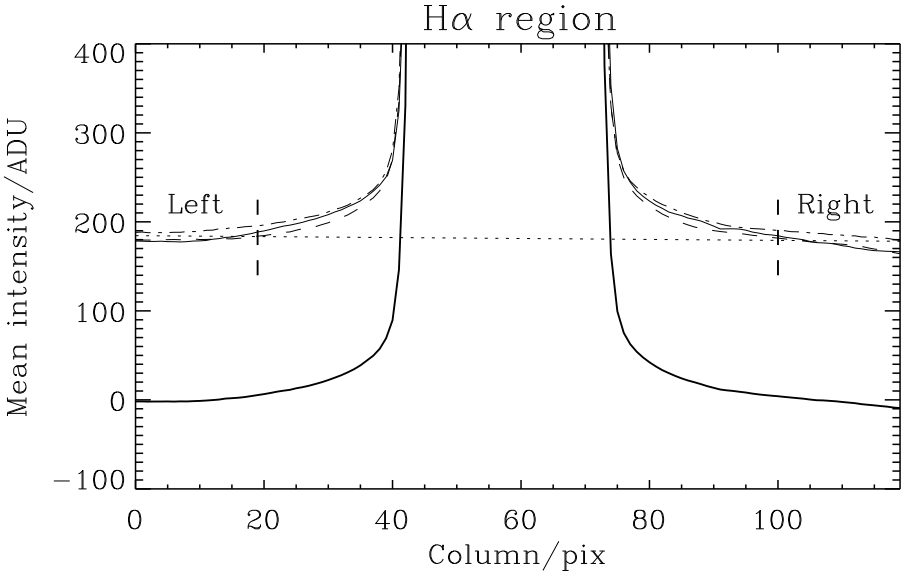

Figure 3.14: Row collapsed flat field sub-images for the region around the H_α spectral line. Lower, middle, and upper sub-image are indicated by *thin solid*, *dashed*, and *dash-dotted lines*, respectively (see text). *Thick dashed lines* indicate the left and right column intervals used for scattered light estimation. *Dotted line* is the calculated scattered light level. *Thick solid line* indicates the master flat corrected for scattered light.

Any gradient in the row direction is neglected, and the scattered light level is calculated as the straight line from the mean left level to the mean right level (Fig. 3.14, *dotted line*) and subtracted using **scatlight_sub_region.pro**.[22]

After all these laborious efforts to calibrate the raw CCD images, the images

[21] This is discussed in more detail in Chapter 4, Sect. 4.1.3.

[22] The mean left and right levels are found through a mean in the row direction followed by a median in the column direction of each left and right regions indicated by the thick dashed lines in Fig. 3.14. Only using the median would introduce jumps in the estimated scattered light level, due to grouped pixel values (i.e. the sorted pixel values provide a staircase array). These effects were tested using **test_res_overscanstrip.pro**.

"cleansed" of instrumental effects are ready to be transformed into 1D spectra used for the spectral analysis (Chapter 4).[23]

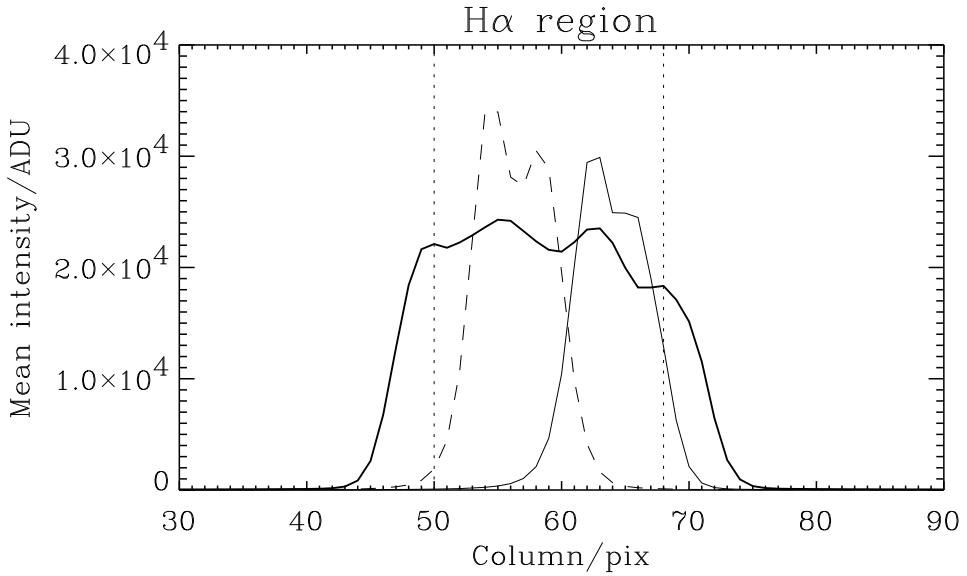

Figure 3.15: *Thick solid line* indicates the mean master flat field. *Dotted lines* indicate the position of the chosen boundaries of the spectral order. *Thin solid* and *dashed lines* are stellar spectra from two different nights, showing representative extremes of the star position along the slit (within the same night shifts of maximum 5 pixels are observed). The small "valley" at the center of the stellar spectrum (*dashed line*) is due to the defocused annulus like stellar image, observed at good seeing conditions (also seen in Fig. 2.2).

3.2.3 Extraction of 1D spectra

The extraction process described in this section, is more straight forward than the "standard" echelle spectra extraction (Rasmussen & Dall, 2001). The orders are not traced and fitted to low order polynomials, since the orders in the small sub-images to a good approximation are straight, like long slit spectra.

The extraction is done within a certain spectral order boundary defined as the length of the slit, and is a collapse, of the 2D spectrum to a 1D spectrum in the column direction[24], which is perpendicular to the dispersion. The intrinsic left and right edges of the spectral order (i.e. the slit boundaries) are to a good approximation described by the shape of the master flat image. In interpreting the boundaries from

[23]There has been no correction for the light coming from the background sky because it can be neglected for the short exposures used in this investigation.

[24]I investigated the slit alignment relative to the column direction using **slit_align_test.pro** in order to collapse the 2D spectra properly. The slope between the column direction and the direction along the slit is ~ 0.01 (mostly due to the irregularity of the slit; see left side in Fig. 3.13). From the left to the right spectral boundaries this corresponds to ~ 0.2 pixel deviation (see also Fig. 2.2, *dashed line*, page 30).

the master flat shape, one has to take into account that the flat field shape displayed shifts $|\delta x| \lesssim 1$ pixel during the entire observing run. To be on the safe side, not including the slit boundaries, the boundaries were chosen well inside the "plateau" of the master flat field (cf. Fig. 3.15). The trade-off, which one should be aware of, is lost signal when the stellar image drifts along the slit and gets too close either to the left or the right chosen boundary. The lost signal is the tail falling outside the defined boundaries (see Fig. 3.15 thin solid and dashed lines). The result of this, is a slightly irregular 1D spectrum in the case of extreme drift due to the aligning process which do not affect the spectral analysis, however (cf. Chapter 4).

The extraction including the flat fielding procedure of Eq. 3.10 is performed using **one_dim_collaps.pro**, and examples of the final 1D spectra are plotted in Fig. 3.16. The choice of boundaries is optimized based on the highest S/N in the following spectral analysis of a few "test" nights.

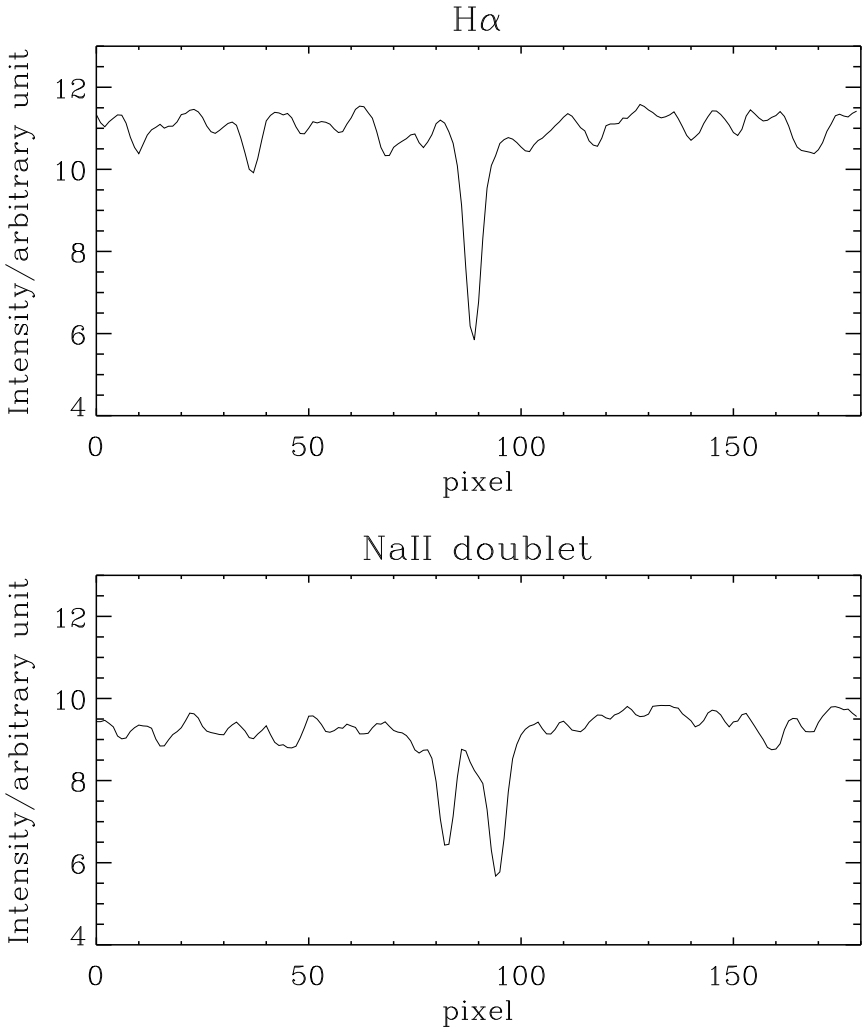

Figure 3.16: **Top plot:** Collapsed sub-image of the H_α order including the H_α absorption line (Wavelength coverage is: 6511 Å-6615 Å). **Bottom plot:** Collapsed sub-image of the NaII doublet order including the NaII absorption lines (Wavelength coverage is: 5850 Å-5940 Å). In these short sub-images the temperature difference between the flat field lamp and the star is not seen (flat continuum).

Chapter 4

Spectral analysis

This chapter will mainly describe the spectral analysis related to the equivalent width measurements (Sect. 4.1). The second data set comprised of radial velocity measurements was provided as calibrated data points, ready to use in the time series analysis (cf. Chapter 5), hence these data are only shortly introduced (Sect. 4.2).

The spectral analysis of the equivalent width data set includes the extraction from the 1D spectra of the line index, I_{EW}, used to measure the oscillations of ξ Hya. The values of I_{EW} derived here comprise the time series which are analysed in Chapter 5 in order to detected stellar oscillations.

An outline is given of the different strategies followed in order to obtain the optimum measure of the stellar oscillations based on the equivalent width data. In addition, a rather large noise was encountered, which proved to be significant. A discussion of it and its possible origins are included.

4.1 Measuring the equivalent width

This section describes the attempt to detect the tiny stellar oscillations by studying variations in the equivalent width $\delta W/W$ (cf. Sect. 1.4).

The quantity which is extracted from the stellar spectra is the line index, I_{EW} (cf. Sect. 4.1.1), which is assumed to be proportional to the equivalent width, W, defined in Sect. 1.4 (cf. Eq. 1.11, page 17). Due to the proportionality of I_{EW} and W, the relative change in the equivalent width is equal to the relative change in the line index ($\delta W/W = \delta I_{EW}/I_{EW}$). In the determination of I_{EW}, one does not need to calibrate the continuum and to fit line profiles in order to count the total flux over the spectral line, which is necessary using the definition of W. I_{EW} is simply a sum of counts over a range of pixels within a given weight function or line-filter where the continuum is found from a robust linear fit (cf. Sect. 4.1.1).

The spectral absorption line used in the following spectral analysis is H_α, unless otherwise specified.

4.1.1 Extracting I_{EW} using *Ix*

The calculation of I_{EW} used in this investigation is performed by a program called *Ix* (Dall, 2001). The way *Ix* calculates the equivalent width is shortly summarized in the following steps (cf. Fig. 4.1):

- Fit a straight line to the continuum around the spectral line, where the continuum fit is performed by weighting the spectrum with a continuum-filter which has two "peaks", one at each side of the line, and goes to zero near the line.
- With the calculated continuum fit, the line center is defined as the position that will maximize the sum over the line in a given line-filter.
- Finally, after fixing the continuum-filter to the line center, I_{EW} is calculated as the sum over the line in a given line-filter, which is usually the same line-filter used to locate the line center.

Beside a list of the 1D spectra to be examined, *Ix* needs a few parameter files, where the most important parameters are given in Table 4.1.

Table 4.1: *Ix* input parameters

Parameter	Specification	Value
dl	Position of left continuum-filter	35
dr	Position of right continuum-filter	135
cl	Half width of left continuum-filter	25
cr	Half width of right continuum-filter	25
cgauss	Gaussian order of continuum-filter[a]	8
pos	First guess for line-filter position	90
b	Half width of line-filter	4/10/20/30
gauss	Gaussian order of line-filter	8

[a] *cgauss* specifies the smoothness of the Gaussian filter: $\exp(-(\frac{x-x_0}{b})^{cgauss})$.

Normally one would set the *Ix* input parameters in order to minimize the point-to-point scatter in the time series, but this is not always the optimum choice. Minimization of the noise which has a characteristic time scale close to what is expected for the stellar oscillations is the actual aim, as minimizing the high frequency noise could introduce significant noise at the time scale of the oscillations. This problem is analysed in the following sections.

4.1.2 Minimizing high frequency scatter

In Sect. 3.2.3 it was mentioned that the choice of the spectral order boundaries, before the collapse into 1D spectra, was based on the highest S/N. Spectra of a few test nights were collapsed with different boundaries, and the line indices were calculated by *Ix*. The boundaries which in general provided the highest S/N were chosen as the global boundaries and fixed for all spectra.

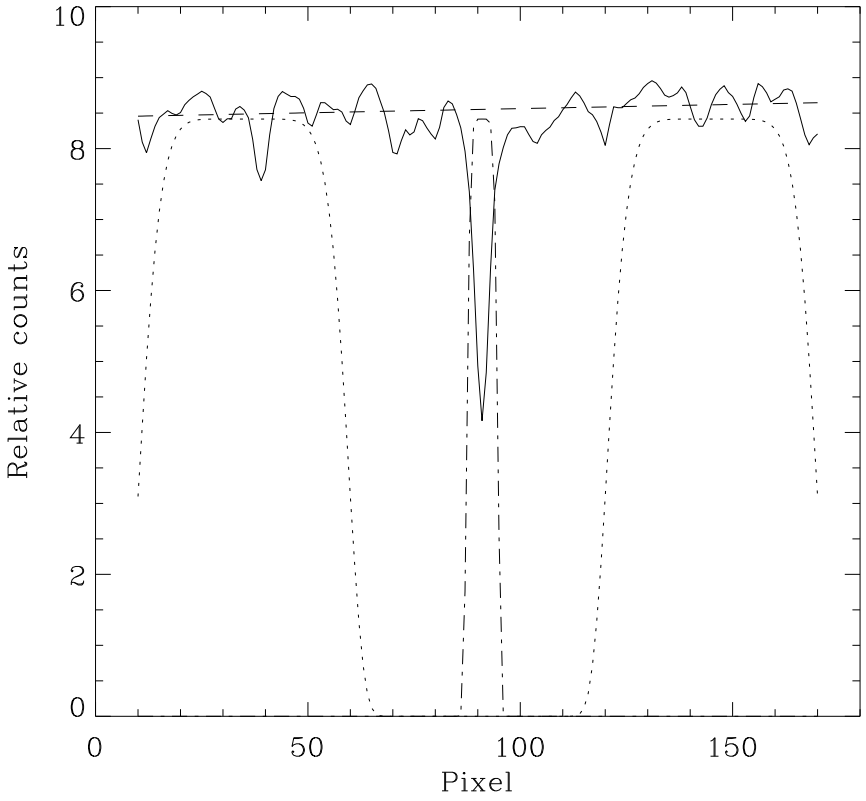

Figure 4.1: Spectrum around the H_α line (*solid line*). The *dotted line* indicates the continuum-filter used by *Ix* to calculate a stable continuum indicated with the *dashed line*. The *dashed-dot line* is the line-filter over which the line is integrated in order to calculate the line index I_{EW}. The *Ix* input parameters are: $dl = 35$, $dr = 145$, $cl = cr = 25$, $cgauss = gauss = 8$, and $b = 4.0$ (see text).

The input parameters for *Ix* were chosen to minimize the point-to-point scatter. The S/N was not particular sensitive to the choice of continuum-filter, however the line-filter had a large effect. It turned out that most single night time series had a maximum in S/N when b was approximately 4.0,[1] hence this value was chosen.

To determine the appropriate set of parameter values is a multidimensional problem necessitating some trial-and-error. The same set of values were finally used for all nights in order to avoid parameter-dependent changes from night to night. An example of a spectrum and the chosen filters is plotted in Fig. 4.1.

To choose the gauss order is a trade-off between sensitivity in signal and noise, a very high order gauss[2] provides a very sensitive line index and is therefore not a

[1] This line-filter width is approximately the same as the width of the H_α line itself (corresponding to FWHM ~ 3 Å).

[2] When the gauss order goes to infinity, the filter converges into a box filter.

very robust measure of the equivalent width. A gauss order of 8 seemed to produce fairly stable time series.

The final point-to-point S/N was roughly 500, a factor of two below the expected value based on pure photon noise, which therefore cannot be the only noise source (cf. Sect. 2.1.1, page 27).

De-correlation

The time series of the fairly narrow, line-filter with $b = 4.0$ showed several drift effects during the night, and a lot of work was done to understand and correct for these drifts by de-correlating the signal against different parameters i.e. airmass, continuum- level and slope, line position, position of the stellar image along the slit, and the width of the stellar image[3].

Fig. 4.2 shows an example of a single night time series including the expected signal (of arbitrary phase). In addition, similar time series of six other nights are

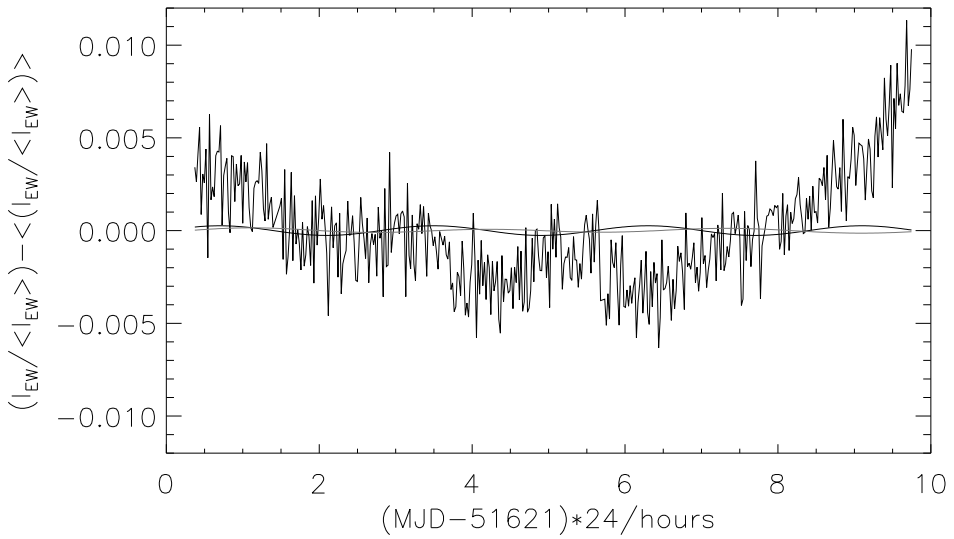

Figure 4.2: Time series of night 17/03-00, with the following input parameters for *Ix*: $dl = 35$, $dr = 145$, $cl = cr = 25$, $cgauss = gauss = 8$, and $b = 4.0$ (see text, Sect. 4.1.1). The smooth sinusoidal *solid black line* indicates the expected stellar signal based on the $1/g$-scaling from Kjeldsen & Bedding (2001) (cf. Eq. 1.9, page 11; Table 1.2, page 22) only considering the expected dominant mode of an arbitrary phase. The *solid grey line* indicates a simulated stellar signal using the frequencies and their amplitudes and random phases of the four most dominant modes measured from the entire data set of radial velocities (cf. Chapter 5).

shown in Fig. 4.3, which shows the rather complex behaviour of the signal due to different noise factors from night to night.

[3]The stellar position along the slit and its width were calculated using **calc_star_pos_parm.pro**.

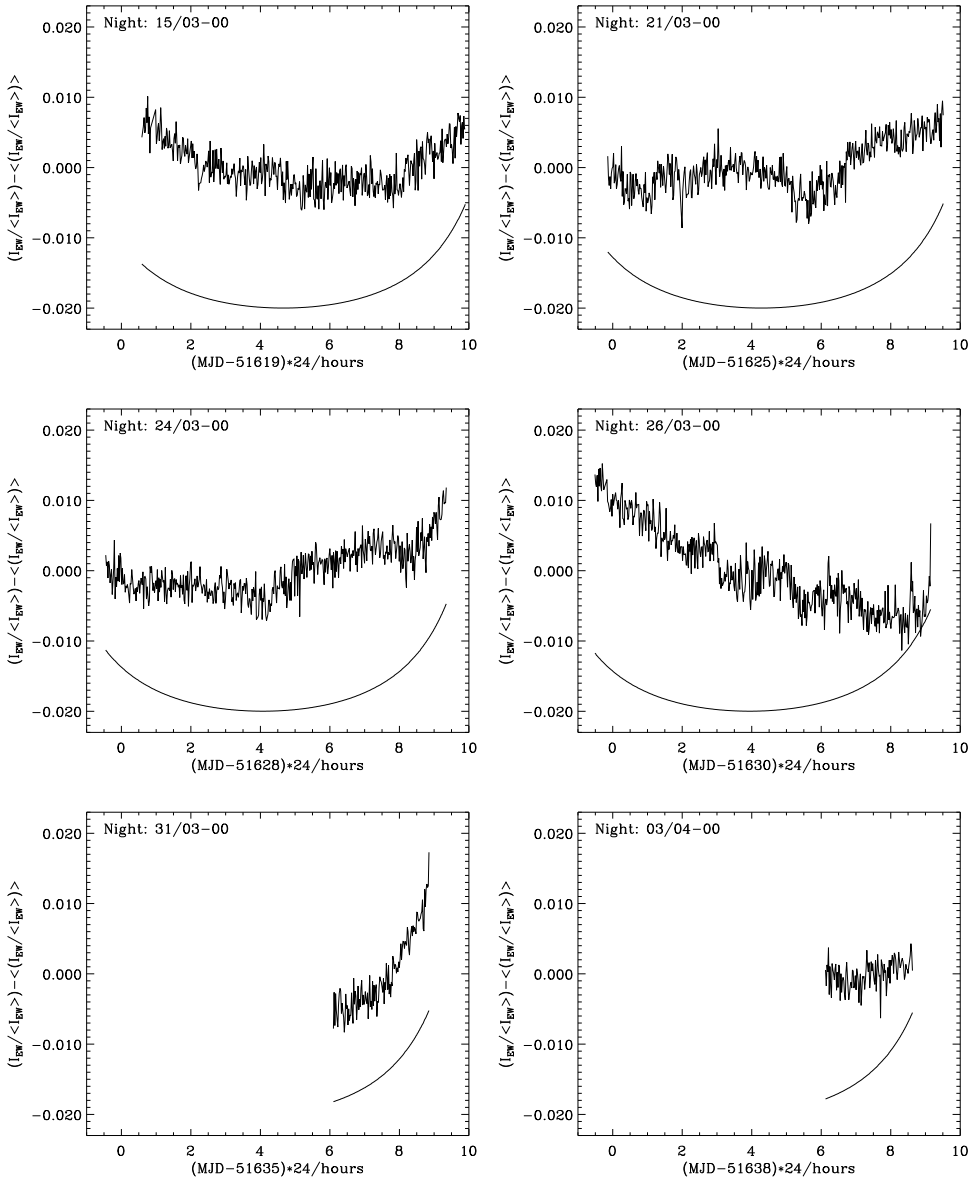

Figure 4.3: Time series of six nights (date indicated at each plot), with the following input parameters for *Ix*: $dl = 35$, $dr = 145$, $cl = cr = 25$, $cgauss = gauss = 8$, and $b = 4.0$ (see text, Sect. 4.1.1). The raw data has been corrected for a daily offset, which could be up to 1%. The smooth solid curve indicates the scaled airmass shifted $(0.01 \cdot (\text{airmass} - 1) - 0.02)$ to match the y-ranges of the plot.

It is evident that some airmass-like effect is present, and for several nights the line index jumps significantly (cf. Figs. 4.2, 4.3). In order to understand these effects, and thus to be able to correct them, the correlation behaviour between the line index and the variety of known parameters is carefully investigated. Fig. 4.4 shows an example of a time series (the same as shown in Fig. 4.2) together with some of the corresponding parameters for which correlation effects were investigated.

The jump effect: During the observations, for approximately every 100 images the telescope was repositioned so that the stellar image would not drift away from the slit (see Fig. 4.4, *second panel*; and Fig. 2.2 on page 30). The observed jumps in the time series of I_{EW} are clearly related to the position of the stellar image relative to the slit (see example in Fig. 4.4). Even though the position of the stellar image *along* the slit at various intervals shows the same trend, it is certainly not linearly related to the effect seen in I_{EW} (Fig. 4.4, *first panel*)[4].

A parameter which represents the relative stellar image position perpendicular to the slit (i.e. the dispersion direction), is missing in order to explain the full motion of the stellar image relative to slit. The line position could however contain information of the motion in the dispersion direction (Fig. 4.4, *fifth panel*), but how it is exactly related to the stellar image position on the slit in that direction is not known (e.g. due to the non-regular slit shape; discussed in Sect. 4.1.3, page 70). Therefore the knowledge of the motion of the stellar image relative to the slit is restricted to the direction *along* the slit.

De-correlating this jump effect could not be performed properly with the parameters available and had to be done manually. The jumps in the stellar image position along the slit were located using the following two programs:

- **find_jumps.pro** which located the positions in the time series where a jump occurred of the stellar position along the slit. In addition, the observation log was consulted to see when repositioning was noted, and the cases of logged repositioning which were not detected by **find_jumps.pro** were added to the list of known jumps.

- **correct_jumps.pro** used the list of positions in the time series where a jump in the stellar image position was noted as input. At each corresponding position in the I_{EW} time series a robust linear fit based on 25 consecutive data points[5] was performed on both sides of a noted jump point, and the data was shifted up or down in order to set the two fits continuous at the jump point[6].

[4]Some jumps in the position of the stellar image do not effect I_{EW} and the I_{EW} value at the jumps was not always going from a higher to a lower value, which one may conclude from e.g. Fig. 4.2.

[5]This interval corresponds to a $\sim$ 30 min time span which is only 15% of the period of the expected dominant mode.

[6]The slopes of the linear fits were free parameters for both left and right fits because the slope could change dramatically after a jump.

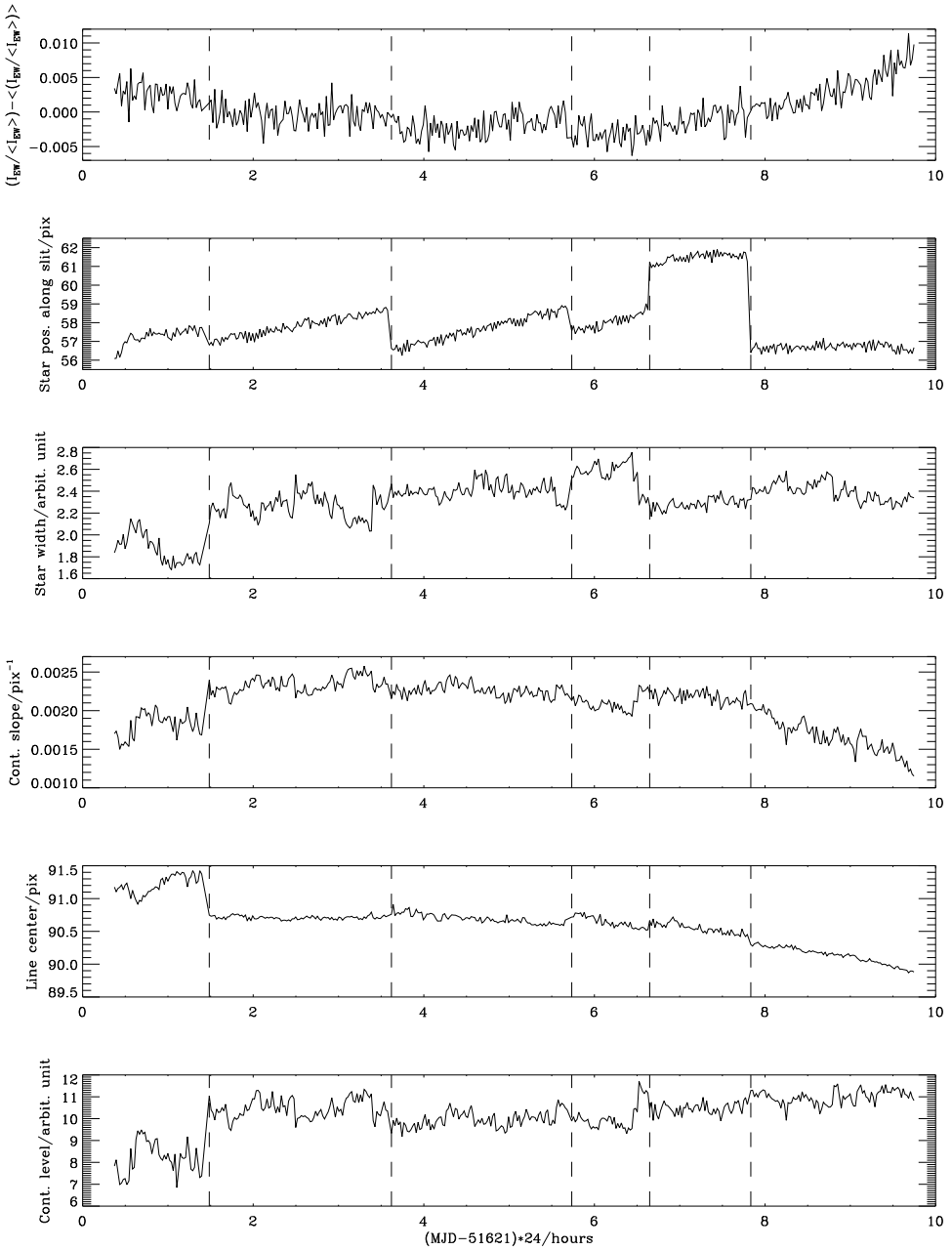

Figure 4.4: Time series of night 17/03-00: I_{EW} (*top panel*), stellar image position along the slit (*second panel*), width of stellar image on the slit (*third panel*), continuum slope (*fourth panel*), H_α line center (*fifth panel*), and continuum level (*bottom panel*). The time of repositioning the telescope is indicated with vertical *dashed lines* in all panels. The fourth dashed line is most likely due to a mechanical turning point of the telescope, which causes a jump not controlled by the observer. It was verified that this jump occurred at nearly the same sidereal time each night, indicating its cause: mechanical relaxation.

Even though the jumps were found independently of the jumps in the I_{EW} time series, the periodicity in the occurrence of jumps is very close to the time scale of the expected stellar signal, hence care should be taken when correcting for an effect of this nature.

The airmass-like effect: Since the slow drift seen as an airmass-like effect was not clearly pronounced during the entire time series it was not obvious how to deal with it. For several nights the correlation between I_{EW} and airmass changes dramatically when passing near the point of minimum airmass, while some nights did not show significant correlation at all. Fig. 4.5 shows three examples of the correlation between I_{EW} and airmass.

A large sample of harmonic oscillators of different periods and phases were simulated and the corresponding amplitude spectra were calculated for different window functions, using the fast Fourier transform (FFT) of IDL. The simulated pure signals are de-correlated against airmass and new amplitude spectra are calculated. The reduction in amplitude of the main peak in the amplitude spectrum was noted (for this simulated de-correlation **harm_fft.pro** is used). The simulations showed that a divided de-correlation[7], rather than de-correlating a night as one block, could be very dangerous, reducing the stellar signal to approximately 30-60%, dependent on the exact window function and the phase and period of the signal. For a full night (9.5 hours) though, the amplitude was only reduced to 80-90%.

From these simulations it was obvious that de-correlating the short nights (cf. Fig. 4.3, *bottom left panel* and *bottom right panel*) would nearly remove the stellar signal. Both divided and non-divided de-correlation was performed independently (using **de_corr_for_airmass.pro**) for all nights, in order to determine which de-correlation method provided the optimum amplitude spectrum (cf. Chapter 5).

4.1.3 Unstable line profiles

The point-to-point scatter is twice as large as expected from pure photon noise (cf. Sect. 4.1.2 page 66) and some relatively large drifts, most likely related to the changes of the stellar image and with time scales close to the expected stellar signal, are seen in the time series.

It is extremely difficult, and to some extend impossible, with the available data to determine what or why it happens that the line index is so sensitive to how the stellar image falls on the slit. What is known is that the slit is in a poor condition (cf. Fig. 2.2, page 30.) e.g. affecting the effective slit width and the line center which moves (Fig. 4.4 *fifth panel*) when the stellar image moves along the slit because the

[7]Divided de-correlation is de-correlating first part of the night (before airmass = 1), and the last part (after airmass = 1) independently (cf. Fig. 4.5).

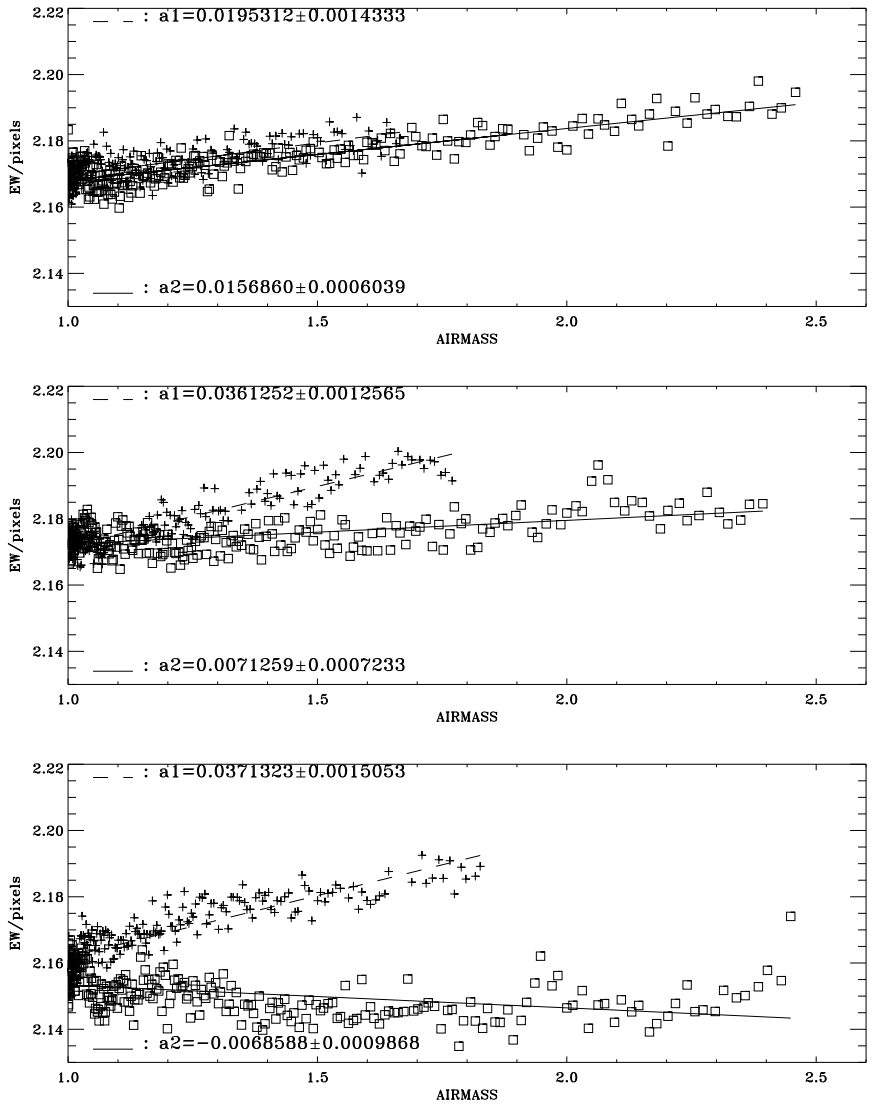

Figure 4.5: The line index vs. airmass for three different nights (*top panel*: 17/03-00, *middle panel*: 20/03-00, and *bottom panel*: 26/03-00). The first part of the night (before airmass = 1) indicated by *plus symbols*, and the last part of the night indicated by *square symbols* are fitted independently (*dashed* and *solid line*, respectively). The slope of the linear fits are indicated at each panel.

center of the slit (Fig. 2.2, *dashed line*) depends on the stellar image position along the slit[8].

One should imagine the large defocused stellar image moving around on the rough slit while the exact shape of the stellar image is changing due to both seeing conditions and telescope focus, which is continually adjusted in order to keep a high light level and to prevent saturation of the CCD[9].

Fig. 4.6 shows a close-up of the H_α line between two successive images at four different times in the time series (see figure caption). At most jumps only significant changes in the line depth and possibly the wings are seen (Fig. 4.6, *second left-* and *right-panels*), while for some jumps a significant shift of the line center is observed. This is probably influenced by the fact that the right part of the slit is not "centered" at the same position as its central part as mentioned in the paragraph describing the jump effect (cf. Fig. 4.6, *first left-* and *right-panels*). If one compares the four upper panels (around jumps) with the four bottom panels (no jumps) it is clearly that the H_α line shape changes significantly when a jump occurs.

The effect is even more pronounced when comparing spectra that are not successive but say 5-10 minutes apart with a jump in between, indicating that the repositioning of the telescope had a certain relaxation time[10]. The effect is also seen when comparing a spectrum at airmass $\simeq 1$ with one at high airmass (~ 2.5). From the investigation of the H_α line it can be concluded that *the observed jumps and the airmass-like effect in the line index is a real effect hidden in the data* and not due to the analysis.[11]

It is not unlikely that light from the defocused stellar image could be reflected at the edges of the slit. Since these edges are presumably rather rough and the exact shape of the stellar image and its position on the slit is unknown, it is not possible to estimate the effect of such light reflection. The intrinsic noise at both high and low frequency in the data could therefore be due to the constantly changing reflection of light on the slit edges, affecting the scattered light in the dispersion direction which cannot be corrected in the data reduction phase[12].

Another explanation could be a change in the instrument profile, due to the changing stellar image on the irregular slit. Plots similar to Fig. 4.6 *second right*

[8]The shift in slit center seen from Fig. 2.2 *dashed line* can be ~ 0.5 pixel in good agreement with the jumps seen in the line center (e.g. Fig. 4.4 *fifth panel*). The larger but more slowly variation of the line position is probably due to a general drift at high airmass e.g. flexure in DFOSC.

[9]These focus adjustments were performed several times per hour.

[10]and/or that the observer was refocusing the telescope in small steps at the first few images after a repositioning which also seems to affect the H_α line shape.

[11]The high frequency noise, which is at a higher level than expected from pure photon noise, possibly has the same cause as the jumps and the airmass-like effect.

[12]It was tested if a significant change of the scattered light outside the spectral order could be measured for spectra around a jump. Such a change could indicate that possible scattered light in the dispersion direction was changing likewise. No significant change in the scattered light outside the spectral order was detected, however.

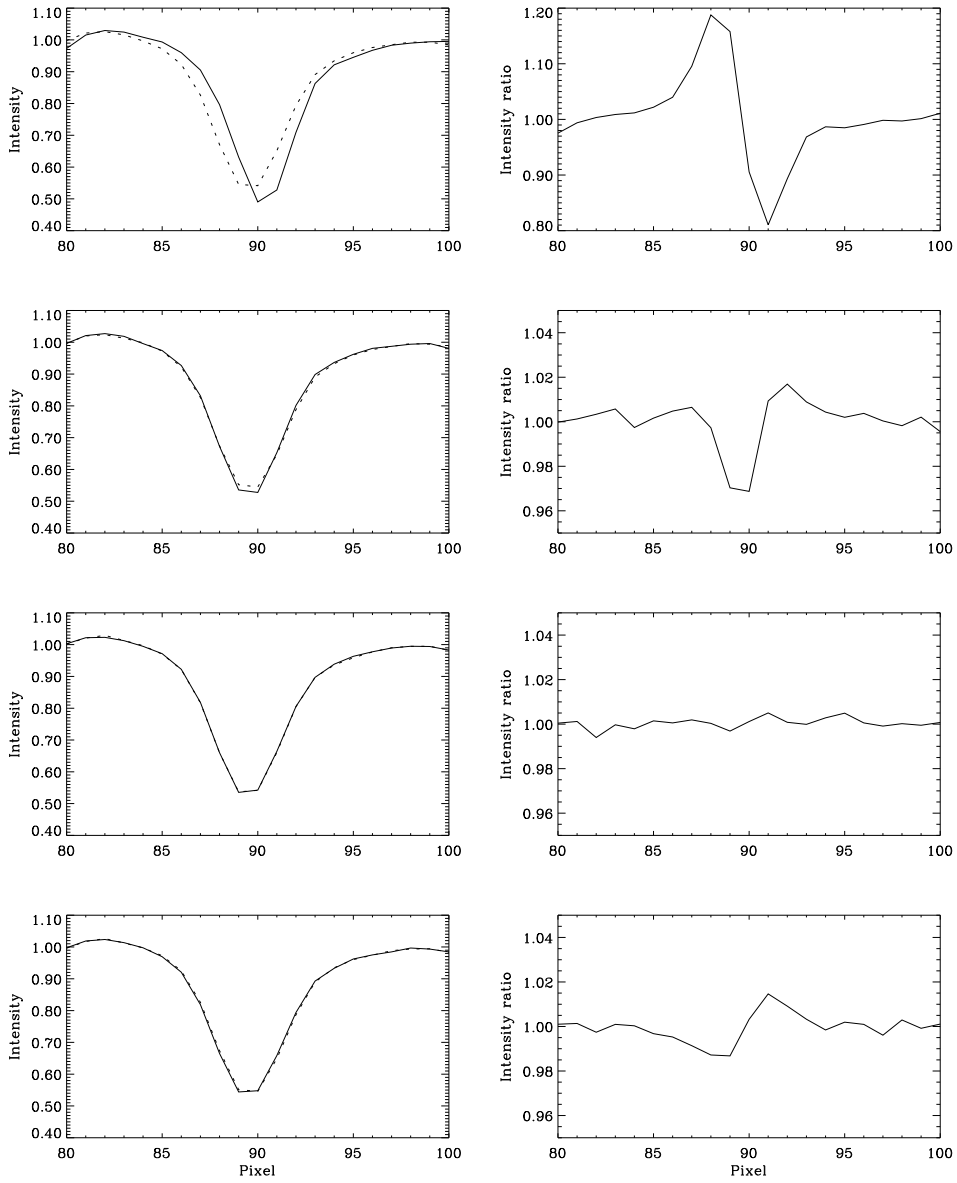

Figure 4.6: **Left panels:** The H_α line at four different times in the time series from night 17/03-00. Each panel shows two successive normalized spectra (solid spectrum followed by dotted spectrum). The *first* and *second* (left) panels are comparing spectra around a jump (the first and second jump seen in Figs. 4.2, 4.4, respectively), whether the *third* and *fourth* panels are spectra where no jump is located (randomly chosen). **Right panels:** The ratio between the corresponding normalized spectra (solid line divided by dashed line) showed to their left (It should be noted that the scale of the first panel is not the same as the others.).

panel supports the explanation that the changes in the stellar image and its motion causes the changing line profiles. The changing line profiles are in fact often seen as a shallower line core and broader wings after a repositioning of the telescope, which often moves the stellar image from the narrow right part of the slit to the broader central part (cf. Fig. 4.4, page 69 and Fig. 2.2 on page 30).

It was stated by Knudsen (2000) that the dominant changes of I_{EW} seen at the ends of the nights (in the current thesis referred to as the airmass-like effect) was due to a lowering of the fitted continuum level caused by stronger telluric lines at high airmass, since some of these lines were included in the continuum fit of Knudsen (2000). Thus the effect was stated to be due to the analysis and not intrinsic in the data. Through comparison of the continuum level and I_{EW} it cannot be confirmed that the continuum level can explain the dominant changes of I_{EW} as stated by Knudsen (2000). Therefore, the effect is rather a real effect in the spectra as mentioned above.

The airmass-like drift and the jumps had characteristic time scales just above and below the period of the expected dominant mode of ξ Hya, respectively. With a data set so noisy at all frequencies as the one used for the equivalent width method *it is practically impossible to remove the airmass-like drift and the jumps without removing the stellar signal itself* (cf. Chapter 5). This conclusion lead to an improved strategy of extracting the line indices, which does not rely on the minimization of the high frequency noise.

4.1.4 The improved strategy

Time series based on line-filters broader than $b = 4.0$ pixels have a higher point-to-point scatter, but at roughly $b \gtrsim$ 7-10 the line index gets rather insensitive to the jumps. On the other hand the airmass-like effect gets significantly more pronounced when going to higher b values.

In the improved analysis three normalized time series W_{10}, W_{20}, and W_{30} are constructed based on the line indices $I_{EW,b=10}$, $I_{EW,b=20}$, and $I_{EW,b=30}$, respectively. An example of a spectrum and the chosen line-filters is shown in Fig. 4.7. These time series all contain roughly the same stellar signal but are affected differently by the dominant noise source, namely the airmass-like effect[13]. The S/N which for $b = 4$ was ~ 500, is now ~ 400, ~ 300, and ~ 250, for the single night time series based on the three new filters.

Combined time series are constructed assigning weights to each time series: $W_{\rm final} = W_{10}^a W_{20}^b W_{30}^c$, where a+b+c=1. A similar technique was implemented by Kjeldsen et al. (1999a). It turned out that including all three time series did not produce a $W_{\rm final}$ which was significantly better than the combination of only two of

[13]Jumps still present in these broad filtered time series behaved more regularly than in the case of narrow filters.

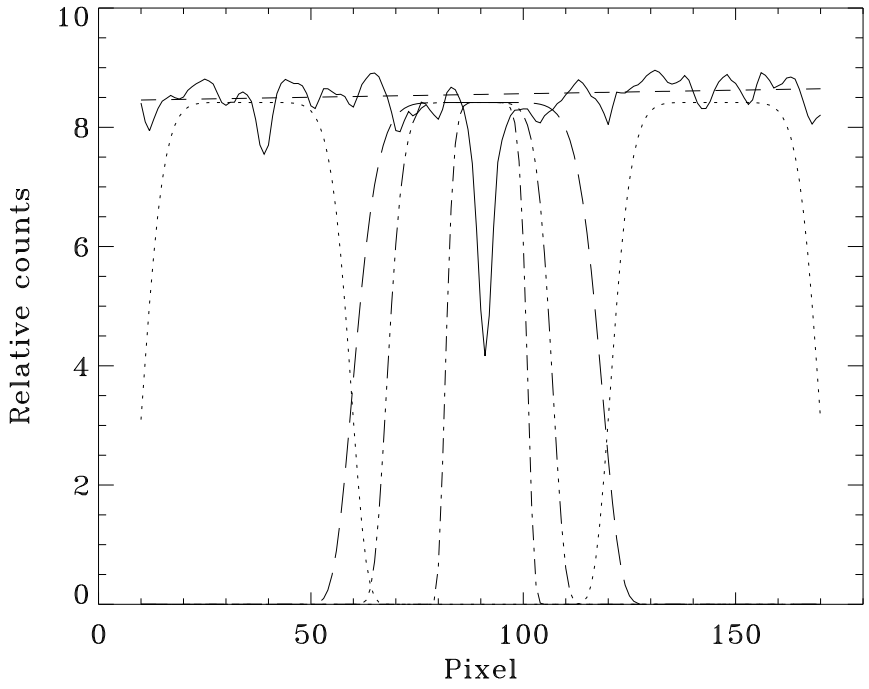

Figure 4.7: Spectrum around the H_α line (*solid line*). The *dotted line* indicates the continuum-filter used by *Ix* to calculate a stable continuum indicated with the *dashed line*. The *Ix* input parameters are: $dl = 35$, $dr = 145$, $cl = cr = 25$, $cgauss = gauss = 8$, and line-filter width $b = 10$ (*dash-dot line*), $b = 20$ (*dash-dot-dot-dot*), and $b = 30$ (*long-dash*).

them[14]. So in practice either a, b or c was set to zero. In the first case ($a = 0$) $b = 1 - c_{a=0}$, in the second case $a = 1 - c_{b=0}$, and the third case $a = 1 - b_{c=0}$, thus providing three different combinations:

$$W_{\mathrm{final},a=0} = W_{20}\left(\frac{W_{30}}{W_{20}}\right)^{c_{a=0}}, \tag{4.1}$$

$$W_{\mathrm{final},b=0} = W_{10}\left(\frac{W_{30}}{W_{10}}\right)^{c_{b=0}}, \tag{4.2}$$

$$W_{\mathrm{final},c=0} = W_{10}\left(\frac{W_{20}}{W_{10}}\right)^{b_{c=0}}. \tag{4.3}$$

The filter ratio part can be regarded as the correction with no stellar signal content, while the first part (W_{20} and W_{10}, respectively) contain approximately the same

[14]Combining the time series of Eq. 4.1-4.3 in the same way as W_{10}, W_{20}, and W_{30} are combined to create $W_{\mathrm{final},a=0}$, $W_{\mathrm{final},b=0}$, and $W_{\mathrm{final},c=0}$ creates time series including all three time series (W_{10}, W_{20}, and W_{30}). These combined time series did not show a further reduction of the low frequency noise compared to $W_{\mathrm{final},a=0}$, $W_{\mathrm{final},b=0}$, and $W_{\mathrm{final},c=0}$. The technique of combining the time series is described in the following.

stellar signal, but including different noise contributions. Hence the stellar signal is unaffected by these weighted filters, and it is only a matter of finding the exponents $c_{a=0}$, $c_{b=0}$, and $c_{c=0}$ in order to minimize the noise which behaves regularly with varying line-filter width.

The equations of $W_{\rm final}$ can be transformed to:

$$\log(W_{20}) = c_{a=0} \cdot \log\left(\frac{W_{20}}{W_{30}}\right) , \quad (4.4)$$

$$\log(W_{10}) = c_{b=0} \cdot \log\left(\frac{W_{10}}{W_{30}}\right) , \quad (4.5)$$

$$\log(W_{10}) = b_{c=0} \cdot \log\left(\frac{W_{10}}{W_{20}}\right) , \quad (4.6)$$

hence the exponents $c_{a=0}$, $c_{b=0}$, and $b_{c=0}$ are found as the slope in the $\log(W_{20})$ vs. $\log(W_{20}/W_{30})$, $\log(W_{10})$ vs. $\log(W_{10}/W_{30})$, and $\log(W_{10})$ vs. $\log(W_{10}/W_{20})$ plots, respectively.[15] An example of such correlation plot is seen in Fig. 4.8, which shows the correlation between the time series $\log(W_{10})$ and $\log(W_{10}/W_{30})$ from a single night. The dashed line indicates the slope $c_{b=0}$.

Fig. 4.9 shows the time series $W_{{\rm final},a=0}$, for the same nights as plotted in Fig. 4.3. To remove outlying data points the time series was median filtered by a sliding boxcar with a width which corresponds to approximately 30 minutes.

As described in Sect. 2.1.2, the NaII doublet was also investigated, but the noise level in the time series is in that case even worse compared to the time series based on the H_α line. The change in I_{EW} during a single night is roughly 6%. Even when using the new strategy described above, the NaII time series was extremely noisy at time scales comparable to the expected oscillation frequency of ξ Hya. The NaII data are not further discussed.

Summary of the equivalent width measurements

- Line indices, based on a variety of line-filter widths, have been extracted (using *Ix*; Dall (2001)) from the 1D spectra of both H_α and the NaII doublet in order to construct time series.
- For all line-filter widths, the corresponding time series and their combinations, are relatively noisy. The high frequency component (point-to-point scatter) is at least twice as large as the expected photon noise.
- The low frequency component of the noise with time scales close to the expected stellar oscillation signal is e.g. seen as jumps and airmass-like effects.

[15] This technique had also been tried for narrow filters (small b), but when the line-filter width was close to the spectral line width the effect of the noise was very irregular related to the b parameter (e.g. the jumps and the airmass-like effect were inversely dependent on the line-filter width). Hence no correlation could be found between the narrow filters say $\log(W_{3.4})$ and $\log(W_{3.4}/W_{4.6})$.

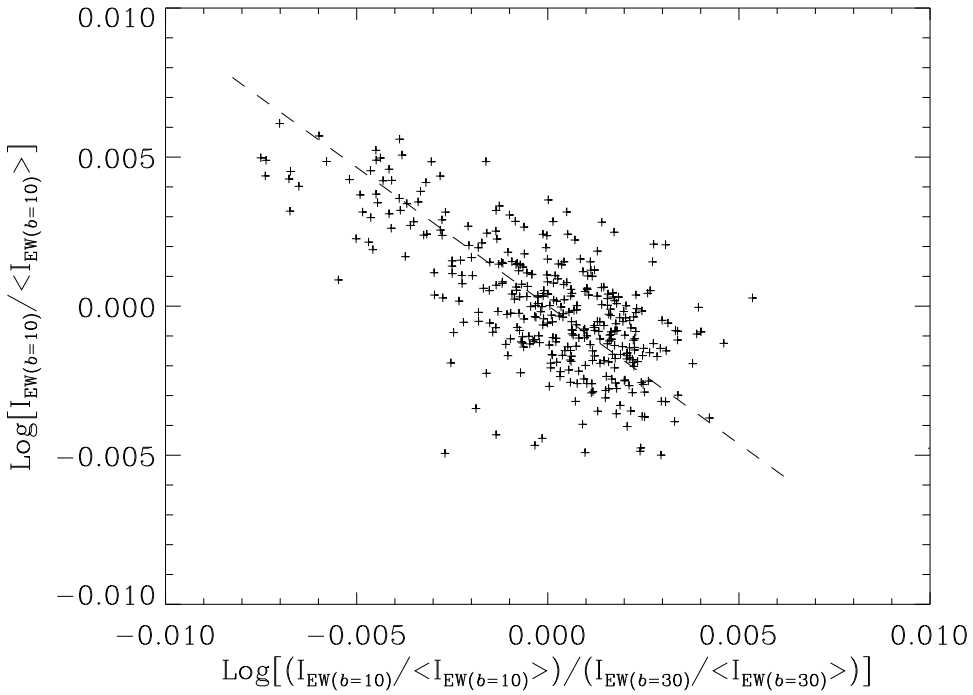

Figure 4.8: Correlation plot of the time series $\log(W_{10})$ and $\log(W_{10}/W_{30})$ from 22/03-00. The dashed line indicates the slope $c_{b=0}$.

These effects are shown to be due to real changes hidden in the data unaffected by the carefully performed reduction of the CCD images, and thus also independent on the algorithm used to extract the line indices.

- Possible explanations of these very large noise levels are discussed. The line profile investigation of the H_α line seems to indicate that the defocused stellar image moving around on the rough-edged slit while the exact shape of the stellar image changes could lead to constant changes in the instrument profile. Another possible explanation is that scattered light in the dispersion direction changes which cannot be corrected during CCD reductions.

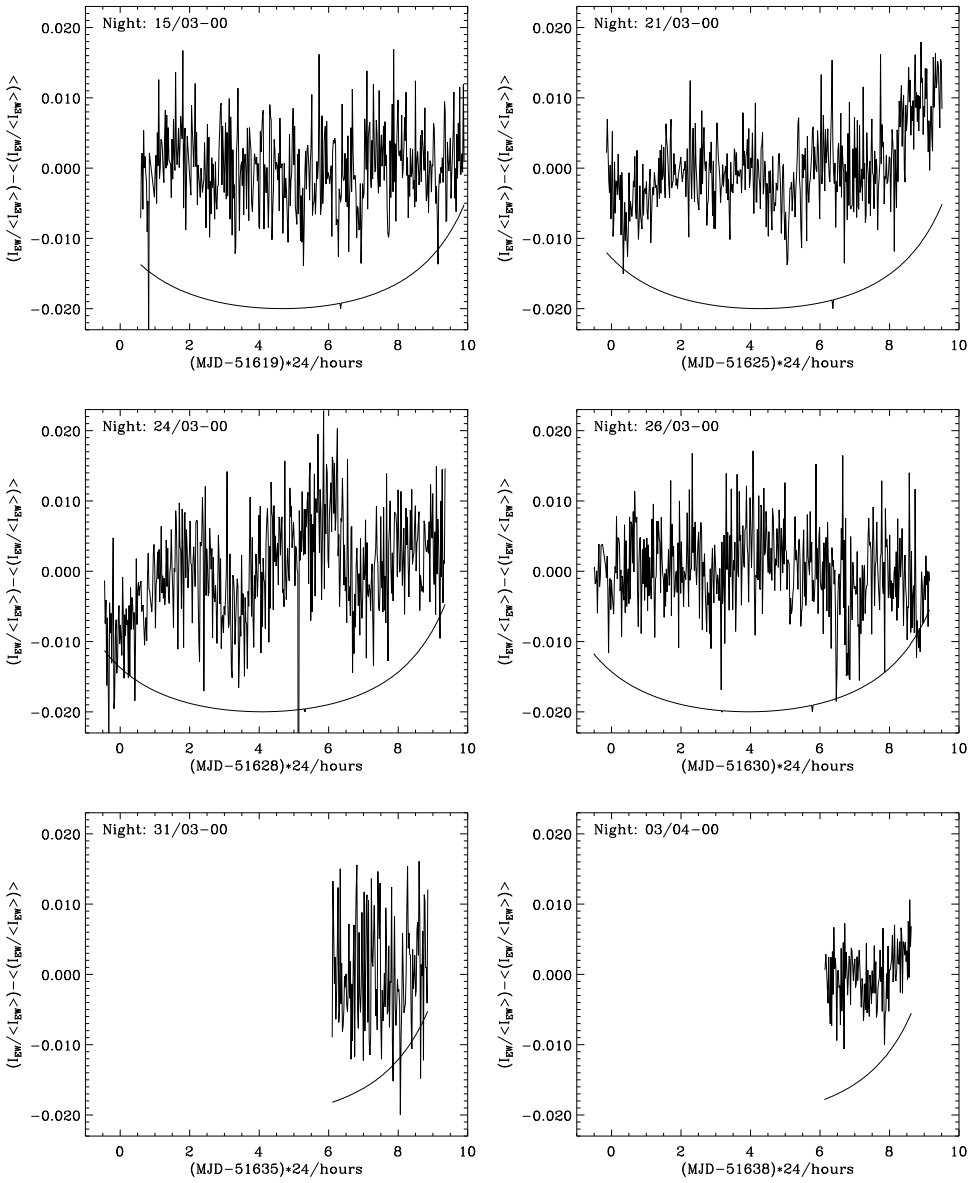

Figure 4.9: Time series of six nights (date indicated at each plot), optimized using the combination of W_{20} and W_{30} ($W_{\mathrm{final,a=0}}$; see text, page 74). The smooth solid curve indicates the scaled airmass shifted $(0.01 \cdot (\mathrm{airmass} - 1) - 0.02)$ to match the y-ranges of the plot. The plot is similar to Fig. 4.3. The time series are plotted before any reduction of high frequency scatter has been performed, which uses a median filter boxcar of 30 minutes width.

4.2 Measuring the radial velocity

This section shortly presents the measured radial velocity data obtained from the CORALIE spectra (Sect. 2.2).

The extraction of the radial velocity (cf. Sect. 1.4) from the stellar spectra were performed by F. Carrier using the method described in Bouchy & Carrier (2001, and references herein), and will not be discussed further in this thesis. The only corrections applied to the raw radial velocity time series is a subtraction of the mean per night. The time series used in the further time series analysis (cf. Chapter 5) is presented in Fig. 4.10.

The standard deviation of the measurements is 4.6 m/s and is mostly due to the oscillations. The uncertainties due to photon and detector noise vary between 0.7 and 1.6 m/s with a mean of 0.86 m/s. The error bars in Fig. 4.10, *bottom panel* are estimated errors based on $\sigma_{\mathrm{white-noise}} = 2.33\,\mathrm{m/s}$ (found from the mean level in the amplitude spectrum at high frequencies; cf. Sect. 5.2) and scaled to the photon noise of each measurement.

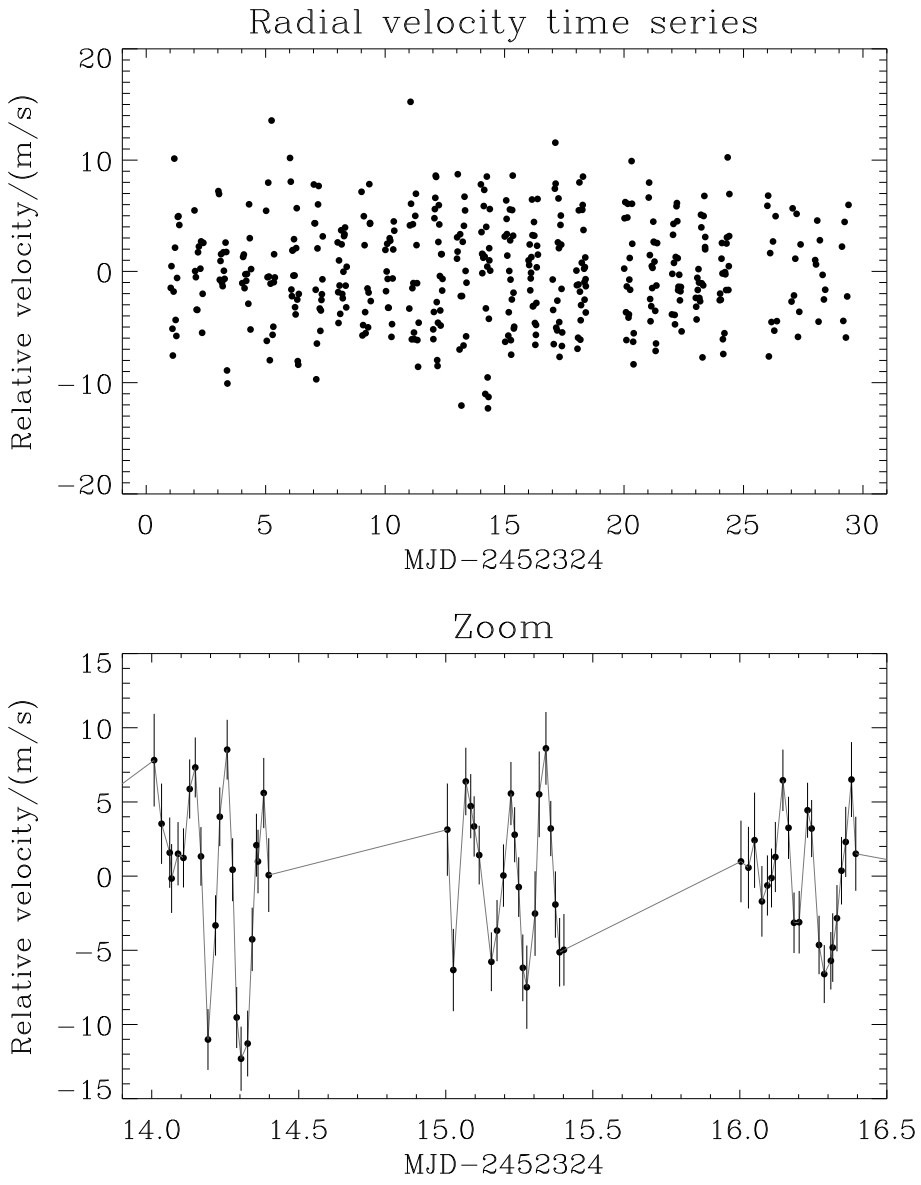

Figure 4.10: **Top panel:** Full time series of the radial velocity measurements (only corrected for the mean of each night). **Bottom panel:** A zoom-in of the middle part of the time series where each data point is connected with straight grey lines to illustrate that the oscillations are clearly seen because of the excellent signal to noise. The error bars are estimated errors based on $\sigma_{\mathrm{white-noise}} = 2.33\,\mathrm{m/s}$ (cf. Sect. 5.2) and scaled to the photon noise of each measurement.

Chapter 5

Time series analysis

This chapter will outline the analysis of the two data sets, the equivalent width time series (Sect. 5.1) and the radial velocity time series (Sect. 5.2). Sect. 5.1 will include a description of how the different corrections of the time string (cf. Chapter. 4) affect the final amplitude spectrum in the entire frequency range from 0 Hz to the Nyquist frequency ($\sim 6500\,\mu$Hz). In addition, a complete noise diagram from $50\,\mu$Hz to $5000\,\mu$Hz for the DFOSC time series data is presented (Fig. 5.4), which can be a very useful target selection tool. Sect. 5.2 will include a detailed asteroseismic frequency analysis which leads to a determination of the density of ξ Hya.

5.1 The equivalent width time series

In this section there will be a presentation of the time series analysis related to the equivalent width time series, including amplitude spectra of the different time series based on both narrow and broad line-filter widths (cf. Sect. 4.1).

The program used to calculate the amplitude spectra of the time series (**ampl_spec_calc.pro**) is based on the Fourier analysis program written by Kjeldsen (1992). The weights assigned to each data point in the time series are derived from the local point-to-point scatter calculated using **individ_variance.pro**[1].

5.1.1 The narrow line-filter time series

Amplitude spectra of the time series based on the narrow line-filter width (b = 4.0 pixel) are shown in Fig. 5.1 and Fig. 5.2. The raw time series produces an amplitude spectrum with a mean noise level of ~ 300 ppm (Fig. 5.1, *top panel*) in the range of the expected stellar signal (80-110 μHz). Subtracting the nightly mean reduces the noise to ~ 230 ppm (Fig. 5.1, *bottom panel*). Including the corrections of the jumps and the airmass-like effect further reduces the noise to ~ 170 ppm

[1] The calculation of the local point-to-point scatter of the time series discussed in Sect. 5.1.1 also included a sigma-clipping process in an iterative loop (using **parm_variance.pro**).

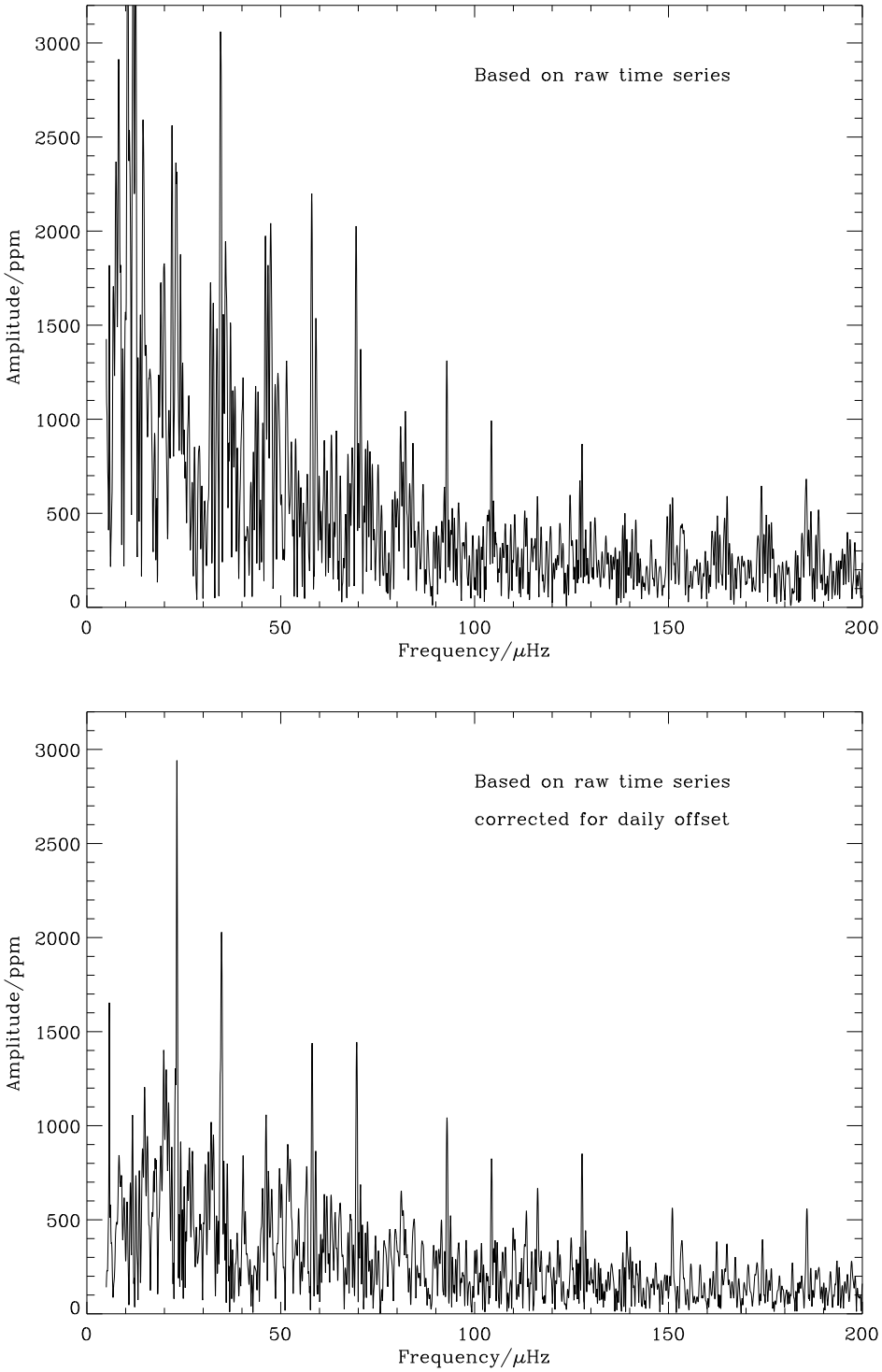

Figure 5.1: Amplitude spectra of the narrow line-filter time series. *Top panel*: The raw time series. *Bottom panel*: Time series corrected for the offset (mean) per night.

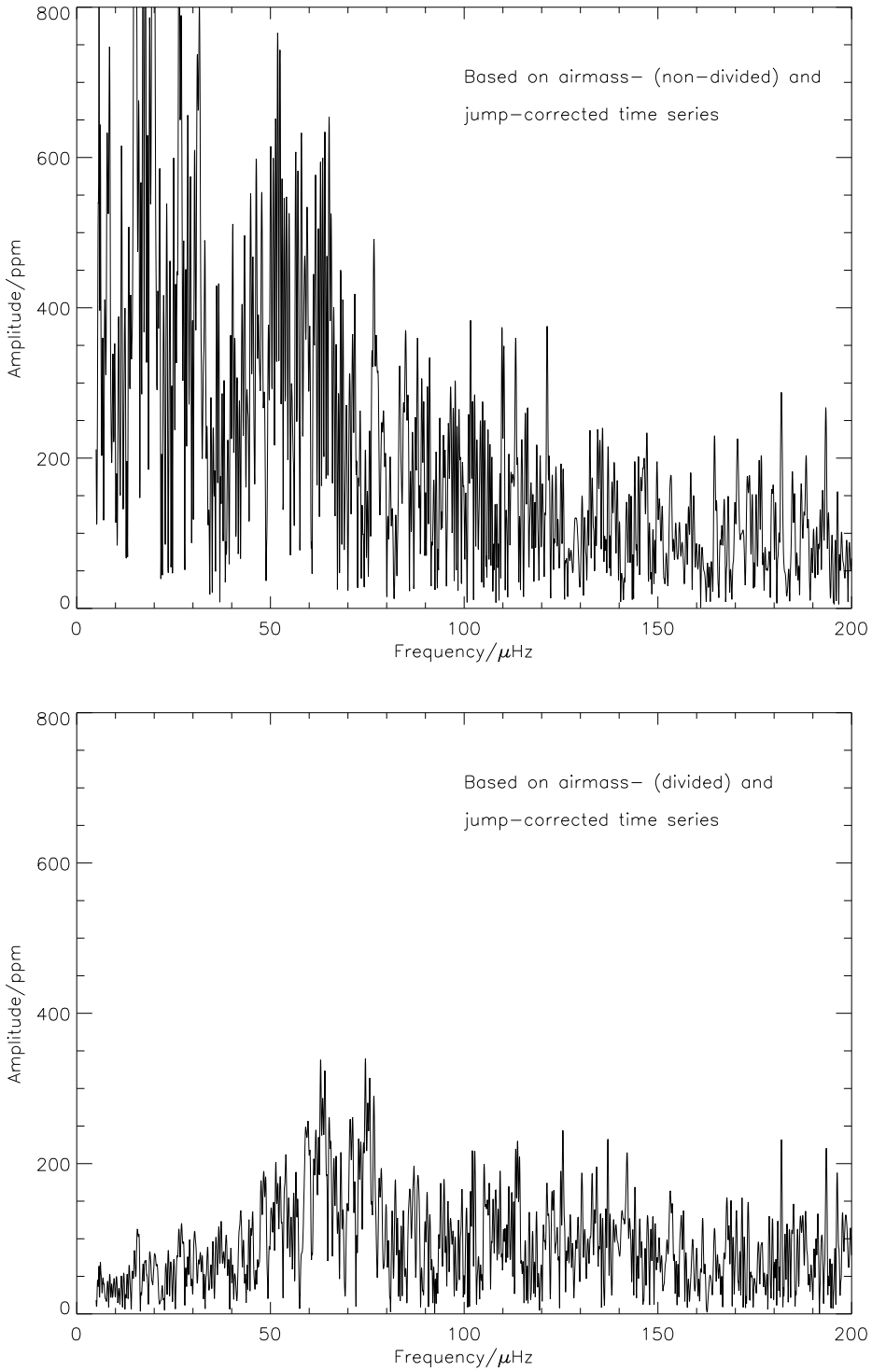

Figure 5.2: Amplitude spectra of the narrow line-filter time series. *Top panel*: Time series corrected for offset, jumps and airmass-like effect (non-divided; cf. Chapter 4, page 70). *Bottom panel*: Time series corrected for offset, jumps and airmass-like effect (divided). Note that the ordinate scale is changed by a factor of four compared to Fig. 5.1.

and ~ 100 ppm for non-divided and divided airmass de-correlation (cf. Chapter 4, page 70), respectively (Fig. 5.2, *top-* and *bottom panel*). The white noise level[2] of ~ 70 ppm is reached for frequencies above $\sim$ 700-800 μHz in the *bottom-* and *top panel* in Fig. 5.1. The de-correlation lowers the frequency threshold that separates the frequency interval into a lower and a upper part, the former being dominated by $1/f$-noise and the latter dominated by a white noise (including the photon noise). For the non-divided de-correlation the white noise dominates for frequencies above $\sim 500\,\mu$Hz, while the divided de-correlation lowers this value to roughly $200\,\mu$Hz (Fig. 5.2)[3].

The divided de-correlated time series shows an effective reduction of power at the low frequency end of the amplitude spectrum. This is because the airmass de-correlation acts like a high-pass filter, so the divided de-correlation is more efficient up to somewhat higher frequencies than the non-divided de-correlation.

The simulations described in Sect. 4 (page 70) and the fact that the amplitude spectrum of the divided de-correlation is nearly flat (at a value of roughly the white noise) from $\sim 100\,\mu$Hz to $\sim 6500\,\mu$Hz (the Nyquist frequency) indicate that the de-correlation process has been so efficient that only the white noise is left in the time series, hence only a very small fraction of the stellar signal has probably survived in the *bottom panel* of Fig. 5.2. Since the divided de-correlation seems to be too efficient, the peak at roughly 60-80 μHz in the amplitude spectrum close to the expected signal ($\sim 90\,\mu$Hz) is probably a spurious peak (cf. Fig. 5.2, *bottom panel*). This peak probably originate due to the power reduction in the relatively high noise background at the low frequency end. Hence based on this spectrum, it is not possible to conclude if the peak at $\sim$ 60-80 μHz is partly due to excess of power originating from the stellar signal or not.

The expected stellar signal is ~ 280 ppm (cf. Table 1.2). Compared to the noise one could expect to see a few oscillation peaks interfering positively with the noise in Fig. 5.1 and probably also in Fig. 5.2, *top panel*. In Sect. 5.2 it is shown that the actual stellar signal is only ~ 2 m/s based on the time series covering one month of observation in radial velocity. Assuming that the scaling relations (cf. Eqs. 1.7, 1.9; Sect. 1.2.1) predict a similar oscillation amplitude in velocity and in equivalent width, the measured stellar signal of ~ 2 m/s in the velocity observations (cf. Sect. 5.2.1) can be estimated to be roughly 70 ppm in the equivalent width time series presented in this section. Hence it would not be possible to see the stellar signal in any of the panels in Figs. 5.1, 5.2.

5.1.2 The improved strategy time series

In order to remove outlying data points, the time series created using the method outlined in Sect. 4.1.4 are median filtered by a sliding boxcar with a width corresponding to approximately 30 minutes.

[2]The white noise level is roughly twice as large as the expected photon noise.

[3]The noise is derived fitting "$a\frac{1}{f^2}+b$" to the power spectrum using **one_over_f_noise.pro**.

Two examples of the amplitude spectra of $W_{\mathrm{final},b=0}$ (Eq. 4.2) are shown in Fig. 5.3. The *top panel* can be regarded as the raw time series (not corrected for a daily offset), while the *bottom panel* is corrected for a daily offset. Since the stellar signal is unaffected by the value of the exponents $c_{a,b,c=0}$, the *bottom panel* should be the best obtainable amplitude spectrum[4] of the spectra presented in Fig. 5.3. The frequency defining the white noise dominated and $1/f$ noise dominated parts of the spectrum is in these plots $\sim 800\,\mu$Hz and $\sim 400\,\mu$Hz, respectively. These values clearly show that the amplitude spectrum shown in Fig. 5.3, *bottom panel*, is based on the best technique to reduce the $1/f$ noise component, without affecting the stellar signal significantly.

It is quite evident that the stellar signal is impossible to detect in the equivalent width time series by comparing the amplitude spectra of the equivalent width time series in Figs. 5.1, 5.2, and 5.3 with the one based on the actual measured stellar signal in the radial velocity time series also shown[5] in Fig. 5.3, *bottom panel*. The peaks in the frequency range 50-120 μHz of the amplitude spectrum shown in Fig. 5.3, *bottom panel* (solid grey line) have been identified using the same method as described in Sect. 5.2.2. There is no correlation between these peaks, which are most likely noise peaks, and the peaks detected from the radial velocity measurements (cf. Sect. 5.2).

In the frequency interval of the expected stellar oscillation signal, the noise level in the equivalent width time series is dominated by non-white noise, which is a factor of ~ 10 larger than the noise in the radial velocity time series[5]. It will therefore not be feasible to use DFOSC to attain a detection similar to that obtained using the radial velocity data, due to the observing time scale necessary for that. In fact, a rough estimate of the required observing time would be ~ 10 years.

The $1/f$ noise component of the *bottom panel* in Fig. 5.3 is plotted in Fig. 5.4 (*solid black line*)[6]. The white noise from Fig. 5.3 is also indicated (*solid grey line*).

For any given star, if one has an estimated amplitude and dominant oscillation frequency combined with the expected photon noise and neglects any other white noise contributions, one can use Fig. 5.4 to estimate the approximate S/N level obtainable using the DFOSC in the current setup for a similar investigation (cf. Chapter 2). This would be a quite useful tool to select targets which are suitable for asteroseismic investigations using DFOSC. In the specific case of solar-like oscillations, the expected stellar oscillation amplitudes (using $1/g$ scaling) for stars with an effective temperature of 5000 K and 4000 K are plotted (*dashed line* and *dash-*

[4]The offset correction of the mean per night reduces the low frequency noise. It is a fairly safe filter, not affecting the stellar signal significantly.

[5]The amplitude spectrum based on the radial velocity measurements has been scaled (assuming that Eqs. 1.7, 1.9 scale correctly) to ppm in equivalent width by 34 ppm/(m/s).

[6]The $1/f$ noise quoted in Fig. 5.4 has been compared to a similar asteroseismic investigation (Knudsen, 2000) performed with DFOSC. The $1/f$ noise in the time series of Knudsen (2000) (fitted to the original data, using **one_over_f_noise.pro**) was five times larger than the $1/f$ noise quoted in Fig. 5.4, and three times larger than the $1/f$ noise seen in Fig. 5.1, *top panel*.

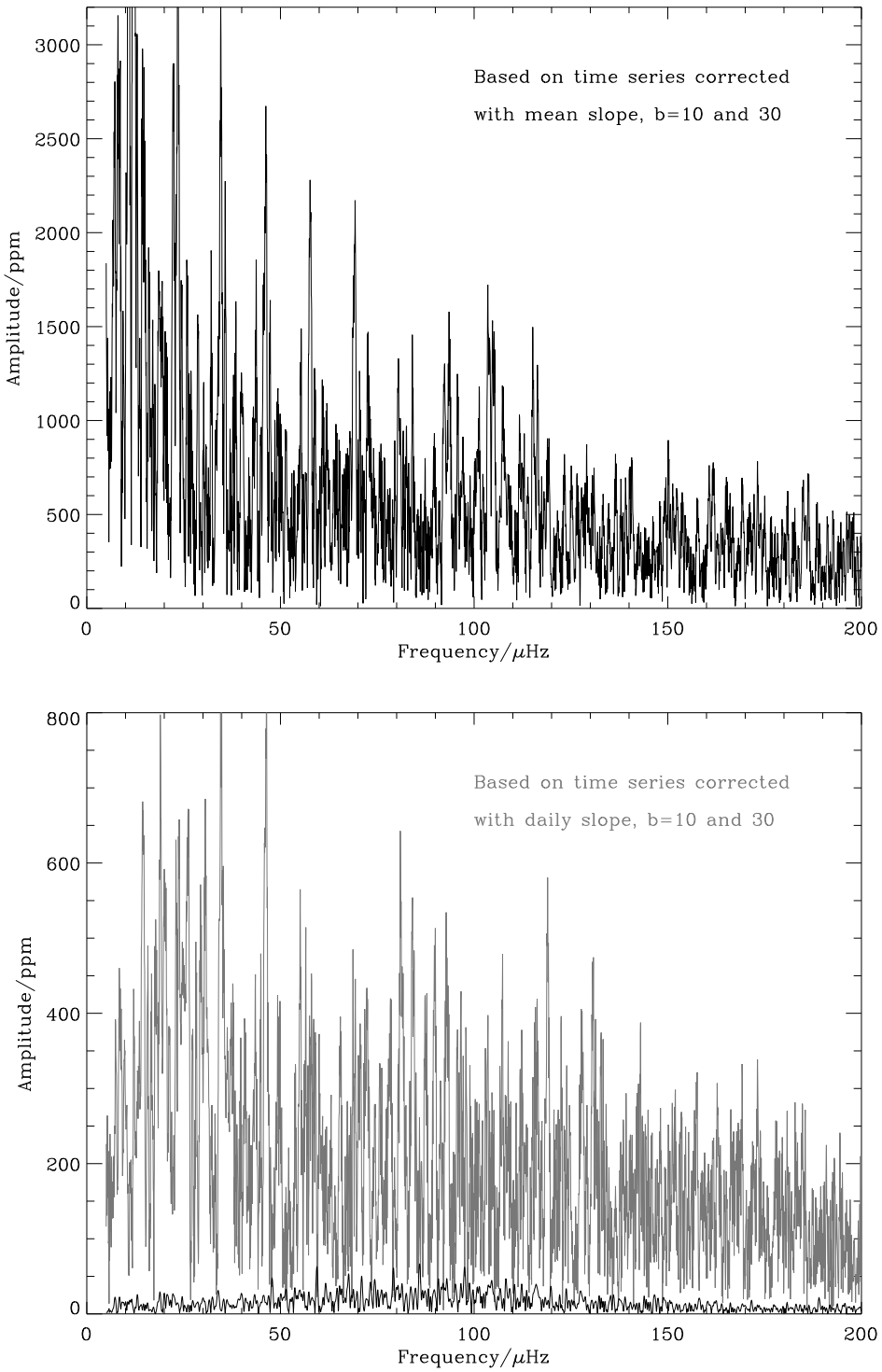

Figure 5.3: Amplitude spectra of the wide line-filter time series ($W_{\mathrm{final},b=0}$, Eq. 4.2). *Top panel* shows the example where $c_{b=0} = \langle c_{b=0,i} \rangle$, i being the index of the data set from night i. At the *bottom panel* $c_{b=0} = c_{b=0,i}$. The black line at the bottom of this panel is the observed amplitude spectrum from the radial velocity data, scaled to ppm (34 ppm/(m/s); see text) in the equivalent width. The maximum oscillation peak is roughly 70 ppm).

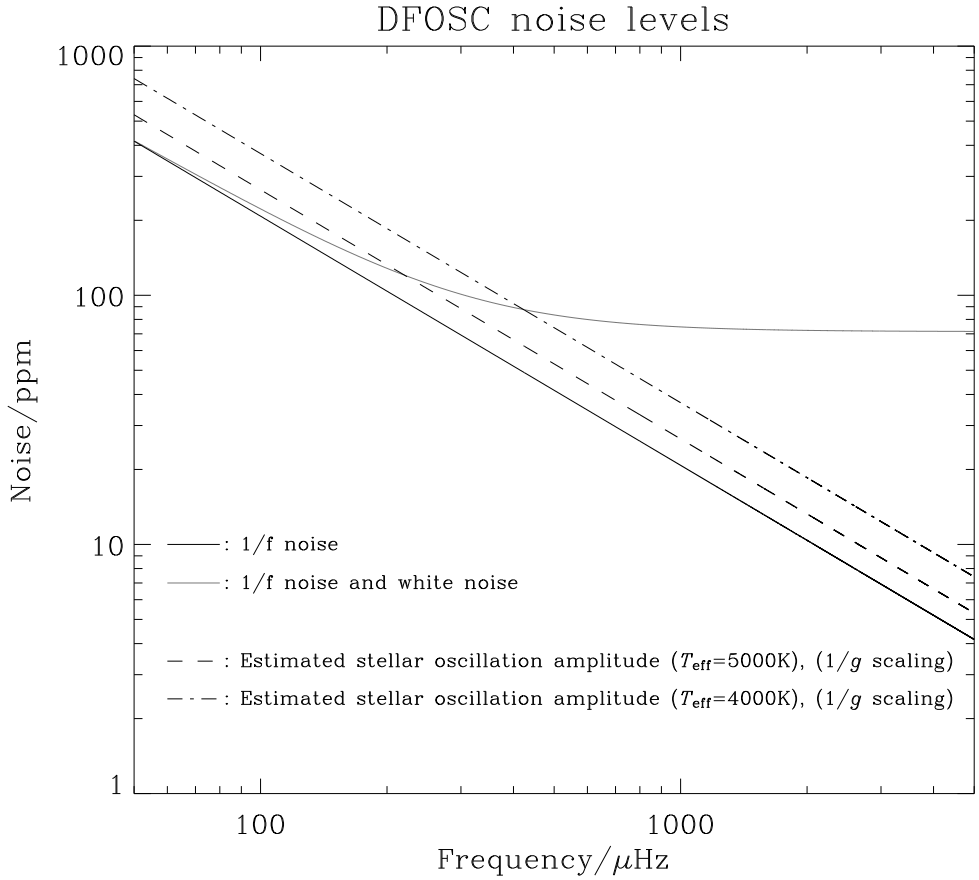

Figure 5.4: Noise diagram of the DFOSC with the setup described in Sect. 2.1.2, page 28. *Solid black line:* $1/f$ noise component which fits the amplitude spectrum shown in the *bottom panel* of Fig. 5.3. *Solid grey line:* Indication of the additional white noise ($\sim$ 2 times the photon noise) which has been fitted to an amplitude spectrum similar to Fig. 5.3 *bottom panel*, but without low-pass filtering with a median filter boxcar. *Dash-* and *dash-dot lines* show the expected stellar oscillation amplitudes for solar-like oscillations in stars with effective temperatures of 5000 K or 4000 K, respectively. The expected amplitudes are derived using the $1/g$ scaling (Eq. 1.7) which predicts amplitudes $\sim$ 1.8 times higher than the L/M scaling (Eq. 1.6) for an effective temperature of 5000 K.

dot line, respectively). The expected solar-like oscillation amplitudes are derived by combining Eqs. 1.4, 1.9 (Sect. 1.2.1)[7] using $\partial \ln W / \partial \ln T = 7$ (cf. page 18), and $L \propto R^2 T_{\rm eff}^4$:

$$\begin{aligned}
\frac{\delta W}{W} &= \frac{\partial \ln W}{\partial \ln T_{\rm eff}} \times \frac{L/\mathrm{L}_\odot}{(M/\mathrm{M}_\odot)(T_{\rm eff}/\mathrm{T}_{\rm eff,\odot})^5} \times (1.0 \pm 0.1)\,\mathrm{ppm} \\
&= \frac{(R/\mathrm{R}_\odot)^2}{(M/\mathrm{M}_\odot)(T_{\rm eff}/\mathrm{T}_{\rm eff,\odot})} \times (7.0 \pm 0.7)\,\mathrm{ppm} \\
&= \frac{(R/\mathrm{R}_\odot)^2 (T_{\rm eff}/\mathrm{T}_{\rm eff,\odot})^{1/2}}{(M/\mathrm{M}_\odot)\,3050} \times \frac{3050}{(T_{\rm eff}/\mathrm{T}_{\rm eff,\odot})^{3/2}} \times (7.0 \pm 0.7)\,\mathrm{ppm} \\
&= (\nu_{\rm max}/\mu\mathrm{Hz})^{-1} \times (T_{\rm eff}/\mathrm{T}_{\rm eff,\odot})^{-3/2} \times (2250 \pm 225)\,\mathrm{ppm}\,. \qquad (5.1)
\end{aligned}$$

5.1.3 Summary: The equivalent width time series

- The unexpected noise in the time series discussed in Chapter 4 is shown to be crucial in the amplitude spectra, which are totally dominated by $1/f$ noise in the frequency range of the expected stellar oscillation signal.
- Time series based on single line-filters could not be de-correlated against other parameters in order to reduce the $1/f$ noise to an acceptable level without reducing the stellar signal dramatically. This problem could not be solved using time series based on single line-filters because the time scale of the stellar signal was too close to the time scale of the instrumental instability which caused the large $1/f$ noise. The best solution was a combination of time series each based on wide line-filters of different widths.
- Investigating the power spectra showed that the $1/f$ noise of the raw time series was the dominant noise component for frequencies below $\sim 800\,\mu$Hz. By de-correlation or combination of different line-filters it was possible to reduce this regime to below 400-500 μHz, though still including the frequency range of the expected oscillation stellar signal.
- Even without the large $1/f$ component of the noise, so the total noise consisted only of the white noise, it would at best be possible to detect only excess of power and not provide individual frequencies, since the actual stellar signal (cf. Sect. 5.2) is roughly equal to the white noise (~ 70 ppm), assuming that the scaling relations Eqs. 1.7, 1.9 are applicable.
- It was tested that the peaks in the amplitude spectrum of the equivalent width measurements at the frequency range of the stellar signal were not similar to the oscillation frequencies detected later (cf. Sect. 5.2) from the radial velocity measurements.

[7] Note that Eq. 1.9 is based on the most optimistic amplitude scaling of the two presented in this thesis (Eq. 1.6 (L/M scaling) and Eq. 1.7 ($1/g$ scaling)).

- Due to the drifts discussed in Chapter 4, which introduce the relatively high noise level in the low frequency end of the amplitude spectrum, it can be concluded that the DFOSC is not suitable for asteroseismic investigations of solar-like oscillations using the equivalent width method (cf. Fig. 5.4).

5.2 The radial velocity time series

This section will give a detailed description of the time series analysis related to the radial velocity time series. The amplitude spectrum of this time series is analysed in order to verify if excess of power is positioned at the expected frequency and amplitude (Sect. 5.2.1). Extracted frequencies (Sect. 5.2.2) are used for mode identification (Sect. 5.3) and the observed large frequency separation is compared to a theoretical frequency spectrum from a pulsation model leading to a determination of the density of ξ Hya (Sect. 5.3.4). Further, the damping time of the oscillations and the validity of the extracted frequencies are discussed, e.g. based on simulations.

The time series (shown in Fig. 4.10) based on the radial velocity measurements described in Sects. 2.2, 4.2 is analysed using **Period98** (Sperl, 1998). The data points are weighted with the photon and detector noise.

The amplitude spectrum and the corresponding window function are shown in Fig. 5.5. Not only is a very clear excess of power in a broad envelope seen in the frequency range 40-140 μHz, but several individual frequencies can be identified. *This is the most firm evidence of solar-like oscillations in a giant star*, and this detection resulted in a ESO press release (see Aerts et al., 2002) and a subsequent paper (Frandsen et al., 2002) (**Paper I**).

Even though the observation period is too short to get a well defined envelope peak of the excess power due to the stochastic nature of the excitations, it seems that the peak of the envelope would be roughly at 80-100 μHz in good agreement with the prediction $\nu_{\rm max} = 93(15)\,\mu$Hz (cf. Table 1.2).

The mean error of each measurement in the time series is estimated from the mean level in the amplitude spectrum at high frequency (160-190 μHz) which is $\mu_{\rm amp} = 0.20$ m/s. Assuming the noise is Gaussian, this implies a mean error of each measurement in the time series of $\langle\sigma_{\rm measure}\rangle = \mu_{\rm amp}\sqrt{N/\pi} = 2.33$ m/s (Kjeldsen & Bedding, 1995), where $N = 433$ is the number of data points.

5.2.1 Amplitude and damping

Taking the noise level into account using $A_1^2 = A_{\rm osc}^2 + (8.7 \pm 2.3)\mu_{\rm amp}^2$ (Kjeldsen & Bedding, 1995, their A3), one can estimate an amplitude of the highest peak (A_1) of ~ 1.7 m/s, which is a factor of 4.7 smaller than the prediction of 8.2 m/s using $1/g$ scaling. The L/M scaling predicts an amplitude of 4.7 m/s, a factor of 2.7 larger than measured (cf. Table 1.2). It should be noted that the measured amplitude depends on the particular degree of the mode which is detected, since the observations are affected by the so-called response function (Sect. 1.2.1), which depends

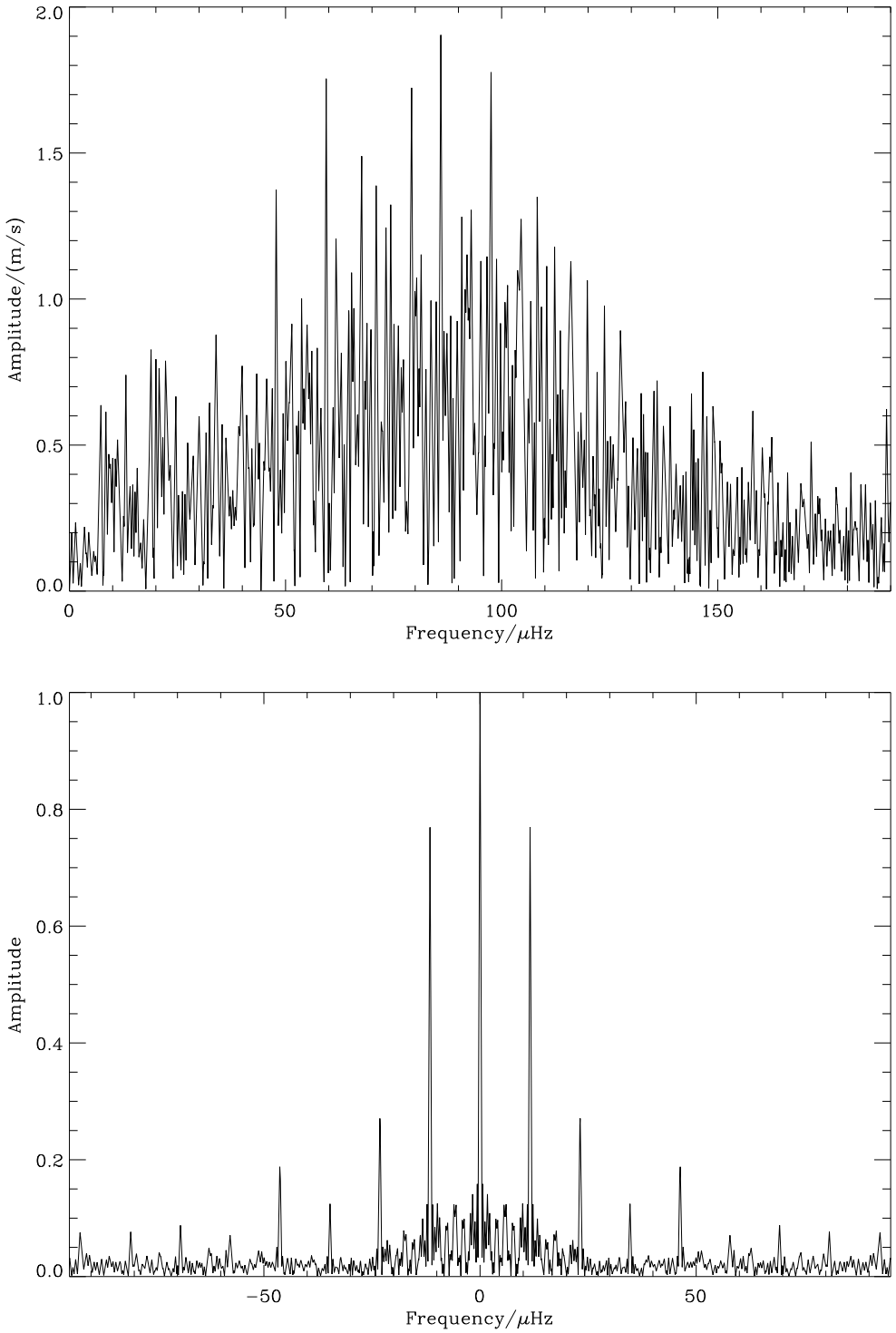

Figure 5.5: **Top panel:** Amplitude spectrum of ξ Hya based on the radial velocity measurements. The Nyquist frequency is $\sim 200\,\mu$Hz. The amplitude is indicated in m/s, and can be scaled to ppm by 34 ppm/(m/s) assuming that the scaling relations (cf. Eqs. 1.7, 1.9; Sect. 1.2.1) scale correctly for red giant stars. **Bottom panel:** Window function of the radial velocity time series. Both top- and bottom panels are oversampled with a frequency step of $0.01\,\mu$Hz (0.25 times the frequency resolution).

on the measured oscillation quantity (radial velocity, equivalent width etc.) and degree l of the oscillation. The observed oscillation amplitude also depends on the observing time relative to the damping time of the mode. If $T_{\rm obs} \gg T_{\rm damping}$, the observed amplitude would be underestimated compared to the predictions by the scaling relations. Hence care should be taken when comparing measured amplitudes with the scaling relations.

Subsequent to the ESO press release (Aerts et al., 2002) Houdek & Gough (2002) made theoretical predictions for the amplitude, including the damping rate as a function of frequency, for ξ Hya. They predict the amplitude of the highest peak to be 2.3 m/s. This can be compared directly to the scaling relations of Kjeldsen & Bedding (1995) (cf. Eqs. 1.6, 1.7), since the models of Houdek & Gough (2002) are calibrated to the same solar velocity amplitude ($v_{\rm osc,\odot} = 23.4\,$cm/s) as that used by Kjeldsen & Bedding (1995). The scaling relations predict amplitudes which are a factor of 2 and 3.5 larger than the result of Houdek & Gough (2002) for the L/M and $1/g$ relations, respectively. This clearly indicates that these simple scalings from the Sun does not hold for giant stars like ξ Hya.

The damping rate for ξ Hya at $90\,\mu$Hz is predicted to be $\sim 0.1\,\mu$Hz (Houdek & Gough, 2002) corresponding to a damping time of $\sim 17\,$days, which cannot be resolved by the current data set.

In addition to the result of Houdek & Gough (2002), the damping time has been investigated through simulations. Twenty simulated time series are constructed with an input white noise of 0.2 m/s and the same window function and point-to-point weights as the real time string. There are twelve input frequencies distributed in a Gaussian envelope around $90\,\mu$Hz with individual frequency amplitudes ranging from 0.4-1.5 m/s.

Three typical examples of simulated amplitude spectra, each of different damping time, are shown in Fig. 5.6. In contrast to the predictions of Houdek & Gough (2002), Fig. 5.6 could indicate that the damping time is in the order of one week, since the amplitude spectra based on long damping times are too "clean" compared to the observed spectrum, which is quite dense (cf. Fig 5.5, *top panel*). However, it should be noted that this is not a definite proof that the actual damping time is significantly shorter than predicted by Houdek & Gough (2002).

Introducing a more densely packed input frequency pattern of twenty frequencies in the range 60-120 μHz but with a long damping time also reproduces a dense amplitude spectrum, similar to the observed one (cf. Fig. 5.7). The simulated time series of the more densely packed input frequency pattern assumes that many modes are excited to an observable amplitude with a mean separation of only $3\,\mu$Hz. This is roughly half the expected large frequency separation, which implies that a substantial number of detected frequencies are due to non radial modes (cf. Sect. 5.3.1, page 100 and 101, and Sect. 5.3.2).

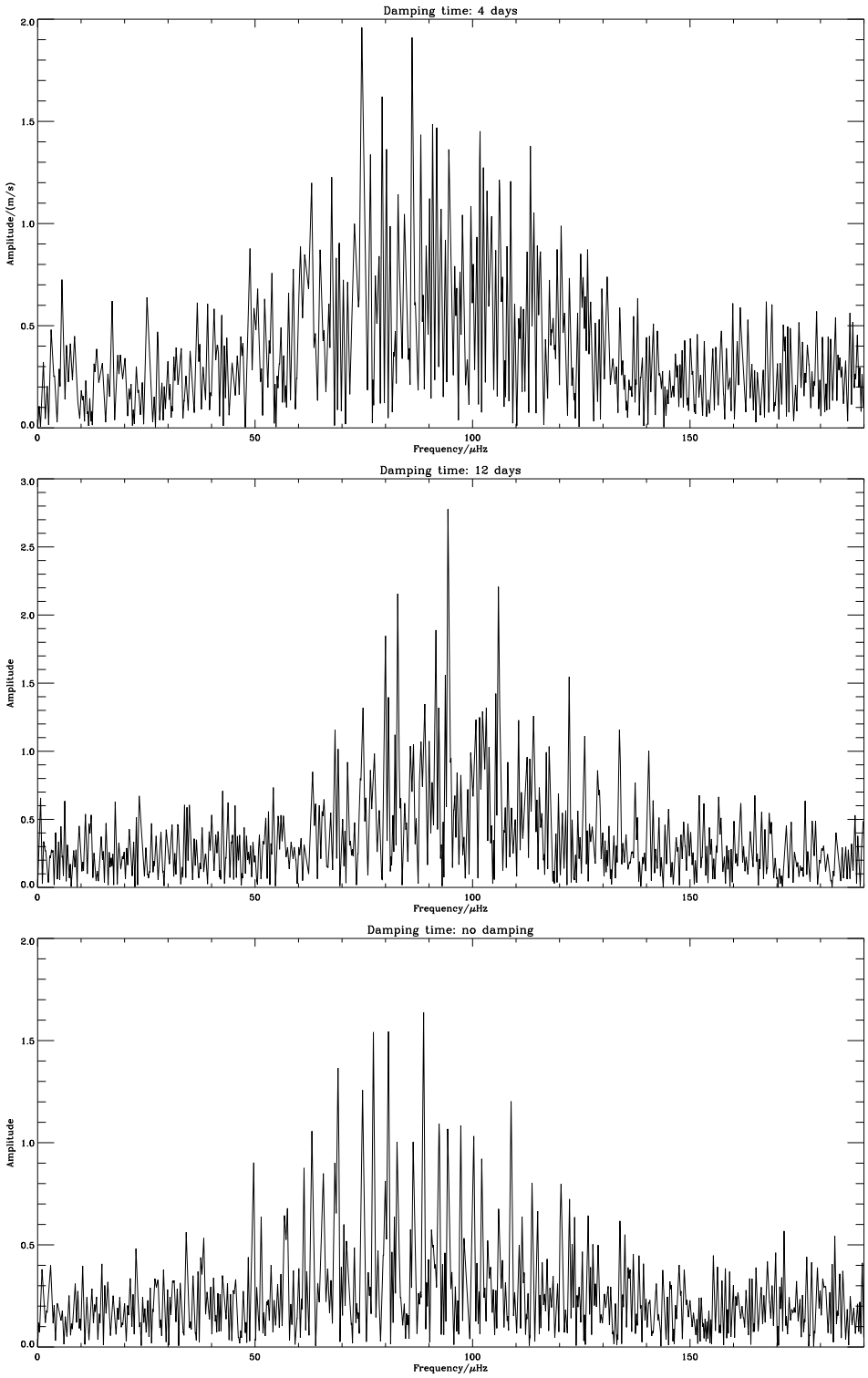

Figure 5.6: Amplitude spectra of the simulated time series. Each panel has indicated the corresponding damping time in the title.

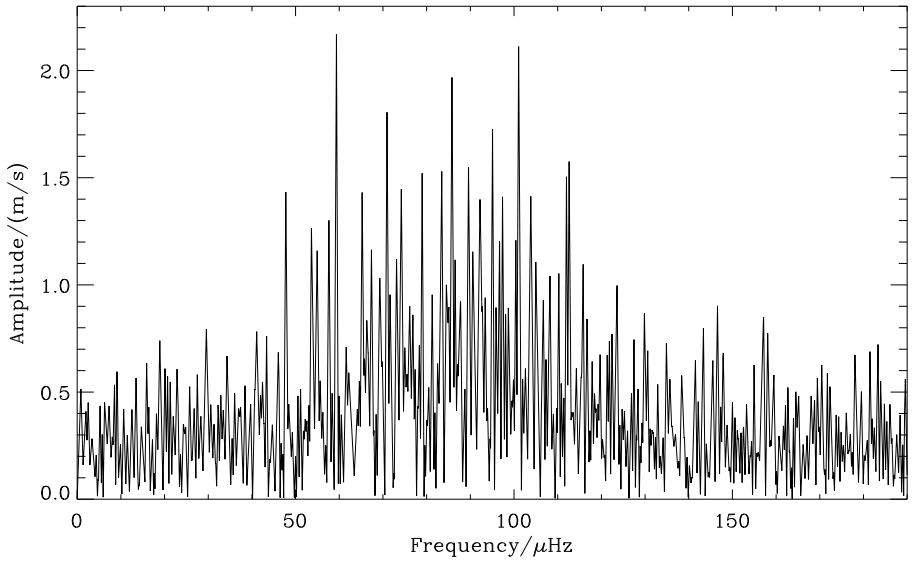

Figure 5.7: Amplitude spectrum of a simulated time series with the same window function, point-to-point weights, as in the observed time series. The mean noise is 0.2 m/s and the input signal is 20 frequencies covering 60-120 μHz with amplitudes ranging from 0.8 m/s to 1.9 m/s. The damping time is infinite.

5.2.2 Finding the frequencies

To be able to separate distinct modes, their frequency separation, $\delta\nu$, should be larger than the frequency resolution ($1/T$, where T is the total time span of the time series). The frequency separation should at least be $\delta\nu \simeq 2.5/T = 1.02\,\mu$Hz to be sure that the frequencies can be separated (Loumos & Deeming, 1978).

The frequency determination using **Period98** can be itemized in the following way:

- Calculate the amplitude spectrum and locate the frequency and the amplitude of the highest peak.
- Fit frequency, amplitude, and phase to the time series, with the obtained frequency and amplitude as input guesses.
- Subtract the best fit from the time series and recalculate the amplitude spectrum, then locate the highest peak.
- Fit the new and the former frequencies simultaneously to the time series etc.

The amplitude spectrum is not based on Fast Fourier Transform, as the data are not equally spaced in time and the Fourier analysis includes weights of each data

point[8]. The fit to the data is as follows

$$A(t) = \text{offset} + \sum_{i=1}^{n} A_i \sin(2\pi(F_i \cdot t + P_i)) \ , \tag{5.2}$$

where n is the number of frequencies which are fitted simultaneously, and A, F, and P are the amplitude, frequency, and phase, respectively. The fitting procedure is done in two steps. First, the frequency found from the amplitude spectrum is fixed and the amplitude and phase are adjusted. Afterwards an improved fit is calculated, where frequency, amplitude, and phase are adjusted at the same time. When an additional frequency is added to the set of identified frequencies, it will be fitted simultaneously with the former identified frequencies. From the entire list of identified frequencies one has the opportunity to use only a user-defined subset in the fitting, which is believed to be real, and recalculate the fit (for further details see Sperl, 1998).

The list of frequencies found in the amplitude spectrum following the procedure described in the former paragraph can be seen in Table 5.1. The frequencies are

Table 5.1: Oscillation frequencies and amplitudes for ξ Hya

Designation	Frequency/(μHz)	Amplitude/(m/s)	S/N
F1	85.95(5)[a]	1.87(21)[a]	6.2
F2	59.42(5)	1.86	6.2
F3	79.13(5)	1.68	5.6
F4	108.21(6)	1.48	4.9
F5	95.26(5)	1.83	6.1
F6	101.21(6)*	1.43	4.8
F7	112.26(8)*	1.09	3.6
F8	116.02(7)**	1.25	4.2
F9	105.08(6)**	1.31	4.4
F10	65.31(8)	1.03	3.4
F11	73.35(8)	1.07	3.6
F12	103.75(8)**	1.01	3.4
F13	98.75(8)	1.09	3.6

[a] The errors are derived from: $\sigma_f = 1/(T_{\rm obs}\cdot {\rm S/N}\cdot\sqrt{2})$, and $\sigma_{\rm amp} = \langle\mu_{\rm amp}\rangle/\sqrt{2}$, (see text).
* Indistinguishable frequencies (F6+11.57 μHz)$-$F7$\lesssim \delta\nu \simeq 1\,\mu$Hz.
** Indistinguishable frequencies $|$(F8$-$11.57 μHz) $-$ (F9,F12)$| \lesssim \delta\nu \simeq 1\,\mu$Hz.

shown in the order with which they are found using the procedure itemized above. F1 is the highest peak of the raw amplitude spectrum (cf. Fig. 5.5, *top panel*), F2 the highest peak after F1 is subtracted, etc.

Fig. 5.8 shows 6 steps of the frequency extraction process, out of the 13 in total, using **Period98** starting from the original amplitude spectrum, where more and

[8]It was tested that the Fourier analysis performed by **Period98** gave the same result as **ampl_spec_calc.pro** used for the analysis of the equivalent width time series.

more frequencies are subtracted successively from the time series until only a noise spectrum is left (Fig. 5.8, left side from top to bottom followed by right side from top to bottom). Since the fitting of the different harmonic oscillators is performed simultaneously, frequencies which are found at a later stage can end up with a higher amplitude than a frequency found earlier.

The significance of each mode is given as S/N in Table 5.1, which is calculated with respect to a mean noise level derived as the average of the mean level in the amplitude spectrum at the high frequency end, 145-185 μHz ($\langle\mu_{\rm amp,1}\rangle = 0.24\,{\rm m/s}$), and of the low frequency end, 5-45 μHz ($\langle\mu_{\rm amp,2}\rangle = 0.36\,{\rm m/s}$) which finally gives $\langle\mu_{\rm amp}\rangle = 0.30\,{\rm m/s}$.

The errors in the frequency and amplitude indicated in Table 5.1 are derived using the following formulae. The mean noise ($\langle\mu_{\rm amp}\rangle = 0.30\,{\rm m/s}$) can be separated in two orthogonal components, an amplitude component ($\sigma_{\rm amp}$) and a phase component (σ_ϕ) ($Amp_{\rm peak}$ denotes the amplitude of the peak):

$$\sigma_{\rm amp} = \frac{\langle\mu_{\rm amp}\rangle}{\sqrt{2}} \tag{5.3}$$

$$\sigma_\phi = \frac{\langle\mu_{\rm amp}\rangle}{Amp_{\rm peak}\times\sqrt{2}}\,. \tag{5.4}$$

Using ${\rm S/N} = Amp_{\rm peak}/\langle\mu_{\rm amp}\rangle$ and the relation $\sigma_f = \sigma_\phi/T_{\rm obs}$ one obtains:

$$\sigma_f = \frac{1}{T_{\rm obs}\times{\rm S/N}\times\sqrt{2}}\,. \tag{5.5}$$

5.3 Mode identification

In this section, the extracted frequencies and corresponding amplitudes from the amplitude spectrum of ξ Hya (cf. Table 5.1) are analysed, which includes a discussion of the validity of the individual frequencies listed in Table 5.1. Furthermore, an assumed frequency distribution of equally spaced radial modes is fitted to the observed frequency spectrum in order to determine a large frequency separation, which provides a determination of the stellar density. To study the nature of the oscillations detected in ξ Hya, it is necessary to compare the observed frequency spectrum with predictions from a pulsation model. A theoretical frequency spectrum of radial modes based on the stellar parameters of ξ Hya (cf. Sect. 1.5) is presented for comparison. This comparison is used to estimate the oscillation damping time and the stellar mass.

5.3.1 Autocorrelation

If it is assumed that the frequency spectrum of ξ Hya shows an equally spaced frequency pattern, which is expected from model calculations (cf. Sect. 5.3.4), one can

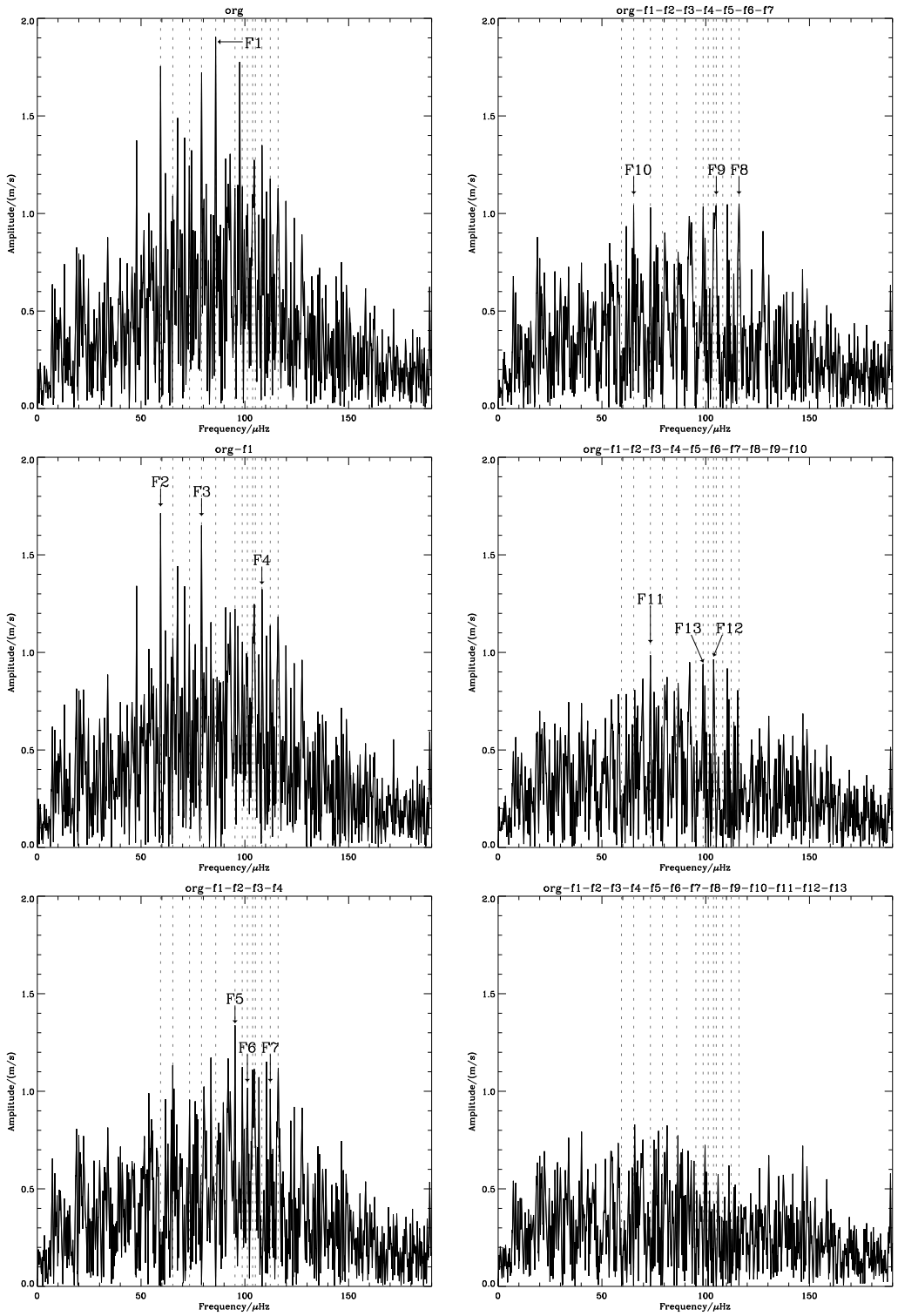

Figure 5.8: Amplitude spectra of the radial velocity time series. The extraction of frequencies can be followed from *top left* to *bottom left* followed by *top right* to *bottom right*. To save space, not all 13 individual extraction steps are shown. The extracted frequencies are denoted in the same way as in Table 5.1. All extracted frequencies are indicated by *vertical dotted grey lines* to clarify the amplitude variation during the extraction process.

find the general separation in this pattern by calculating the autocorrelation function. The autocorrelation function is derived using **auto_corr.pro**, which includes a weight function defining the part of the power spectrum of interest. In this case the autocorrelation function can be expressed as

$$autocorr(\delta f) = \sum_{f=f_{\min}}^{f_{\max}} (p(f) \cdot p(f+\delta f) \cdot W(f)) \tag{5.6}$$

where δf is the frequency separation, p is the power, and W is a weight function.

The autocorrelation function of the raw spectrum is shown in Fig. 5.9. The top

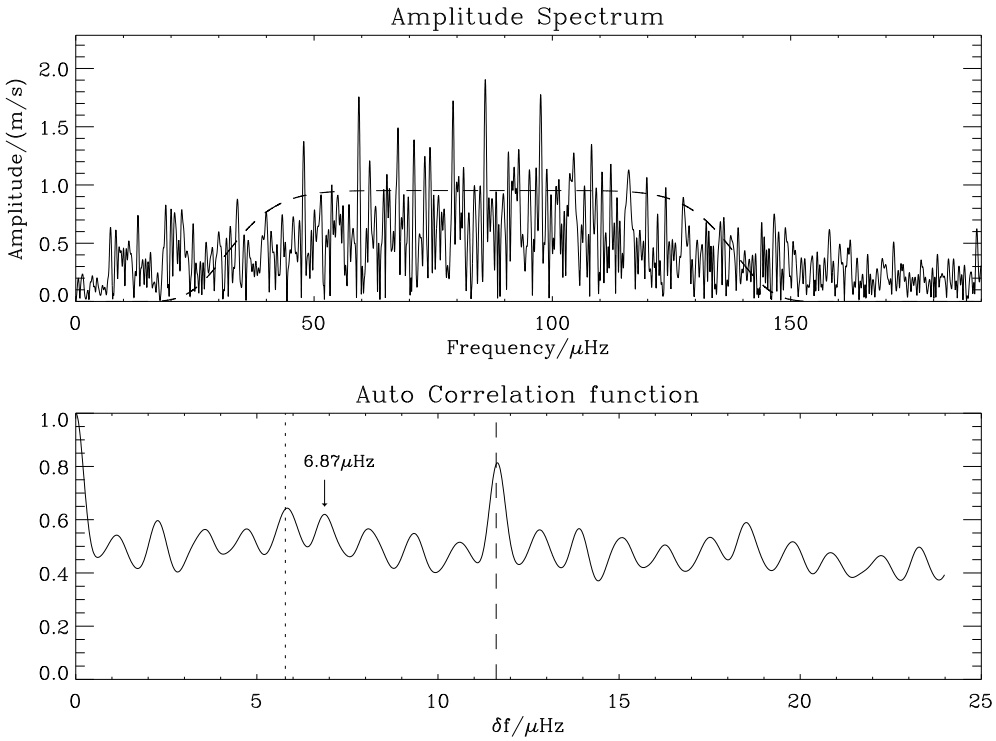

Figure 5.9: **Top panel:** Raw amplitude spectrum similar to Fig. 5.5 (*top panel*), with the weight function indicated as the dashed Super-Gauss curve. **Bottom panel:** Autocorrelation function of the raw spectrum. The structure from the side-bands are clearly seen as a large peak at 1/day ($11.574\,\mu$Hz) indicated with a *dashed line*. In addition, the half of the daily alias ($5.787\,\mu$Hz) is indicated with a *dotted line*.

panel shows the amplitude spectrum and the weight function W, and the bottom panel shows $autocorr(\delta f)$ (cf. Eq. 5.6). The frequency corresponding to 1/day= $11.574\,\mu$Hz is indicated by the dashed line and a very clear peak is seen at this position in the autocorrelation function. Further, at $1/2\times 11.574\,\mu$Hz there is another significant peak, indicated by a dotted line.

Due to the clear alias problems, most of the peaks visible in the autocorrelation function are not independent, because they are "reflections" of one another around

the $11.574\,\mu$Hz and $5.787\,\mu$Hz peaks (cf. Fig. 5.9), and thus due to correlations between the side-bands and frequency separations. This correlation will be explicitly explained below. It means that there are at most four independent peaks, and since the expected large frequency separation is $\Delta\nu_{0,\mathrm{expect}} = 7.0(7)\,\mu$Hz (cf. Table 1.2), the peaks within the frequency range 5.787-11.574 μHz are further analysed. Within that range, the frequencies of the four peaks are: $6.87\,\mu$Hz, $8.07\,\mu$Hz, $9.35\,\mu$Hz, and $10.60\,\mu$Hz, where the peak at $6.87\,\mu$Hz is the most significant. From these frequencies the other frequencies seen in Fig. 5.9 (bottom panel) can be found as:

$$f_{\mathrm{correlation}} = (\pm n \times 11.574 \pm m \times f_{\mathrm{peak}})\,\mu\mathrm{Hz}\,, \tag{5.7}$$

where n and m are integers and f_{peak} is one of the four frequencies quoted above. This is because of the correlations between the side-bands and frequency separations as mentioned above.

Setting $n = -m = 2$ and $f_{\mathrm{peak}} = 6.87$ in Eq. 5.7 gives $9.41\,\mu$Hz ($\sim 9.35\,\mu$Hz), hence this frequency can also be explained as a correlation between side-bands and a frequency separation of $6.87\,\mu$Hz. Therefore, only three frequency separations are likely to be independent: $6.87\,\mu$Hz, $8.07\,\mu$Hz, and $10.60\,\mu$Hz.

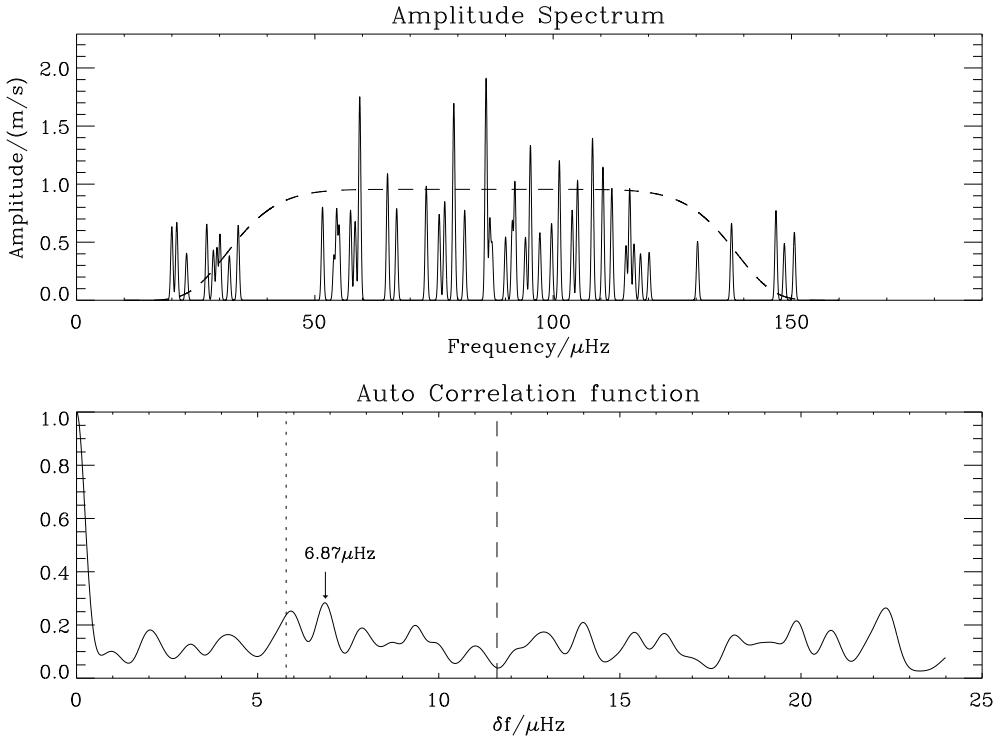

Figure 5.10: **Top panel:** CLEANed amplitude spectrum, with the weight function indicated as the dashed Super-Gauss curve. **Bottom panel:** Autocorrelation function of CLEANed spectrum. The structure from the side-bands is clearly removed relative to Fig. 5.9. The *dashed line* and *dotted line* are the same as in Fig. 5.9.

An additional test of the frequency separation is performed on the CLEANed frequency spectrum. This is done to avoid the problems caused by the side-band structure.

The CLEANed spectrum is obtained by subtracting 50 frequencies from the raw amplitude spectrum one by one, as described in Sect. 5.2.2. For each detected peak, a Gaussian envelope with the same amplitude as the peak is constructed with a width corresponding to the frequency resolution ($1/T_{\rm obs} = 0.4\,\mu$Hz). The final CLEANed spectrum and its autocorrelation function are shown in Fig. 5.10. After the side-band structure has been removed from the amplitude spectrum, the peak at $11.57\,\mu$Hz (*vertical dashed line*) is totally removed and the $6.87\,\mu$Hz is more pronounced relative to other features visible in the autocorrelation function[9].

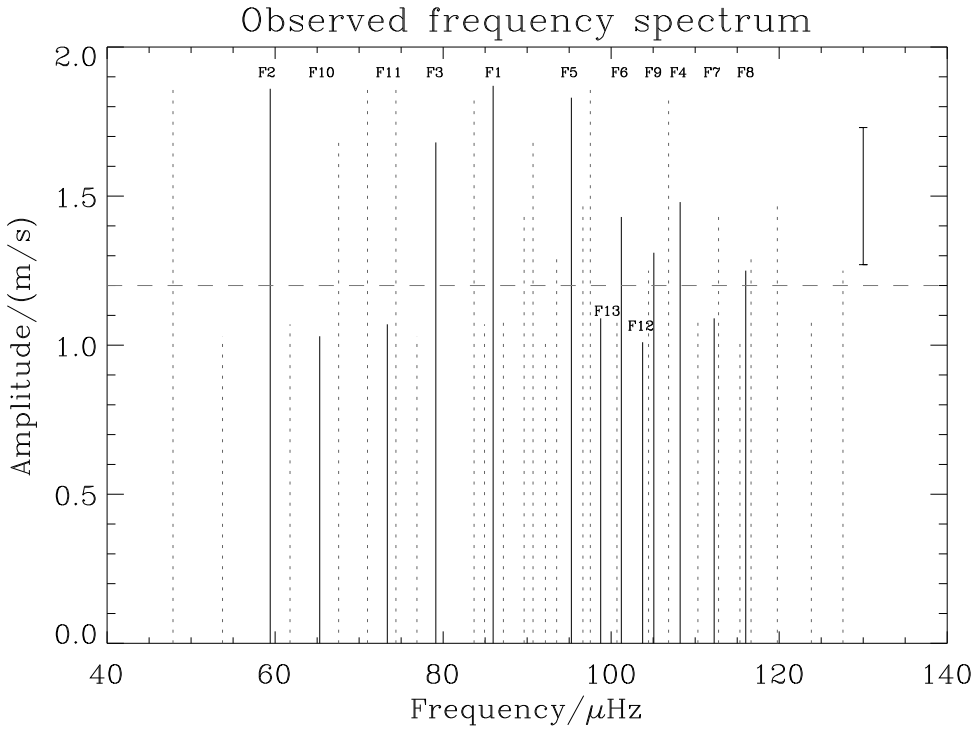

Figure 5.11: Observed frequency spectrum based on the frequencies and amplitudes given in Table 5.1 (*solid black lines*). The first side-bands of each frequency are indicated by *dotted grey lines* with amplitudes equal to their corresponding center frequency to clarify their connection. In addition, an error bar at $130\,\mu$Hz indicates the typical error ($\pm 1\sigma$) in the measured amplitude and the width of the bar is the approximate frequency separation, $\delta\nu \simeq 1\,\mu$Hz, required to separate distinct modes based on the current data set. The horizontal *grey dashed line* shows the 4σ level.

The frequency spectrum based on the frequencies and amplitudes given in Table 5.1 is plotted in Fig. 5.11. It can be clearly seen that the first five peaks (F2, F10,

[9]The significance of the peak at $6.87\,\mu$Hz in the autocorrelation function has to be determined through simulations.

F11, F3, and F1) are distributed with nearly equal spacing. A linear fit to these frequencies as a function of n, a suitable order for each mode, provides a frequency separation of $\Delta\nu_{0,\mathrm{obs1}} = 6.69(18)\,\mu$Hz, which is in good agreement with the results from the autocorrelation function. The scatter of the observed frequencies relative to the predicted frequencies based on $\Delta\nu_{0,\mathrm{obs1}}$ is $\sigma_{\mathrm{obs1}} = 0.50\,\mu$Hz. If the order n is matched to the model spectrum (cf. Table 5.4, page 107) the fit to the asymptotic relation is:

$$f_{\mathrm{obs1}}(n) = 5.8(1.8) + n \times 6.69(18)\,\mu\mathrm{Hz}\,, \tag{5.8}$$

resulting in the following values for the first five frequencies:

n=8	59.27(38) μHz
n=9	65.96(27) μHz
n=10	72.65(22) μHz
n=11	79.34(27) μHz
n=12	86.03(38) μHz

The quoted errors are based on an extrapolation formalism.

The higher frequency end of the spectrum seems at first to be more chaotic than the first five frequencies, showing no clear separation. This could indicate that modes of different degree l are observed, a possibility which should be investigated by calculating pulsation models. But, as a first step, it is investigated whether these peaks can be explained as radial modes. In order to do so, some of the frequencies are regarded as side-bands, and thus shifted by $\pm 11.574\,\mu$Hz. In fact, simulations show that, depending on the oscillation damping time, it is expected that side-bands should be detected and therefore it cannot be expected that all frequencies listed in Table 5.1 are center frequencies (cf. Sect. 5.3.5).

Extrapolating the fit based on the frequencies F2, F10, F11, F3, and F1 (Eq. 5.8) to cover the entire frequency range of the detected frequencies listed in Table 5.1 provides the following expected frequencies:

n=13	92.72(52) μHz
n=14	99.41(67) μHz
n=15	106.1(81) μHz
n=16	112.8(97) μHz
n=17	119.5(1.1) μHz
n=18	126.2(1.3) μHz

The observed frequencies which fit into this scheme are (within 1-2σ of the extrapolation) shown in Table 5.2. The observed frequency spectrum based on the "Interpreted" frequencies in Table 5.2 is shown in Fig. 5.12. As discussed in Sect. 5.2.2 the required separation between mode frequencies, $\delta\nu$, should be larger than $\sim 1\,\mu$Hz in order to separate individual modes. In the above arrangement of observed frequencies, F12 and F9 are averaged though they are separated by $1.33\,\mu$Hz, and hence regarded as one non separable frequency.

Table 5.2: Equally spaced frequencies for ξ Hya (Case 2)

Observed frequency		Expected mode	Interpreted frequency	
F2	59.42 μHz	f(n=8)	f(n=8) =	59.42 μHz
F10	65.31 μHz	f(n=9)	f(n=9) =	65.31 μHz
F11	73.35 μHz	f(n=10)	f(n=10) =	73.35 μHz
F3	79.13 μHz	f(n=11)	f(n=11) =	79.13 μHz
F1	85.95 μHz	f(n=12)	f(n=12) =	85.95 μHz
F12	103.75 μHz	f(n=13) + 11.57	f(n=13) =	92.18 μHz
F9	105.08 μHz	f(n=13) + 11.57	f(n=13) =	93.51 μHz
F13	98.75 μHz	f(n=14)	f(n=14) =	98.75 μHz
F5	95.26 μHz	f(n=15) − 11.57	f(n=15) =	106.83 μHz
F7	112.26 μHz	f(n=16)	f(n=16) =	112.26 μHz
F6	101.21 μHz	f(n=16) − 11.57	f(n=16) =	112.78 μHz
F4	108.21 μHz	f(n=17) − 11.57	f(n=17) =	119.78 μHz
F8	116.02 μHz	f(n=18) − 11.57	f(n=18) =	127.59 μHz

Recalculating the fit based on all frequencies of order $8 \leq n \leq 18$, provides the following relation[10]:

$$f_{\rm obs2}(n) = 4.9(8) + n \times 6.77(6)\,\mu{\rm Hz}\,, \tag{5.9}$$

hence $\Delta\nu_{0,\rm obs2} = 6.77(6)\,\mu$Hz. The scatter of the observed frequencies relative to the predicted frequencies based on Eq. 5.9 is $\sigma_{\rm obs2} = 0.57\,\mu$Hz. The corresponding fit is shown in Fig. 5.13.

All the listed frequencies in Table 5.1 are through the above analysis explained as radial modes.

5.3.2 Second solution

If one does not stick to the autocorrelation function, but simply shifts a few observed frequencies by $\pm 11.574\,\mu$Hz, it is possible to find at least one additional solution for the large frequency separation in the range $\Delta\nu_{0,\rm expect} = 7.0(7)\,\mu$Hz (scaling prediction).

The result of these shifts in the frequency spectrum is shown in Table 5.3, and the corresponding frequency spectrum is shown in Fig. 5.14 (see caption). Both pairs, (F5, F4) and (F13, F1), are separated by more than the required frequency separation ($\delta\nu \simeq 1\,\mu$Hz), and hence could be non-radial modes. However, in the following calculation of the frequency separation based on all frequencies shown in Fig. 5.14, (F5, F4) and (F13, F1) are assumed to be non separable radial modes.

Calculating the fit based on all the frequencies of order $8 \leq n \leq 16$, provides the following relation[10]:

$$f_{\rm obs3}(n) = 2.6(9) + n \cdot 7.02(7)\,\mu{\rm Hz}\,, \tag{5.10}$$

[10]If two observed peaks are assigned to the same mode, their mean frequency is used in the fit.

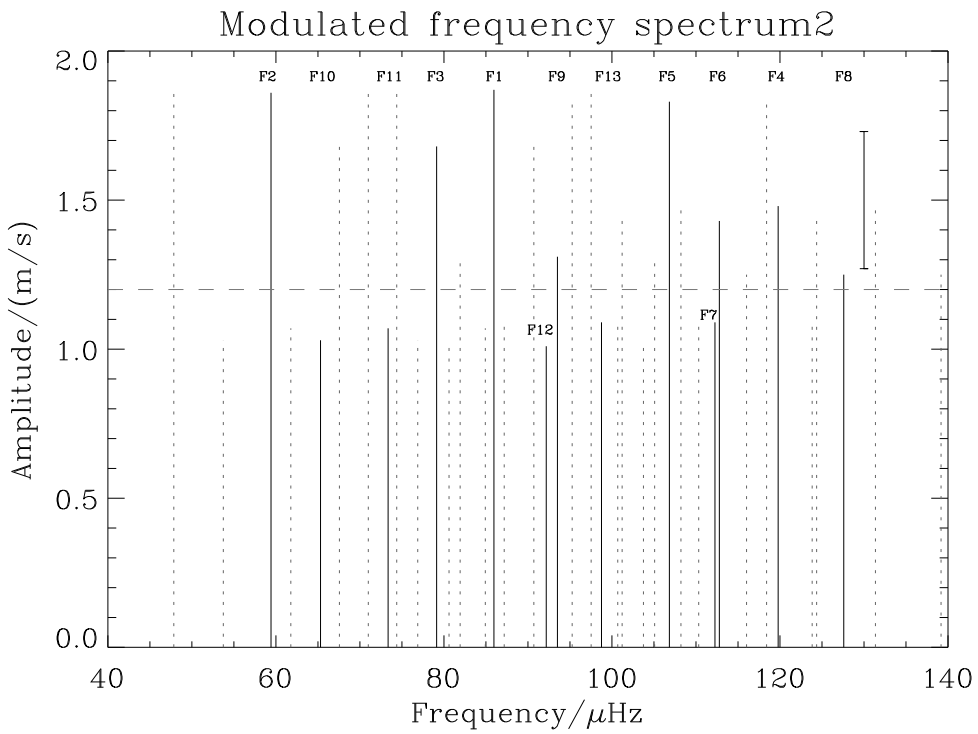

Figure 5.12: (See caption of Fig. 5.11). The following frequencies have been shifted (shift given in parenthesis): F4 ($+11.574\,\mu$Hz), F5 ($+11.574\,\mu$Hz), F6 ($+11.574\,\mu$Hz), F8 ($+11.574\,\mu$Hz), F9 ($-11.574\,\mu$Hz), and F12 ($-11.574\,\mu$Hz) with respect to the detected frequencies given in Table 5.1.

and hence gives $\Delta\nu_{0,\mathrm{obs3}} = 7.02(7)\,\mu$Hz. The scatter of the observed frequencies relative to the predicted frequencies based on Eq. 5.10 is $\sigma_{\mathrm{obs3}} = 0.54\,\mu$Hz. The corresponding fit is shown in Fig. 5.15.

5.3.3 Comparison and discussion of the two solutions

The large frequency separation ($\Delta\nu_{0,\mathrm{obs1}}$) based on only the first five frequencies (F2, F10, F11, F3, F1) is consistent with that based on all 13 frequencies ($\Delta\nu_{0,\mathrm{obs2}}$). This is indeed expected since the former were used to find the right ordering of all the observed frequencies in order to obtain $\Delta\nu_{0,\mathrm{obs2}}$. In the following only $\Delta\nu_{0,\mathrm{obs2}}$ and $\Delta\nu_{0,\mathrm{obs3}}$ will therefore be compared, designated as Case 2 and Case 3, respectively.

Based on the scatter of the observed frequencies modulated by alias shifting around their fits $f_{\mathrm{obs2}}(n)$ and $f_{\mathrm{obs3}}(n)$ ($\sigma_{\mathrm{obs2}} = 0.57\,\mu$Hz, $\sigma_{\mathrm{obs3}} = 0.54\,\mu$Hz), it is not possible to determine which of the two solutions is best. However, if only modes with a detection of S/N$>$ 4 (cf. Figs. 5.12, 5.14) are considered, differences can be seen. The scatter around the fits is now $\sigma_{\mathrm{obs2}} = 0.46$, and $\sigma_{\mathrm{obs3}} = 0.74$, which implies that $\Delta\nu_{0,\mathrm{obs2}} = 6.77(6)\,\mu$Hz gives a better fit to the high S/N peaks.

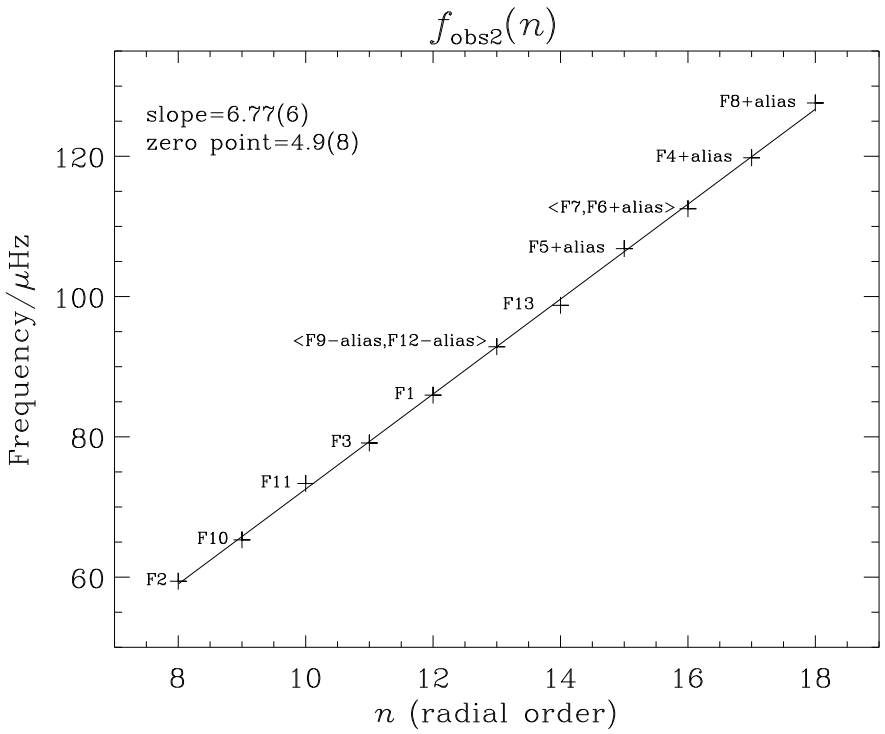

Figure 5.13: The observed frequencies with S/N > 3.4 plotted versus radial order n predicted by a pulsation model (cf. Sect. 5.3.4). Some frequencies are shifted by the daily alias as shown in Table 5.2. Closely spaced frequencies are averaged, providing 11 distinct frequencies of the total 13 detected (cf. Table 5.1).

A visualization of the goodness of fit of the two models is shown in Fig. 5.16, where the calculated frequencies based on Eqs. 5.9, 5.10 are compared to the observed amplitude spectrum. From Fig. 5.16, it is seen that the $\Delta\nu_{0,\mathrm{obs2}} = 6.77(6)\,\mu$Hz model fits the amplitude spectrum best for the most significant peaks, and therefore must be regarded as the most likely of the two possibilities.

It should be noted that the density of peaks, both center peaks and their sidebands, is high in the observed frequency spectrum (cf. Fig. 5.11). Therefore it is not surprising that more than one possible solution for the large frequency separation is found when the shifting of frequencies is allowed. Even though it can look like the separation is known with a small uncertainty, this result needs confirmation from extended observations, which should be based on a multi-site observing campaign in order to reduce the alias problems. In the following, both solutions will be compared to the theoretical frequency spectrum.

Table 5.3: Equally spaced frequencies for ξ Hya (Case 3)

Observed frequency		Expected mode	Interpreted frequency	
F2	59.27 μHz	f(n=8)	f(n=8) =	59.27 μHz
F10	65.96 μHz	f(n=9)	f(n=9) =	65.96 μHz
F11	73.35 μHz	f(n=10)	f(n=10) =	72.65 μHz
F3	79.34 μHz	f(n=11)	f(n=11) =	79.65 μHz
F1	85.95 μHz	f(n=12)	f(n=12) =	85.95 μHz
F13	98.75 μHz	f(n=12) + 11.57	f(n=12) =	87.18 μHz
F9	105.08 μHz	f(n=13) + 11.57	f(n=13) =	93.51 μHz
F6	101.21 μHz	f(n=14)	f(n=14) =	101.21 μHz
F7	112.26 μHz	f(n=14) + 11.57	f(n=14) =	100.69 μHz
F4	108.21 μHz	f(n=15)	f(n=15) =	108.21 μHz
F5	95.26 μHz	f(n=15) − 11.57	f(n=15) =	106.83 μHz
F8	116.02 μHz	f(n=16)	f(n=16) =	116.02 μHz
F12	103.75 μHz	f(n=16) − 11.57	f(n=16) =	115.32 μHz

5.3.4 Comparison with theory

Based on the evolutionary model which gives the best fit to ξ Hya (cf. Fig. 1.5, *thick solid line*, page 23), a pulsation model has been calculated (Teixeira, 2002) providing a model frequency spectrum for the radial modes ($l = 0$)[11]. The individual frequencies derived by the pulsation model are shown in Table 5.4.
For comparison, the asymptotic relation is fitted to the model spectrum. Fits to the frequencies with $8 \leq n \leq 18$ and to those with $8 \leq n \leq 16$ are calculated. These are then compared to the fits obtained from the observed frequencies (Eqs. 5.9, 5.10).

The fit to the model $8 \leq n \leq 18$ modes is

$$f_{\rm model2}(n) = 5.9(3) + n \times 7.24(2)\,\mu{\rm Hz}\,, \tag{5.11}$$

with a scatter around the fit of $\sigma_{\rm model2} = 0.21\,\mu$Hz. Based on the model $8 \leq n \leq 16$ modes, the fit is

$$f_{\rm model3}(n) = 6.3(3) + n \times 7.20(2)\,\mu{\rm Hz}\,, \tag{5.12}$$

with a scatter around the fit of $\sigma_{\rm model3} = 0.18\,\mu$Hz.

Determination of the asteroseismic mass

The ratios between observed and model frequency separations are:

$$\Delta\nu_{0,{\rm obs2}}/\Delta\nu_{0,{\rm model2}} = 0.9345(84) \tag{5.13}$$

$$\Delta\nu_{0,{\rm obs3}}/\Delta\nu_{0,{\rm model3}} = 0.975(11)\,. \tag{5.14}$$

Since $\Delta\nu_0 \propto \sqrt{\rho}$, the observations suggest that ξ Hya has a lower density than that predicted by the evolutionary model by a factor of 0.873(16) (case 2) and 0.950(21)

[11] It is expected that the radial p-modes will dominate the amplitude spectrum for giant stars (Dziembowski et al., 2001, Fig. 2). This has to be confirmed by a detailed theoretical investigation of ξ Hya's mode properties.

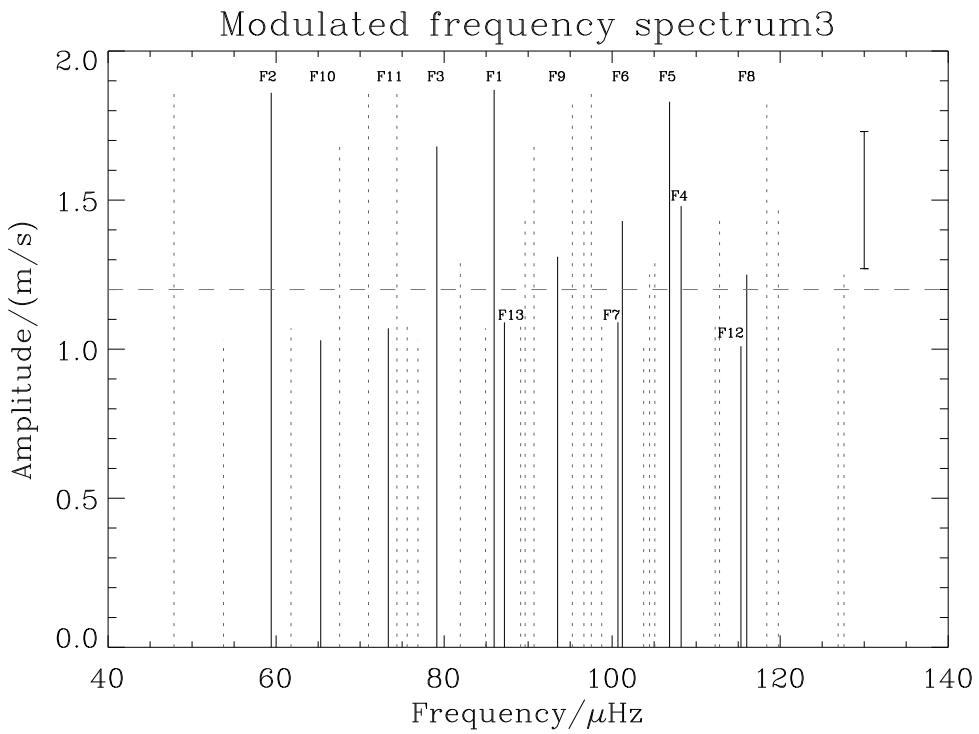

Figure 5.14: (See caption of Fig. 5.11). The following frequencies have been shifted (shift given in parenthesis): F5 ($+11.574\,\mu$Hz), F7 ($-11.574\,\mu$Hz), F9 ($-11.574\,\mu$Hz), F12 ($+11.574\,\mu$Hz), and F13 ($-11.574\,\mu$Hz) with respect to the detected frequencies given in Table 5.1.

(case 3), respectively. These numbers and the quoted mass and radius of ξ Hya (cf. Table 1.2) imply the following asteroseismic densities:

$$\begin{aligned} \text{Case2}: \quad \rho_{\xi\text{Hya}}/\rho_\odot &= 0.002384(37) \\ \text{Case3}: \quad \rho_{\xi\text{Hya}}/\rho_\odot &= 0.002593(51)\,, \end{aligned}$$

where $\rho_\odot = 1.390\,\text{g/cm}^3$. The deviation between the predicted and the observed density can be due to both an actual larger radius than quoted in this investigation and/or a lower mass. If the deviation is regarded as coming purely from an incorrect mass determination, the new mass would be: Case 2: $M/\text{M}_\odot = 2.68$, Case 3: $M/\text{M}_\odot = 2.92$. Fixing the mass at the adopted value, implies a change in the radius: Case 2: $R/\text{R}_\odot = 10.88$, Case 3: $R/\text{R}_\odot = 10.60$, which in both Case 2 and Case 3 is within the quoted error of the radius (cf. Table 1.2).

A lower mass could be in agreement with the possibility that ξ Hya is actually a helium core burning star rather that a hydrogen shell burning star which is the state assumed in the current evolution and pulsation models (see Fig. 1.5 page 23 and Fig. 1.6 page 24). In addition, a lower mass could also indicate that the evolutionary code should include some degree of overshoot, which is not the case in the current models (Christensen-Dalsgaard, 1982). An interferometric measurement

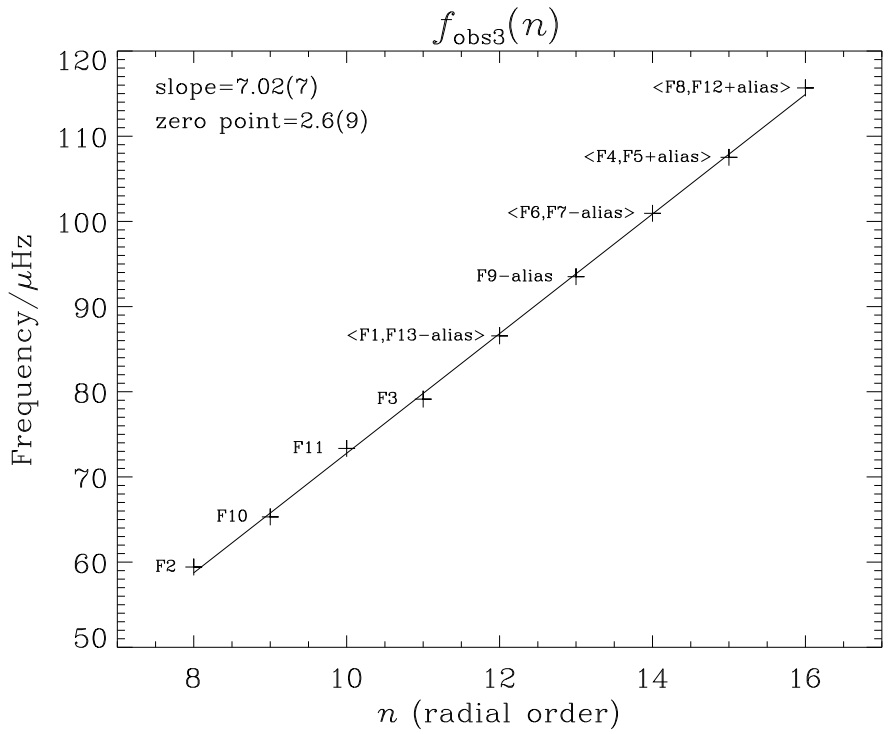

Figure 5.15: The observed frequencies with S/N > 3.4 plotted versus radial order n predicted by a pulsation model (cf. Sect. 5.3.4). Some frequencies are shifted by the daily alias as shown in Table 5.3. Closely spaced frequencies are averaged, providing 9 distinct frequencies of the total 13 detected (cf. Table 5.1).

of ξ Hya could provide a constraint on the radius[12] and hence, in combination with the asteroseismic results, also on the mass, which is not very well determined from fits with evolutionary tracks (cf. Sect. 1.5).

Estimating the damping time

In order to determine the absolute deviations between the observed and the theoretical frequencies, the theoretical frequencies are scaled with the derived ratios between observations and models (Eqs. 5.13, 5.14). Further, these scaled model frequencies are used to estimate the damping time of the oscillations in ξ Hya.

The new fit to the $8 \leq n \leq 18$ modes after scaling the model frequencies, using the density ratios, is

$$f_{\rm model2a}(n) = 5.5(3) + n \times 6.77(2)\,\mu{\rm Hz}\,, \tag{5.15}$$

with a scatter around the fit of $\sigma_{\rm model2a} = 0.20\,\mu$Hz. Compared to Eq. 5.9, a shift

[12] The precision of such measurement is expected to be $\lesssim 5\,\%$.

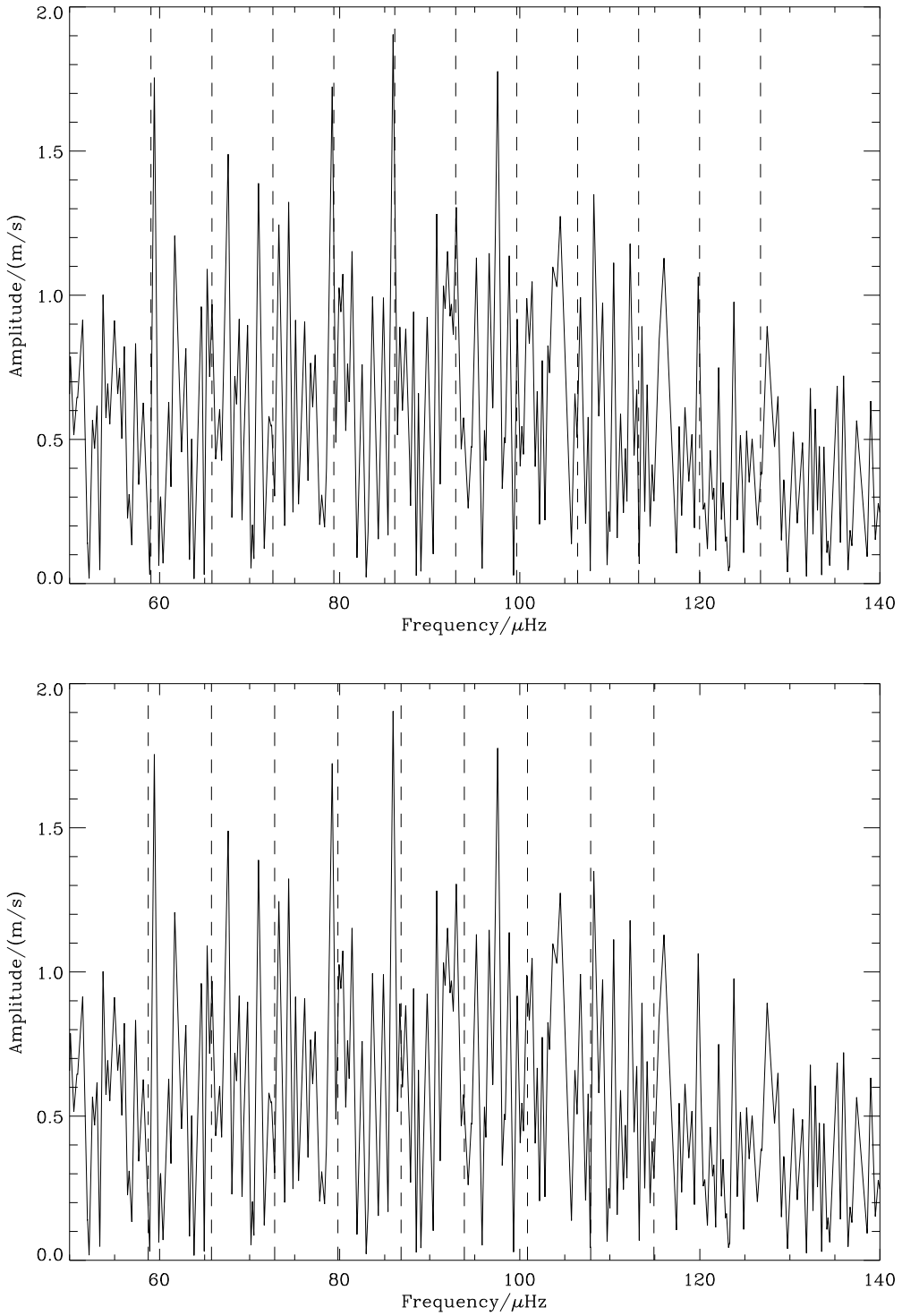

Figure 5.16: **Top panel:** Amplitude spectrum (similar to Fig. 5.5) compared to $f_{\rm obs2}(n) = 4.9(8)+n\cdot 6.77(6)\,\mu$Hz (*dashed lines*). **Bottom panel:** Amplitude spectrum compared to $f_{\rm obs3}(n) = 2.6(9) + n \cdot 7.02(7)\,\mu$Hz (*dashed lines*).

Table 5.4: Model frequencies for the radial modes ($M/\mathrm{M}_\odot = 3.07$, $Z = 0.019$, Age: 283.1 Myr)

Mode	Frequency
f(n=1)	11.70 μHz
f(n=2)	20.34 μHz
f(n=3)	28.10 μHz
f(n=4)	35.61 μHz
f(n=5)	43.21 μHz
f(n=6)	50.53 μHz
f(n=7)	57.23 μHz
f(n=8)	64.11 μHz
f(n=9)	71.33 μHz
f(n=10)	78.31 μHz
f(n=11)	85.26 μHz
f(n=12)	92.52 μHz
f(n=13)	99.87 μHz
f(n=14)	107.16 μHz
f(n=15)	114.42 μHz
f(n=16)	121.75 μHz
f(n=17)	129.15 μHz
f(n=18)	136.52 μHz
f(n=19)	143.81 μHz

of "model" − "observation"= 0.6 μHz on the absolute frequencies is found between observations and the scaled model frequencies. Based on the the $8 \leq n \leq 16$ modes the fit is

$$f_{\mathrm{model3a}}(n) = 6.2(3) + n \times 7.02(2)\,\mu\mathrm{Hz}\,, \tag{5.16}$$

with a scatter around the fit of $\sigma_{\mathrm{model3a}} = 0.17\,\mu$Hz. This fit should be compared to Eq. 5.10, which gives a shift on the absolute frequencies of "model" − "observation"= 3.6 μHz.

The larger shift for Case 3 does not necessarily imply that $\Delta\nu_{0,\mathrm{obs2}} = 6.77(6)\,\mu$Hz is a better solution. Shifts between model and observational frequencies in the solar case also deviate by several μHz for frequencies close to the acoustic cut-off (Balmforth, 1992). However, there is as yet no study on the extent to which a similar effect will occur for red giant stars, and hence no conclusions can be drawn on the deviation between observed and model frequencies.

The approximate scatter of the scaled model frequencies is in both Case 2 and Case 3 $\sim 0.19\,\mu$Hz, while the scatter for the observed frequencies is roughly $\sim 0.56\,\mu$Hz in both cases. The larger scatter for the observed frequencies is partly due to the intrinsic uncertainty in the frequency determination (σ_f) (cf. Eq. 5.5) which is $\sigma_f \sim 0.07\,\mu$Hz for a S/N in the range corresponding to the detected frequencies ($3.4 \leq$ S/N ≤ 6.2, cf. Table 5.1). The additional observed scatter of $0.52\,\mu$Hz could be due to a mode damping time shorter than the observation period. A short damping time would broaden the frequency peaks in the amplitude spectrum,

and hence the detected frequencies would scatter more. As a rough first estimate, the residual scatter of $0.52\,\mu$Hz could correspond to a damping time of ~ 22 days. The relation between damping time, peak broadening, and uncertainty in frequency determination should be investigated by simulations similar to those described in Sect. 5.2.1.

5.3.5 Simulation of peak validity

The validity of the detected frequencies has been tested with simulations. Twenty simulated time series similar to the observed time series but with different damping times are analysed using the same method as applied on the observed data set. When no damping is assumed (infinite damping time) and down to a damping time of approximately two weeks, $\sim 90\%$ of the detected peaks with S/N > 4.0 in the corresponding amplitude spectra are real, while the rest are aliases. As the damping time gets shorter, more aliases and additional spurious peaks are detected. For damping times of roughly one week, 20-50% of the detected frequencies are aliases, with a chance of detecting false peaks of $\sim$30%. These tests should however be confirmed by a more extensive simulation sample.

Based on the above simulations, the work of Houdek & Gough (2002), which predicts a damping time for ξ Hya of approximately three weeks, indirectly indicates that the frequencies in Table 5.1 with S/N > 4.0 are not likely to be affected very much by aliasing. However, the simulations which tests the damping time through the crowding of peaks in the amplitude spectrum (cf. Sect. 5.2.1) and the analysis of the scatter of observed and theoretical frequencies around the asymptotic relation (cf. Sect. 5.3.4) could indicate that the damping time is in fact shorter. This implies that aliasing could have a significant impact on the detected frequencies with S/N > 4.0.

5.3.6 Summary: The radial velocity time series

- The giant star ξ Hya shows the most firm evidence of solar-like oscillations in a highly evolved star (cf. Fig. 5.5).

- The predicted frequency of the highest peak in the amplitude spectrum of $93 \pm 15\,\mu$Hz (Eq. 1.4; cf. Table 1.2) is shown to be in excellent agreement with the power distribution in the observed amplitude spectrum (Fig. 5.5).

- The amplitude estimates from both the L/M and $1/g$ scaling relations (Eqs. 1.6, 1.7; cf. Table 1.2) are higher (a factor of 2.7 and 4.7, respectively) than the observed value of ~ 1.7 m/s. However, model calculations (Houdek & Gough, 2002) of the amplitude of the highest peaks yield a value in better agreement with observation. Based on these results, it can be concluded that the scaling relations do not in general apply for red giant stars such as ξ Hya.

- 11 or 9 individual frequencies are detected which can be explained as equally

spaced radial modes with a separation of $6.77 \pm 0.06\,\mu$Hz or $7.02 \pm 0.07\,\mu$Hz, in good agreement with the scaling-prediction ($7.0(7)\,\mu$Hz).

- The current data set is not good enough (due to alias problems) to conclude if non-radial modes are present in the data, and which large separation, if any, is the right one, though some indications favour $\Delta\nu_0 = 6.77 \pm 0.06\,\mu$Hz.
- Comparing the model and the observed frequencies indicates a density which is 10% lower than that of the model calculations.
- Due to uncertainty in the oscillation damping time, the validity of the individual detected frequencies is not exactly known. Detailed simulations are needed to estimate the validity of each detected frequency.

Chapter 6

Discussion and conclusion

This chapter will give a discussion of the results I have obtained and presented in this thesis. It will include concluding remarks and future prospects of what should be done to improve the current results in order to gain the full potential of asteroseismology on red giant stars.

The main result

The main result presented in this thesis, *the detection of solar-like oscillations in a giant star*, paves the road for the extension of the region of stars in the HR-diagram in which the asteroseismic tools known from solar-like stars can be applied.

This result has shown that red giant stars are promising targets for asteroseismic investigations, and this strongly suggests that *red giant stars should be taken into account during the target selection of the future asteroseismic space missions* like RØMER/MONS (Kjeldsen et al., 2000), COROT (Baglin & The COROT Team, 1998), and Eddington (an accepted ESA mission). Furthermore the new spectrograph HARPS, which will be installed at the ESO 3.6m telescope at La Silla in 2003, will be able to revolutionize asteroseismology and in particular red giant asteroseismology.

Because the current target star, ξ Hya, is much more evolved than the solar-like stars in which oscillations have been detected (cf. Fig. 1.3), the detection of solar-like oscillations in this star can give insight to how the asteroseismic properties of stars changes from the ZAMS to the red giant stars. This is in fact *the first time the scaling relations describing the characteristics of solar-like oscillations ($\nu_{\max}$, ν_0, $n_{\max}$, $v_{\rm osc}$; cf. Table 1.2) have all been tested with a firm detection of solar-like oscillations in a star so different from their scaling zero point, the Sun.*

The specific goals achieved

The goals of this investigation (cf. Sect. 1.3) have all been achieved, and the achievements are discussed in the following.

The amplitude spectrum of the time series shows a *clear excess of power* in a broad envelope centered at roughly $90\,\mu$Hz, similar to the power spectrum of the Sun. (cf. Fig. 5.5). This is in *very good agreement with the prediction* ($\Delta\nu_{\rm max} = 93(14)\,\mu$Hz), which is based on the assumption that the location in frequency space of the power excess scales with the acoustic cut-off frequency (Brown et al., 1991).

The amplitudes in velocity of the strongest modes are slightly below 2 m/s, which is significantly lower than the values predicted by the scaling relations using L/M (Kjeldsen et al., 1995) and $1/g$ (Kjeldsen & Bedding, 2001) (cf. Sect. 1.2.1).

Subsequent to the first publication of the results from this current investigation (Aerts et al., 2002; Frandsen et al., 2002) (**Paper I**), Houdek & Gough (2002) predicted the amplitude of the strongest mode of ξ Hya to be 2.3 m/s. Based on the result of Houdek & Gough (2002) and the observed amplitudes *it can be concluded that the scaling relations of Kjeldsen et al. (1995); Kjeldsen & Bedding (2001) do not in general apply to red giant stars like ξ Hya.*

If a shift of one daily alias ($11.57\,\mu$Hz) of a few frequencies is allowed *the observed frequencies can be explained by radial modes.* This is in good agreement with the predictions of Dziembowski et al. (2001), and to a large degree they *follow the asymptotic relation* (cf. Eq. 1.2). Using the frequency shifting, at least two fits to the asymptotic relation can be obtained and give
$f_{\rm obs2}(n) = (4.9(8)+6.77(6)\times n)\,\mu$Hz and $f_{\rm obs3}(n) = (2.6(9)+7.02(7)\times n)\,\mu$Hz, based on the order n from the model calculations made so far, if one includes only radial modes. Hence the *large separation* is $\Delta\nu_{\rm obs2} = 6.77(6)\,\mu$Hz or $\Delta\nu_{\rm obs3} = 7.02(7)\,\mu$Hz, which is in fairly good agreement with the first attempts at model calculations (cf. Sect. 5.3.4) and the scaling relation (cf. Eq. 1.3). The observed large separation corresponds to a mass of $M_2/M_\odot = 2.68$ or $M_3/M_\odot = 2.92$ using a fixed radius of $R/R_\odot = 10.4$.

The techniques

In order to achieve the goals discussed above, two independent data sets were obtained using two different techniques: the equivalent width data set obtained with DFOSC and the radial velocity data set obtained with the CORALIE spectrograph (cf. Chapter 2), the latter providing the evidence for solar-like oscillations in the target star ξ Hya presented in this thesis.

The very laborious reduction of the equivalent width data set, included *a new very high precision CCD linearity test* (cf. Sect. 3.1.2). The precision of this linearity test is at least 100 ppm in the entire intensity range of the CCD, and roughly 10 ppm in the intermediate range (3000-40000 ADU). This test can in principle be applied to any CCD used for observational programs requiring very high accuracy.

Despite, using different techniques to extract the equivalent width from the stellar spectra based on the DFOSC data set, no stellar oscillation signal has been

detected from this data set. This null result has two major explanations: 1) the stellar signal is 3-5 times smaller than expected, and 2) the noise level at the frequency range of the expected stellar signal is at least a factor of 3 larger than the photon noise (cf. Fig. 5.3). The extra instrumental noise introduced by drifts in DFOSC has been investigated, but no definite conclusion can be drawn on the origin of this noise based on the available data (cf. Sect. 4.1.3). It is evident that this extra noise is hidden in the raw data and it is not due to the data reduction method. However, there are indications that the cause is an unstable instrumental line profile, which excludes DFOSC as a suitable spectrograph for the detection of solar-like oscillations. A reasonable extension of the observation time will not reduce the noise to the desirable level (cf. Fig. 5.4).

Current limitations and future investigations

From the present data set and level of model calculations it cannot be determined if some of the detected frequencies are in fact due to non-radial modes. This is because the validity of the individual detected frequencies cannot be quantified, due to alias problems. The alias problems are strongly dependent on the damping, which cannot be measured accurately with the current data set.

If the damping time predicted by Houdek & Gough (2002) is adopted, limited simulations indicate that the detected frequencies with S/N > 4.0 are $\sim 90\%$ likely to be real, not aliases. This means that the frequencies are not likely to be shifted by one daily alias to the extent done in the current analysis (cf. Sect. 5.3). However, the large separation will not change significantly when no frequencies are shifted (Frandsen et al., 2002) (**Paper I**).

In addition to making more extended simulation tests than those used here, one could analyse whole surface integrated solar data (i.e. BiSON data), applying the same technique as the one used in the current investigation of oscillations in ξ Hya. Adopting a similar window and sampling relative to $\nu_{\mathrm{max},\odot}$ could provide a test of the effects of damping on the alias problems, and hence the validity of the detected peaks, by comparison with known solar results.

Both a multi-site observing campaign of ξ Hya and an extended observation period would be a significant improvement towards these ends in order to reduce the alias problem and to attain higher frequency resolution so that more closely spaced peaks and the damping time of the modes could be resolved.

The observational improvements should be accompanied by more thorough pulsation model calculations to provide a detailed frequency spectrum with relative amplitudes of individual radial and non-radial modes.

It has been shown that the exact evolutionary state of ξ Hya is not well known due to the very densely packed evolutionary tracks for stars at or near the red giant phase (cf. Fig. 1.2). It is argued that ξ Hya, from statistical considerations, is most likely a helium core burning star which has already passed the tip of the Hayashi track where the triple-alpha process ignites (cf. Fig. 1.6). However, the evolutionary

code available (Christensen-Dalsgaard, 1982) stops before the ignition of the triple-alpha process, hence the pulsation model for the helium core burning star has not been calculated.

An obvious improvement of the modeling would be to calculate a pulsation model for the helium core burning case. The likely dramatic changes in the core after the convection zone has penetrated deeply into the star just before helium ignition might result in a different frequency spectrum than the hydrogen burning core model used in this investigation. In addition, one could search for dredged up CN processed material in the stellar atmosphere in order to get indications of whether or not ξ Hya has passed the Hayashi track and hence has begun the dramatic mixing of the outer gas layers due to the deep convection zone in this phase (Wallerstein et al., 1994).

Furthermore, the degree of overshoot in the evolutionary model plays a significant role in the determination of mass and evolutionary state (cf. Fig. 1.6). This has to be investigated in more detail, and it might turn out that the degree of overshoot is distinguishable in the frequency spectrum and hence could be tested applying asteroseismology.

Yet another uncertainty in the modeling is the differences between different evolutionary codes. This is seen for example if one compares the evolutionary tracks based on the code of Christensen-Dalsgaard (1982) (cf. Fig. 1.5) with those of Girardi et al. (2000) (cf. Fig. 1.6). This problem also needs to be resolved.

In order to extend the current results, some possible targets are suggested in Table 6.1 below. These three targets fill in the rather large jump between ξ Hya and the solar-like region in the HR-diagram (cf. Fig. 6.1) and are in a similar phase as ξ Hya, but with masses closer to solar. All suggested targets are chosen so that a spectrograph similar to CORALIE should be able to make clear detection of oscillations based on the results already known from this instrument.

Clear detection of oscillations in these targets will provide a link from the more solar-like oscillation patterns as seen in e.g. the Sun or α Cen to the more puzzling frequency distribution as observed in ξ Hya. It could indicate trends of the mode characteristics which would strengthen the interpretations of how the asteroseismic parameters develop, and hence the stellar evolution of stars from at the ZAMS to the red giant phase.

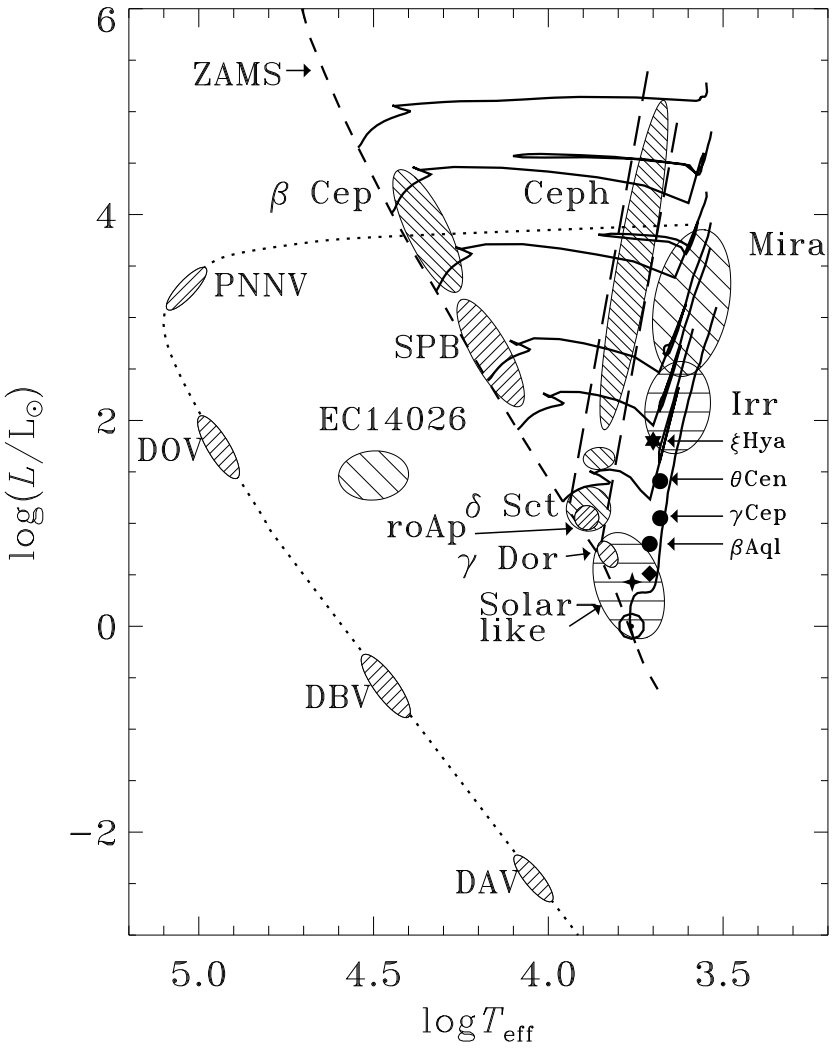

Figure 6.1: The Hertzsprung-Russell diagram with indicated names and approximate locations of known groups of variable stars. The diagonal and the two parallel vertical dashed lines indicate the ZAMS and the instability strip, respectively. Stellar evolutionary tracks of different masses are shown as thick solid lines. The single symbols to the right of the instability strip indicate the position of ξ Hya, the stars of Table 6.1, and a few solar-like stars (also indicated in Fig. 1.3). The stellar designations of these stars are (most luminous first): ξ Hydrae (six hooked star); θ Centauri, γ Cephei, β Aquilae (circles); δ Eridani (diamond); β Hydri (four hooked star); α Centauri and the Sun (both $\odot$). (The figure is slightly modified compared to the original, which has kindly been supplied by J. Christensen-Dalsgaard.).

Table 6.1: New suggested targets

Designation/Unit	Value & (error)		
Star ID/Name	HR 5288/θ Cen	HR 8974/γ Cep	HR 7602/β Aql
(RA J2000.5)	$14^h\ 06^m\ 40\overset{s}{.}8$	$23^h\ 39^m\ 22\overset{s}{.}1$	$19^h\ 55^m\ 20\overset{s}{.}3$
(Dec J2000.5)	$-36°\ 22'\ 12\overset{''}{.}0$	$+77°\ 38'\ 07\overset{''}{.}0$	$+06°\ 24'\ 29\overset{''}{.}0$
V/mag	2.06	3.21	3.71
Spectral type	K0 III	K1 III	G8 IV
$L/\mathrm{L}_\odot$	26(3)	11.1(4)	6.25(23)
$M/\mathrm{M}_\odot$	1.7(2)	1.67(19)	1.45(11)
T_{eff}/K	4790(70)	4750(100)	5090(50)
[Fe/H]	0.03(10)	-0.07(3)	-0.17(4)
v_{osc}/m/s[a]	3.6(6)	1.6(2)	1.0(1)
$\Delta\nu_0/\mu$Hz	8.5(8)	15.9(1.4)	28.1(1.6)
ν_{max}/μHz	101(13)	230(34)	450(40)
Maximum sample interval/minutes	~ 30	~ 10	~ 6

[a] The amplitude in velocity is estimated from the L/M scaling.

Bibliography

Aerts, C., Mass, T. Carrier, F., Burnet, M., de Medeiros, J., Bouchy, F., Frandsen, S., Stello, D., Kjeldsen, H., Christensen-Dalsgaard, J., Teixeira, T. C., Pijpers, F. P., & Bruntt, H. (2002). Ultrabass sounds of the giant star xi hya. first asteroseismological observation of a star very different from the sun. ESO PR 10/02.

Allen, C. W. (1973). *Astrophysical quantities*. London: University of London, Athlone Press, —c1973, 3rd ed.

Appourchaux, T., Fröhlich, C., Andersen, B., Berthomieu, G., Chaplin, W. J., Elsworth, Y., Finsterle, W., Gough, D. O., Hoeksema, J. T., Isaak, G. R., Kosovichev, A. G., Provost, J., Scherrer, P. H., Sekii, T., & Toutain, T. (2000). Observational Upper Limits to Low-Degree Solar g-Modes. ApJ, **538**, 401–414.

Baglin, A. & The COROT Team (1998). Asteroseismology from space - The COROT experiment. In *IAU Symp. 185: New Eyes to See Inside the Sun and Stars*, volume 185, pages 301+.

Bahcall, J. N. & Pinsonneault, M. H. (1992). Standard solar models, with and without helium diffusion and the solar neutrino problem. *Reviews of Modern Physics*, **64**, 885–926.

Baker, N. & Kippenhahn, R. (1962). The Pulsations of Models of δ Cephei Stars. With 17 Figures in the Text. *Zeitschrift Astrophysics*, **54**, 114+.

Balmforth, N. J. (1992). Solar Pulsational Stability - Part Two - Pulsation Frequencies. MNRAS, **255**, 632+.

Bedding, T. R., Kjeldsen, H., Reetz, J., & Barbuy, B. (1996). Measuring stellar oscillations using equivalent widths of absorption lines. MNRAS, **280**, 1155–1161.

Bedding, T. R., Butler, R. P., Kjeldsen, H., Baldry, I. K., O'Toole, S. J., Tinney, C. G., Marcy, G. W., Kienzle, F., & Carrier, F. (2001). Evidence for Solar-like Oscillations in β Hydri. ApJ, **549**, L105–L108.

Belmonte, J. A., Jones, A. R., Palle, P. L., & Roca Cortes, T. (1990). Global acoustic oscillations on α Bootis. ApJ, **358**, 595–609.

Blackwell, D. E. & Lynas-Gray, A. E. (1998). Determination of the temperatures of selected ISO flux calibration stars using the Infrared Flux Method. A&AS, **129**, 505–515.

Bouchy, F. & Carrier, F. (2001). P-mode observations on α Cen A. A&A, **374**, L5–L8.

Brewer, J. & Storm, J. (1999). *Observing at the Danish 1.54-m Telescope. A User's Manual for the TCS and DFOSC.* ESO, 1.10 edition. LSO-MAN-ESO-22100-00002.

Brown, T. M. & Gilliland, R. L. (1994). Asteroseismology. ARA&A, **32**, 37–82.

Brown, T. M., Gilliland, R. L., Noyes, R. W., & Ramsey, L. W. (1991). Detection of possible p-mode oscillations on Procyon. ApJ, **368**, 599–609.

Brown, T. M., Kennelly, E. J., Korzennik, S. G., Nisenson, P., Noyes, R. W., & Horner, S. D. (1997). A Radial Velocity Search for p-Mode Pulsations in η Bootis. ApJ, **475**, 322+.

Bruntt, H. (2002). Private communication.

Bruntt, H., Catala, C., Garrido, R., Rodríguez, E., Stütz, C., Knoglinger, P., Mittermayer, P., Bouret, J. C., Hua, T., Lignières, F., Charpinet, S., Van't Veer-Menneret, C., & Ballereau, D. (2002). Abundance analysis of targets for the COROT/MONS asteroseismology missions. I. Semi-automatic abundance analysis of the gamma Dor star HD 49434. A&A, **389**, 345–354.

Buzasi, D., Catanzarite, J., Laher, R., Conrow, T., Shupe, D., Gautier, T. N., Kreidl, T., & Everett, D. (2000). The Detection of Multimodal Oscillations on α Ursae Majoris. ApJ, **532**, L133–L136.

Carrier, F., Bouchy, F., Kienzle, F., Bedding, T. R., Kjeldsen, H., Butler, R. P., Baldry, I. K., O'Toole, S. J., Tinney, C. G., & Marcy, G. W. (2001). Solar-like oscillations in vec β Hydri: Confirmation of a stellar origin for the excess power. A&A, **378**, 142–145.

Carrier, F., et al. (2002). Poster. In *Asteroseismology across the HR diagram.* Kluwer Academic Publishers. in press.

Cayrel de Strobel, G., Soubiran, C., Friel, E. D., Ralite, N., & Francois, P. (1997). A catalogue of [Fe/H] determinations: 1996 edition. A&AS, **124**, 299–305.

Christensen-Dalsgaard, J. (1982). On solar models and their periods of oscillation. MNRAS, **199**, 735–761.

Christensen-Dalsgaard, J. (1995). Stellar Structure and Evolution. Lecture notes, Aarhus Universitet, August 1995, Fourth edition.

Christensen-Dalsgaard, J. (1998a). Stellar Oscillations. Lecture notes, Aarhus Universitet, February 1998, Fourth edition.

Christensen-Dalsgaard, J. (1998b). The 'Standard' Sun Modelling and Helioseismology. *Space Science Reviews*, **85**, 19–36.

Christensen-Dalsgaard, J. (2002). Helioseismology. Accepted for publication in Modern Phys. Rev.

Christensen-Dalsgaard, J. & Frandsen, S. (1983). Stellar 5 min oscillations. Sol. Phys., **82**, 469–486.

Cochran, W. D. (1988). Confirmation of radial velocity variability in Arcturus. ApJ, **334**, 349–356.

Cox, J. P. (1980). *Theory of stellar pulsation.* Research supported by the National Science Foundation Princeton, NJ, Princeton University Press, 1980. 393 p.

Cox, J. P., King, D. S., & Stellingwerf, R. F. (1972). Theoretical Pulsation Constants and Cepheid Masses. ApJ, **171**, 93+.

Dall, T. H. (2001). *Spectroscopic analysis of Delta Scuti stars.* Ph.D. thesis, Institut for Fysik og Astronomi, Aarhus Universitet.

di Benedetto, G. P. (1998). Towards a fundamental calibration of stellar parameters of A, F, G, K dwarfs and giants. A&A, **339**, 858–871.

Dziembowski, W. A., Gough, D. O., Houdek, G., & Sienkiewicz, R. (2001). Oscillations of α UMa and other red giants. MNRAS, **328**, 601–610.

Edmonds, P. D. & Gilliland, R. L. (1996). K Giants in 47 Tucanae: Detection of a New Class of Variable Stars. ApJ, **464**, L157–+.

Eggleton, P. P., Faulkner, J., & Flannery, B. P. (1973). An Approximate Equation of State for Stellar Material. A&A, **23**, 325+.

Flower, P. J. (1996). Transformations from Theoretical Hertzsprung-Russell Diagrams to Color-Magnitude Diagrams: Effective Temperatures, B-V Colors, and Bolometric Corrections. ApJ, **469**, 355+.

Frandsen, S., Carrier, F., Aerts, C., Stello, D., Maas, T., Burnet, M., Bruntt, H., Teixeira, T. C., de Medeiros, J., Bouchy, F., Kjeldsen, H., Pijpers, F., & Christensen-Dalsgaard, J. (2002). The detection of Solar-like oscillations in the G7 giant star ξ Hya. Submitted to A&A, (**Paper I**).

Fuhrmann, K., Axer, M., & Gehren, T. (1993). Balmer lines in cool dwarf stars. 1. Basic influence of atmospheric models. A&A, **271**, 451+.

Gabriel, A. H. & the GOLF Team (1998). Search for g-mode Frequencies in the GOLF Oscillations Spectrum. In *Structure and Dynamics of the Interior of the Sun and Sun-like Stars*, pages 61+.

Gilliland, R. L., Brown, T. M., Kjeldsen, H., McCarthy, J. K., Peri, M. L., Belmonte, J. A., Vidal, I., Cram, L. E., Palmer, J., Frandsen, S., Parthasarathy, M., Petro, L., Schneider, H., Stetson, P. B., & Weiss, W. W. (1993). A search for solar-like oscillations in the stars of M67 with CCD ensemble photometry on a network of 4 M telescopes. AJ, **106**, 2441–2476.

Girardi, L., Bressan, A., Bertelli, G., & Chiosi, C. (2000). Evolutionary tracks and isochrones for low- and intermediate-mass stars: From 0.15 to 7 $M_{\odot}$, and from Z=0.0004 to 0.03. A&AS, **141**, 371–383.

Glebocki, R., Gnacinski, P., & Stawikowski, A. (2000). Catalog of Projected Rotational Velocities. *Acta Astronomica*, **50**, 509–515.

Goldreich, P. & Keeley, D. A. (1977). Solar seismology. II - The stochastic excitation of the solar p-modes by turbulent convection. ApJ, **212**, 243–251.

Gray, D. F. (1992). *The observation and analysis of stellar photospheres.* Cambridge Astrophysics Series, Cambridge: Cambridge University Press, 1992, 2nd ed., ISBN 0521403200.

Gray, D. F. & Nagel, T. (1989). The granulation boundary in the H-R diagram. ApJ, **341**, 421–426.

Guenther, D. (2001). Asteroseismology of subgiants. *Proceedings of the SOHO 10/GONG 2000 Workshop: Helio- and asteroseismology at the dawn of the millennium, 2-6 October 2000, Santa Cruz de Tenerife, Tenerife, Spain. Edited by A. Wilson, Scientific coordination by P. L. Pallé. ESA SP-464, Noordwijk: ESA Publications Division, ISBN 92-9092-697-X, 2001, p. 379 - 383*, **464**, 379+.

Guenther, D. B., Demarque, P., Buzasi, D., Catanzarite, J., Laher, R., Conrow, T., & Kreidl, T. (2000). Evolutionary Model and Oscillation Frequencies for α Ursae Majoris: A Comparison with Observations. ApJ, **530**, L45–L48.

Hatzes, A. P. & Cochran, W. D. (1993). Long-period radial velocity variations in three K giants. ApJ, **413**, 339–348.

Hatzes, A. P. & Cochran, W. D. (1994a). Short-period radial velocity variations of α Bootis: Evidence for radial pulsations. ApJ, **422**, 366–373.

Hatzes, A. P. & Cochran, W. D. (1994b). The radial velocity variability of the K giant β Ophiuchi. 1: The detection of low-amplitude, short-period pulsations. ApJ, **432**, 763–769.

Hatzes, A. P. & Cochran, W. D. (1998). Stellar Oscillations in K Giant Stars. In *ASP Conf. Ser. 154: Cool Stars, Stellar Systems, and the Sun*, volume 10, pages 311+.

Henry, G. W., Fekel, F. C., Henry, S. M., & Hall, D. S. (2000). Photometric Variability in a Sample of 187 G and K Giants. ApJS, **130**, 201–225.

Hoffleit, D. & Jaschek, C. (1982). *The Bright Star Catalogue*. The Bright Star Catalogue, New Haven: Yale University Observatory (4th edition), 1982.

Horner, S. (1996). A Search for Pulsations in Four Late-Type Giants. ApJ, **460**, 449+.

Houdek, G. & Gough, D. O. (2002). Modelling pulsation amplitudes of ξ Hydrae. *Submitted to* MNRAS.

Houdek, G., Balmforth, N. J., Christensen-Dalsgaard, J., & Gough, D. O. (1999). Amplitudes of stochastically excited oscillations in main-sequence stars. A&A, **351**, 582–596.

Iben, I. (1967). Stellar evolution within and of the main sequence. *ARA&A*, **5**, 571–626.

Iglesias, C. A., Rogers, F. J., & Wilson, B. G. (1992). Spin-orbit interaction effects on the Rosseland mean opacity. ApJ, **397**, 717–728.

Kjeldsen, H. (1992). *High-precision photometry*. Ph.D. thesis, Institut for Fysik og Astronomi, Aarhus Universitet.

Kjeldsen, H. & Bedding, T. R. (1995). Amplitudes of stellar oscillations: the implications for asteroseismology. A&A, **293**, 87–106.

Kjeldsen, H. & Bedding, T. R. (2001). Current status of asteroseismology. *Proceedings of the SOHO 10/GONG 2000 Workshop: Helio- and asteroseismology at the dawn of the millennium, 2-6 October 2000, Santa Cruz de Tenerife, Tenerife, Spain. Edited by A. Wilson, Scientific coordination by P. L. Pallé. ESA SP-464, Noordwijk: ESA Publications Division, ISBN 92-9092-697-X, 2001, p. 361 - 366*, **464**, 361+.

Kjeldsen, H., Bedding, T. R., Viskum, M., & Frandsen, S. (1995). Solarlike oscillations in η Boo. AJ, **109**, 1313–1319.

Kjeldsen, H., Bedding, T. R., Frandsen, S., & dall, T. H. (1999a). A search for solar-like oscillations and granulation in alpha CEN A. MNRAS, **303**, 579–587.

Kjeldsen, H., Bedding, T. R., Frandsen, S., dall, T. H., Thomsen, B., Christensen-Dalsgaard, J., Clausen, J. V., Petersen, J. O., & Andersen, M. I. (1999b). MONS: A Proposal for a Danish Satellite. In *ASP Conf. Ser. 173: Stellar Structure: Theory and Test of Connective Energy Transport*, pages 353+.

Kjeldsen, H., Bedding, T. R., & Christensen-Dalsgaard, J. (2000). MONS: Measuring Oscillations in Nearby Stars. In *ASP Conf. Ser. 203: IAU Colloq. 176: The Impact of Large-Scale Surveys on Pulsating Star Research*, pages 73+.

Knudsen, M. R. (2000). *Measuring oscillations in the roAp star HR1217 using echelle-spectroscopy. An oblique pulsator in a new perspective.* Master's thesis, Institut for Fysik og Astronomi, Aarhus Universitet.

Leighton, R. B., Noyes, R. W., & Simon, G. W. (1962). Velocity Fields in the Solar Atmosphere. I. Preliminary Report. ApJ, **135**, 474+.

Lejeune, T., Cuisinier, F., & Buser, R. (1998). A standard stellar library for evolutionary synthesis. II. The M dwarf extension. A&AS, **130**, 65–75.

Loumos, G. L. & Deeming, T. J. (1978). Spurious results from Fourier analysis of data with closely spaced frequencies. Ap&SS, **56**, 285–291.

Mallik, S. V. (1999). Lithium abundance and mass. A&A, **352**, 495–507.

Martić, M., Schmitt, J., Lebrun, J.-C., Barban, C., Connes, P., Bouchy, F., Michel, E., Baglin, A., Appourchaux, T., & Bertaux, J.-L. (1999). Evidence for global pressure oscillations on Procyon. A&A, **351**, 993–1002.

Matthews, J. M., Kuschnig, R., Walker, G. A. H., Pazder, J., Johnson, R., Skaret, K., Shkolnik, E., Lanting, T., Morgan, J. P., & Sidhu, S. (2000). Ultraprecise Photometry from Space: The MOST Microsat Mission. In *ASP Conf. Ser. 203: IAU Colloq. 176: The Impact of Large-Scale Surveys on Pulsating Star Research*, pages 74–75.

McLean, I. S. (1996). *Electronic imaging in astronomy. Detectors and instrumentation.* Chichester, UK Wiley, 1996 Physical description xxx, 472 p. Series Wiley-PRAXIS series in astronomy and astrophysics Published in association with Praxis Publishing, Chichester ISBN0471969710.

McWilliam, A. (1990). High-resolution spectroscopic survey of 671 GK giants. I - Stellar atmosphere parameters and abundances. ApJS, **74**, 1075–1128.

Mermilliod, J.-C., Mermilliod, M., & Hauck, B. (1997). The General Catalogue of Photometric Data (GCPD). II. A&AS, **124**, 349–352.

O'Toole, S. J., Bedding, T. R., Kjeldsen, H., Dall, T. H., & Stello, D. (2002). Time-series spectroscopy of pulsating sdB stars - II. Velocity analysis of PG1605+072. MNRAS, **334**, 471, (**Paper II**).

Pasquini, L., de Medeiros, J. R., & Girardi, L. (2000). Ca II activity and rotation in F-K evolved stars. A&A, **361**, 1011–1022.

Perryman, M. A. C., Lindegren, L., Kovalevsky, J., Hoeg, E., Bastian, U., Bernacca, P. L., Crézé, M., Donati, F., Grenon, M., van Leeuwen, F., van der Marel, H., Mignard, F., Murray, C. A., Le Poole, R. S., Schrijver, H., Turon, C., Arenou, F., Froeschlé, M., & Petersen, C. S. (1997). The HIPPARCOS Catalogue. A&A, **323**, L49–L52.

Pijpers, F. P. (2002). Private communication.

Queloz, D., Casse, M., & Mayor, M. (1999). The Fiber-Fed Spectrograph, a Tool to Detect Planets. In *ASP Conf. Ser. 185: IAU Colloq. 170: Precise Stellar Radial Velocities*, pages 13–+.

Rasmussen, M. B. & Dall, T. H. (2001). *Reducing Echelle Spectra using IRAF. The official five-minute guide*. Institut for Fysik og Astronomi, Aarhus Universitet, 1.8 edition.

Sandage, A. R. & Tammann, G. A. (1968). A composite period-luminosity relation for Cepheids at mean and maximum light. ApJ, **151**, 531.

Smith, P. H., McMillan, R. S., & Merline, W. J. (1987). Evidence for periodic radial velocity variations in Arcturus. ApJ, **317**, L79–L84.

Sperl, M. (1998). *Manual for Period98: A period search-program for Windows and Unix*, v1.0.4 edition.

Stello, D. (2000a). Detection of oscillations on α Ursae Majoris? Internal report.

Stello, D. (2000b). The problem of the Pleiades distance. Constraints from nearby field stars. Internal report.

Stello, D. & Nissen, P. E. (2001). The problem of the Pleiades distance. Constraints from Strömgren photometry of nearby field stars. A&A, **374**, 105–115, (**Paper III**).

Tassoul, M. (1980). Asymptotic approximations for stellar nonradial pulsations. ApJS, **43**, 469–490.

Teixeira, T. C. (2002). Private communication; work in progress.

Toutain, T. & Froehlich, C. (1992). Characteristics of solar p-modes - Results from the IPHIR experiment. A&A, **257**, 287–297.

Ulrich, R. K. (1986). Determination of stellar ages from asteroseismology. ApJ, **306**, L37–L40.

Walker, G. A. H., Yang, S., Campbell, B., & Irwin, A. W. (1989). Yellow giants - A new class of radial velocity variable? ApJ, **343**, L21–L24.

Wallerstein, G., Bohm-Vitense, E., Vanture, A. D., & Gonzalez, G. (1994). The lithium content and other properties of F2-G5 giants in the Hertzsprung Gap. AJ, **107**, 2211–2221.

Winget, D. E., Nather, R. E., Clemens, J. C., Provencal, J., Kleinman, S. J., Bradley, P. A., Wood, M. A., Claver, C. F., Frueh, M. L., Grauer, A. D., Hine, B. P., Hansen, C. J., Fontaine, G., Achilleos, N., Wickramasinghe, D. T., Marar, T. M. K., Seetha, S., Ashoka, B. N., O'Donoghue, D., Warner, B., Kurtz, D. W., Buckley, D. A., Brickhill, J., Vauclair, G., Dolez, N., Chevreton, M., Barstow, M. A., Solheim, J. E., Kanaan, A., Kepler, S. O., Henry, G. W., & Kawaler, S. D. (1991). Asteroseismology of the DOV star PG 1159 - 035 with the Whole Earth Telescope. ApJ, **378**, 326–346.

Appendix A

Stability of the DFOSC flat field lamp

This appendix shows the results of the stability test of the DFOSC flat field lamp which was used in the CCD linearity test in Sect. 3.1.2.

Since the linearity test only used the 12s and 40s exposures from each linearity sequence (3×1s, 3×3s, 3×12s, 3×40s, 3×12s, 3×3s, 3×1s, 3×0s), only these are used in the following test. Each group of three images is medial filtered to one image per exposure time and corrected for overscan and bias (cf. Sect. 3.1.1). The total amount of detected counts is calculated for each image and divided by the requested exposure time (12s or 40s). Normalized by their common mean value, these relative counts are plotted versus time (cf. Fig. A.1).

When linearity test images were made, it was mostly in multiple sequences of 3-6 sequences (cf. Table 2.2, page 33) that covered 2-3 hours. Thus it was possible to detect intensity variations in the DFOSC flat field lamp over a few hours.

The largest variability of the flat field lamp during multiple linearity sequences made on a single day was observed on 16/03/00 which included a total of four sequences. Fig. A.1 shows the relative counts of the 12s and 40s exposures versus a time axis from all linearity sequences made on 16/03/00. The 12s exposures (*plus* symbols) fall clearly below the 40s exposures (*square* symbols) due to dead time. The dead time introduces an error in the expected relative exposure time (12s/40s) of $\sim 0.25\%$, which is $\sim 30\,\mathrm{msec}$. This has an effect in the inversion process used to calculate the gain from measured *gain ratio maps* (cf. Sect. 3.1.2, page 52). In addition, one can see a clear trend of increasing intensity from the first to the last linearity sequence. This trend was observed for all linearity sequences, though the one plotted in Fig. A.1 is the most pronounced. The increasing intensity with time is clear evidence that the flat field lamp is heating up, which seems to take approximately 2 hours to reach maximum intensity, after which a smaller variation around the equilibrium is expected.

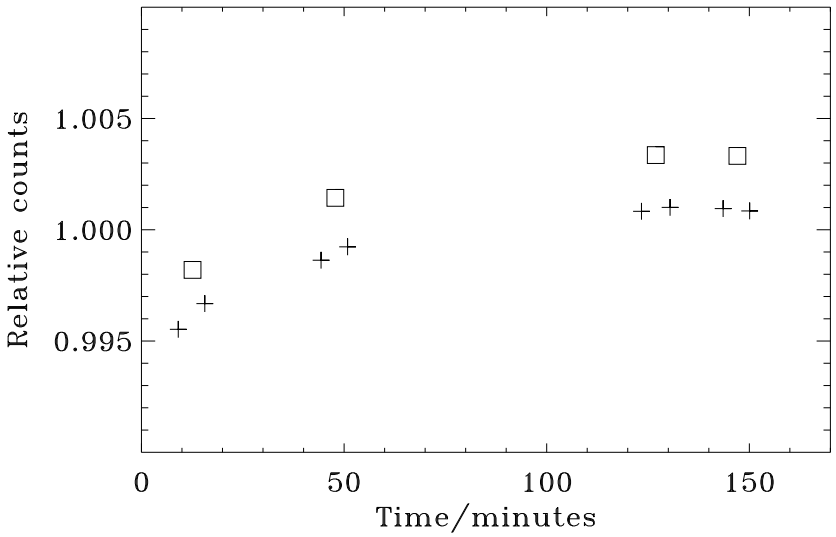

Figure A.1: Relative number of counts of twelve linearity images obtained on 16/03/00 each divided by their corresponding exposure time, showing a drift of the flat field lamp during the four sequences made that day. The *plus* symbols indicate 12s exposures and the *square* symbols are 40s exposures. Each measurement is the total amount of detected counts, normalized to 1.0, of the median filtered image which is bias and overscan corrected.

All linearity sequences were performed before the flat field lamp had reached its maximum intensity, and this affects the linearity test via drifts of the 1D intensity curves used to create the gain ratio maps (cf. Fig. 3.5, page 48). These drifts would presumably be significantly smaller if the linearity sequences were started after the flat field lamp had been turned on for a few hours.

Paper I:

Detection of solar-like oscillations in the G7 giant star ξ Hya

S. Frandsen, F. Carrier, C. Aerts, D. Stello, T. Maas, M. Burnet, H. Bruntt, T.C. Teixeira, J.R. de Medeiros, F. Bouchy, H. Kjeldsen, F. Pijpers, & J. Christensen-Dalsgaard, A&A, *submitted*, (2002)

Astronomy & Astrophysics manuscript no. August 19, 2002
(DOI: will be inserted by hand later)

Detection of Solar-like Oscillations in the G7 Giant Star ξ Hya*

S. Frandsen[1], F. Carrier[2], C. Aerts[3], D. Stello[1], T. Maas[3], M. Burnet[2], H. Bruntt[1], T. C. Teixeira[4,1], J. R. de Medeiros[5], F. Bouchy[2], H. Kjeldsen[1,6], F. Pijpers[1,6], and J. Christensen-Dalsgaard[1,6]

[1] Institut for Fysik og Astronomi, Aarhus Universitet, Universitetsparken, Bygn. 520, DK-8000 Aarhus C, Denmark
e-mail: srf@ifa.au.dk
[2] Observatoire de Genève, 51 chemin de Maillettes, CH-1290 Sauverny, Switzerland
e-mail: fabien.carrier@obs.unige.ch
[3] Katholieke Universiteit Leuven, Instituut voor Sterrenkunde, Celestijnenlaan 200 B, B - 3001 Leuven, Belgium
e-mail: conny@ster.kuleuven.ac.be
[4] Centro de Astrofísica da Universidade do Porto, Portugal
[5] Departamento de Física, Universidade Federal do Rio Grande do Norte, 59072-970, Natal, RN, Brazil
[6] Teoretisk Astrofysik Center, Danmarks Grundforskningsfond

Received ; accepted

Abstract. We report the first firm discovery of solar-like oscillations in a giant star. We monitored the star ξ Hya (G7III) continuously during one month with the CORALIE spectrograph attached to the 1.2m Swiss Euler telescope. The 433 high-precision radial-velocity measurements clearly reveal multiple oscillation frequencies in the range 50 – 130 μHz, corresponding to periods between 2.0 and 5.5 hours. The amplitudes of the strongest modes are slightly smaller than $2\,\mathrm{m\,s^{-1}}$. Current model calculations are compatible with the detected modes.

Key words. asteroseismology – solar type oscillations – giant stars

1. Introduction

Doppler studies with high-precision instruments and reduction algorithms have been refined dramatically, mainly in the framework of the search for exoplanets. These refinements have led to a breakthrough in the observations of solar-type oscillations, which have now been found repeatedly (Procyon, Martic et al. 1999; β Hyi, Bedding et al. 2001; α Cen A, Bouchy & Carrier 2001; δ Eri, Carrier et al. 2002). The signal-to-noise ratio (S/N) in the oscillation frequency spectra is, for each of these cases, so good that the resemblance with the solar oscillation spectrum is obvious.

Observations of solar-like oscillations in the giant star α UMa have been claimed by Buzasi et al. (2000), based upon space photometry gathered with the star tracker of the WIRE satellite. However, the interpretation of these reported oscillations frequencies is not straightforward. Guenther et al. (2000) find a possible solution in terms of a sequence of radial modes with a few missing orders for a star of 4.0–4.5 $M_\odot$. The observations are not supported by theoretical calculations by Dziembowski et al. (2001).

Velocity observations of Arcturus provide evidence for solar-type oscillations with periods from 1.7 to 8.3 days and a frequency separation of evenly spaced modes of $\Delta\nu \sim 1.2$ μHz (Merline, 1999).

In this *Letter*, we provide clear and unambiguous evidence of the presence of solar-type oscillations in the giant star ξ Hya ($m_V = 3.54$). This star has a mass close to $M = 3.0\,M_\odot$, and is thus considerably heavier than the Sun. Moreover, its luminosity amounts to $L \sim 61\,L_\odot$ and its effective temperature $T_{\rm eff} = 5000$ K, which places the star among the giants. In the current *Letter* we present the first results of our study. Detailed modelling will be presented, when completed, in a subsequent paper.

2. The radial-velocity measurements

The ξ Hya observations were made during one full month (2002 February 18 - March 18) with CORALIE, the high-resolution fiber-fed echelle spectrograph (Queloz et al. 2001) mounted on the 1.2-m Swiss telescope at La Silla (ESO, Chile). During the stellar exposures, the spectrum of a thorium lamp carried by a second fiber is simultaneously recorded in order to monitor the spectrograph's stability and thus to obtain high-precision velocity measure-

Send offprint requests to: S. Frandsen
* Based on observations obtained with the CORALIE spectrograph on the 1.2-m Swiss Euler telescope at La Silla, Chile.

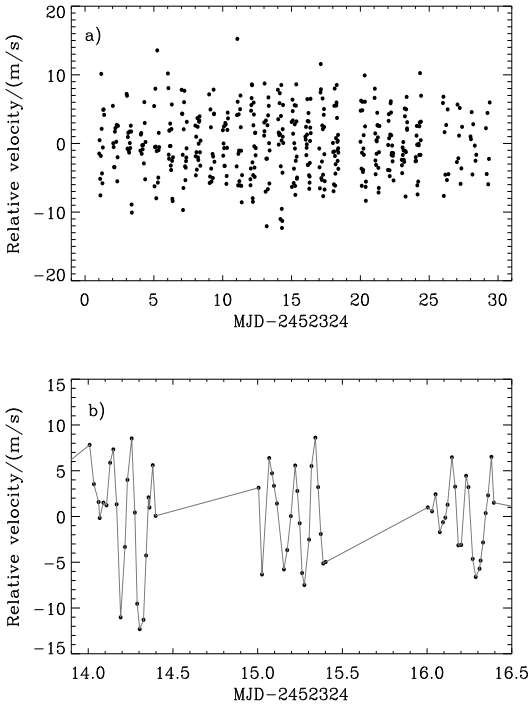

Fig. 1. Radial-velocity measurements of ξ Hya. The dispersion reaches 4.6 m s^{-1}. **a)** The whole time string; **b)** zoom of a small part of the time series.

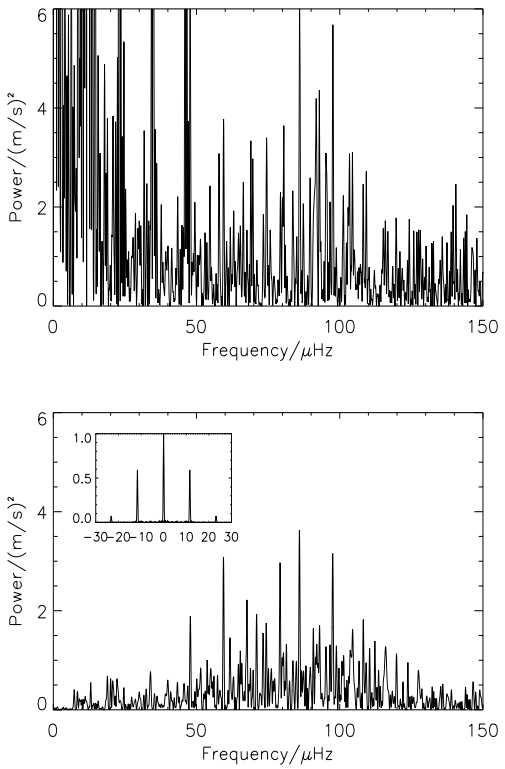

Fig. 2. Power spectrum for ξ Hya. Modes are clearly present in the range 50–130 μHz, corresponding to periods of 2.0-5.5 hours. The upper panel is the power spectrum of the time series using one single spectrum as the reference. The lower panel is for the time series derived using one reference spectrum per night.

ments. The spectra were extracted at the telescope, using the INTER-TACOS (INTERpreter for the Treatment, the Analysis and the COrrelation of Spectra) software package developed by D. Queloz and L. Weber at the Geneva Observatory (Baranne et al. 1996). The wavelength coverage of these spectra is 3875-6820 Å, recorded on 68 orders. By taking about 2 measurements every hour, a total of 433 optical spectra was collected. The exposure times were typically 180 s and the S/N ratio for all spectra was in the range of 110–230 at 550 nm.

By the use of the optimum-weight procedure (Bouchy et al. 2001), radial velocities are computed for each night relative to the highest S/N spectrum obtained in the middle of the night. This method requires a Doppler shift that remains small compared to the line-width (smaller than 100 m s^{-1}) (Bouchy & Carrier 2001). Since the Earth's motion can introduce a Doppler shift larger than 800 m s^{-1} during a whole night, each spectrum is first corrected for the Earth's motion before deriving the radial velocities. This is achieved by shifting all spectra with the Earth's velocity at the time of observation and by subsequent rebinning, so that the spectra all have the same wavelength values. The mean radial velocity for each night is then subtracted. The resulting velocities are shown in Fig. 1. The rms scatter of the time series is 4.6 m s^{-1} and is largely due to the oscillations. The mean error on each measurement is 2.3 m s^{-1}.

3. Time-series analysis

The power spectrum of the 433 data points is presented in Fig. 2. In order to show that the excess power in the lower panel in the range 50–130 μHz is not due to elimination of power at low frequencies by the reduction procedure, we show a power spectrum in the upper panel where no correction for drift has been applied. Although more noisy the increase in power between 50 μHz and 130 μHz is also evident in the upper panel. A set of oscillation modes is clearly present, with a power distribution that is remarkably similar to that seen in the Sun and other stars on or near the main sequence, although obviously at much lower frequency. The spectrum displays the characteristic near-uniform spacing of the dominant peaks.

To characterize this pattern we have calculated the autocorrelation of the power spectrum. In order to eliminate the effect of the noise, we have ignored all points with amplitudes below a given threshhold (1.2 m s^{-1}). In Fig. 3 the alias at 1 c/d stands out clearly, but in addition a spacing $\Delta\nu \sim 6.8$ μHz is present in the power spectrum. This is consistent with the visual impression of a regular pattern present in the the power spectrum (Fig. 2).

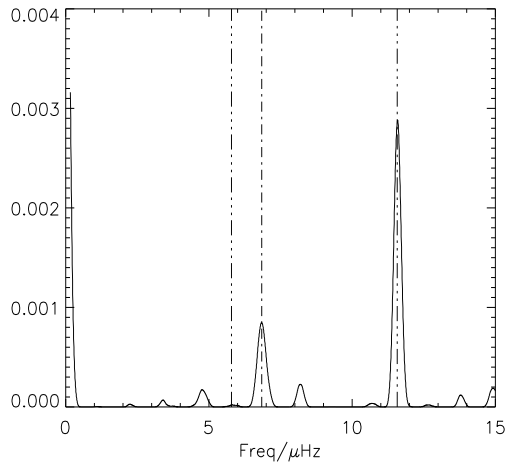

Fig. 3. Autocorrelation of the power spectrum for ξ Hya. All points with amplitude $v < 1.2$ m s^{-1}have been set to zero. The dash-dot-dot-dot vertical lines mark the position of the 11.574 μHz daily alias and half of it, and the dash-dot line indicates the peak pointing to a frequency spacing of 6.8 μHz.

The expected velocity amplitude for solar-like oscillations scales as L/M according to Kjeldsen & Bedding (1995). Using the stellar parameters from Sect. 4 and a mass of 3.0 $M_\odot$ (Sect. 4) we find $v_{\rm osc,pred} = 4.6\,{\rm m\,s^{-1}}$. The observed amplitudes in Fig. 2 are only about one third of this prediction. Recent calculations by Houdek & Gough (2002), however, indicate that the simple scaling law of Kjeldsen & Bedding (1995) does indeed not apply. They predict a velocity amplitude $v = 2.3\,{\rm m\,s^{-1}}$, slightly higher than the ones observed by us for ξ Hya.

The stochastic nature of solar-like oscillations implies that a timestring of radial velocities cannot be expected to be a set of coherent oscillations and can therefore not be reproduced perfectly by a sum of sinusoidal terms. As a starting point it is nevertheless a good assumption to try to fit the radial-velocity data of ξ Hya by such a set of functions, as the lifetimes are expected to exceed the length of the observing run (Houdek & Gough 2002). We have performed an iterative fit using different methods, among which Period98 (Sperl 1998) and a procedure by Frandsen et al. (2001). A signal with a S/N above 4 is detected at 9 frequencies. When a fit based upon these 9 frequencies is removed from the time series, 5 additional peaks still occur but with a too low S/N to accept them without additional confirmation (hence we do not list them). After removing the 14 frequencies, only a noise spectrum is left. The results for the 9 frequencies are presented in Table 1, where the S/N indicated is calculated from the remaining noise in the amplitude spectrum at the position of each mode. The noise is slightly higher in the range of the modes than at high frequencies, where $\sigma = 0.2\,{\rm m\,s^{-1}}$. The frequencies of the modes with amplitudes above $1.5\,{\rm m\,s^{-1}}$, i.e., of the five highest-amplitude modes, are unambiguous. Dividing

Table 1. Oscillation frequencies detected in the radial velocities of ξ Hya ordered by amplitude. Formal errors of the fit are given in parenthesis as errors of the last digits. The S/N is calculated by dividing the amplitude by the noise in a 10 μHz bin in the residual spectrum centered on the frequency of the mode. Frequencies in italic indicate modes, where the frequency detection methods disagree on the correct alias.

ID	Frequency		Amplitude	S/N
	c/d	μHz	m s^{-1}	
F1	5.1344(26)	59.43	1.85(23)	6.6
F2	6.8366(27)	79.13	1.84(23)	5.8
F3	7.4265(29)	85.96	1.76(23)	5.3
F4	8.2318(32)	95.28	1.65(23)	5.1
F5	9.3507(33)	108.22	1.59(23)	6.0
F6	*8.7399(36)*	101.16	1.36(22)	4.5
F7	10.0287(43)	116.07	1.25(23)	5.0
F8	*9.0831(44)*	105.13	1.24(24)	4.3
F9	*8.5339(40)*	98.77	1.23(23)	4.1

the dataset in two, four out of five modes with S/N > 5.0 are present in each set. For lower S/N the alias problems lead to a risk that false detections are made. This has been verified by simulations. Modes with S/N < 5 must be considered with some caution. Confirmation of these frequencies is needed by additional observations. We have performed analyses of several sets of simulated data assuming a variety of lifetimes in order to verify the validity of the identified modes. The details of such simulations will be published in a subsequent paper.

The first seven modes can be ordered in a sequence of modes, which fits the straight line

$$\nu(n) = \nu_0 + 7.1 * n \qquad (1)$$

where n is an integer (the order of the mode). Some n values are missing. The maximum deviation from the line is 1.1 μHz. This is similar to the results reported for Arcturus (Merline, 1999) and α UMa (Guenther et al., 2000). The first seven modes could all be radial modes.

From the present data, we cannot firmly exclude that Frequency F8 in Table 1 corresponds to the same mode as F7. The two modes are resolved, but if the damping time is short, they might be different realizations of the same mode.

4. First interpretation

In order to study the nature of the oscillations detected in ξ Hya, it is necessary to compare the observed frequency spectrum with model predictions, taking into account the constraints on the three observational stellar parameters $T_{\rm eff}$, L and Z. We have redetermined the atmospheric parameters and use $T_{\rm eff} = 5000 \pm 100$ K, $L = 61.1 \pm 6.2$ $L_\odot$, $\log g = 2.85$, [M/H] $= 0.06 \pm 0.07$ ($Z = 0.019 \pm 0.006$) and $v \sin i = 1.8 \pm 1.0$ km s^{-1}. Details of how these values were obtained will be reported in a subsequent paper.

Using the evolution code of Christensen-Dalsgaard (1982), evolutionary tracks were produced, spanning the

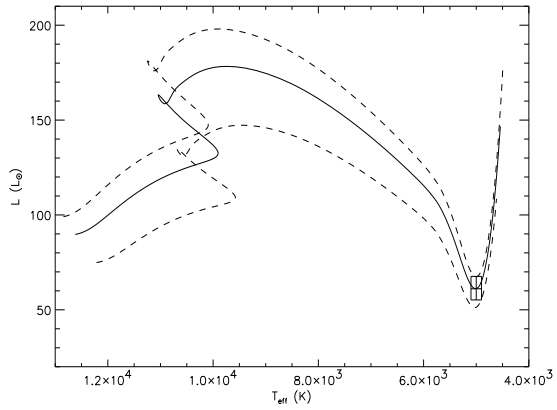

Fig. 4. Hertzsprung-Russell diagram with evolutionary tracks for $Z = 0.019$ for masses $3.07 M_\odot$ (solid line), 2.93 and $3.15 M_\odot$ (lower and upper dashed lines, respectively). The location of ξ Hya in the diagram is given by the error box.

error box defined by the uncertainties of $T_{\rm eff}$, L and Z. The model tracks were computed using the EFF equation of state (Eggleton et al. 1973), OPAL opacities (Iglesias, Rogers & Wilson 1992), Bahcall & Pinsonneault (1992) nuclear cross sections, and the mixing-length formalism (MLT) for convection.

The evolutionary track passing through the observed ($T_{\rm eff}$, L) corresponds to a mass of $3.07 M_\odot$ for $Z = 0.019$ (Fig. 4). Oscillation frequencies were calculated for the model in that track closest to the observed location of ξ Hya in the HR diagram. The average separation between radial modes in the range 50–100 μHz is $\Delta\nu_{\rm theo} = 7.2\,\mu$Hz in agreement with the observational value.

Radial modes are expected to dominate the spectrum for giant stars (cf. Dziembowski et al. 2001, Fig. 2). Further analysis of the spectrum is beyond the scope of the current discovery paper and will be done in a forthcoming paper, dealing in detail with the issue of modelling and considering also the possibility that ξ Hya could be a core helium burning star with a smaller mass.

5. Conclusions

The main conclusions of this study are as follows. Solar-like oscillations have been firmly discovered in the bright G7III star ξ Hya. The amplitudes of the strongest modes are somewhat below $2\,{\rm m\,s^{-1}}$. The observed frequency distribution of the modes detected (Table 1) is in agreement with theoretically calculated frequencies both in terms of the spacing and the absolute values. The modes with the largest amplitudes can be well matched with radial modes that have an almost equidistant separation around 6.8 μHz.

A most important and exciting result of our study is the confirmation of the possibility, suggested by the results reported on α UMa and Arcturus, to observe solar-like oscillations in stars on the red giant branch. This opens the red part of the HR diagram for detailed seismic studies. The latter require an accuracy within the range of current and future ground-based instruments. Such future studies will only be successful if an extremely high stability of the instrument is achieved and if one performs multisite observing campaigns covering several months in order to resolve the frequency spectrum of the oscillations and to eliminate the aliasing problems.

Acknowledgements. CA and TM acknowledge the Fund for Scientific Research of Flanders under project G.0178.02 for its financial support of the Leuven contribution to the CORALIE observations of ξ Hya and of the PhD position of TM. Part of this work was supported financially by the Swiss National Science Foundation. Support was received as well from the Danish National Science Foundation through the establishment of the Theoretical Astrophysics Center, from Aarhus University and from the Danish Natural Science Research Council. TCT is supported by research grant SFRH/BPD/3545/2000 of the *Fundação para a Ciência e a Tecnologia*, Portugal.

References

Bahcall, J. N., & Pinsonneault, M. H. 1992, Rev. Mod. Phys., 64, 885
Baranne, A., et al. 1996, A&AS, 119, 1
Bedding, T. R., et al. 2001,
Bouchy, F., & Carrier, F. 2001, A&A, 374, L5
Bouchy, F., Pepe, F., & Queloz, D. 2001, A&A, 374, 733
Buzasi, D., et al. 2000, ApJ, 532, L133
Carrier, F., et al. 2002, in "Asteroseismology across the HR diagram", Kluwer Academic Publishers, in press
Christensen-Dalsgaard, J. 1982, MNRAS, 199, 735
Dziembowski, W. A., Gough, D. O., Houdek, G., & Sienkewicz, R. 2001, MNRAS, 328, 601
Eggleton, P. P., Faulkner, J., Flannery, B. P. 1973, A&A, 23, 325
Frandsen, S., et al. 2001, A&A 376, 175
Guenther, D.B. et al. 2000, ApJ, 520, L45
Houdek, G., & Gough, D. O. 2002, MNRAS, submitted
Iglesias, C. A., Rogers, F. J., & Wilson, B. G. 1992, ApJ, 397, 717
Kjeldsen, H., & Bedding, T. R 1995, A&A, 293, 87
Martic, M. et al. 1999, A&A, 351, 993
Merline, W.J. 1999, in "Precise Stellar Radial Velocities", IAU Coll. 170, Eds. J.B. Hearnshaw & C.D. Scarfe, ASP Conf. Ser. Vol. 185, 187
Queloz, D., et al. 2001, The Messenger, 105, 1
Sperl M. 1998, Comm. in Asteroseismology (Vienna), 111, 1

Paper II:

Time-series spectroscopy of pulsating sdB stars - II. Velocity analysis of PG1605+072

S. J. O'Toole, T. R. Bedding, H. Kjeldsen, T. H. Dall, & D. Stello, MNRAS, 334, 471, (2002)

Mon. Not. R. Astron. Soc. **334,** 471–480 (2002)

Time-series spectroscopy of pulsating sdB stars – II. Velocity analysis of PG 1605+072★

S. J. O'Toole,[1]† T. R. Bedding,[1] H. Kjeldsen,[2] T. H. Dall[3] and D. Stello[3]
[1]*School of Physics, University of Sydney, NSW 2006, Australia*
[2]*Theoretical Astrophysics Center, Aarhus University, DK-8000, Aarhus C, Denmark*
[3]*Institute of Physics and Astronomy, Aarhus University, DK-8000, Aarhus C, Denmark*

Accepted 2002 March 27. Received 2002 March 25; in original form 2002 March 13

ABSTRACT

We present the analysis of time-resolved spectroscopy of the pulsating subdwarf B (sdB) star PG 1605+072. From our main observing run of 16 nights we have detected velocity variations at five frequencies that correspond to those found in photometry. Based on these data, there appears to be change in amplitude of the dominant modes over about a year. However, when we include extra observations to improve the frequency resolution, we find that some of the frequencies are split into two or three. Simulations suggest that the apparent amplitude variation can be at least partially explained by a series of very closely spaced frequencies around the two strongest modes. By combining observations taken over ~ 300 d we conclude that some of the closely spaced modes are caused by one mode the amplitude of which is varying, however this frequency is still within $\sim 1\,\mu$Hz of an apparently stable frequency. Because of this kind of complexity and uncertainty we advise caution when trying to identify oscillation modes in this star.

Key words: stars: individual: PG 1605+072 – stars: interiors – stars: oscillations – subdwarfs.

1 INTRODUCTION

The discovery of pulsations in hot subdwarf B (sdB) stars provides an excellent opportunity to probe sdB interiors using asteroseismological analysis. While it is generally accepted that sdBs are the field analogues of extreme horizontal branch (EHB) stars, many questions remain about their formation and evolution. sdB stars (like their EHB counterparts) are He-core burning, with $20000\,\mathrm{K} \lesssim T_{\rm eff} \lesssim 40000\,\mathrm{K}$ and $5.2 \lesssim \log g \lesssim 6.2$ (Saffer et al. 1994).

D'Cruz et al. (1996) showed that one possible mechanism for EHB (and sdB) formation is strong mass loss on the red giant branch. They found that the mass-loss efficiency required to produce EHB stars does not vary greatly with metallicity, which might explain the existence of EHB stars in both metal-rich populations (some clusters and possibly elliptical galaxies; Dorman, Norris & Gross 1995) and metal-poor populations (e.g., Whitney et al. 1994). Binary interaction is one possible mechanism for such mass loss, an idea first introduced by Mengel, Norris & Gross (1976). Indeed, at least ~ 60 per cent of sub-dwarfs appear to have main-sequence companions (Allard et al. 1994; Jeffery & Pollacco 1998).

Pulsating sdBs (also known as EC 14026 stars) typically have periods of 100–200 s, photometric amplitudes < 10 mmag, and oscillate in p as well as possibly g modes. The pulsations are thought to be driven by an opacity bump owing to the ionization of heavy elements such as Fe at temperatures of $\sim 2 \times 10^5$ K in the sdB envelope (Charpinet et al. 1997).

Of all the known pulsating sdBs, PG 1605+072 has the most extreme properties, with the richest power spectrum (around 50 modes), the longest periods (up to ~ 550 s), and the lowest surface gravity ($\log g \sim 5.25$) (Kilkenny et al. 1999). The low gravity implies that the star may have evolved off the EHB; this hypothesis is supported by modelling by Kawaler (1999).

In Paper I (O'Toole et al. 2000) we reported the detection of Doppler variations in PG 1605+072. The dominant frequencies detected corresponded to those found in photometry (Kilkenny et al. 1999), and we also found evidence of a wavelength dependence of the oscillation amplitude of the Balmer lines. In this paper we present new radial velocity observations covering a much longer time span. We do not confirm the wavelength dependence, but we do see evidence for very closely spaced frequencies, similar to the findings of Kilkenny et al. (1999). We also compare our results with those of Woolf, Jeffery & Pollacco (2002), who observed this star with higher signal-to-noise ratio and spectral

★Based on observations made with the Danish 1.54-m telescope at ESO, La Silla, Chile, and on observations made with the Nordic Optical Telescope, operated on the island of La Palma jointly by Denmark, Finland, Iceland, Norway and Sweden in the Spanish Observatorio del Roque de Los Muchachos of the Instituto de Astrofísica de Canarias.

†E-mail: otoole@physics.usyd.edu.au

dispersion, but over a much shorter time span (see Section 7). We will discuss equivalent width measurements from our spectra in a future paper.

2 OBSERVATIONS

The bulk of the observations were made on 11 nights over a 16-day period in 2000 May (see Table 1), using the DFOSC spectrograph on the Danish 1.54-m telescope at La Silla, Chile and the ALFOSC spectrograph mounted on the 2.56-m Nordic Optical Telescope on La Palma in the Canary Islands. To increase the frequency resolution of the amplitude spectrum and allow detection of very closely spaced oscillation modes, we also obtained observations at La Silla for about 1 hour per night in 2000 March–April, before the main run (see Table 2).

Table 1. Spectroscopic observations of PG 1605+072. LS = La Silla; NOT = Nordic Optical Telescope.

UT date	Telescope	No. of hours	No. of spectra
2000 May 11	Danish	6.87	370
2000 May 12	Danish	6.45	300
2000 May 16–17	NOT	7.31	337
2000 May 17–18	NOT	8.12	376
2000 May 18	Danish	6.75	319
2000 May 19	Danish	6.77	375
2000 May 19–20	NOT	8.40	473
2000 May 20	Danish	6.61	370
2000 May 21	Danish	2.69	146
2000 May 22	Danish	6.69	374
2000 May 23	Danish	6.67	369
2000 May 25	Danish	6.62	346
2000 May 26	Danish	1.24	70
Total		81.19	4225

Table 2. Spectroscopic observations of PG 1605+072 in March-April 2000.

UT date	No. of hours	No. of spectra
2000 March 18	0.30	12
2000 March 20	1.43	77
2000 March 21	0.45	25
2000 March 22	0.45	25
2000 March 23	0.57	32
2000 March 24	0.65	37
2000 March 25	0.72	41
2000 March 26	0.93	45
2000 March 27	0.93	52
2000 March 28	0.83	45
2000 March 29	1.17	59
2000 March 30	1.05	59
2000 March 31	1.07	59
2000 April 01	1.15	57
2000 April 04	1.03	65
2000 April 05	1.42	77
2000 April 06	1.47	80
2000 April 07	1.55	85
2000 April 08	1.65	90
2000 April 09	1.57	86
2000 April 10	1.70	95
2000 April 11	1.90	99
2000 April 12	1.23	65
Total	25.22	1367

The La Silla data (March to May) consisted of single-order spectra projected on to a 2K LORAL CCD. Pixel binning (to reduce readout noise) and windowing (to reduce readout time) gave 66×500 pixel spectra with a total wavelength range of 3650–5000 Å and a dispersion of 1.65 Å pixel^{-1}. The resolution was $\sim$6 Å, set by a slit width of 1.5 arcsec. The exposure time was 46 s, with a dead time of about 16 s. The average number of photons per Å in each spectrum was about 1700. A similar setup was used in previous observations (see Paper I).

The NOT data were similar, with 66×500 binned pixels covering a wavelength range of 3550–5000 Å. The dispersion was 1.65 Å pixel^{-1} and the resolution was $\sim$8 Å, set by a slit width of 1.0 arcsec. The exposure time was 50–70 s, with a dead time of only 5 s. There was an average of about 8000 photons per Å in each frame. The data from both telescopes were timestamped in Modified Julian Date by the telescope computers to an accuracy of less than one second.

3 REDUCTIONS

Bias subtraction, flat-fielding and background light subtraction were carried out using IRAF, and 1D spectra were extracted using an Optimal Extraction algorithm (Horne 1986). A cubic spline was fitted to the continuum level, and the spectra were normalized to a continuum value of unity.

The spectrum of PG 1605+072 is dominated by Balmer lines (see Fig. 1). Also present are some weak lines from He I (e.g., λ4471 and λ4922) and He II (e.g., λ4686). The Balmer lines are ideal to determine Doppler variations. A template spectrum was created by averaging 20 high-quality spectra from each night. By using a different template for each night, we are effectively applying a high-pass filter to the data.

To avoid pixelization effects in the cross-correlation analysis, all spectra, including templates, were oversampled by a factor of 40 (using linear interpolation), and all but the Balmer line in question (one of Hβ, Hγ, Hδ, Hϵ and H8) was cropped from each.

These spectra were modified further by subtracting 1.0 such that the continuum level was approximately zero. The result was passed through a half-cosine filter to smooth the transition to zero at the ends.

Each resulting template was then cross-correlated with its respective spectra to obtain pixel displacements. The velocities were obtained by using the known wavelengths of the Balmer lines to convert this displacement into wavelength and then Doppler shift. See Paper I for further details.

The velocity curve for Hγ is shown in Fig. 2. It has not been corrected for slow instrument drifts. The high quality of the NOT data (3rd, 4th and 7th panels) – owing to its larger aperture – suggests that fainter and/or shorter-period pulsating sdBs could be observed with this telescope.

4 TIME-SERIES ANALYSIS

Because the quality of the observations varies through the data set, we performed frequency analysis using a weighted Fourier transform (Kjeldsen & Frandsen 1992), where weights were assigned to each night in the 2000 May data set according to the internal scatter. Weights for the March–April data were assigned to groups containing approximately the same number of observations as one night in the May data.

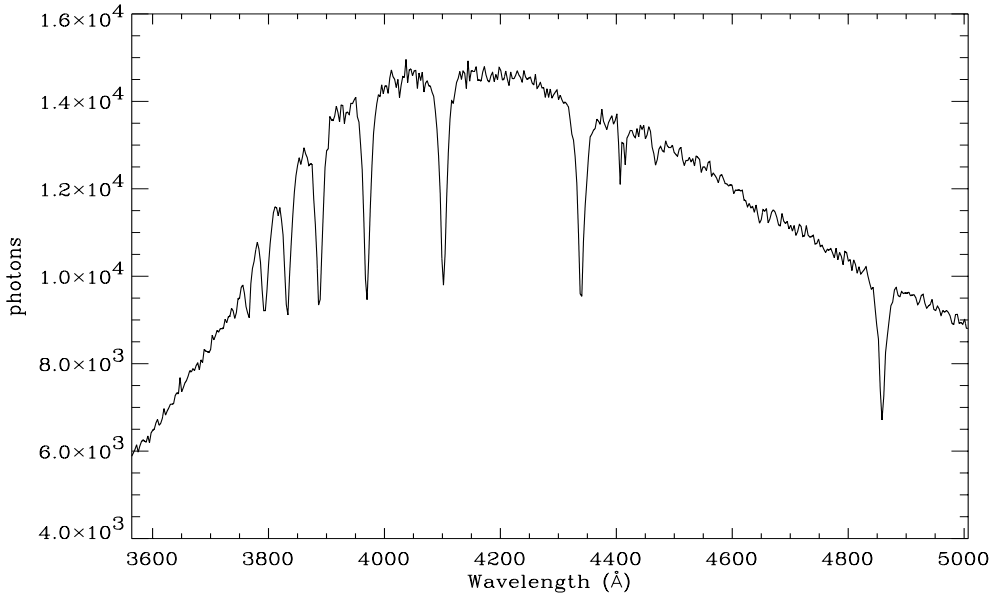

Figure 1. Typical spectrum of PG 1605+072 obtained at the Nordic Optical Telescope. The Balmer sequence is visible from Hβ to H12, as well as the He I λ4471Å line. The feature at $\sim$4410-Å is a bad CCD column.

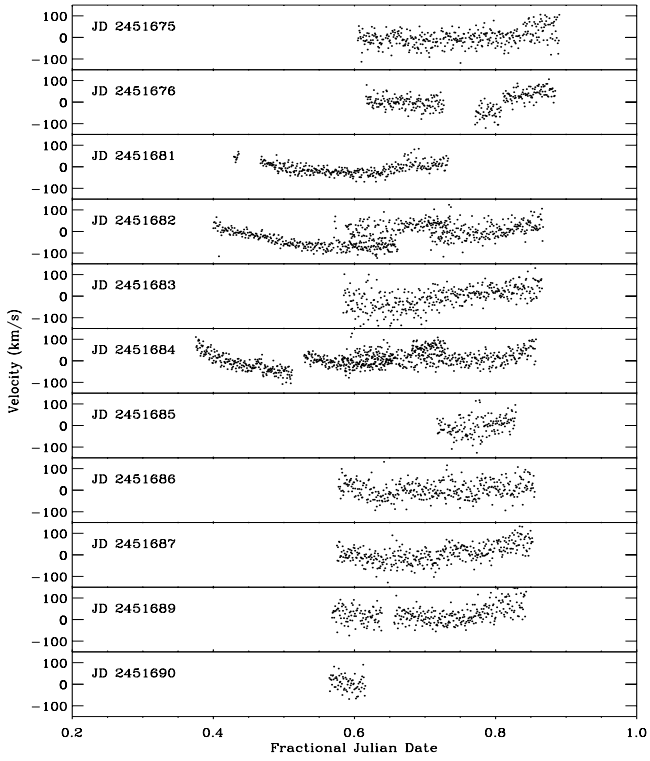

Figure 2. Velocity curve for Hγ from 2000 May. No instrumental variation has been corrected for. There is a three-day gap between the second and third panels from the top.

4.1 Velocities of individual Balmer lines

The amplitude spectra of the five velocity time-series from May 2000 are shown in Fig. 3. There does not appear to be any substantial variation in velocity amplitude between the Balmer lines. We have analysed all five time-series, using the non-linear least-squares multifrequency fitting software PERIOD98 (Sperl 1998). The frequencies found are shown in Table 3. The same technique was applied to the data presented in Paper I (July 1999) and these frequencies are shown in Table 4. White noise levels in the amplitude spectra are typically $\sim 1000\,\mathrm{m\,s^{-1}}$ for each line in the 1999 July data, and $600-700\,\mathrm{m\,s^{-1}}$ in the 2000 May data.

The major difference between the two sets of frequencies is the detection of the peaks at 1985 and 2075 μHz in the 2000 May data set. In Paper I it was uncertain whether the non-detection of the latter (found to be the dominant mode in photometry by Kilkenny et al. 1999) in any of the individual Balmer line time-series, was as a result of variable amplitude or beating between closely spaced modes. With a slightly longer time-series and reduced noise, this mode is clearly detected in all Balmer lines. Somewhat surprising

Table 3. Frequencies (in μHz) for five Balmer lines found from the 2000 May data.

Hβ	Hγ	Hδ	Hϵ	H8
	1891.26			1891.34
1985.73	1985.68	1985.58	1985.73	1985.79
2075.64	2075.72	2075.68	2075.68	2075.68
2102.21	2102.20	2102.17	2102.18	2102.24
2742.71	2742.68	2742.64	2742.70	2742.69

Table 4. Frequencies (in μHz) for five Balmer lines found from the 1999 July data.

Hβ	Hγ	Hδ	Hϵ	H8
	1891.02	1891.00	1890.91	
2102.14	2102.14	2102.11	2102.12	2102.12
2742.73	2742.47	2742.69	2742.67	2742.61

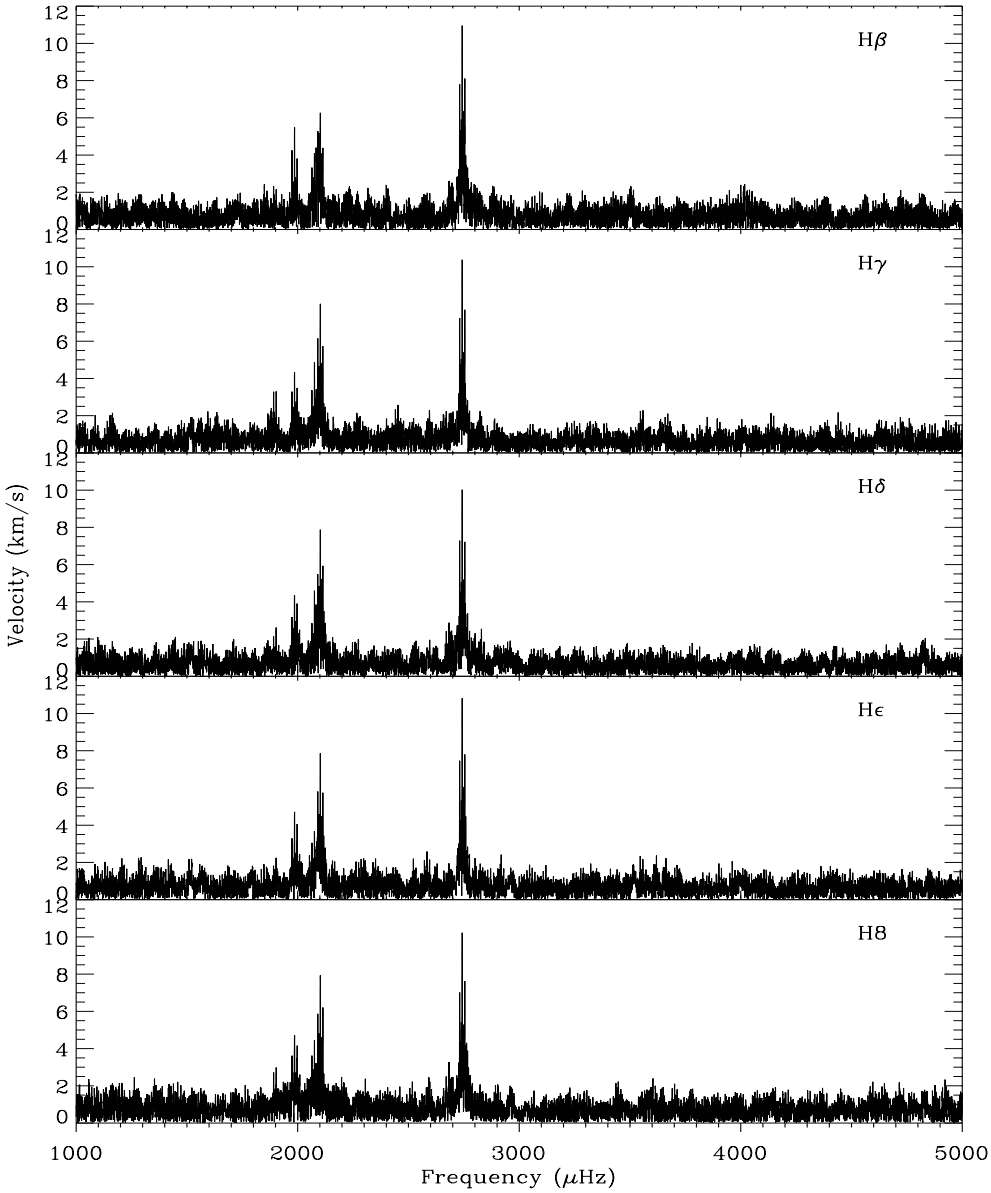

Figure 3. Amplitude spectra of five Balmer lines. No amplitude variation is evident in the dominant modes.

is the detection of the mode at 1985 μHz, as this was found in photometry to have an amplitude of only 3.3 mmag, whereas the four other modes detected had amplitudes greater than 13.9 mmag. This mode may have variable amplitude or may be a series of unresolved modes. There is evidence for the latter possibility from Kilkenny et al. (1999), who found three modes around 1985 μHz. As discussed further below, it is clear that the crowded frequency spectrum of PG 1605+072 severely complicates the interpretation of the observations.

In Paper I we reported the possible wavelength dependence of Balmer-line velocity amplitudes (see fig. 3 of that paper). Here, we have tried to confirm this result. First, we found the weighted average frequencies of each of the four modes that were detected in all Balmer lines. These frequencies were then simultaneously fitted to each time-series, giving amplitudes and phases for each mode.

Fig. 4 shows Balmer-line velocity amplitudes as a function of wavelength for these four modes. Error bars indicate the white noise level in the 3000–5000 μHz region, where there appears to be no excess power. For three of the modes, there is no clear evidence for any wavelength dependence. For the 2102 μHz mode (triangles), all lines except Hβ appear to have the same amplitude, with the Hβ amplitude being slightly lower. We do not feel this difference is significant enough to claim wavelength dependence, particularly as this peak may in fact be a combination of several closely spaced modes.

4.2 Combined time-series

To reduce noise and perhaps detect more frequencies, we have combined the time-series for the five Balmer lines. Before doing

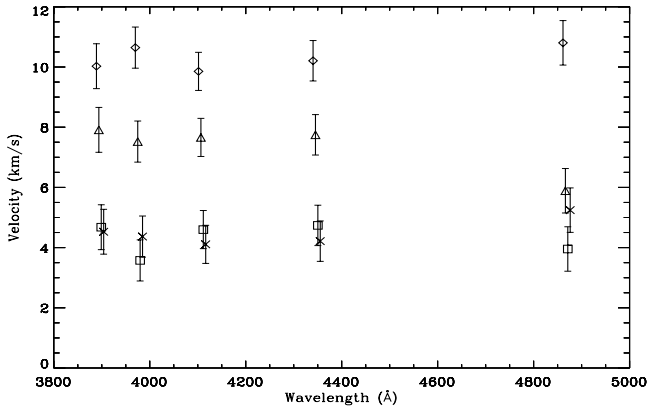

Figure 4. Velocity amplitude as a function of wavelength. Diamonds represent the mode at 2742 μHz, triangles for 2102 μHz, squares for 2075 μHz and crosses for 1985 μHz. Small offsets to some points have been added in the wavelength direction to improve clarity. There is no clear dependence of amplitude on wavelength.

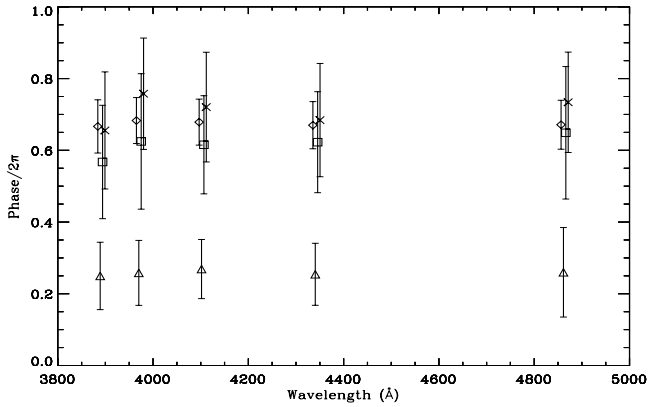

Figure 5. Oscillation phase as a function of wavelength. Symbols are the same as in Fig. 4. Small horizontal offsets have been added for clarity.

this, we checked whether the oscillation phases were the same for each mode in each time-series. This is simply a matter of examining the phases found at fixed frequency. Relative phases are plotted as a function of wavelength for each mode in Fig. 5, with errors determined using simple complex arithmetic (see Baldry et al. 1998). There is no evidence for phase variation with wavelength, leaving us free to combine the time-series.

To do this, we simply averaged the velocity at each observation. This was possible since the weighting for each Balmer line was approximately the same. Weights were again derived from the internal scatter of each night. Combined time-series were constructed, for both 1999 July and 2000 May. The two resulting amplitude spectra are shown in Fig. 6. There appears to be amplitude variation over the 10-month interval between the observations, which we discuss in Section 5. The white noise level is now 555 $\mathrm{m\,s^{-1}}$ for the 1999 July data set and 425 $\mathrm{m\,s^{-1}}$ for the 2000 May data set, an improvement of ∼45 per cent over the best single-line amplitude spectra.

The fitted frequencies are shown in Table 5. The third column contains the differences in frequency between the two sets of data. The lengths of our two sets of observations are $\sim 7.9 \times 10^5$ s (1999 July) and $\sim 1.3 \times 10^6$ s (2000 May). If the formal frequency resolution is given by $1/T$, then the corresponding resolutions are ∼1.26 μHz and ∼0.77 μHz, respectively. Comparing these values with those in the third column of Table 5, we see that we have been able to estimate the frequency to much better than the formal resolution. In the final column we show the frequencies found from photometry, and again we see agreement that is better than the formal resolution. This is not surprising: at high signal-to-noise ratio, the frequency of a strong peak in the power spectrum can be estimated to a precision many times better than the formal frequency resolution.

Table 5. Frequencies found after combining all Balmer lines in the 1999 July and 2000 May data sets. Note that $\Delta\nu = \nu_{2000} - \nu_{1999}$. The final column shows frequencies found by Kilkenny et al. (1999) for comparison.

ν_{2000} (μHz)	ν_{1999} (μHz)	$\Delta\nu$ (μHz)	Kilkenny et al. (1999)
1891.19	1890.98	−0.21	1891.42
1985.75	–	–	1985.32
2075.68	2075.29	−0.39	2075.76
2102.21	2102.15	−0.06	2101.65
2742.71	2742.63	−0.08	2742.72

Table 6. 2000 frequencies, periods and amplitudes measured from the extended time-series. The fourth column shows the amplitudes found using the 2000 frequency solution, the fifth column shows the difference between the frequencies found in this paper and those found in photometry (Kilkenny et al. 1999), and the sixth column shows photometric amplitude rank.

ν (μHz)	P (s)	V_{2000} ($\mathrm{km\,s^{-1}}$)	V_{1999} ($\mathrm{km\,s^{-1}}$)	$\nu_{\mathrm{vel}} - \nu_{\mathrm{phot}}$ (μHz)	Rank n
1891.01	528.82	1.99	3.18	−0.41	5
1985.75	503.59	4.13	0.63	+0.43	8
2075.72	481.76	4.27	2.11	−0.04	1
2101.57	475.83	3.40	4.97	−0.08	3
2102.48	475.63	8.47	11.1	+0.04	32
2102.83	475.55	3.66	3.05	−0.45	2
2269.84	440.56	1.75	0.90	−0.27	6
2742.47[a]	364.63	4.45	3.57	−0.25	4[a]
2742.85	364.58	7.17	2.87	+0.13	4
2765.09	361.65	1.97	0.29	−0.20	21

[a] This mode can also be identified as one of the extra frequencies found in an extended time-series in table 4 of Kilkenny et al. (1999).

4.3 Extended time-series

To improve the frequency resolution still further, we now add the data from 2000 March–April (Table 2) to the 2000 May series. For the extended time-series ($T \sim 5.9 \times 10^6$ s) the formal frequency resolution is ∼0.17 μHz. The longer time-series does add complications however, since the number of alias peaks in the amplitude spectrum increases significantly. There is a gap of 45 d between the midpoints of the two time-series, leading to aliasing that splits each peak into multiplets separated by ∼0.25 μHz. The spectral window of each time-series is shown in Fig. 7. This includes the window function of all the 1999–2000 combined, which is discussed in Section 6. The extra aliasing is evident in the top two panels.

The frequencies and amplitudes determined from the extended

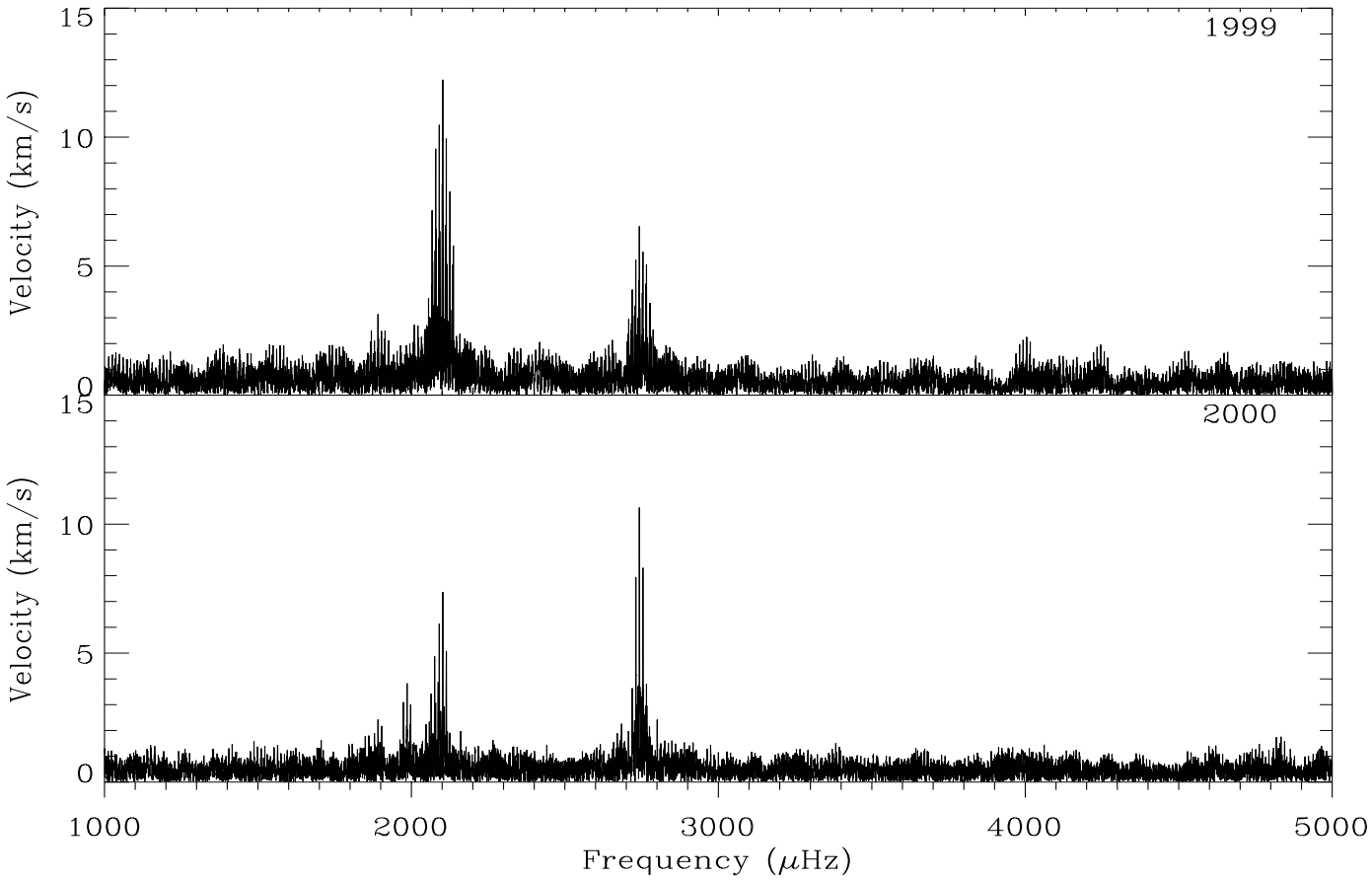

Figure 6. Amplitude spectra for 1999 July (top) and 2000 May (bottom) based on a combined Balmer line time-series. Note the apparent change in amplitudes.

(2000 March–May) time-series are shown in Table 6. The white noise level for this time-series is 370 m s^{-1}, and we use this as an error for the velocity amplitudes in column 3. The peaks at 2102 and 2742 μHz, both shown as single in Tables 3 and 4, are now resolved into three and two peaks, respectively. Also shown are the differences in frequency when compared with photometry. If we take into account both our frequency resolution and the ambiguity from alias peaks, the frequencies we find are in excellent agreement with those found in photometry (Kilkenny et al. 1999). In particular, the multiplicity of the peaks at 2102 and 2742 μHz agrees with the extended time-series ($T \sim 33$ d) used by Kilkenny et al. (1999), who found four frequencies around 2102 μHz and four around 2742 μHz. They also found five frequencies around 2075 μHz, six around 2270 μHz and three around 1985 μHz. We have not detected these extra frequencies. It is not clear whether these multiple peaks are real or whether they caused by amplitude variability. We will for the moment consider them to be real, but will address this question in more detail in Section 5.

In Table 6, we note that the peaks at 2102.48 μHz and 2765.09 μHz are matched with quite low-amplitude modes found in photometry (~1 mmag), chosen because they are the closest in frequency. The latter frequency can also be identified with a higher amplitude mode detected by Koen et al. 1998. We note also that 2765.09 μHz is separated from ~2742 μHz by twice the one cycle per day alias frequency (i.e. 2×11.57 μHz). The mode at 2742.47 μHz is also identified with a low amplitude mode, however it was only found in the extended time-series of Kilkenny et al. (1999). Again, we have matched these modes purely because they are the closest in frequency. This appears to give further evidence for amplitude variability.

To further quantify this variability, we have fit the frequencies derived from the 2000 observations to our 1999 data. The amplitudes from the fit are shown in the fourth column of Table 6, next to the amplitudes from the 2000 observations for comparison. Errors in velocity are taken to be the white noise level (555 m s^{-1}). There are clearly large variations in most peaks (even more so, considering that the weakest 1999 amplitudes should be considered as upper limits).

5 SIMULATIONS

How well resolved are the closely spaced multiplets at 2102 μHz and 2742 μHz shown in Table 6? To answer this, we show the regions in question in Figs 8 and 9. From the top panel of Fig. 8 it is clear that the frequency resolution is sufficient to resolve the power at 2102 μHz into at least two peaks, perhaps three. The two frequencies found around 2742 μHz also appear to be resolved in Fig. 9. In the bottom panel of Fig. 6 it appears that the peak around 2742 μHz is higher than the one around 2102 μHz, however Table 6 shows the opposite. This can be explained by examining the amplitude spectra (shown in Fig. 10) around 2102 μHz after each frequency is removed. It is still not clear, however, whether these

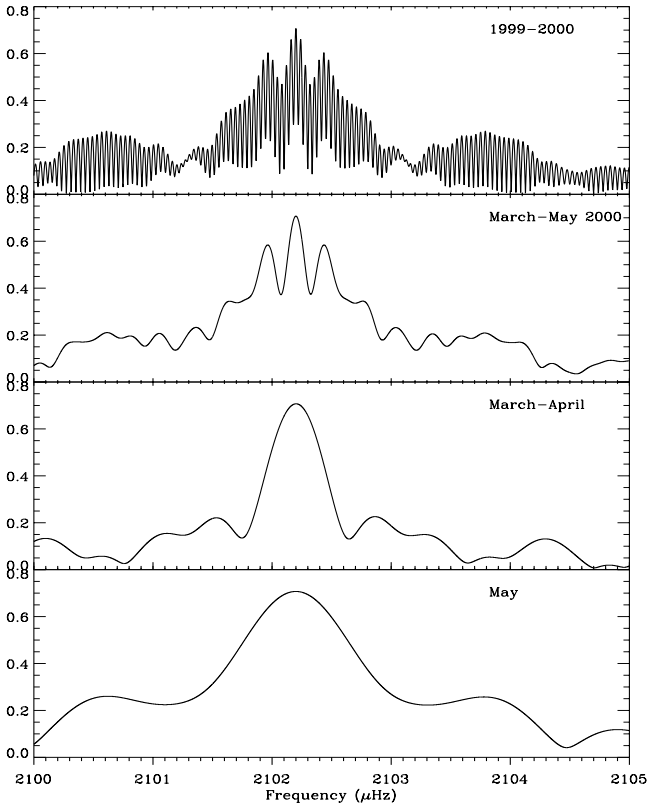

Figure 7. Spectral window (in amplitude) for 1999–2000, 2000 March–May, March–April and May data sets in the range 2100–2105 μHz. Alias peaks are seen in the top two panels with a ∼0.25μHz spacing, and in the top panel.

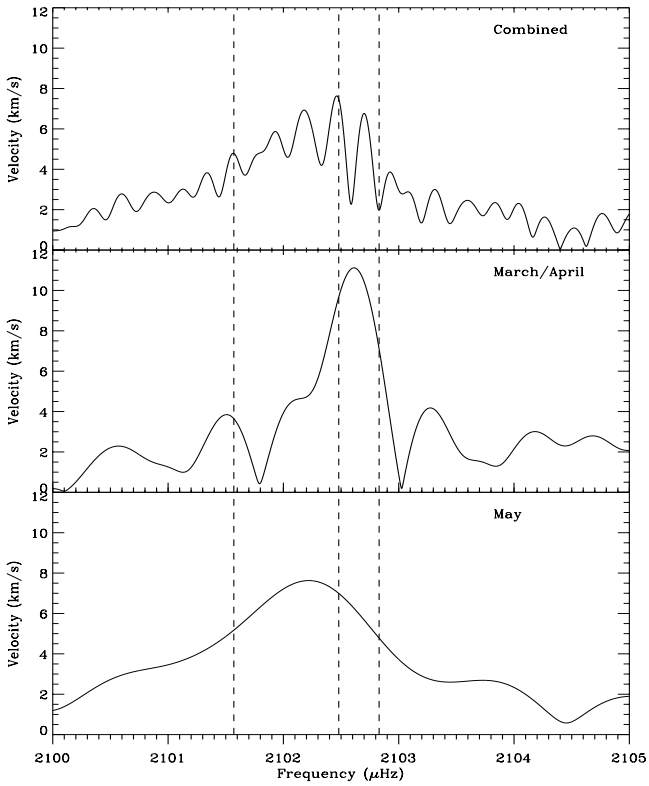

Figure 8. Amplitude spectra for the combined, March/April and May data sets in range 2100–2105 μHz. The dashed lines indicated frequencies measured from the extended time-series.

frequencies are real or an artefact of the variation in amplitude of one frequency.

To investigate these effects further, we have created simulated time-series for both our sets of observations (1999 and 2000). The inputs are the 10 frequencies measured from the time-series with the highest frequency resolution (i.e., 2000) with their corresponding amplitudes. Note that each simulation had exactly the same input amplitudes and frequencies, and only the phases were randomized. We have used two different noise levels, $\sim 600\,\mathrm{m\,s^{-1}}$ and $\sim 300\,\mathrm{m\,s^{-1}}$, as these bracket the noise in our observations. The same phases were used at both noise levels. The basic features of the two different groups of spectra are the same, implying that noise does not play a significant role in the shape of the amplitude spectrum. A selection of simulated amplitude spectra with noise $\sim 600\,\mathrm{m\,s^{-1}}$ are shown in Fig. 11 using the 2000 window function.

The most interesting feature of the majority of these spectra is the variability of the amplitudes of the peaks at ∼2102 μHz and at ∼2742 μHz. This observed variability does not depend strongly on the window function and arises from beating between the closely spaced modes around these two frequencies. However in Table 5 there is only a small difference (<0.1 μHz) between frequencies measured in 1999 July and 2000 May. If there were two or more frequencies beating, we would expect the peaks to move by more than this difference, since the measured frequencies span a range of ∼1.3 μHz.

Kilkenny et al. (1999) found two frequencies around 2102 μHz in both halves of their ∼15 night time-series, as well as in the full series. They also found weak 'satellite' frequencies near almost all of the highest amplitude peaks. We find only one peak at 2102 μHz in our 2000 May observations, however weighting the data may degrade the frequency resolution. The middle panel of Fig. 8 suggests that two peaks may be clearly resolved in the 2000 March/April observations. If we assume there are three frequencies around 2102 μHz, we detect two frequencies in ∼90 per cent of our simulations. It seems that our detection of only one peak may be due simply to chance. Around 2742 μHz only one frequency is always resolved, with the second frequency resolved ∼50 per cent of the time. This suggests a minimum of two frequencies around 2102 μHz, and possibly two around 2742 μHz. Two frequencies around 2742 μHz is supported by Reed (2001), who finds a similar separation (∼0.3 μHz) in a re-analysis of the Kilkenny et al. (1999) observations. By combining all of our data (1999–2000), we are in a position to make one final test.

6 COMBINATION OF ALL OBSERVATIONS

If we combine all of our observations (1999–2000), we find that the amplitudes of each peak is approximately the same ($\sim 8\,\mathrm{km\,s^{-1}}$). This implies that the oscillations are coherent over this one year period, and we can therefore perform a frequency analysis on the time-series. Combining all of the data introduces fine structure in the spectral window, as shown in the top panel of Fig. 7 in the region around 2100 μHz. The frequencies we measure from this time-series are the same as those found in the 2000 March–May data, except around 2102.5 μHz, where we now find

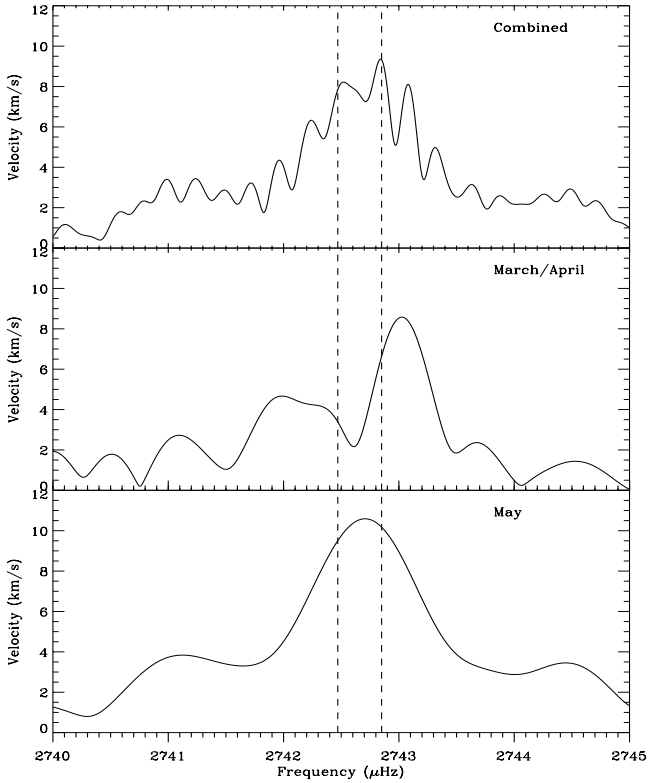

Figure 9. Same as Fig. 8 except in the range 2740–2745 μHz.

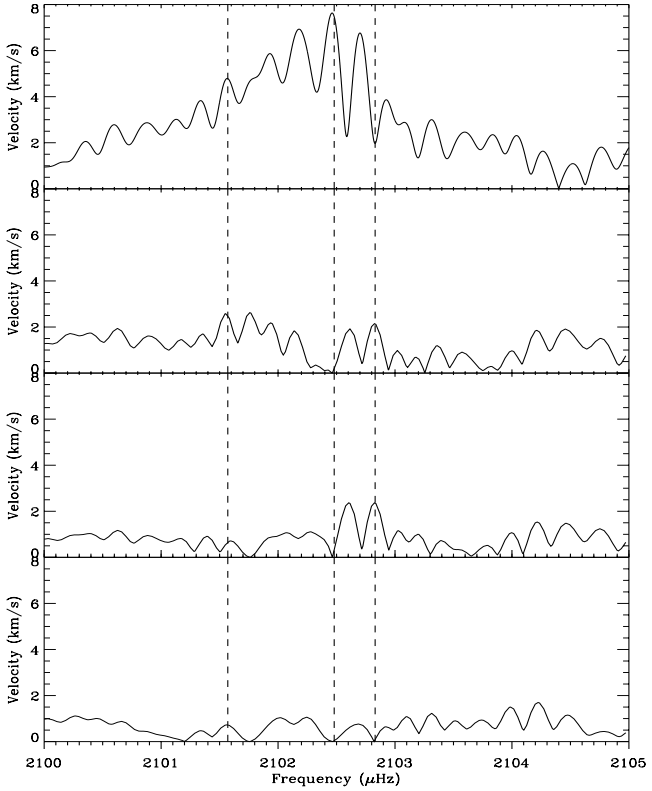

Figure 10. Amplitude spectra of the 2100–2105 μHz region showing the successive removal of three closely spaced frequencies.

three frequencies instead of two. These frequencies, while they describe the observations (see Fig. 12), are split such that we consider them to be caused by amplitude variation. The two frequencies not found in 1999–2000, but found in the 2000 March–May data (2269.84 and 2765.09 μHz), we consider marginal detections. We can now conclude that the frequencies in Table 7, derived from the 2000 March–May observations, are real.

7 COMPARISON WITH WOOLF ET AL. (2002)

Our observations were by coincidence concurrent with those of Woolf et al. (2002), so we are in a position to examine some of their findings. First, based on data taken over 16.3 h across a 32.1-h period, they found an apparent power shifting between modes, which we also find, and attribute to both amplitude variability over time and beating between closely spaced frequencies. They also found evidence for rotational splitting of the 2742 μHz mode, and derived a rotational period of 12.6 ± 2.8 h. This is not in agreement with Heber, Reid & Werner (1999), who derived an upper limit on the rotational period of 8.7 h from spectral analysis. While the pulsations cause some broadening of the spectral lines, the pulsation amplitudes are not high enough to shift Heber et al. (1999)'s upper limit into the range found by Woolf et al. The rotational splitting they found is ∼11 μHz, which is very close to one cycle per day. Because of this, the reality of this splitting should probably be treated with scepticism.

Some of our observations overlap with Woolf et al.'s, and we have plotted in Fig. 13 the amplitude spectrum of the two nights closest in time to theirs. Our observations for this period start at MJD 51675.1 and finish at MJD 51676.4, while the Woolf et al. start at MJD 51675.9 and finish at MJD 51677.25. The dashed lines in the figure indicate the frequencies found by Woolf et al, which appear to be one cycle per day alias peaks. The dotted lines indicate the frequencies found in this paper. For comparison we have shown the spectral window of our observations in the top panel. The dashed lines correspond very well to the alias peaks in our spectral window, and we conclude that this is most likely what Woolf et al., have identified, although the central peak (which we have identified with the frequency found in photometry) is not apparent in their amplitude spectra. We feel timing errors may be a possible explanation for the splitting, and lack of this central peak.

8 DISCUSSION

The model of Kawaler (1999) is the best pulsation model for PG 1605+072 produced so far, although it only matches five of the dominant frequencies from Kilkenny et al. (1999) (they detected up to 55 frequencies, although some may be artefacts of amplitude variation). Kawaler's model predicts an equatorial velocity of $\sim 130\,\mathrm{km\,s^{-1}}$ leading to a rotational period of around 3 h, in agreement with the upper limit found by Heber et al. (1999) of $P_{\mathrm{rot}} < 8.7\,\mathrm{h}$ ($v \sin i = 39\,\mathrm{km\,s^{-1}}$).

What are the possible reasons for modes which are so closely spaced? Rotation has already been mentioned, however the minimum rotational splitting for an $l = 1$ mode is ∼16 μHz to first order, and for an $l = 2$ mode is ∼27 μHz. This is based on the maximum rotational period of Heber et al. (1999), and assumes that the star oscillates in g modes (Kawaler 1999) in a similar way to a white dwarf. This is not the case, however, since unlike white

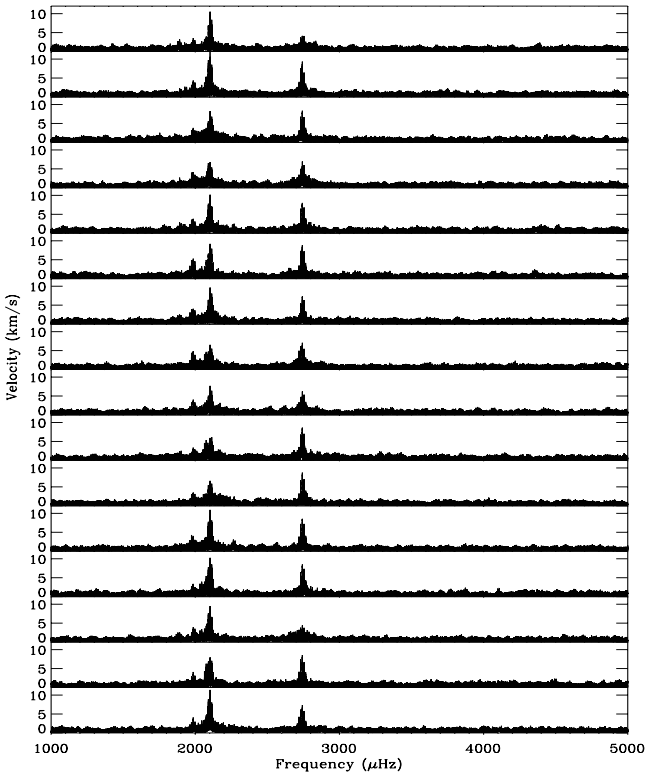

Figure 11. Simulated amplitude spectra using the 10 frequencies from Table 6 as input. These spectra are based on the window function of all observations from 2000. It is clear that the variable amplitude of the highest peaks is due to beating.

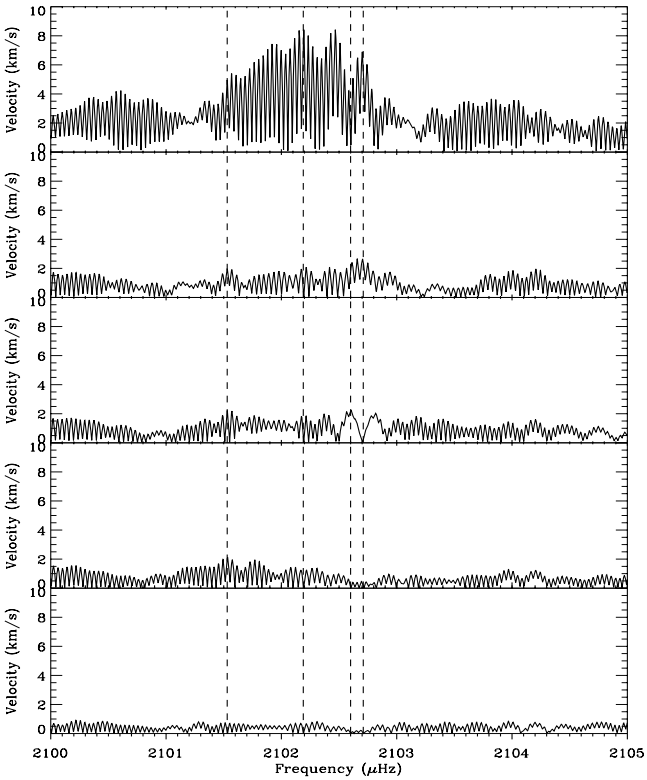

Figure 12. Same for Fig. 10, except with combined 1999 and 2000 time-series.

dwarfs, horizontal motion does not dominate vertical motion on the surface of sdBs; in fact, they are of the same order (Kawaler, private communication). Despite this, the splitting values above are minima, so it is clear rotation is not the only effect causing splitting. Strong magnetic fields also cause splitting of oscillation modes, however little work has been done to measure fields of sdBs. Finally, we feel that amplitude variability over several months can explain at least some of the observed splittings. More detailed modelling of PG 1605+072 using the so-called second generation pulsating sdB models of Charpinet, Fontaine & Brassard (2001) may help to answer these questions.

9 CONCLUSIONS

Of all the pulsating sdBs currently known, PG 1605+072 is clearly one of the most interesting. Using our newest observations we make several conclusions.

(i) From our main campaign we have detected seven oscillation frequencies from velocity variations in the star. These frequencies are shown in Table 7. Most of these correspond to the strongest oscillation frequencies found in photometry.

(ii) We find the velocity amplitudes and phases in the individual Balmer lines to be equal and cannot confirm the wavelength dependence of amplitude seen in Paper I.

(iii) Apparent amplitude variability between our two sets of observations can be explained by a combination of beating between closely spaced modes and amplitude variability.

Table 7. Detected frequencies and periods in velocities of PG 1605+072. These are based on the 2000 March–May observations, but also found in a time-series of all observations (1999–2000).

Frequency (μHz)	Period (s)
1891.01	528.82
1985.75	503.59
2075.72	481.76
2101.57	475.83
2102.48[a]	475.63
2742.47	364.63
2742.85	364.58

[a] We include this frequency as representative of a mode with variable amplitude around 2102.5 μHz.

(iv) To fully resolve and identify as many closely spaced frequencies as possible, it is necessary to have both good time coverage to reduce aliasing effects, and most importantly for PG 1605+072, to have a time-series that is as long as possible, thus improving the frequency resolution in the amplitude spectrum.

(v) We can explain the possible rotational splitting of the 2742-μHz peak claimed by Woolf et al. (2002) as an aliasing effect (possibly caused by incorrect time stamps), since our observations are concurrent.

PG 1605+072 offers asteroseismologists several challenges. It

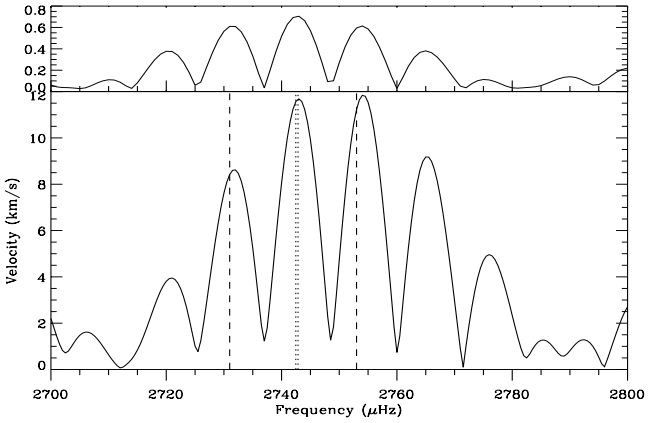

Figure 13. Amplitude spectrum of nights MJD 51675.1−51676.4 (bottom), showing no rotational splitting of the 2742 μHz mode. The frequencies found by Woolf et al. (2002) are plotted as dashed lines. The peaks they correspond to are alias peaks. For comparison, the frequencies found in this work are plotted as dotted lines. The window function for the two nights (top) is also shown.

has many oscillation frequencies, although some have variable amplitudes; it has longer periods than most other pulsating sdBs, however it is rotating fast enough that rotationally split modes may be unequally spaced; it may be oscillating in p or g modes or a combination of both. Further theoretical work is needed in these areas. We feel that despite these challenges, a campaign of simultaneous photometry and spectroscopy will help to answer the questions we have raised here, and perhaps allow us to comprehend one of the least understood phases of stellar evolution.

ACKNOWLEDGMENTS

This paper is based on observations made with the Danish 1.54-m telescope at ESO, La Silla, Chile, and on observations made with the Nordic Optical Telescope, operated on the island of La Palma jointly by Denmark, Finland, Iceland, Norway and Sweden in the Spanish Observatorio del Roque de Los Muchachos of the Instituto de Astrofísica de Canarias.

The authors would like to thank Steve Kawaler for helpful discussions. This work was supported by an Australian Postgraduate Award (SJOT), the Australian Research Council, the Danish National Science Research Council through its Center for Ground-based Observational Astronomy, and the Danish National Research Foundation through its establishment of the Theoretical Astrophysics Center.

REFERENCES

Allard F., Wesemael F., Fontaine G., Bergeron P., Lamontagne R., 1994, AJ, 107, 1565
Baldry I. K., Bedding T. R., Viskum M., Kjeldsen H., Frandsen S., 1998, MNRAS, 295, 33
Charpinet S., Fontaine G., Brassard P., Chayer P., Rogers F. J., Iglesias C. A., Dorman B., 1997, ApJ, 483, L123
Charpinet S., Fontaine G., Brassard P., 2001, PASP, 113, 775
D'Cruz N. L., Dorman B., Rood R. T., O'Connell R. W., 1996, ApJ, 466, 359
Dorman B., O'Connell R. W., Rood R. T., 1995, ApJ, 442, 105
Heber U., Reid I. N., Werner K., 1999, A&A, 348, L25
Horne K., 1986, PASP, 98, 609
Jeffery C. S., Pollacco D. L., 1998, MNRAS, 298, 179
Kawaler S. D., 1999, in Solheim J. E., Meistas E. G., eds, ASP Conf. Ser. Vol. 169, 11th European Workshop on White Dwarfs. Astron. Soc. Pac., San Francisco, p. 158
Kilkenny D. et al., 1999, MNRAS, 303, 525
Kjeldsen H., Frandsen S., 1992, PASP, 104, 413
Koen C., O'Donoghue D., Kilkenny D., Lynas-Gray A. E., Marang F., Van Wyk F., 1998, MNRAS, 296, 317
Mengel J. G., Norris J., Gross P. G., 1976, ApJ, 204, 488
O'Toole S. J. et al., 2000, ApJ, 537, L53
Reed M. D., 2001, PhD thesis, Iowa State Univ.
Saffer R. A., Bergeron P., Koester D., Liebert J., 1994, ApJ, 432, 351
Sperl M., 1998, available for from ftp://dsn.astro.univie.ac.at/pub/Period98/
Whitney J. H. et al., 1994, AJ, 108, 1350
Woolf V. M., Jeffery C. S., Pollacco D. L., 2002, MNRAS, 329, 497

This paper has been typeset from a TEX/LATEX file prepared by the author.

Paper III:

The problem of the Pleiades distance. Constraints from Strömgren photometry of nearby field stars

D. Stello, & P. E. Nissen, A&A, 374, 105, (2001)

A&A 374, 105–115 (2001)
DOI: 10.1051/0004-6361:20010665

Astronomy & Astrophysics

The problem of the Pleiades distance

Constraints from Strömgren photometry of nearby field stars

D. Stello and P. E. Nissen

Institute of Physics and Astronomy (IFA), University of Aarhus, 8000 Aarhus, Denmark
e-mail: pen@ifa.au.dk

Received 3 April 2001 / Accepted 7 May 2001

Abstract. The discrepancy between the Pleiades cluster distance based on Hipparcos parallaxes and main sequence fitting is investigated on the basis of Strömgren photometry of F-type stars. Field stars with the same metallicity as the Pleiades have been selected from the m_1 index and a technique has been developed to locate the ZAMS of these field stars in color-magnitude diagrams based on the color/temperature indices $b-y$, $v-y$, and β. Fitting the Pleiades to these ZAMS relations results in a distance modulus of 5.61 ± 0.03 mag in contrast to the Hipparcos modulus of 5.36 ± 0.06 mag. Hence, we cannot confirm the recent claim by Grenon (1999) that the distance problem is solved by adopting a low metallicity of the Pleiades ($[\mathrm{Fe/H}]_{\mathrm{Pleiades}} = -0.11$) as determined from Geneva photometry. The metallicity sensitivity of the ZAMS determined by the field stars is investigated, and by combining this sensitivity in all three color/temperature indices $b-y$, $v-y$, and β we get a independent test of the Pleiades distance modulus which support our value of 5.61 mag. Furthermore, the field star sample used for the comparison is tested against theoretical isochrones of different ages to show that evolutionary effects in the field star sample are not biasing our distance modulus estimate significantly. Possible explanations of the Pleiades distance problem are discussed and it is suggested that the discrepancy in the derived moduli may be linked to a non-spherical shape of the cluster.

Key words. open clusters and associations: individual: Pleiades – stars: Hertzsprung-Russell (HR) and C–M diagrams – stars: distances – stars: evolution – stars: abundances

1. Introduction

The Hipparcos Space Astrometry Mission has provided accurate absolute trigonometric parallaxes for roughly 120 000 stars, which are distributed all over the sky, and hence relatively accurate distance measurements for stars at a much larger distance than previous obtainable from ground based observations. This has given the opportunity to compare distances of several open clusters derived from direct trigonometric measurements with those derived from main sequence (MS) fitting. For some of the clusters there are discrepancies between the derived distances, but in most cases the differences are within the estimated uncertainties. An exception is the Pleiades for which the distance modulus derived using the mean of the Hipparcos parallaxes is almost 0.3 mag smaller than that derived using the MS fitting technique. Possible explanations of this anomaly are:

1. The errors of the MS fitting technique may be underestimated. This could arise from difficulties in the technique itself, or it could be due to serious errors in the adopted chemical composition of the Pleiades cluster.
2. There may be systematic errors on small angular scales in the sky of the Hipparcos parallaxes which are underestimated. This could bias the inferred distance to clusters that only cover a small angular area in the sky.

If these possibilities can be excluded we may have to draw the important conclusion that the theory of stellar structure and evolution is incomplete or in other words: the Vogt-Russell theorem that the location of a star in the Hertzsprung-Russell diagram is uniquely determined by its mass, age, and composition is violated. It is this aspect of the Pleiades distance problem that makes it so interesting.

The mean parallax of the Pleiades cluster inferred from the Hipparcos data ranges from 8.60 ± 0.24 mas (Mermilliod et al. 1997) to 8.45 ± 0.25 mas (van Leeuwen 1999). These parallaxes correspond to a distance

Send offprint requests to: D. Stello,
e-mail: stello@ifa.au.dk

interval of 116 ± 3 pc to 118 ± 4 pc or a distance modulus interval of 5.33 ± 0.06 mag to 5.37 ± 0.07 mag. These distance moduli should be compared with those found from the MS fitting method. Pinsonneault et al. (1998) find a distance modulus of 5.60 ± 0.05 mag, based on an extensive multi color MS fitting analysis. They make use of several open clusters to check for different possible error sources, and both isochrones and an empirical Hyades MS are used as the zero point of the ZAMS. Pinsonneault et al. (1998) suggest that the discrepancy between the results from Hipparcos and the MS fitting method is due to spatial systematic errors on small angular scales in the Hipparcos data (Pinsonneault et al. 1998, Fig. 20) which are larger than expected (Lindegren 1988, 1989, 1997). From a comparison of the Pleiades MS with those of the Hyades and α Persei clusters Eggen (1998) also concludes that the Hipparcos parallax distance of the Pleiades may be in error by some 10%. An investigation of the possible spatial systematic errors in the Hipparcos data is performed by Narayanan & Gould (1999) who confirm the distance modulus of around 5.6 mag by an estimate of 5.58 mag, though with a fairly large error of ± 0.18 mag. Their investigation is based on a variant of the moving cluster method to get distances for each individual cluster member. On the basis of the stated spatial systematic errors in the Hipparcos data Robichon et al. (1999) make an extensive investigation of this problem, which makes use of the method of analyzing Hipparcos intermediate data described by van Leeuwen & Evans (1998). They recalculate the Hipparcos parallaxes and find a distance modulus of 5.36 ± 0.06 mag for the Pleiades which is the value adopted in this paper for comparisons.

Recently, Grenon (1999) has claimed that the Pleiades distance problem is solved by adopting a cluster metallicity of $[\mathrm{Fe/H}]_{\mathrm{Pleiades}} = -0.11$ as determined from Geneva photometry instead of $[\mathrm{Fe/H}]_{\mathrm{Pleiades}} \simeq 0.0$ as determined from high resolution spectroscopy (Boesgaard & Friel 1990). In particular, Geneva photometry points to a large difference in the metallicity of Praesepe and Pleiades ($\Delta[\mathrm{Fe/H}] = 0.28$). To a large extent this explains the offset between the two clusters in various color-magnitude diagrams (Robichon et al. 2000).

The purpose of the current study is to investigate the discrepancy between the Pleiades distance inferred from the Hipparcos mean parallax and from the MS fitting method by comparing Strömgren $uvby - \beta$ photometry of Pleiades F-type stars with field stars having the same metallicity as the Pleiades. We start out with a presentation of the Pleiades cluster and field star data followed by the calibration formulas and selection of stars used for the rest of the reductions. Then the MS fitting analysis is described including the fitting technique, which has been developed to locate the ZAMS of the field star sample, and how we test the age range of the field stars. Furthermore, a metallicity sensitivity analysis is presented and finally we discuss possible answers to the Pleiades problem including the suggestion that the discrepancy in the derived distance moduli could be a real effect caused by the structure of the cluster.

2. MS fitting with Strömgren photometry

The Pleiades, shifted to the distance inferred from the Hipparcos mean parallax, are compared to nearby field stars of the same metallicity in a color-magnitude diagram. This is done to see if the ZAMS defined by the field stars (hereafter denoted $\mathrm{ZAMS_{Field}}$) does coincide with the Pleiades MS. Further, the distance modulus of the Pleiades is inferred from a best fit by the comparison of the Pleiades MS and the $\mathrm{ZAMS_{Field}}$. This investigation also includes a sensitivity analysis of the $\mathrm{ZAMS_{Field}}$ locus to changes in [Fe/H]. The analysis is performed for F-type stars, and in three color/temperature indices $b-y$, $v-y$, and β, to check for robustness and possible hidden errors in the MS fitting technique.

The advantage of using field stars to define the zero point of the distance modulus is that the investigation will be purely empirical, and not affected by some possible lacking ingredients in the theoretical calculations of the isochrones. So this investigation only relies on the Vogt-Russell theorem (Sect. 1). The shape of the Pleiades MS turns out to be very similar to the $\mathrm{ZAMS_{Field}}$ shape and hence we avoid the problem of fitting to isochrones which do not match the cluster MS at every temperature interval. Using F-type stars gives the opportunity to correct for interstellar reddening and to estimate [Fe/H], based on the Strömgren indices and available empirical calibration formulas. The assumed shape of the $\mathrm{ZAMS_{Field}}$ used for the comparison between the Pleiades MS and the field stars is found by a second-order robust least squares fit to the Pleiades stars.

2.1. Data

The $uvby-\beta$ data for the Pleiades is taken from Table II of Crawford & Perry (1976) (hereafter CP76), which contains members classified as F-type stars by CP76. The mean error of one observation, was determined from the internal scatter in the measurements of all the Pleiades stars (Table I CP76), and were given as follows, $\sigma(\beta) = 0.011$, $\sigma(b-y) = 0.009$, $\sigma(m_1) = 0.011$, and $\sigma(c_1) = 0.012$ (CP76). Taking into account that each star has been observed about 5 times we obtain the following typical mean errors of the mean indices of one star: $\sigma(\beta) = 0.005$, $\sigma(b-y) = 0.004$, $\sigma(m_1) = 0.005$, and $\sigma(c_1) = 0.005$ mag.

The magnitudes of the stars in CP76 were adopted from Johnson & Mitchell (1958) (based on the UBV system), so to get the Strömgren values (y transformed to V) the star magnitudes are taken from the WEBDA database (Mermilliod 2000). For about half of the stars the Strömgren value is not available, and the magnitudes are taken to be the average of the V values from UBV observations (also given in the WEBDA database). It is noted that for stars with both $uvby$ and UBV photometry, the V magnitudes agree within ± 0.02 mag.

The field star data has been taken from a catalogue of ∼30 000 stars observed in $uvby-\beta$ (Olsen 1999). This catalogue has been made by merging five published catalogues; all by E. H. Olsen. The sample used in this investigation (F-type stars) is based on three of these catalogues (Olsen 1983, 1988, 1994). The overall rms internal error of one observation is $\sigma(V) = 0.005$, $\sigma(b-y) = 0.004$, $\sigma(m_1) = 0.006$, $\sigma(c_1) = 0.007$, and $\sigma(\beta) = 0.007$. These errors are the conservative ones, in some of the catalogues they were in fact ∼0.002 mag smaller, but the conservative ones are adopted in this investigation. The majority of the stars were observed only once and a few 2 or 3 times, so the errors in the mean photometric values per star are not significantly different from the errors stated above.

The absolute magnitudes are derived using the reddening corrected apparent magnitudes V_0 (transformed from y), and the Hipparcos parallaxes (ESA 1997). The mentioned possible spatial systematic error in the Hipparcos parallaxes does not affect the locus of the $\mathrm{ZAMS_{Field}}$, because it can only have effects on small angular scales, and the field stars are distributed "randomly" all over the sky. Thus the error contributions from the parallaxes in the zero point for the $\mathrm{ZAMS_{Field}}$ is the global parallax error, which is less than 0.1 mas (Arenou et al. 1997).

In addition to the internal errors for the Pleiades photometry by CP76 and for the field stars by Olsen (1999) there could be systematic differences between the two sources. Especially the β index is critical, because the reddening and hence the corrected color indices $(b-y)_0$ and $(v-y)_0$ is determined from β (Sect. 2.2.1). It is, however, very unlikely that systematic errors in β could be large enough to explain the offset between the Pleiades and the field stars, which is of the order of 0.02 mag in β if we adopt the Hipparcos distance modulus of the Pleiades. In this connection we note that photometric observations of the β index is quite straightforward; no extinction correction is needed and the transformation to the standard system is linear without color terms. As discussed by Olsen (1983), systematic differences in β obtained with different telescopes and filter sets are 0.005 mag at most. Furthermore, we note that two of the Pleiades F-type stars from CP76 (Hz II 739 and 948) happen to be in Olsen (1999). The differences (Olsen − CP76) are 0.007 and 0.008, respectively. This does not point to any large systematic errors, and a correction for this difference would in fact increase the offset of the Pleiades with respect to the field stars, but of course we cannot draw any strong conclusions from two stars only.

2.2. Calibration and selection

2.2.1. Reddening

To correct for reddening, the color excess is determined for individual stars as $E(b-y) = (b-y) - (b-y)_0$, where $(b-y)_0$ is found by an iterative calculation based on the empirical calibration given by Crawford (1975a):

$$(b-y)_0 = 0.222 + 1.11\Delta\beta + 2.7\Delta\beta^2 - 0.05\delta c_0 - (0.1 + 3.6\Delta\beta)\delta m_0, \quad (1)$$

where

$$\delta c_0 = c_0 - c_{0,\mathrm{ZAMS}}(\beta),\ \delta m_0 = m_{0,\mathrm{Hyades}}(\beta) - m_0, \quad (2)$$

$$c_0 = c_1 - 0.20 \cdot E(b-y),\ m_0 = m_1 + 0.30 \cdot E(b-y), \quad (3)$$

and $\Delta\beta = 2.72 - \beta$. The standard relation between β, $m_{0,\mathrm{Hyades}}$, and $c_{0,\mathrm{ZAMS}}$ is found by interpolation between the data points given in Table I by Crawford (1975a). The iterative procedure uses the four Strömgren indices for each star, and an initial guess for the color excess as input data. The output (individual color excesses) was obtained when $E(b-y)$ converged at the 0.0001 level. The expected error for $E(b-y)$ is found as

$$\sigma[E(b-y)] = \left[\sigma^2(b-y) + \sigma^2[(b-y)_0]\right]^{1/2}, \quad (4)$$

where

$$\sigma[(b-y)_0] = \left[\sigma^2(\Delta\beta)(1.11 + 5.4\Delta\beta + 3.6\delta m_0)^2 + \sigma^2(\delta m_0)(0.1 + 3.6\Delta\beta)^2 + 0.05^2\sigma^2(\delta c_0)\right]^{1/2}, \quad (5)$$

with $\sigma(\Delta\beta) = \sigma(\beta)$, $\sigma(\delta m_0) \simeq \sigma(m_1)$, and $\sigma(\delta c_0) \simeq \sigma(c_1)$. An estimate of this error is obtained by inserting the mean values of $\Delta\beta$ and δm_0 from the samples. For the Pleiades stars it is $\sigma[E(b-y)]_{\mathrm{Pleiades}} = 0.008$ mag, while it for the field stars is $\sigma[E(b-y)]_{\mathrm{Field}} = 0.010$ mag.

2.2.2. [Fe/H] calibration

To be able to select nearby field stars with the same metallicity as the Pleiades, [Fe/H] is calculated for the Pleiades using the empirical calibrations of Nissen (1981). The calibration formula is as follows:

$$[\mathrm{Fe/H}] = -[10.5 + 50(\beta - 2.626)]\delta m_0 + 0.12 \quad (6)$$

where δm_0 is like in Eq. (2), and the constant of 0.12 is the adopted $[\mathrm{Fe/H}]_{\mathrm{Hyades}}$. The adopted $[\mathrm{Fe/H}]_{\mathrm{Hyades}}$ does not affect the result of the comparison of the Pleiades with the field stars, because it is only relative. But the estimate of the absolute $[\mathrm{Fe/H}]_{\mathrm{Pleiades}}$ value is of course dependent on the assumed $[\mathrm{Fe/H}]_{\mathrm{Hyades}}$. The expected error in this calibration is obtained by a procedure similar to that presented in Sect. 2.2.1, but this time $\sigma(\delta m_0) = \sigma(m_0)$ is used. The results are $\sigma([\mathrm{Fe/H}])_{\mathrm{Pleiades}} = 0.07$ and $\sigma([\mathrm{Fe/H}])_{\mathrm{Field}} = 0.07$.

2.2.3. Reduction step by step

The criterion for being an F-type star is set to be $2.59 < \beta < 2.72$, which is the β range used by Crawford (1975a) and Nissen (1981) for their calibration formulas (reddening and metallicity).

To keep as many Pleiades members as possible, no stars from Table II (CP76) are rejected as a start except Hz II 948 which appear to be a non-member in both CP76 and the WEBDA database. For each member star the reddening is calculated by the procedure described in Sect. 2.2.1, and their photometry measurements are individually corrected. The mean reddening obtained is $\langle E(b-y)\rangle_{\rm Pleiades} = 0.031 \pm 0.004$ mag[1], and the star-to-star rms scatter is $S[E(b-y)]_{\rm Pleiades} = 0.022$ mag. Compared with the expected error of the $E(b-y)$ determination ($\sigma[E(b-y)]_{\rm Pleiades} = 0.008$ mag), this indicates significant star-to-star reddening differences across the cluster. The mean color excess for the Pleiades obtained here is in quite good agreement with former results obtained from other investigations, which in general are in the range of about 0.03–0.04 mag (e.g. Pinsonneault et al. 1998 used $E(b-y) = 0.7 \times 0.04$ mag $\simeq 0.03$ mag; here using the relation between $E(b-y)$ and $E(B-V)$ from Crawford 1975b).

The reddening corrected m_0 values together with the β observations are then used as input in Eq. (6), to get the Pleiades metallicity. The mean value derived is $\langle[{\rm Fe/H}]\rangle_{\rm Pleiades} = 0.01 \pm 0.02$[1]. This value is in very good agreement with spectroscopic results, which mostly come out with a near solar metallicity for the Pleiades (e.g. Boesgaard & Friel 1990). The star-to-star rms scatter is $S([{\rm Fe/H}])_{\rm Pleiades} = 0.13$, which is somewhat larger than the expected error ($\sigma([{\rm Fe/H}])_{\rm Pleiades} = 0.07$).

From the catalogue of field stars, used in this investigation, there are 12 658 stars which have $2.59 < \beta < 2.72$ (thus F-type stars), but 1194 stars of this group do not have Hipparcos parallaxes, so the absolute magnitude could not be derived, and they are therefore rejected. For each star in the remaining sample the reddening is calculated, as described in Sect. 2.2.1, and the photometry of every star is individually corrected. Due to statistical fluctuations and a low mean reddening of the field star sample ($\langle E(b-y)\rangle = 0.009$) some stars turn out to have slightly negative values of $E(b-y)$. In order to avoid any bias these negative values were not changed. Finally, the reddening corrected m_0 values and the β observations can be used as input data in Eq. (6), to derive the metallicity for every star.

We choose a metallicity range of $-0.10 < [{\rm Fe/H}] < 0.12$ which is comparable to the Pleiades mean metallicity plus/minus a representative estimate of the metallicity scatter, and the number of F-type field stars remaining in this interval is 3389. The mean [Fe/H] of the remaining sample is not equal to $\langle[{\rm Fe/H}]\rangle_{\rm Pleiades}$ because the metallicity profile of the original field star sample peaks around [Fe/H] = −0.15, thus [Fe/H] for the remaining sample is slightly shifted (by 0.01 dex) to a lower [Fe/H]. But since this is only half the error of the mean of the Pleiades [Fe/H] the effect is ignored.

150

[1] This value is based on all stars from Table II of CP76 except the likely non-members Hz II 739 and Hz II 948 (see Sect. 2.3).

An additional selection of the field stars is made on the basis of the relative parallax error. If the M_{V_0} vs. $(b-y)_0$ diagram is considered, the error in the absolute magnitude M_{V_0} of the field stars is affected by the errors in V_0, $(b-y)_0$, and the distance modulus (through π, the parallax). From the errors given in Sects. 2.1 and 2.2.1, the error in V_0 can be estimated as: $\sigma(V_0) = [\sigma^2(V) + (4.3\,\sigma[E(b-y)]_{\rm Field})^2]^{1/2} = 0.044$ mag. The size of the effect on $\sigma(M_{V_0})$ from $\sigma[(b-y)_0]$ depends on the slope of the ZAMS in the color region of interest. A test plot is made to find the approximate slope, and it is found to be ∼12. The effect from $\sigma(\pi)/\pi$, on the distance modulus, is found by differentiating the relation $(m-M) = 5\log(\frac{1}{\pi}) - 5$, with respect to π^{-1}, where $(m-M)$ is the distance modulus. This now leads to the following expression:

$$\sigma(M_{V_0}) \simeq [\sigma^2(V_0) + (12\,\sigma[(b-y)_0])^2 + (2.17\,\sigma(\pi)/\pi)^2]^{1/2} \quad (7)$$

The optimized choice of the upper limit of $\sigma(\pi)/\pi$, is when $2.17\,\sigma(\pi)/\pi \sim \max\{\sigma(V_0),\ 12\,\sigma[(b-y)_0]\} \sim 0.12$ mag (where $\sigma[(b-y)_0]_{\rm Field} = 0.010$ mag; Eq. (6)), which suggests $\sigma(\pi)/\pi \sim 0.05$. If a similar consideration is made in the M_{V_0} vs. $(v-y)_0$ or M_{V_0} vs. β diagram, the suggestion would be $\sigma(\pi)/\pi \sim 0.04$. To avoid different samples of field stars in the three investigation parts, parallax measurements to a 5% accuracy are chosen, which left a sample of 782 stars. This seems to be the most reasonable choice, since the sample is large enough to make a clear definition of the ZAMS, and a lower error always is desirable.

2.3. MS fitting analysis

The MS fitting analysis is carried out in three diagrams M_{V_0} vs. $(b-y)_0$, M_{V_0} vs. $(v-y)_0$, and M_{V_0} vs. β. Often only the $(b-y)_0$ case will be illustrated in the figures, but the results of the other diagrams will be given. Though β is not a color, all three diagrams will in the following be denoted color-magnitude diagrams, and the specification "F-type" stars will be omitted, thus "the stars" or "all the stars" simply refers to the sample of F-type stars used in this investigation. A test plot of the Pleiades showed that there was an outlying star which was significantly cooler than the rest of the sample, and ∼1 mag above the Pleiades MS (it has spectral type G0; Mendoza 1956). The star is rejected as a likely non-member. The Pleiades mean color excess and metallicity did not change significantly if the G0 star was included in the sample or not. The changes were only 0.002 mag in the average color excess, and $\langle[{\rm Fe/H}]\rangle$ changed by 0.003 dex.

With the errors stated in Sects. 2.1 and 2.2.1 the estimated error per one star in M_{V_0} for the field stars (Eq. (7)), is in the range of 0.14–0.17 mag for all three examined color-magnitude diagrams (smallest for the $(v-y)_0$ diagram, and largest for the $(b-y)_0$ and β diagrams, which is expected since the ZAMS in the $(v-y)_0$ diagram is less steep than in the other two diagrams).

In Fig. 1 the field stars are plotted together with the Pleiades stars adopting the Hipparcos mean parallax of

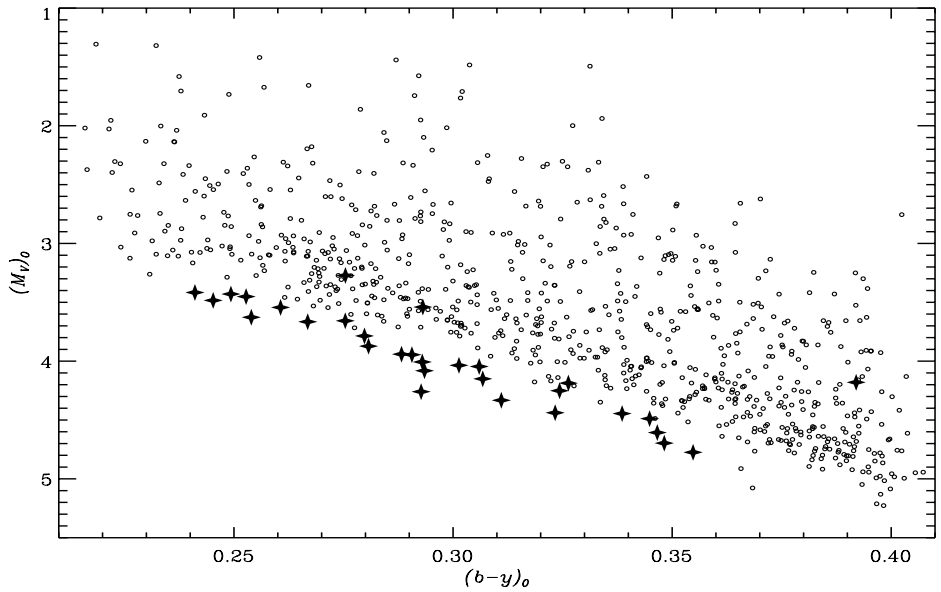

Fig. 1. Color-magnitude diagram of the selected field stars with $-0.10 <$ [Fe/H] < 0.12 and $\sigma(\pi)/\pi < 0.05$ (empty circles), compared to the Pleiades (filled stars) adopting the Hipparcos inferred distance modulus of 5.36 mag (from Robichon et al. 1999). The Pleiades star at the cooler end of the diagram is a G0 star and most likely a non-member, and the two stars (Hz II 1338 and 1912) about 0.6 mag brighter than the mean relation defined by the others Pleiades stars are binaries.

the cluster. This plot clearly shows the discrepancy between the locus of the field stars and that of the Pleiades. The plots in all three color-magnitude diagrams look quite similar. In addition to the deviating G0 star there are two Pleiades stars (Hz II 1338 and 1912) which are ∼0.6 mag brighter than the mean relation defined by the others. According to Mermilliod et al. (1992), one of the stars is a spectroscopic binary, and the other a visual binary, in agreement with their shift in brightness.

2.3.1. The stellar magnitude distribution

To get an estimate of the distance modulus of the Pleiades we have to analyze the magnitude distribution, relative to the Pleiades MS, of the field stars which define our zero point of the ZAMS locus. The observed magnitude distribution is a convolution of the underlying evolutionary distribution of the field star sample and a Gaussian profile coming from the observational errors in M_{V_0}.

A robust least squares fit (second-order) (Freudenreich 1999) of the Pleiades MS is made in the V_0 vs. color diagrams. The derived polynomial of the Pleiades MS is used to define the shape of the $\mathrm{ZAMS_{Field}}$. To find the distance modulus of the Pleiades the polynomial is shifted by the magnitude which make it fit to the $\mathrm{ZAMS_{Field}}$. The advantage of this method is that the robust least squares fit of the Pleiades MS will not be significantly affected by the stars which lie far from the Pleiades MS. This means that e.g. double stars will not bias the locus of the Pleiades MS significantly. The disadvantage is that the shifted Pleiades MS fit may not match the $\mathrm{ZAMS_{Field}}$ perfectly, because the shape of the fitted Pleiades MS is sensitive to the small sample of Pleiades data points (29 stars). The shifting of the Pleiades MS is done by calculating the individual distance moduli of every field star with respect to the polynomial fit of the Pleiades MS. This give the magnitude distribution of the field stars relative to the Pleiades MS. All the distance moduli are evaluated as input in the likelihood function which is the simultaneous probability function of all data points. The probabilities of the individual data points are described by the result of the convolution mentioned above. The underlying evolutionary distribution is approximated by $\propto \exp(-x/\tau)$ with a sharp edge at the $\mathrm{ZAMS_{Field}}$ locus, where τ is the fall-off rate due to evolution and binarity of the star sample. The width of the Gaussian is characterized by the observational error $\sigma(M_{V_0})$. The mathematical expression of the convoluted function is:

$$f(u) = \frac{p_1}{p_2}\exp\left(\frac{p_4^2}{2p_2^2} - \frac{u-p_3}{p_2}\right)\frac{1}{\sqrt{2\pi}p_4}\int_{-\infty}^{y}\exp\left(-\frac{v^2}{2p_4^2}\right)\mathrm{d}v$$
$$= \frac{p_1}{2p_2}\exp\left(\frac{p_4^2}{2p_2^2} - \frac{u-p_3}{p_2}\right)\left(1+\mathrm{Errf}\left(\frac{y}{\sqrt{2}p_4}\right)\right) \quad (8)$$

where $y = u - p_3 - p_4^2/p_2$, p_1 is the normalization constant, $p_2 = \tau$, p_3 is the $\mathrm{ZAMS_{Field}}$ locus, $p_4 = \sigma(M_{V_0})$, and Errf(t) is the IDL error function. A best fit is obtained when the likelihood function takes its maximum value which we find by changing τ, $\sigma(M_{V_0})$, and the locus of the sharp edge of the $\mathrm{ZAMS_{Field}}$ as free parameters.

The underlying evolutionary distribution (dashed line) together with the convoluted function of best fit (thick line) is shown in Fig. 2. Additionally, the individual distance moduli are binned and over plotted to illustrate the

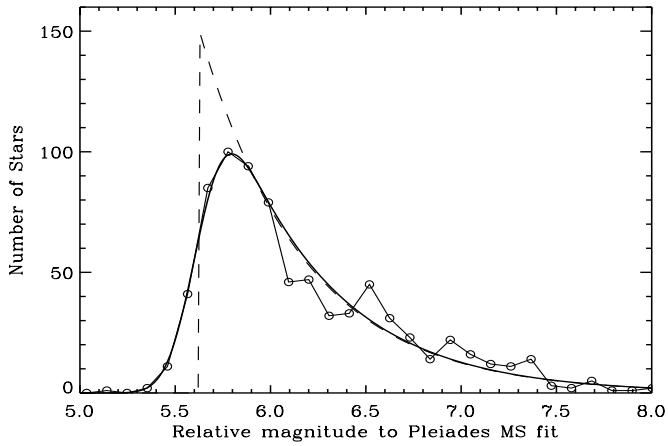

Fig. 2. The field star magnitude distribution, with respect to the polynomial fit of the Pleiades MS, in the M_{V_0} vs. $(b-y)_0$ diagram. Empty circles shows the individual distance moduli binned, with a bin size of 0.1 mag and connected with the thin line. Dashed line indicates the assumed underlying star distribution without observational errors defining the point of the $\mathrm{ZAMS_{Field}}$. The thick line is the best fit to the data of the convolution of the underlying star distribution with a Gaussian profile which corresponds to the observational error.

field star magnitude distribution for comparison (thin line and empty circles). The point of the $\mathrm{ZAMS_{Field}}$, is the vertical dashed line.

The fitted $\sigma(M_{V_0})_{\mathrm{Field}}$ for all three color-magnitude diagrams end up in the range 0.12–0.13 mag which is near the expected errors derived in Sect. 2.3 on page 108. It indicates that the shape of the Pleiades polynomial matches the $\mathrm{ZAMS_{Field}}$ shape very well in all three color-magnitude diagrams. The Pleiades distance modulus found by the fits are: 5.62 ± 0.02 mag, 5.61 ± 0.02 mag, and 5.61 ± 0.03 mag in the $(b-y)_0$, $(v-y)_0$, and β diagram respectively. The stated errors are the quadrature sum of two errors. The first comes from the uncertainty in the vertical positions of the Pleiades MS fits, which is the star to star scatter around the Pleiades MS fit divided by the square root of the number of stars ($S_{V_0,\mathrm{Pleiades}}(\text{Pleiades MS fit})/\sqrt{\#\text{stars}}$). For the three color-magnitude diagrams these errors are: 0.019 mag, 0.017 mag, and 0.031 mag in the $(b-y)_0$, $(v-y)_0$, and β diagram respectively[2]. The second error is found as the points where the log likelihood function has fallen by 0.5 from its maximum value by changing the Pleiades distance modulus step by step around its optimum value, and optimizing the two other parameters for every step. The $\pm 1\sigma$ interval is approximated by a symmetric interval around the maximum value by a parabola fit of the log likelihood function. This approximation gives sufficient precision. For the three color-magnitude diagrams these errors are: 0.014 mag, 0.015 mag, and 0.015 mag in the $(b-y)_0$, $(v-y)_0$, and β diagram respectively.

It is important that the left tail of the field star's magnitude distribution is fitted well because this is the region where the $\mathrm{ZAMS_{Field}}$ has to be found. The extremely good fit at the left tail of Fig. 2 supports the trustfulness of the method used in this investigation. The right tail is more affected by the evolutionary and binary distribution of the field star sample, and it could be argued that the assumed exponential fall-off at the right part of the profile is rather simplified, but changing it would not affect the fitted $\mathrm{ZAMS_{Field}}$ locus significantly because this part of the diagram is separated by several standard errors from the $\mathrm{ZAMS_{Field}}$ locus.

The method of finding the distance modulus presented here seems very robust because the distance moduli, errors in the distance moduli and $\sigma(M_{V_0})$ are consistent with one another and their estimates in the three color-magnitude diagrams. By changing the underlying evolutionary distribution it is seen that the estimated distance moduli are quite stable. We consider the following different underlying star distributions. Assume the underlying fall-off to be in two steps. First a rather steep fall-off followed by a less steep fall-off. This scenario would fit the Gaussian to be wider (but could still be consistent with the estimates given in Sect. 2.3 on page 108), and the Pleiades distance modulus would be fitted to be slightly larger ($\mathrm{ZAMS_{Field}}$ closer to observed maximum density). The only way to get a lower estimated distance modulus is by assuming a slower fall-off for the right tail of the underlying distribution; the extreme being a wide box function with one edge at the $\mathrm{ZAMS_{Field}}$. Under this assumption the $\mathrm{ZAMS_{Field}}$ will be at the point of half maximum of the observed distribution, which in this case means a lower distance modulus by less than 0.05 mag, but at the cost of an unacceptable bad fit to the data. One can of course get an even lower estimate if it is assumed that the underlying star density will increase on the right side of the $\mathrm{ZAMS_{Field}}$ in Fig. 2, which means that the maximum density of the underlying distribution is above the $\mathrm{ZAMS_{Field}}$. But the extremely good fits at the left tail (Fig. 2) and the consistent determinations of the Gaussian widths tell us that the underlying star distribution must have a sharp edge as indicated in Fig. 2. To see if the field star sample does indeed contain stars not evolved significantly away from the ZAMS, the sample is compared with a series of isochrones in Sect. 2.3.2, and the assumed underlying evolutionary distribution is tested by the aid of evolutionary tracks.

Figure 3 shows a plot similar to Fig. 1, but instead of the adopted Pleiades distance modulus of Hipparcos the estimated value of 5.62 mag, which make the fitted Pleiades MS polynomial match the $\mathrm{ZAMS_{Field}}$, has been used. Furthermore, the polynomial fit to the Pleiades MS is shown, shifted by 5.62 mag (solid line) and by 5.36 mag (dashed line). It is easy to see that the Pleiades shifted by 5.62 mag gives a much better fit to the field stars compared to the Hipparcos value.

[2] These errors are from slightly around one to 3/2 times larger than the pure observational scatter in $V_{0,\mathrm{Pleiades}}$ and show different real effects like binarity, which introduces extra scatter around the perfect ZAMS locus.

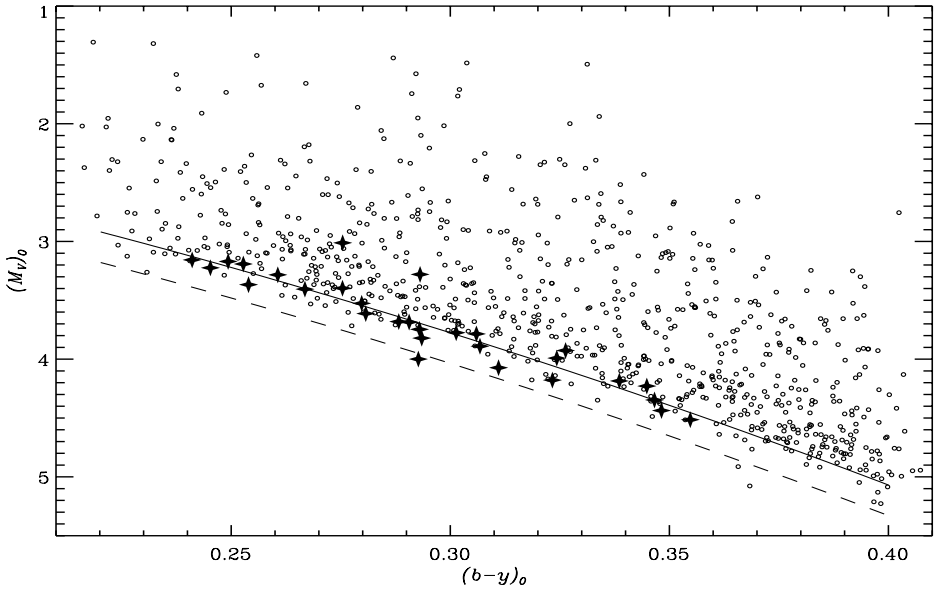

Fig. 3. Color-magnitude diagram of the selected field stars with $-0.10 <$ [Fe/H] < 0.12 and $\sigma(\pi)/\pi < 0.05$ (empty circles), compared to the Pleiades (filled stars) (excluding the likely non-member) adopting the distance modulus of 5.62 mag, which make the Pleiades MS match the $\mathrm{ZAMS_{Field}}$. The solid line is the polynomial fit to the Pleiades MS, and the dashed line indicates the location of the Pleiades MS according to the Hipparcos distance.

2.3.2. The age range

The age of the field star sample which is used to determine the Pleiades distance modulus is analyzed by plotting isochrones of different ages together with the field stars.

The isochrones used are taken from Lejeune & Schaerer (2001), those they denote as "basic grid" with solar metallicity. The effective temperature coming from the isochrones is transformed to the $(b-y)_0$ color index by the calibration of Alonso et al. (1996) using a mean value of the c_1 index in their Eq. (9). The possible systematic error in $(b-y)_0$ from this transformation is of the order of 0.02 mag.

Figure 4 shows the field stars in the color-magnitude diagram and five isochrones of ages: 100 Myr, 500 Myr, 1 Gyr, 1.5 Gyr, and 2 Gyr. It is evident that the sample of field stars contains many stars with ages below or around 1.5 Gyr, which are all the stars at the left side of or around the 1.5 Gyr isochrone. Since we safely can assume that the age of the field stars is distributed uniformly in the plotted color range there must also be many field stars of ages around or less than 1.5 Gyr at the right side of the plot say in the range $0.30 < (b-y)_0 < 0.40$. There may be a systematic offset of the isochrones with respect to the $\mathrm{ZAMS_{Field}}$ due to systematic errors in the $T_{\rm eff}$ calibration, but Fig. 4 shows that the evolutionary effects on the isochrones from 100 Myr (approximate age of the Pleiades cluster) to 1.5 Gyr is rather negligible in the color range $0.30 < (b-y)_0 < 0.40$. In that range we still see the discrepancy between the position of the Pleiades and the $\mathrm{ZAMS_{Field}}$ if the Hipparcos distance is adopted. Hence,

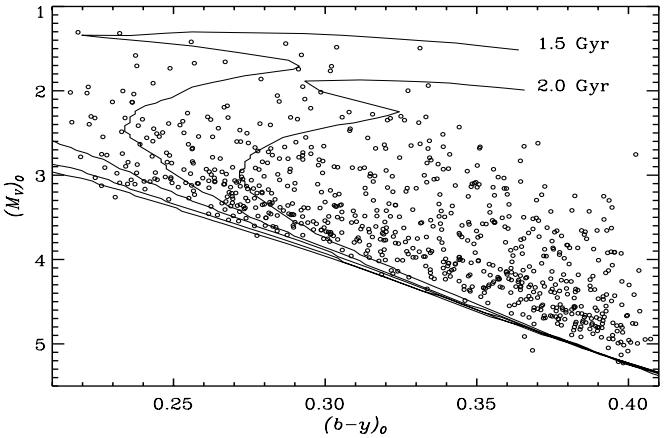

Fig. 4. Color-magnitude diagram of the selected field stars with $-0.10 <$ [Fe/H] < 0.12 and $\sigma(\pi)/\pi < 0.05$, compared to five isochrones representing the ages: 100 Myr, 500 Myr, 1 Gyr, 1.5 Gyr, and 2 Gyr.

we conclude that the discrepancy cannot be explained as due to evolution away from the ZAMS of the field star population.

As an additional check, evolutionary tracks from Lejeune & Schaerer (2001) have been used to calculate the theoretical stellar magnitude distribution at a given $(b-y)_0$ in order to see how well it agrees with the underlying evolutionary distribution of M_V adopted in Sect. 2.3.1. We assume a constant star formation rate for solar metallicity stars over the lifetime of the galactic disk (∼8 Gyr) in agreement with the age-metallicity diagram

(Fig. 14) of Edvardsson et al. (1993), and a constant initial mass function over the small mass range corresponding to a given $(b-y)_0$. The calculated magnitude distribution is similar to the underlying evolutionary distribution of M_V adopted in Sect. 2.3.1, i.e. with a sharp edge at the ZAMS and a steep evolutionary fall-off. The fall-off is less steep at the blue end of the $(b-y)_0$ range and somewhat steeper at the red end, and the fall-off has a tendency of a two-step function; first a steeper part followed by a less steep part. As discussed in Sect. 2.3.1 on page 110 this could indicate that our fitted Pleiades distance modulus is slightly underestimated. Altogether, we conclude that the assumed underlying evolutionary magnitude distribution of our field stars is supported by models for the stellar evolution.

2.4. [Fe/H] sensitivity of $ZAMS_{Field}$

It is known that the ZAMS locus is dependent on the metallicity, such that low metallicity stars define a fainter ZAMS than the high metallicity stars. To be able to test if the discrepancies in the Pleiades distance could be explained as a possible error in the adopted Pleiades metallicity, we have analyzed how much the locus of the $\mathrm{ZAMS_{Field}}$ changes as a function of the metallicity.

The selected sample for this part of the investigation consists of all F-type field stars in the catalogue of Olsen (1999), which have a relative error in the parallax measurement less than 5%. This selection gives a sample of 2309 stars. Five plots, each representing field stars in different metallicity intervals, are then made. The intervals are ± 0.10 dex wide in [Fe/H], ranging from -0.45 to $+0.15$ dex, and with a 0.10 dex overlap from one interval to the next.

Distance moduli for the Pleiades are found for the five metallicity intervals in all three color-magnitude diagrams. The method is similar to that presented in Sect. 2.3.1, and the individual distance moduli from every diagram is plotted together in Fig. 5. The indicated error bars in Fig. 5 are larger for the data points representing the lower metallicity intervals, which is a result of less stars falling in the lower metallicity bins. By analyzing the fits to the field star density profile of the lower metallicity intervals it was observed that the fitting function (see Sect. 2.3.1 Eq. (8)) did not fit the left tail of the distribution as well as shown in Fig. 2 simply because of the few data points available. Linear least squares fits are made to the result of all three color-magnitude diagrams in the metallicity range $-0.35 < \mathrm{[Fe/H]} < 0.05$ (dashed lines), and additional fits where the two lowest metallicity points are ignored (solid lines).

The metallicity sensitivity from the three color-magnitude diagrams is found to be (solid lines):

$$\begin{aligned} \Delta\langle M_{V_0}\rangle_{\mathrm{ZAMS}} &= +0.01(9)\,\Delta\mathrm{[Fe/H]}, \text{ from } \beta \\ \Delta\langle M_{V_0}\rangle_{\mathrm{ZAMS}} &= -0.40(9)\,\Delta\mathrm{[Fe/H]}, \ (b-y)_0 \\ \Delta\langle M_{V_0}\rangle_{\mathrm{ZAMS}} &= -0.76(9)\,\Delta\mathrm{[Fe/H]}, \text{ and } (v-y)_0. \end{aligned} \qquad 154$$

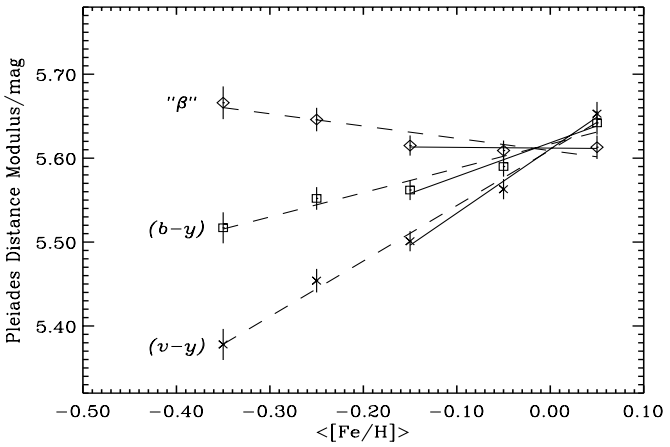

Fig. 5. Metallicity sensitivity of the $\mathrm{ZAMS_{Field}}$ in the three investigated color-magnitude diagrams: β (diamonds), $(b-y)$ (squares), and $(v-y)$ (×'s). Solid and dashed lines are least squares fits (see text).

The trend is the same for both solid and dashed lines, though solid lines show a higher metallicity sensitivity in $(b-y)_0$ and $(v-y)_0$ and no significant sensitivity in the β diagram. We believe that the relations indicated by the solid lines are the most correct since the lower metallicity bins may suffer from small evolutionary effects due to a larger percentage of more evolved stars. That the highest metallicity sensitivity is observed in the $(v-y)_0$ diagram and the lowest in the β diagram is expected since line blanketing from the metal lines affects the spectrum more at the short wavelengths, thus v is more affected than b which is again more affected than y. We note that Grenon (1999) finds a much larger shift $\Delta\langle M_{V_0}\rangle_{\mathrm{ZAMS}} = -1.67\,\Delta\mathrm{[Fe/H]}$ based on Geneva photometry, though the error of the metallicity sensitivity coefficient is not given. His relation refers, however, to early K-dwarfs and it is not clear on which color index it is based. A direct comparison can therefore not be made to the shifts we are finding for the F-type stars.

Figure 5 supports that the metallicity of the Pleiades is around the solar value as determined from the m_1 index if the adopted Hyades metallicity is ∼0.12 dex. Only for this metallicity can we get consistent results of the distance modulus from all three color-magnitude diagrams. The inferred distance modulus is in the range 5.58–5.64 mag. We also see that a Hipparcos distance modulus of 5.36 mag is not consistent with one metallicity value. The $(v-y)_0$ diagram demands $\mathrm{[Fe/H]} \sim -0.35$, the $(b-y)_0$ diagram $\mathrm{[Fe/H]} \sim -0.70$, and the β diagram cannot be fitted to a distance modulus of 5.36 mag no matter the chosen metallicity of the field stars.

From the above metallicity sensitivity analysis one could conclude that the β diagram gives the most reliable estimate of the distance modulus, because it is rather insensitive to metallicity deviations between field stars and Pleiades stars, and furthermore it is insensitive to interstellar reddening. It should, however, be remembered that

the β diagram has the largest error in the distance modulus determination (0.03 mag); 3/2 the size of the $(b-y)_0$ and $(v-y)_0$ diagram errors. If we combine the distance moduli from all three color-magnitude diagrams the final distance modulus is: $(m-M)_0 = 5.61 \pm 0.03$ mag [3].

3. Discussion and conclusion

The extensive multi color MS fitting analysis based on Strömgren photometry (this paper) gives a Pleiades distance modulus of 5.61 ± 0.03 mag (the mean value from all three color-magnitude diagrams), which is in very good agreement with the distance modulus given by the multi color MS fitting analysis of Pinsonneault et al. (1998) who find a distance modulus of 5.60 ± 0.05 mag. On the other hand, the distance modulus derived from the Hipparcos parallaxes are all in the range of 5.33–5.37 mag, which is not consistent with the former results, and the quoted errors. Even if the quoted errors from MS fitting are not representative for the actual uncertainty in this method, it must, from the current investigation, be concluded that the Hipparcos distance modulus is not consistent with the ZAMS of nearby field stars (Fig. 1). Thus, either are the Hipparcos parallaxes affected by systematic errors, which are significantly larger than expected, or there is something unexpected about the Pleiades cluster.

If the discrepancy is caused by some anomaly of the Pleiades, one possible explanation is the metallicity. Extensive investigation of this possibility has been performed (e.g. Pinsonneault et al. 1998 and the current investigation presented in Sect. 2.4), and from these results, supported by the spectroscopic metallicity determination by Boesgaard & Friel (1990), it seems very unlikely that the adopted Pleiades metallicity around the solar value is more than 0.05 dex from the true value. Even a deviation of 0.1 dex is far too small to explain the discrepancy and it would lead to inconsistent results from the different color-magnitude diagrams. In addition, the relative comparison between the Pleiades and field stars of the same metallicity (Sect. 2) ensures that the possible difference in the relative metallicities are so small that a metallicity deviation can be ruled out. Hence, we cannot confirm the recent claim by Grenon (1999) that the Pleiades problem is solved by adopting a low metallicity, $[\mathrm{Fe/H}]_{\mathrm{Pleiades}} = -0.11$, of the cluster. Furthermore, the large metallicity difference between the Hyades and the Pleiades based on Geneva photometry, $\Delta[\mathrm{Fe/H}] = 0.25 \pm 0.03$, is inconsistent with the difference, $\Delta[\mathrm{Fe/H}] = 0.11 \pm 0.03$, which we derive from Strömgren photometry.

Another possibility is an abnormal helium abundance of the Pleiades. To see which value of Y would be required to change the Pleiades MS locus by 0.3 mag, a calculation is made by Pinsonneault et al. (1998), who find that the value is as high as $Y \simeq 0.37$. The study of Nissen (1974) revealed no intrinsic scatter in Y greater than approximately 10% in nearby MS field B stars; much smaller than the 30%–40% change in Y required for the Pleiades. There are, however, investigations which indicate large cluster to cluster scatter in the helium abundance (Nissen 1976; Lyubimkov 1977), and it has been suggested that this is the key explanation to the Hyades c_1-anomaly (Strömgren et al. 1982). To test if this is the explanation of the Pleiades problem too, an attempt should be made to measure the surface helium abundance of the hot stars in the Pleiades and other young clusters spectroscopically.

Recently, van Leeuwen (1999) has suggested that the Pleiades problem is caused by an age effect, and claims that other very young open clusters show the same deviation as the Pleiades. The investigation of van Leeuwen (1999) is based on a comparison in the color-magnitude diagram (with the metallicity-sensitive $B-V$ color) of nine open clusters, all shifted to their Hipparcos mean distance. But this is done without correcting for differences in the metallicity abundances first. A test of the age effect is made by Pinsonneault et al. (2000), based on 8 clusters (incl. the Hyades and Pleiades) and no age effect is seen in the difference between the MS fitting and Hipparcos distances. If the youth of the Pleiades has a significant effect on the Pleiades MS locus, one might also expect that young field stars would show the same effect. The study of Soderblom et al. (1998) of chromospherically active (and therefore assumed young) stars gave, however, no indications of that. In our own sample of field stars very few are expected to be as young as the Pleiades so we cannot test the suggestion of van Leeuwen (1999). It should be emphasized, however, that the explanation given by van Leeuwen (1999) of the Pleiades problem as an age effect, mostly relies on the relative shift between the Pleiades and Hyades in the temperature range where no obvious evolutionary effects away from the ZAMS are seen (corresponding to $(b-y)_0 > 0.30$ mag or $(B-V)_0 > 0.50$ mag). Furthermore, the age explanation of van Leeuwen (1999) is in disagreement with theoretical models of stellar evolution, which predict negligible evolution away from the ZAMS during the first couple of billion years of the lifetime of late F-type stars (see isochrones in Fig. 4).

Some investigations give hints of spatial systematic errors in the Hipparcos parallaxes which are larger than expected (Pinsonneault et al. 1998; Narayanan & Gould 1999). In addition, there is a statistical correlation caused by the imperfect distribution of data points over the ellipse described by the parallactic motion. In particular, for a star on the ecliptic, equal numbers of measurements should be obtained on both sides of the Sun. This was not fulfilled for Hipparcos, and caused correlations (ρ_α^π) between right ascension and parallax (ESA 1997, vol. 1, p. 325). Pinsonneault et al. (1998) questioned if this type of correlation would have an effect on the parallax values. But from the extensive test by Robichon et al. (1999) of this issue it must be concluded that the correlations

[3] The distance modulus found by CP76, based on all 30 member stars in their Table II, was $(m-M)_0 = 5.53 \pm 0.04$ mag, and by rejecting four stars, probably double stars or non-members, their result was $(m-M)_0 = 5.60 \pm 0.03$.

ρ_α^π do not introduce significant errors in the Hipparcos parallaxes.

What if the whole controversy, about the Pleiades distance modulus, is caused by a real effect? What will the effects on the MS fitting and Hipparcos results be, if the cluster is non-spherical (sphericity has until now been implicitly assumed)? The angular size of the Pleiades cluster can be approximated by the size of the region covered by the member stars used in the investigation of e.g. Narayanan & Gould (1999). This gives a radius of $\sim 6^\circ$ which, at a distance of 130 pc, corresponds to a radius of $\simeq$14 pc. A typical real difference in the cluster member distances would then be around 14 pc which corresponds to a 1 mas difference in the parallax. There is no reason why non-sphericity of the Pleiades should not be the case. There is plenty of evidence that open clusters can be non-spherical e.g. NGC 2264 (the Cone Nebulae), and actually Raboud & Mermilliod (1998) have shown that the distribution of the Pleiades stars projected on the sky is elliptical with an ellipticity of 0.17. It could be that the cluster has a more oblong shape in the direction of the line of sight say with a length that is twice the projected diameter. One could then imagine the following scenario: the first born bright stars (O and B-type) forms in one part of the gas cloud, and they start to blow the gas cloud in one initial direction, and therefore these stars will end up at one end of this deformed shape (as observed in the NGC 2264 case), and the fainter stars (F and G-type) will form a "tail" (as an overall trend). So if we see this shape head-on there will be a trend that the brightest B-type stars are closer to us, and the later classes are further away. Because the calculation of the Hipparcos mean parallax gives the largest weight to the brighter stars, the result will be a slightly shorter distance than the actual mean cluster distance (Pinsonneault et al. 1998, Fig. 20). On the other hand, the MS fitting method relies mostly on the fainter stars (A to G-type), which are farther away. These stars are located in the color-magnitude diagram, where the slope of the ZAMS is less steep, and therefore they give the smallest errors in the distance estimates (additionally for many clusters the hotter stars are also evolved away from the ZAMS). So this means that the distance found from MS fitting will be larger than found from Hipparcos parallaxes, and possibly closer to the actual mean cluster distance. Such oblong shape of the cluster, could indicate a kinematic history that does not follow the usual assumptions, which also explains why Robichon et al. (1999) find unusual features in the kinematics of the Pleiades. The consequence of this is that the assumptions used by Narayanan & Gould (1999) does not hold. One could argue that if the Pleiades have such non-spherical shape, it would be expected that some fainter stars (which have larger distances) were present near the center of the cluster in e.g. Fig. 20 of Pinsonneault et al. (1998). But if there is a dark cloud just behind the bright stars as in the NGC 2264 case, none of these stars will be observed.

The idea of a deformed Pleiades cluster is a tempting answer to the Pleiades problem, because it includes most of the evidence presented in this discussion. What is described above, as a possible non-spherical Pleiades cluster, shall be viewed as an illustration or example of the possible effects on the distance determination, due to a deformed and non-symmetrical cluster. Though there are studies of the velocity dispersion among Pleiades cluster members (van Leeuwen 1994) and mass segregation (Raboud & Mermilliod 1998) suggesting that the Pleiades is a bound and quite relaxed system, it could be very interesting to investigate the possibility of a non-symmetrical cluster by e.g. extensive kinematic analysis of the Pleiades. Furthermore, future astrometric space programs will be capable of determining the distances to the individual Pleiades stars with an improved accuracy of 2 to 3 orders of magnitude, compared with Hipparcos. These measurements will provide a very good three-dimensional picture of the Pleiades cluster.

Acknowledgements. We thank F. Grundahl for the merging of The Hipparcos Catalogue and the field stars catalogue, used in this investigation. This research has made use of the SIMBAD database, operated at CDS, Strasbourg, France.

References

Alonso, A., Arribas, S., & Martinez-Roger, C. 1996, A&A, 313, 873
Arenou, F., Mignard, F., & Palasi, J. 1997, in The Hipparcos and Tycho Catalogues, vol. 3, ESA SP-1200 (Paris: ESA), 433
Boesgaard, A. M., & Friel, E. D. 1990, ApJ, 351, 467
Crawford, D. L. 1975a, AJ, 80, 955
Crawford, D. L. 1975b, PASP, 87, 481
Crawford, D. L., & Perry, C. L. 1976, AJ, 81, 419 (CP76)
Edvardsson, B., Andersen, J., Gustafsson, B., et al. 1993, A&A, 275, 101
Eggen, O. J. 1998, AJ, 116, 1810
European Space Agency 1997, The Hipparcos and Tycho Catalogues, ESA SP-1200 (Paris: ESA)
Freudenreich, H. 1999, The IDL Astronomy User's Library, `http://idlastro.gsfc.nasa.gov/homepage.html`
Grenon, M. 1999, in Proc. of 11th Cambridge workshop on cool stars, in press
Johnson, H. J., & Mitchell, R. I. 1958, ApJ, 128, 31
van Leeuwen, F. 1994, in Galactic and Solar System Optical Astrometry, ed. L. V. Morrison, & G. F. Gilmore (Cambridge University Press), 223
van Leeuwen, F. 1999, A&A, 341, L71
van Leeuwen, F., & Evans, D. W. 1998, A&AS, 130, 157
Lejeune, T., & Schaerer, D. 2001, A&A, 366, 538
Lindegren, L. 1988, in Scientific Aspects of the Input Catalogue Preparation II, ed. J. Torra, & C. Turon (Noordwijk: ESA), 179
Lindegren, L. 1989, in The Hipparcos Mission, ESA SP-1111, vol. III, ed. M. A. C. Perryman, et al. (Noordwijk: ESA), 311
Lindegren, L., Froeschle, M., & Mignard, F. 1997, in The Hipparcos and Tycho Catalogues, vol. 3, ESA SP-1200 (Noordwijk: ESA), 323
Lyubimkov, L. S. 1977, Astrofizika, 13, 139

Mendoza, E. E. 1956, AJ, 123, 54
Mermilliod, J.-C., Rosvick, J. M., Duquennoy, A., & Mayor, M. 1992, A&A, 265, 513
Mermilliod, J.-C., Turon, C., Robichon, N., Arenou, F., & Lebreton, Y. 1997, in Hipparcos Venice 97, ed. B. Battrick, & M. A. C. Perryman (Paris: ESA), 643
Mermilliod, J.-C. 2000, WEBDA-Database, `http://obswww.unige.ch/webda/webda.html`
Narayanan, V. K., & Gould, A. 1999, ApJ, 523, 328
Nissen, P. E. 1974, A&A, 36, 57
Nissen, P. E. 1976, A&A, 50, 343
Nissen, P. E. 1981, A&A, 97, 145
Olsen, E. H. 1983, A&AS, 54, 55
Olsen, E. H. 1988, A&A, 189, 173
Olsen, E. H. 1994, A&AS, 106, 257
Olsen, E. H. 1999, Catalogue of *uvby-β* photometry of ∼30 000 stars, private communication
Pinsonneault, M. H., Stauffer, J. R., & Hanson, R. B. 1998, ApJ, 504, 170
Pinsonneault, M. H., Terndrup, D. M., & Yuan, Y. 2000, ASP Conf. Ser. 198, Stellar Clusters and Associations, ed. R. Pallavicini, G. Micela, & S. Sciortino, 95
Raboud, D., & Mermilliod, J.-C. 1998, A&A, 329, 101
Robichon, N., Arenou, F., Mermilliod, J.-C., & Turon, C. 1999, A&A, 345, 471
Robichon, N., Lebreton, Y., Turon, C., & Mermilliod, J.-C. 2000, ASP Conf. Ser. 198, Stellar Clusters and Associations, ed. R. Pallavicini, G. Micela, & S. Sciortino, 141
Soderblom, D. R., King, J. R., Hanson, R. B., et al. 1998, ApJ, 504, 192
Strömgren, B., Olsen, E. H., & Gustafsson, B. 1982, PASP, 94, 5